Mathematical and numerical modeling of turbulent reactive flows using a hybrid LES / PDF methodology

João, Marcelo Vedovoto

THÈSE

Pour l'obtention du Grade de

DOCTEUR DE L'ECOLE NATIONALE SUPERIEURE DE MECANIQUE ET D'AEROTECHNIQUE

(Diplôme National - Arrêté du 7 août 2006)

Ecole Doctorale : SI MMEA, Sciences et Ingénierie en Matériaux, Mécanique, Energétique et Aéronautique

Secteur de Recherche : Energétique, Thermique, Combustion

Présentée par:

João Marcelo VEDOVOTO

****

Mathematical and numerical modeling of turbulent reactive flows using a hybrid LES / PDF methodology

****

Directeurs de Thèse : **Arnaud MURA** et **Aristeu da SILVEIRA NETO**

****

Soutenue le 18 Novembre 2011 devant la commission d'examen

****

- Jury -

M. P. HALDENWANG,	Professeur Université de Provence Marseille, Rapporteur
M. D.A. RADE,	Professeur UFU Uberlandia, Rapporteur
M. J. REVEILLON,	Professeur Université de Rouen, President
M. F.J. SOUZA,	Professeur UFU Uberlandia, Examinateur
M. L.F. FIGUEIRA DA SILVA,	Professeur PUC-Rio, Rio de Janeiro, Examinateur
M. A. DA SILVEIRA NETO,	Professeur UFU, Uberlandia, Examinateur
M. A. MURA,	Chargé de Recherche au CNRS, Institut P', Poitiers, Examinateur

JOÃO MARCELO VEDOVOTO

Mathematical and numerical modeling of turbulent reactive flows using a hybrid LES / PDF methodology

UNIVERSIDADE FEDERAL DE UBERLÂNDIA
FACULDADE DE ENGENHARIA MECÂNICA
2011

JOÃO MARCELO VEDOVOTO

Mathematical and numerical modeling of turbulent reactive flows using a hybrid LES / PDF methodology

Tese apresentada ao Programa de Pós-graduação em Engenharia Mecânica da Universidade Federal de Uberlândia e a Escola doutoral da École Nationale Supérieure de Mécanique et d'Aérotechnique - ENSMA, como parte dos requisitos para a obtenção do título de **DOUTOR EM ENGENHARIA MECÂNICA e DOCTEUR DE L'ENSMA**.

Área de concentração: Transferência de Calor e Mecânica dos Fluidos.

Orientadores: Prof. Dr. Aristeu da Silveira Neto e Dr. Arnaud Mura
Co-Orientador: Prof. Dr. Luis Fernando Figueira da Silva

Uberlândia - MG
2011

To my family

ACKNOWLEDGEMENTS

I would like to express my sincere gratitude to my supervisors Aristeu, Arnaud e Luis Fernando for being examples to be followed. Without their guidance, encouragement and specially patience, this work would not be possible.

Ao CNPq, CAPES, FAPEMIG and PETROBRAS for the financial support and to the School of Mechanical Engineering of the Federal University of Uberlandia, Institute Pprime and ENSMA for all the material support.

To my friends at the MFLab and FEMEC, Zé Reis, Sigeo, Lisita, Ricardo, Leonardo, Felipe, Mariana, Diego, Denise, Gustavo Prado, Gustavo Pires, Pivello, Renato, Rodrigo and Luismar, for the great moments passed in the last four years. Thanks to Tiago Assis Silva and Millena Martins Villar Valle for the friendship and for the great Fortran tips.

To my fiancée Karina, for the support, comprehension, for your love and for always believing in me and don't let me .

Merci aussi aux mes amis de l'ENSMA: Danilo, Tiago, Pedro, Ruben, Laurent et Jean François. Et un merci toute spécial à Madame Jocelyne Bardeau, qui pendant mon séjour en France faisait l'impossible pour nous, les étudiantes étrangers. Vous êtes comme une vrai mère pour nous!

Ao meu pai José Vedovoto e a minha mãe Maria Aparecida, por trabalharem incansavelmente para que eu pudesse sempre me concentrar em meus estudos. Obrigado também pelo exemplo de honestidade, trabalho, integridade que são.

Ao meu irmão Marcos por ser também um exemplo de ser humano e por ser também um exemplo de amor ao conhecimento. A minha irmã Graciela, que sempre foi e sempre

será uma das pessoas mais importantes da minha vida. Obrigado por ser uma pessoa tão iluminada, e sempre uma inspiração para mim. Obrigado também Massao, Emília, Suzana e Patrícia, que também sempre me apoiaram e acreditaram em mim.

To everyone that one way or another contributed to the development of this thesis.

VEDOVOTO, J. M., **Mathematical and numerical modeling of turbulent reactive flows using a hybrid LES / PDF methodology.** 2011. 226 f. PhD Thesis, Universidade Federal de Uberlândia, Uberlândia, Brasil and École Nationale Supérieure de Mécanique et d'Aérotechnique - ENSMA, Poitiers, France.

ABSTRACT

The present work is devoted to the development and implementation of a computational framework to perform numerical simulations of low Mach number turbulent reactive flows. The numerical algorithm designed for solving the transport equations relies on a fully implicit predictor-corrector integration scheme. A physically consistent constraint is retained to ensure that the velocity field is solved correctly, and the numerical solver is extensively verified using the Method of Manufactured Solutions (MMS) in both incompressible and variable-density situations. The final computational model relies on a hybrid Large Eddy Simulation / transported Probability Density Function (LES-PDF) framework. Two different turbulence closures are implemented to represent the residual stresses: the classical and the dynamic Smagorinsky models. The specification of realistic turbulent inflow boundary conditions is also addressed in details, and three distinct methodologies are implemented. The crucial importance of this issue with respect to both inert and reactive high fidelity numerical simulations is unambiguously assessed. The influence of residual sub-grid scale scalar fluctuations on the filtered chemical reaction rate is taken into account within the Lagrangian PDF framework. The corresponding PDF model makes use of a Monte Carlo technique: Stochastic Differential Equations (SDE) equivalent to the Fokker-Planck equations are solved for the progress variable of chemical reactions. With the objective of performing LES of turbulent reactive flows in complex geometries, the use of distributed computing is mandatory, and the retained domain decomposition algorithm displays very satisfactory levels of speed-up and efficiency. Finally, the capabilities of the resulting computational model are illustrated on two distinct experimental test cases: the first is a two-dimensional highly turbulent premixed flame established between two streams of fresh reactants and hot burnt gases which is stabilized in a square cross section channel flow. The second is an unconfined high velocity turbulent jet of premixed reactants stabilized by a large co-flowing stream of burned products.

Keywords: Turbulent Premixed Combustion, Large Eddy Simulation, Low-Mach Number Variable Density Flows.

VEDOVOTO, J. M., **Modélisation mathématique de les écoulements réactifs turbulents en utilisant une méthodologie hybride LES/PDF.** 2011. 226 f. Thèse de doctorat, Universidade Federal de Uberlândia, Uberlândia, Brasil et École Nationale Supérieure de Mécanique et d'Aérotechnique - ENSMA, Poitiers, France.

RÉSUMÉ

Ce travail de Thèse est consacré au développement d'une approche numérique permettant de conduire des simulations "low Mach number" d'écoulements réactifs. L'algorithme d'intégration retenu pour procéder à la résolution des équations de transport repose sur une méthode implicite de prédiction-correction (méthode de projection). Une contrainte physique est retenue pour garantir que le champ de vitesse est résolu correctement. Le code de calcul est soumis à plusieurs séries de vérifications préliminaires basées sur l'emploi de la méthode solution manufacturées pour des conditions incompressibles d'abord puis à masse volumique variable qui permettent de statuer quant à la bonne implémentation des schémas numériques retenus. Les performances de l'outil numérique en terme de stabilité et de robustesse sont elles-aussi analysées dans des situations simples: couche de mélange à densité variable en développement spatial et temporel. Le modèle numérique final repose sur l'emploi d'une méthode hybride LES / PDF. Pour ce qui concerne la représentation de la turbulence, deux fermetures sont implémentées pour représenter l'effet des fluctuations de vitesse non résolues. Il s'agit du modèle de Smagorinsky dans sa version dynamique ou non. La spécification de conditions aux limites turbulentes réalistes est elle-aussi analysée en détail et trois approches différentes sont considérées. Pour ce qui concerne la combustion, l'influence des fluctuations de composition aux échelles non résolues est pris en compte par le biais d'une résolution de la PDF scalaire de sous maille. Le modèle de PDF correspondant repose sur l'emploi d'une méthode de Monte Carlo. Des équations différentielles stochastiques, équivalentes aux équations de Fokker-Planck, sont résolues pour la variable de progrès de la réaction chimique. L'objectif final est aussi de pouvoir procéder, à moyen terme, à des simulations LES en géométries complexes et l'emploi du calcul distribué est essentiel. De ce point de vue, la méthode de décomposition de domaine retenue dans ce travail montre des niveau de performances relativement satisfaisants. Les capacités du modèle numérique résultant de ces développements sont illustrées sur deux configurations expérimentales. La première géométrie correspond à un écoulement très fortement turbulent de réactifs pré-mélangés dans un canal bidimensionnel. La seconde correspond à un jet rapide et non confiné de réactifs pré-mélangés.

Mots-Clés: Combustion turbulente Prémélangée, Simulation des Grandes Échelles, Ecoulements à baisse nombre de Mach avec densité variable.

VEDOVOTO, J. M., **Modelagem matemática de escoamentos reativos turbulentos utilizando uma metodologia hibrida LES/PDF.** 2011. 226 f. Tese de doutorado, Universidade Federal de Uberlândia, Uberlândia, Brasil e École Nationale Supérieure de Mécanique et d'Aérotechnique - ENSMA, Poitiers, France.

RESUMO

O presente trabalho foi dedicado ao desenvolvimento e implementação de uma plataforma computacional destinada a simulações numéricas de escoamentos turbulentos reativos a baixo número de Mach. O algoritmo desenvolvido para a solução de transporte é baseado em um método de projeção totalmente implícito. Uma restrição fisicamente consistente é imposta sobre o campo de correção de pressão para garantir que o campo de velocidade seja corretamente resolvido. A plataforma numérica foi extensivamente verificada utilizando o Método das Soluções Manufaturadas tanto para escoamentos incompressíveis quanto para escoamentos com variação de massa especifica. Dois modelos de turbulência diferentes foram implementados para representar as tensões submalha: o modelo Smagorinsky clássico e os modelo dinâmico. A imposição de condições de contorno turbulentas e realistas na entrada do domínio computacional é estudada em detalhes no presente trabalho. Três metodologias distintas foram implementadas e seus efeitos são analisados tanto para escoamentos inertes quanto reativos. Uma formulação hibrida de Simulação de Grandes Escalas/ Função Densidade de Probabilidade Transportada (LES-PDF) foi adotada. A influência das flutuações da escala submalha do escalar reativo na taxa de reação química filtrada é levada em conta no contexto da PDF Lagrangiana. O modelo de PDF correspondente faz uso da técnica de Monte Carlo: Equações diferenciais estocásticas (SDE), equivalentes às equações de Fokker-Planck são resolvidas para determinar o progresso das reações químicas. Com o objetivo de realizar simulações de grandes escalas de escoamentos turbulentos reativos, o uso de computação distribuída é inevitável. Neste trabalho, um algoritmo de decomposição de domínio foi utilizado e exibiu níveis satisfatórios de speed-up e eficiência. Finalmente, as capacidades do modelo computacional foram ilustrados na simulação de dois casos-teste experimentais distintos: O primeiro é uma chama altamente turbulenta reativa pré-misturada estabilizada entre duas correntes de fluido de alta velocidade de gases frescos e gases quentes queimados. O segundo é um jato turbulento não confinado de alta velocidade de reagentes pré-misturados estabilizados por um escoamento auxiliar em torno do jato principal de gases queimados.
Keywords: Combustão Turbulenta Pré-misturada, Simulação das Grandes Escalas, Escoamentos a Baixo Número de Mach com Massa Específica Variável.

List of Figures

1.1 A 400MW gas turbine, http://www.global-greenhouse-warming.com/gas-as-a-wedge-against-carbon-emissions.html, accessed on 16/08/2011. 3

2.1 Flow visualization of a plane mixing layer between helium (upper) and nitrogen (lower) (BROWN; ROSHKO, 1974). 8

2.2 CO_2 round jet entering air at Re = 30,000. The instabilities developed downstream the nozzle and rapidly become completely turbulent (LANDIS; SHAPIRO, 1951). 9

2.3 Temporal evolution of $Q = 0,1\ [s^{-1}]$ isosurfaces: (a) t=0.1 [s],(b) t=5 [s], (c) t=10 [s],(d) t=20 [s], (e) t=30 [s] e (f) t=40 [s]. (MOREIRA, 2011). 12

2.4 Axial swirler vanes and temperature iso-surface (T=1,000 K) colored by velocity modulus (SELLE et al., 2004). 22

2.5 Energy spectrum of a homogeneous, isotropic turbulence. Kinetic energy, $[E(k)]$ as a function of wave number. Representation in a logarithmic scale. . 23

2.6 Evolution of the chemical reaction rate, temperature and mass fraction of fuel through a laminar flame front. 24

2.7 Regime diagram for premixed turbulent combustion, adapted from Peters (1999). 26

4.1 Schematic representation of variable arrangement in a grid, (a) collocated, (b) staggered. The arrows stand for the vectorial variables, and the circles represent the scalars. 63

4.2 Elementary control volume retained for the discretization of transport equations. 68

4.3 Non-uniform finite-volume grid and distances associated to the face e. 69

4.4 Evolution in physical and scalar sample spaces of notional particles are subject to Eqs. (3.72) and (3.73). 78

4.5 Evolution of the PDF of a illustrative case with particles subjected to Eq. (3.72) and Eq. (3.73). 79

4.6 Weighted interpolation scheme. The solid lines represent the control volume edges, and the dashed lines connects the nodes and a particle p. 83

4.7 Distribution of the progress variable $\tilde{c}$ in the plane xz at $t = 0.03$ s (3000 iterations) (a) Finite Volume method (b) Monte Carlo method. 88

4.8 Distribution of the variance of the progress variable $\tilde{c}$ in the plane xz at $t = 0.03$ s (3000 iterations) (a) Finite Volume method (b) Monte Carlo method. 88

4.9 Assessment on the consistency of the particle scheme: Solid line stands for the Eulerian (constant) density. The dashed line represents the instantaneous value of the density evaluated from the particle density control algorithm, and the dots are the time-averaged value of the density evaluated by such algorithm. 89

4.10 Equivalence between the method of finite volumes and the Monte Carlo method. Time-averaged value of the mean value of the progress variable for different positions along the computational domain. $z^* = z/\delta_m$ is non-dimensionalized based on the initial width of the mixing layer. 89

4.11 Equivalence between the method of finite volumes and the Monte Carlo method. Time-averaged value of the mean value of the variance of the progress variable for different positions along the computational domain. 90

4.12 Two-dimensional temporal mixing layer simulation results for a density ratio $s = 2$ at $t^* = tU_r/L_r = 54$. Contours of the scalar c. The figure in the right hand side presents results for the simulation using the finite volume scheme. In the left hand side, results of the Monte-Carlo simulation. 91

4.13 Two-dimensional temporal mixing layer simulation results for a density ratio $s = 2$ at $t^* = tU_r/L_r = 50$, where t is the physical time. Contours of the variance of the scalar c. The figure in the right hand side presents results for the simulation using the finite volume scheme. In the left hand side, results of the Monte-Carlo simulation. 92

4.14 Time average results for the two-dimensional temporal mixing layer simulation for a density ratio $s = 2$ for number of particles per control volume N_p equal to 50 and 250. Left hand side: scalar quantity c, right hand side: its variance. 93

4.15 Instantaneous probes characterizing the equivalence between the Eulerian and Lagrangian approaches for different ratios of density Top to bottom: $s = 2$, $s = 4$ and $s = 8$. From left to right: the value of the scalar quantity, its variance and the density variations along the z^* axis. 94

5.1 Domain decomposition in a three-dimensional cartesian topology. Np_x, Np_y and Np_z stand for, respectively, the number of processes in the x, y and z directions 97

5.2 Domain decomposition in a cartesian topology. *a*) Original (serial) domain, *b*) one-dimensional decomposition, *c*) two-dimensional and *d*) domain decomposition in the three cartesian directions. 98

5.3 Domain decomposition in a one-dimensional cartesian topology and data exchange scheme for vectorial and scalar variables. 101

5.4 Schematic view of the linked list. The arrows departing for the pointers “prev” and “next” indicate the previous and next data members. 103

5.5 Reallocation of pointers in the process of deleting an node in a linked list. The arrows departing for the pointers “prev” and “next” indicate the previous and next data members. 104

5.6 Original domain sub-divided in 216 sub-domains. Each cubic box of the assembling is assigned to a processor (core). 109

5.7 Speed-up evaluation for the hybrid finite-volume Monte-Carlo method. . . . 110

5.8 Efficiency of the parallel implementation of the hybrid finite-volume Monte-Carlo method. 112

6.1 Decay of the L_2 norm for the zero Mach number manufactured solution with Dirichlet boundary conditions. ■: u, ▲: v, ♦: w, ▼: c, •: p. The solid line stands for the second order decay rate, and the dashed line stands for first order decay rate. Left figure: CDS approach; right: deferred correction approach. 120

6.2 Decay of the L_2 norm of the zero Mach number manufactured solution with mixed boundary conditions. ■: u, ▲: v, ♦: w, ▼: c, •: p. The solid line stands for the second order decay, and the dashed line stands for first order decay. Left figure: CDS approach; right: deferred correction approach. 121

6.3 Evolution of the density field. The isolines stand for equally spaced density levels. 124

6.4 Evolution in time of the L_2 norm. . Left figure: $s = 5$; right: $s = 7$. ■: u, ▲: v, ♦: p, •: c, ►:ρ. The solid line stands for the second order decay, and the dashed line stands for first order decay. 126

6.5 Evolution in time of the L_2 norm, $s = 10$. Single cycle (left), Two cycles (right). ■: u, ▲: v, ♦: p, •: c, ►:ρ. The solid line stands for the second order decay, and the dashed line stands for first order decay. 128

7.1 Sketch of the rescaling/recycling method of Lund et al. (1998) (LUND, 1998) to generate inlet conditions for a zero pressure gradient boundary layer. . . . 134

7.2 R_{13} component of the Reynolds stress tensor as a function of the non-dimensional width of the mixing layer ξ, (BRUCKER; SARKAR, 2007). 143

7.3 Mean velocity profile imposed. $z^* = z/\delta_m$, δ_m is the initial width of the mixing layer 144

7.4 Energy spectra associated to a white noise. 146

7.5 Stress tensor components evaluated from the superposition of white noise over the mean velocity profile. 147

7.6 Comparison of the effects of size of the support (N) on the energy spectra in the method of Klein, Sadiki and Janicka (2003). 148

7.7 Stress tensor components evaluated from the method of Klein, Sadiki and Janicka (2003), for different sizes of filter support. 149

7.8 Stress tensor components evaluated using the method of Smirnov, Shi and Celik (2001), for different numbers of Fourier modes. 151

7.9 Comparison of the effects of number of Fourier modes in the energy spectra in the method of Smirnov, Shi and Celik (2001). 152

7.10 Computational domain used for the simulations of the non-reactive flows. . . 153

7.11 Temporal evolution of the u component of velocity immediately downstream of the flow inlet; (a) White noise, (b) method of Klein, Sadiki and Janicka (2003) and (c) method of Smirnov, Shi and Celik (2001). 154

7.12 Turbulent spectra of a velocity probe for different methods of generation of turbulent inflow data; (a) White noise, (b) method of Klein, Sadiki and Janicka (2003) and (c) method of Smirnov, Shi and Celik (2001). 154

7.13 Fluctuations of $\sqrt{R_{11}}$ for the simulations carried-out with: (a) White noise, (b) method of Klein, Sadiki and Janicka (2003) and (c) method of Smirnov, Shi and Celik (2001). 155

7.14 Turbulent kinetic energy, $k^* = k/U_r^2$, for the simulations carried-out with the method: (a) White noise, (b) , method of Klein, Sadiki and Janicka (2003) and (c) method of Smirnov, Shi and Celik (2001). 156

7.15 Snapshot of the normalized effective turbulent viscosity μ^*_{effec} at $t^* = 586$, for the simulations carried-out with the method: (a) White noise, (b) method of Klein, Sadiki and Janicka (2003) and (c) method of Smirnov, Shi and Celik (2001). 157

7.16 Perspective, top and lateral views of the isosurface of the second invariant of the velocity-gradient tensor $Q = 2^6$, at $t = 0.020$ s. The method of Klein, Sadiki and Janicka (2003) was used. 158

7.17 Mean longitudinal velocity profiles. (•): Moreau and Boutier (1977); method of Smirnov, Shi and Celik (2001) (- - -); method of Klein, Sadiki and Janicka (2003) ($- \cdot -$); white noise ($- \cdot\cdot -$). 159

7.18 $\sqrt{R_{11}}$ stress tensor component. (•): Moreau and Boutier (1977); method of Smirnov, Shi and Celik (2001) (- - -); method of Klein, Sadiki and Janicka (2003) ($- \cdot -$); white noise ($- \cdot\cdot -$). 159

7.19 Turbulent kinetic energy. Method of Smirnov, Shi and Celik (2001) (- - -); method of Klein, Sadiki and Janicka (2003) ($- \cdot -$); white noise ($- \cdot\cdot -$). . . 160

7.20 Prescribed average progress variable inlet and initial profile. 163

7.21 Instantaneous fields of chemical reaction progress variable c - left, and chemical reaction rate $S(c)$ - right. $(i) - E_a = 8,000$ J/mole; $(ii) - E_a = 10,000$ J/mole; $(iii) - E_a = 12,000$ J/mole. The subfigures (a), (b) and (c) are results of simulations with the respective inlet boundary condition methods: white noise superimposition; the method of Klein, Sadiki and Janicka (2003) and the method of Smirnov, Shi and Celik (2001) 165

7.22 Average fields of chemical reaction progress variable c - left, and chemical reaction rate $S(c)$ - right. $(i) - E_a = 8,000$ J/mole; $(ii) - E_a = 10,000$ J/mole; $(iii) - E_a = 12,000$ J/mole. The subfigures (a), (b) and (c) are results of simulations with the respective inlet boundary condition methods methods: white noise superimposition; the method of Klein, Sadiki and Janicka (2003) and the method of Smirnov, Shi and Celik (2001) 166

7.23 Instantaneous fields of chemical reaction rate (a) and chemical reaction progress variable (b). The isosurface presented in Fig. (7.23) is associated with a value of $c = 0.5$. 168

7.24 Evolution of the longitudinal average (top) and RMS (bottom) of the u-component of velocity at the centerline of the channel. 169

7.25 mean temperature profile at $x = 42$ and $x = 122$ mm. 170

8.1 Experimental configuration of the turbulent bunsen burner of Chen et al. (1996). 172

8.2 Location of the flames studied by Chen et al. (1996) in the combustion regime diagram (Borghi coordinates) for premixed turbulent combustion. 173

8.3 Normalized mean and RMS velocity profiles at the burner exit plane, from Chen et al. (1996). 174

8.4 Scalar variable boundary condition at the computational inlet for the round jet. Global and detailed view of the jet region. 175

8.5 Scalar variable c for the cold jet: instantaneous (a) and averaged (b) fields. . 175

8.6 Streamwise evolution of average velocity and kinetic energy profiles for the cold jet. 177

8.7 Radial variation of average velocity and kinetic energy profiles for the cold-flow F3 jet. The solid lines are results of the present thesis, the plus, (+), symbols are numerical results obtained by Yilmaz (2008) and the circles are experimental results of Chen et al. (1996). 178

8.8 Instantaneous fields of the chemical reaction progress variable c, and the chemical reaction rate $S(c)$ at $t^* = 22.5$. 180

8.9 Instantaneous chemical reaction progress variable fields for $t^* = 0$ until $t^* = 22.5$. The non-dimensional time interval between figures is $t^* = 2.5$. 181

List of Tables

5.1 Numerical efficiency and speed-up factor evaluation for various topologies of parallelization. 111

6.1 Obtained convergence rates for Dirichlet boundary conditions and CDS approach for the spatial discretization of the advective terms. 119

6.2 Obtained convergence rates for Dirichlet boundary conditions and deferred-correction approach for the discretization of the advective terms. 119

6.3 Obtained convergence rates for mixed boundary conditions and Central differencing scheme for the advective terms. 120

6.4 Obtained convergence rates for mixed boundary conditions and deferred-correction differencing scheme for the advective terms. 121

6.5 Values of the constant parameters for the variable density numerical simulation. 123

6.6 Obtained convergence rates for low Mach number solution, $s = \rho_0/\rho_1 = 2$. . . 125

6.7 Obtained convergence rates for low Mach number solution, $s = \rho_0/\rho_1 = 5$. . . 125

6.8 Obtained convergence rates for low Mach number solution, $s = \rho_0/\rho_1 = 7$. . 125

6.9 Obtained convergence rates for low Mach number solution, $s = \rho_0/\rho_1 = 10$. . 127

6.10 Obtained convergence rates for low Mach number solution, $s = \rho_0/\rho_1 = 10$, two cycles per iteration. 128

7.1 Constant values used for mean velocity profile. 145

7.2 Values for mean velocity profile retained for the simulation of reactive flows. See Eq. (7.21) 162

7.3 Procedure to evaluate the chemical source term. 164

7.4 Length of the 2D flame brush, based on $\langle c \rangle = 0.9$ in the x direction. 165

7.5 Values of Damköhler number for the different values of activation energy and different methods of generation of inflow turbulent data. 167

Nomenclature

Abbreviations

BDF	-	Backwards Differencing Scheme
$BICGSTAB$	-	Bi-Conjugate Gradient Stabilized
BML	-	Bray, Libby and Moss combustion model
CD	-	coalescence and dispersion micro-mixing model
CDS	-	Central Differencing Scheme
CGD	-	Counter Gradient Diffusion
CFL	-	Courant Friedrich Lewy criteria
CPU	-	Central Processing Unity
CV	-	Control Volume
DNS	-	Direct Numerical Simulation
FDF	-	Filtered Probability Density Function
FGT	-	Flame Generated Turbulence
FV	-	Finite Volume Method
IC	-	Internal Combustion
IEM	-	Micro-mixing model - Interaction by Exchange with the mean
GD	-	Gradient Diffusion
LES	-	Large Eddy Simulation
$LMSE$	-	Linear Mean-Square Estimation micro-mixing model
MCN	-	Modified Crank Nicolson method
MMS	-	Method of Manufactured Solutions
MPI	-	Message Passing interface
$MSIP$	-	Modified Strongly Implicit Procedure
ODE	-	Ordinary Differential Equations
PDE	-	Partial Differential Equations
PDF	-	Probability Density Function
PGS	-	Pressure Gradient scaling
$RANS$	-	Reynolds Averaged Navier Stokes Equations
RMS	-	Root Mean Square
RFG	-	Random Flow Generator
SDE	-	Stochastic Differential Equations
SGS	-	Subgrid scale
UDS	-	Upwind Differencing Scheme
$URANS$	-	Unsteady Reynolds Averaged Navier Stokes Equations
$VSIMEX$	-	variable time step size implicit-explicit methods

Greek

α	-	thermal diffusivity
β_1	-	exponent of temperature of the Arrhenius law
δ_{ij}	-	Kroenecker delta
δ_m	-	width of the mixing layer
δ_j	-	initial width of the shear layer in the jet flow
Δ	-	filter width in LES
Δm_{in}	-	total mass entering each computational volume at each time step
Δx, Δy, Δz	-	respectively, the mesh discretization length in the x, y and z directions
Δt	-	size of time step
η	-	Kolmogorov length scale
ε	-	kinetic energy dissipation
γ_s	-	strong order of convergence
γ_w	-	weak order of convergence
Γ	-	molecular diffusivity
Γ_k	-	molecular diffusivity of the chemical specie k
λ	-	thermal conductivity of the fluid
Λ	-	flame parameter
μ	-	dynamic viscosity
μ_{ef}	-	effective turbulent viscosity
μ_m	-	m-th central statistical moment
μ_{SGS}	-	subgrid (or turbulent) viscosity
ν	-	kinematic viscosity
ρ	-	density
τ_c	-	Chemical time scale
τ_η	-	Kolmogorov time scale
τ_{ij}	-	viscous strain rate tensor
τ_{ij}^{SGS}	-	subgrid scale (SGS) stress tensor
ϕ	-	generic scalar
Φ	-	joint scalar-velocity vectorial fields
ψ	-	sample space of the mass fractions of the chemical species
Ψ	-	sample space of the scalar field
Ψ_α	-	sample space of the α scalar field
Ω_m	-	turbulent frequency determined by LES
$\dot{\omega}_F$	-	rate of fuel consumption
ξ	-	random number ranging between 0 and 1

Latin

a_{ij}	-	transformation matrix based on the Cholesky decomposition
A_τ	-	pre-exponential constant of the Arrhenius law
c	-	Chemical reaction progress variable
$\overline{c}_q$	-	mean values of the progress variable of the auxiliary burner
$\overline{c}_p$	-	mean values of the progress variable of the main duct
C_p	-	mean specific heat at constant pressure of mixture
C_S	-	Smagorinsky constant
C_ω	-	mechanical-to-scalar time-scale ratio
$\widetilde{c"^2}$	-	variance of the scalar c
D	-	nozzle diameter
Da	-	Damköler number
$d\mathbf{W}(t)$	-	increment of the Wiener process
$\mathcal{D}_{No}$	-	square of the distance between a particle and a node No
E_a	-	activation energy
$E(k)$	-	Energy spectrum as a function of wave number
E_n^{tot}	-	*efficiency* of the parallelization
F	-	filter function
h	-	characteristic mesh size in the MMS
h_k	-	specific enthalpy of the chemical specie k
J_{hj}	-	molecular flux of enthalpy in the j direction
J_{kj}	-	molecular flux of the k chemical specie in the j direction
K	-	number of chemical species
Ka	-	Karlovitz number
Ka_δ	-	Karlovitz number based on the inner layer of the premixed laminar flame
k	-	Turbulent kinetic energy or wave number
l	-	integral length scale
l_F	-	laminar flame front thickness
l_δ	-	thickness of the internal layer of laminar flame
Le	-	Lewis number
Le_k	-	Lewis number of the chemical specie k
Ma	-	Mach number
$m^{(l)}$	-	mass of a particle l
m_{FV}	-	mass of fluid in a finite-volume cell of volume V_c
m_{pc}	-	sum of mass of all particles in the cell of volume V_c
$\mathcal{M}_k$	-	molar mass of chemical species
N_B	-	Bray number
N_p	-	number of particles in a finite-volume cell
Np_x, Np_y, Np_z	-	respectively, the number of processes in the x, y and z directions
N_x, N_y, N_z	-	respectively, the filter support size along the directions x, y, z
$P_o(t)$	-	thermodynamic pressure, a function of time only
Pr	-	Prandtl number
p	-	pressure
q	-	convergence rate
$Q_{\alpha j}$	-	subgrid scale (SGS) scalar flux
Q	-	pressure correction in the projection method

R - universal gas constant
R_{ij} - Reynolds stress tensor components
R_j - Jet radius
r_e - error decay ratio
Re - Reynolds Number
R^o - mixture gas constant
$\mathcal{R}$ - set of independent random numbers
$\mathcal{R}_{u,i}$ - set of independent random numbers with zero mean and unity
s - density ratio
S_{in} - inflow surface area
S_n - *speed-up* factor
S_L - laminar speed of a premixed flame
S_h - source term of enthalpy
$\overline{S}(c)$ - filtered chemical reaction rate source term
S_{ui} - represents the body forces in momentum equations
S_k - chemical reaction rate of the k-th species
Sc - Schmidt number
Sc_k - Schmidt number of the chemical specie k
Sc_{SGS} - subgrid Schmidt number
$\tilde{S}_{ij}$ - strain rate tensor of the resolved field
T_a - activation temperature
t_{adv} - maximum allowable size of time step due advective contributions
t_{dif} - maximum allowable size of time step due diffusive contributions
t_{ther} - maximum allowable size of time step due thermal contributions
t_s - execution time for the best serial algorithm on a single processor
t_n - execution time for the parallelized algorithm using n processors
t - time
T - temperature
T_b - temperature of burnt gases
T_u - temperature of fresh gases
U_r - mean velocity between the two flow streams in the mixing layer
$\overline{u}_q$ - mean inflow velocity at the auxiliary burner
$\overline{u}_p$ - mean inflow velocity at the main duct
$\tilde{u}_{ip}$ - i-th component of the velocity vector interpolated at a particle
$u_i(\mathbf{x}, t)$ - velocity components
U_{in} - average velocity normal to the inflow surface
u' - velocity fluctuations
u_tau - hear velocity
$\overline{u_k^b}$ - conditional velocities in burnt mixture
$\overline{u_k^u}$ - conditional velocities in fresh mixture
V_c - Volume of a mesh element
v_η - Kolmogorov velocity scale
$\mathbf{x}$ - spatial coordinates
$\overline{\dot{W}}_F$ - mean reaction rate of fuel inside the flame front
Y_k - mass fractions of the chemical specie k

Contents

1 INTRODUCTION **1**

2 TURBULENT COMBUSTION MODELING **7**

2.1 Turbulence and spatially developing free shear flows 7

2.2 Compressible vs low Mach number approximations 13

2.2.1 Density-based methods 14

2.2.2 Pressure-based methods 16

2.3 Turbulent premixed combustion modeling 18

2.3.1 Large Eddy Simulation 19

2.3.1.1 Characteristic turbulent time, velocity and length scales . . 23

2.3.2 The laminar premixed flame 24

2.3.2.1 Thickness and velocity of a laminar premixed flame 25

2.3.3 Regimes and diagram of premixed turbulent flames 25

2.3.4 Effects of flame fronts on turbulence 27

2.3.5 Combustion models 29

3 MATHEMATICAL MODELING **33**

3.1 Governing equations 34

3.1.1 Filtered transport equations 37

3.1.2 Subgrid closure: the Smagorinsky Model 39

3.1.3 Subgrid closure: the dynamic Smagorinsky Model 40

3.1.4 Subgrid closure: the scalar flux 42

3.1.5 Chemical reaction rate 43

3.1.6 Simplifying assumptions of the chemical kinetics 44

3.2 Turbulent combustion modeling using a Hybrid LES/PDF computational model 48

3.2.1 Transport of the Probability Density Function 49

3.2.1.1 Joint velocity-scalar PDF 50

3.2.1.2 Joint scalar PDF 52

3.2.2 Lagrangian Monte Carlo approach 56

3.2.3 Coupling of the hybrid model solvers 58

4 NUMERICAL MODELING 61

4.1 The finite volume method 62

4.1.1 Temporal approximations and numerical stability 64

4.1.2 Variable time step size approach 65

4.1.3 Spatial discretization of the transport equations 68

4.2 Pressure velocity coupling 71

4.2.1 A physically consistent constraint over the velocity field 71

4.3 Numerical modeling of the system of stochastic differential equations 74

4.3.1 Method of fractional steps applied to the solution of SDE's 75

4.3.2 Operator splitting 78

4.3.3 Treatment of initial and Boundary conditions 80

4.3.4 Numerical aspects associated to the lagrangian Monte Carlo approach 81

4.3.4.1 Initialization of the particle field 82

4.3.4.2 Interpolation of average eulerian quantities to the particle field 82

4.3.4.3 Particles weighting control 83

4.3.4.4 Estimation of average quantities from particle fields 85

4.4 Equivalence between Eulerian and lagrangian approaches 85

4.4.1 Scalar field results for constant-density flows 86

4.4.2 Scalar field results for variable-density flows 90

5 PARALLEL APPROACH 97

5.1 The finite-volume method parallelization 100

5.2 Parallelization of the Lagrangian approach 102

5.2.1 Data structure and linked lists 103

5.2.2 Data exchange between sub-domains 104

5.3 Performance assessment on the parallel approach implemented. 107

6 CODE VERIFICATION 113

6.1 Verification of an incompressible solution 117

6.1.1 Convergence rate analysis 118

6.2 Verification of the low-Mach number solution 122

6.2.1 Convergence rate analysis 124

7 TURBULENT INLET CONDITIONS 131

7.1 Recycling methods 133

7.2 Synthetic turbulence generators 135

7.2.1 White noise based synthetic turbulence generators 135

7.2.2 Digital filters based synthetic turbulence generator 137

7.2.3 Synthetic turbulence generators based on Fourier techniques 139

7.2.4 Assessment of the capability for reproducing prescribed Reynolds stress tensors 142

7.2.4.1 White noise generator 145

7.2.4.2 The method of Klein, Sadiki and Janicka (2003) 147

7.2.4.3 The method of Smirnov, Shi and Celik (2001) 150

7.2.5 Non-reactive flow simulations 152

7.2.6 Application to reactive flows simulations 161

7.2.6.1 Three-dimensional simulations 167

8 APPLICATION TO NON-REACTIVE AND REACTIVE HIGH VELOCITY TURBULENT JET OF PREMIXED REACTANTS 171

8.1 Cold-flow characteristics 173

8.2 The turbulent Bunsen flame F3 179

9 CONCLUDING REMARKS AND FUTURE WORK 183

CHAPTER I

INTRODUCTION

The presence of turbulent flows in practical engineering applications is very frequent, as well as the presence of reactive flows. However, the detailed analysis of these phenomena (turbulence and combustion), and especially the interaction between them is an area that still requires research and understanding. Combustion is a phenomenon that came to mankind since time began, and now, much of the energy used comes from combustion processes. According to Turns (2000), in 1996, 85% of energy use in the U.S., came from combustion sources. In Brazil, as reported by the Ministry of Mines and Energy in 2006 over 80% of energy generated by human beings is related to some process of combustion. This reason alone is enough to motivate scientific research looking for maximum efficiency of any process involving combustion, however, such a dependency also leads to a major source of problems: environmental pollution. Most of the pollutants produced by total or partial combustion of fuels are hydrocarbons, nitrogen (NO_x) and sulfur (SO_x) oxides, carbon monoxide and particulate, are highly toxic and therefore its production has been increasingly regulated and restricted.

The interaction between turbulence and combustion is a complex scenario because both processes may influence, non linearly, each other. Turbulent combustion is characterized by a large range of time and length scales, making the interaction between the two almost impossible to handle numerically without proper modeling approaches. Regarding

the prediction and understanding of such a category of flows, the extensive use of mathematical and numerical techniques is unavoidable. Hence, as the mathematical and numerical methods become more complex. This project aims to develop the understanding of the interaction between turbulence and combustion, through computational simulations of both processes by the joint use of adequate mathematical models and numerical tools to deal with the turbulent combustion in low Mach number flows.

The starting point to begin the modeling of turbulent combustion is to identify the degree of mixture between the reagents, i.e., the fuel and the oxidizer. Traditionally, reactive flows have been separated in two broad classes: premixed and non-premixed combustion. A third regime, sometime considered as a hybrid of the two former ones to a certain extend, has risen. It has been named partially-premixed regime. The physical processes involved and the dynamics of the combustion in each of these configurations are different, hence, each one requiring specific approaches. In the non-premixed combustion fuel and oxidizer are initially separated, to the chemical reactions be able to occur, the mixture between them must happen in a molecular level. Such kind of flames are common to be found in furnaces and industrial burners. Differently of non-premixed flames, in premixed flames the reactants are mixed prior to chemical reactions. The flame is propagated with velocity and thickness that depends on the mixture. This kind of flames are usually found in confined spaces once, depending on the fuel and the equivalence ratio of the mixture, a local increase in the temperature can be enough to trigger the combustion process. It is worth mentioning that this is the regime usually found in internal combustion engines and after burners of gas turbines. Figure (1.1) shows one of this kind of gas turbine.

Figure 1.1: A 400MW gas turbine, http://www.global-greenhouse-warming.com/gas-as-a-wedge-against-carbon-emissions.html, accessed on 16/08/2011.

The development of a numerical platform, aiming the numerical simulation of low Mach number turbulent premixed combustion, is the main subject of the present thesis. Adequate and robust methods for dealing with this kind of flows, where strong variations of density may came from temperature variations, reliable turbulence modeling, verified and accurate numerical methods, correct imposition of boundary conditions for large eddy simulations and stochastic methods for modeling chemical reactions and mixture in turbulent combustion are examples of themes studied in the present work. These knowledge areas have received special attention recently for, at least, one reason in common: as we advance in terms of mathematical modeling, i.e. as the physical problems will be better understood, the computational cost of such methods typically increases, either by more complex models or due its need for increasingly refined meshes, hence the use of distributed computing is unavoidable.

The present report is organized as follows: first a brief review on the literature is made

about the methods retained for the modeling of turbulent combustion. Moreover, in the same chapter it is presented the main characteristics of the flows studied here, spatially developing free shear flows. Chapter 3 reports a detailed description of the whole mathematical modeling retained, i.e., the governing transport equations, as well as the filtering procedure used for the obtention of a set of equation suitable for LES. The turbulence closures retained are also shown in chapter 3. Finally in this chapter, the simplificative assumptions of the chemical kinetics, a detailed demonstration of the transported PDF method used in the present work, and the coupling between the Eulerian and Lagrangian approaches is presented.

In chapter 4 the fully implicit discretization and the variable time-step temporal integration of the finite volume approach retained is presented. The pressure velocity coupling and the physically consistent constraint developed for variable density flows are reported in detail also. Finally, the numerical approach used in the solution of the system of stochastic differential equations (SDE) generated is explained and its consistence with the Eulerian approach is proved for both constant density and variable density flows. Since it is intended to perform large eddy simulations of complex flows, the number of control volumes used to discretize the transport equations can be larger than one million and the number of notional particles retained in the solution of SDEs can amount to over hundreds of millions, the use of distributed computing is mandatory. Chapter 5 is devoted to describe the procedures retained in the parallelization of the aforementioned methods. The speed-up factor and efficiency tests show that the approach implemented is very promising.

During this thesis, a computer code with approximately 30,000 lines was written in Fortran 90. Such a code, named Fluids3D was built to include all the methods explained in the present document. A very important aspect of the development of such a code is that it was extensively verified. Indeed, the procedures followed for the verification of the developed numerical code has been the subject of a recent publication by Vedovoto et al. (2011). Chapter 6 shows how the numerical code was verified in two different situations: in the limit of a zero Mach number flow, and a second set of tests aiming at mimicking the propagation of a analytical corrugated flame front that separates heavy from light gases. The

results showed that the numerical methods implemented has achieved a convergence rate of error decaying equals to two, allowing us to retain it to perform large eddy simulations of turbulent reactive flows.

The specification of the realistic turbulent inflow boundary conditions can be problematic in a LES context. The reason of that is due to the fact that for LES or DNS simulations, where the flow at the inlet is turbulent, the inflow data should consist of an unsteady turbulent velocity signal representative of the turbulence at the inlet. In Chapter 7 three different methods of prescribing turbulent inflow data are assessed and their effects are analyzed for a spatially developing mixing layer.

In the last Chapter, the simulations of a turbulent round reactive jet are presented, first for an inert case, and then for a stoichiometric premixed bunsen flame. Finally, the manuscript is ended by concluding remarks and proposals for future work.

CHAPTER II

TURBULENT COMBUSTION MODELING

The objective of the present chapter is to present a very short survey of the literature concerning the methods retained in the computational modeling of turbulent reactive flows. Furthermore, are presented the main characteristics of spatially developing free shear flows, such as mixing layers and jets, the two main types of flows studied in the present thesis. The existing strategies that are usually employed to develop compressible and incompressible solvers for low Mach number calculations are briefly reviewed, as are the methods retained in the modeling of turbulent reactive flows. The text focuses, then, on the physical phenomena that involve the modeling of turbulent premixed flames, and the possible approaches that can be retained for the simulations of such flames.

2.1 Turbulence and spatially developing free shear flows

The description of turbulence in fluids remains a challenge in both understanding and modeling aspects. The high number of degrees of freedom, combined with a random behavior, makes the task of fully predicting a turbulent flow very difficult. Throughout time, significant attention has been given to turbulent free shear flows. Rayleigh (1880) and Reynolds (1883) were among the first to systematically study turbulence. Pope (2000) proposed a profound analysis on several aspects of turbulent flows.

Although a definition that comprises all characteristics of turbulence is hardly acceptable (SILVEIRA-NETO, 2002), it can be said that turbulence is a three-dimensional, rotational, highly diffusive, highly dissipative, unpredictable phenomenon that occurs at high Reynolds numbers. Such a set of characteristics associates the turbulence in fluids to a highly non-linear character. Moreover, turbulent flows present a wide energy spectra, i.e., in turbulent flows there are structures with different wave numbers, and the interactions between these different structures with characteristic sizes and frequencies constitutes a refined and complex mechanism of energy transfer.

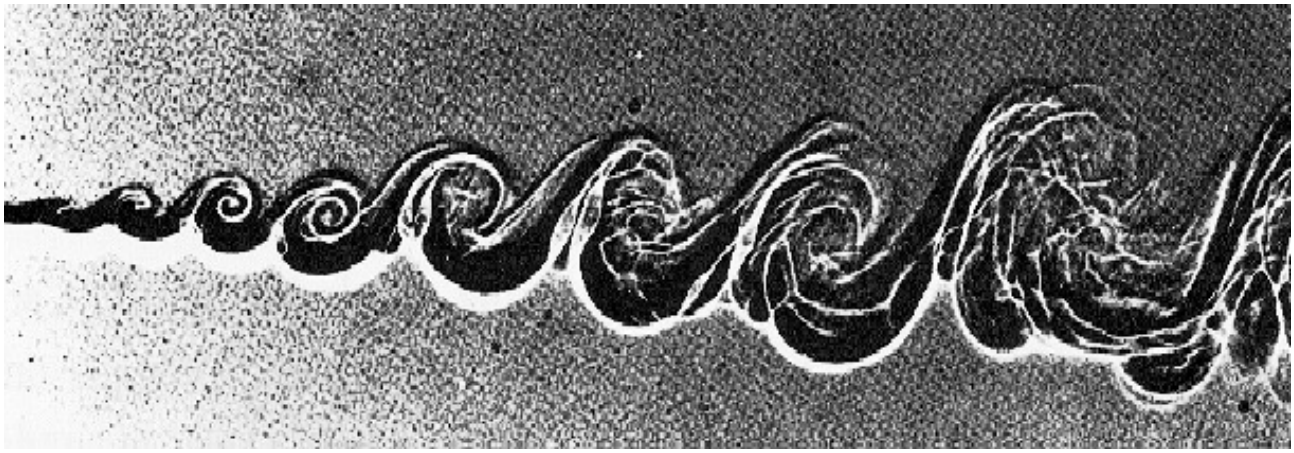

Figure 2.1: Flow visualization of a plane mixing layer between helium (upper) and nitrogen (lower) (BROWN; ROSHKO, 1974).

In the present work the free shear flows are the object of study. Such a class of turbulent flows is characterized by a development that occurs far from obstacles or walls. Thus, turbulence arises due to mean-velocity differences (POPE, 2000). The free shear flows can yet be classified in wakes, mixing layers and jets. The last two types of flows are studied here. Figure (2.1) shows an example of a spatial developing mixing layer. The main features visible in such figure is the presence of large and coherent structures. These are found to be regions of concentrated spanwise vorticity that are coherent over substantial spanwise distances. As the these coherent structures, or eddies, are advected downstream they grow in size and spacing, and decrease in number. Another important characteristic is that an eddy may merge with an adjacent eddy in a pairing process, or it can be torn apart and its

vorticity absorbed by adjacent eddies (POPE, 2000).

Brown and Roshko (1974) and Browand and Latigo (1979) developed pioneering works in the sense of a full experimental characterization of mixing layers. Soteriou and Ghoniem (1995) assessed the effects of free-stream density ratio on low-Mach number developing mixing layers. Direct Numerical Simulations of a temporally evolving shear layer has been performed by Brucker and Sarkar (2007). An important contribution of such a work is that they present a relation in which the non-dimensional thickness of the shear layer is correlated to parcels of the Reynolds stress tensor. Moreover, in Brucker and Sarkar (2007) the influence of turbulent initial conditions on the development of self-similar mixing layers is assessed.

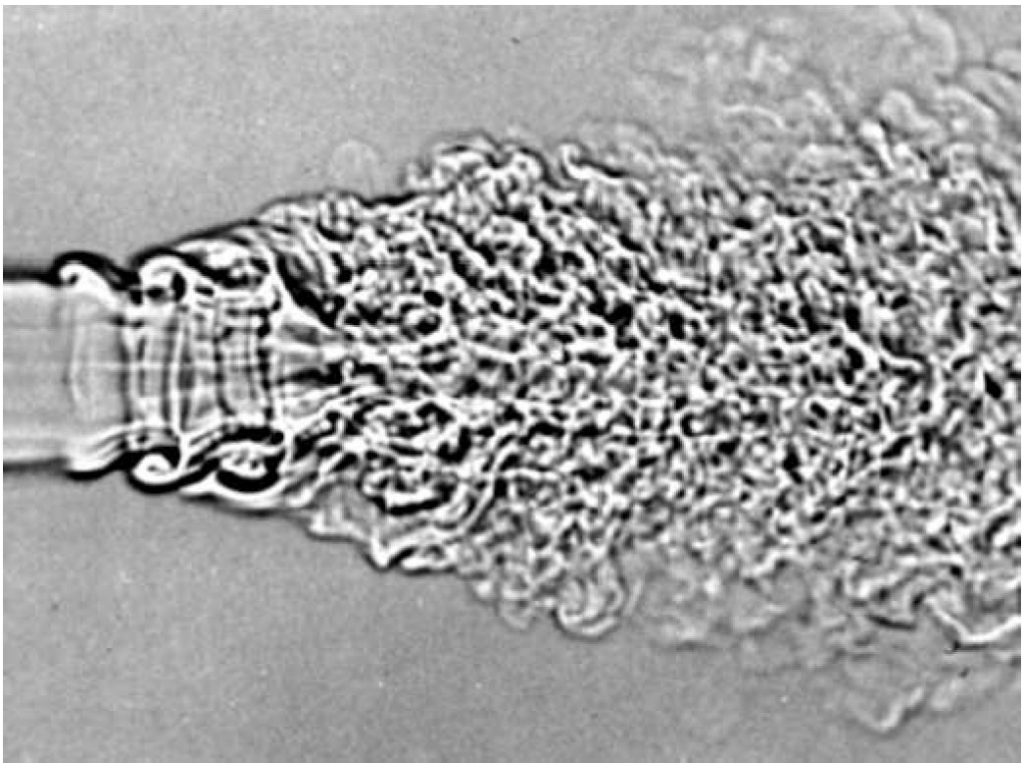

Figure 2.2: CO_2 round jet entering air at Re = 30,000. The instabilities developed downstream the nozzle and rapidly become completely turbulent (LANDIS; SHAPIRO, 1951).

Compared to the planar mixing layer, the development of large turbulent structures (eddies) is significantly different in a jet configuration. In a very general way, it is possible to define a jet as a flow from a confined space entering an open space. Jets can be classi-

fied according to the geometry of the nozzle. In a planar jet, for instance, the nozzle has a rectangular format, whereas a round jet is formed downstream of a circular nozzle. In both cases the transition to turbulence is characterized by the formation of Kelvin-Helmholtz-type primary instabilities, which induce the generation of secondary longitudinal filaments. The interaction of such secondary counter-rotating longitudinal filaments with the primary eddies leads to the formation of transversal oscillations. The latter are amplified and eventually lead the flow to a state of developed turbulence. The primary instabilities are easily notable in Fig. (2.2).

The first investigations on jets include the work of Corrsin (1943), Corrsin and Uberoi (1950a, 1950b). Considering its applicability in several areas of engineering, it is natural that numerous publications analyze turbulent jets from different points of view. Heron et al. (2001), Birch et al. (2003) and Uzun (2003) studied compressible jets in order to understand the interactions between aerodynamic and acoustic noise generation. Hussein, Capps and George (1994) have studied round incompressible jets at high Reynolds numbers, showing that averaged velocity, second, and third order statistical moments depend strongly on the experimental set-up. In the work of Todde, Spazzini and Sandberg (2009) a series of common characteristics of jets at low and moderate Reynolds numbers are evidenced, e.g., the presence of eddies near the nozzle and the existence of the shear layers. Todde, Spazzini and Sandberg (2009) also evidenced and characterized the presence of a potential core in turbulent non-reactive jets.

Boersma, Brethouwer and Nieuwstadt (1998), by performing Direct Numerical Simulations, studied the effects of the inflow conditions on the self-similar region of a round jet. An important result obtained is that an universal self-similarity, in fact, may depend on the boundary conditions at the inlet. Nevertheless they verified that, with an adequate scaling, an universal self-similarity in round jets is still possible. Stanley and Sarkar (1999) studied the effects of the turbulence intensity and shear layer momentum thickness at the nozzle on the evolution and development of a planar jet in both laminar and turbulent regimes. It was found that variations of fluctuation intensity and shear layers affect the rate with which

the jet develops downstream. In fact, higher intensity fluctuations lead to a faster growth of the jet with an asymptotic approach of the centerline turbulent kinetic energy to self-similar values. Xu and Antonia (2002) experimentally examined the effects of the velocity profile at the nozzle on the development of a turbulent round jet. They found that the use of a smooth contraction, leading to a top-hat type profile, leads to a faster jet development to a self-similar behavior than when the flow issues from a long tube, characterized by a velocity profile of a fully developed pipe flow.

The application of Large Eddy Simulations in the study of turbulent non-reactive jets is also a subject of numerous works. Silva and Métais (2002), by using an compact sixth-order scheme in the direction of the development of the jet, and pseudo-spectral methods in the transversal directions, studied the dynamics and control of bifurcating jets, focusing on the analysis of the influence of forcing [1] and the Reynolds number.

Silva and Pereira (2004), simulating a jet in temporal decay, studied the effects of subgrid models in order to analyze the effect of the subgrid-scale (SGS) models on the vortices obtained from LES. The dynamics of the filtered vorticity norm (or filtered enstrophy) was analyzed through the application of a box filter to temporal DNS of turbulent plane jets. The models analyzed were the Smagorinsky, structure function, filtered structure function, dynamic Smagorinsky, gradient, scale similarity, and mixed. Those model results were also compared with DNS results. Silva and Pereira (2004) showed that, in terms of spatial location, all the models used lead to a good correlation between the "real" and "modeled" enstrophy SGS dissipation. Moreover, all the SGS models, even of eddy-viscosity type, are able to provide enstrophy SGS backscatter. However, in terms of statistical behavior the eddy-viscosity models do not provide enough enstrophy backscatter when compared to the non-eddy-viscosity models. LES are carried out and show that the Smagorinsky, structure function, and mixed models cause excessive vorticity dissipation, compared to the other models, and, although the enstrophy SGS dissipation affects mainly the smallest resolved scales, it is argued that it may also affect some low-wave numbers.

[1] The action of imposing an given frequency of fluctuation over the velocity profile at the nozzle

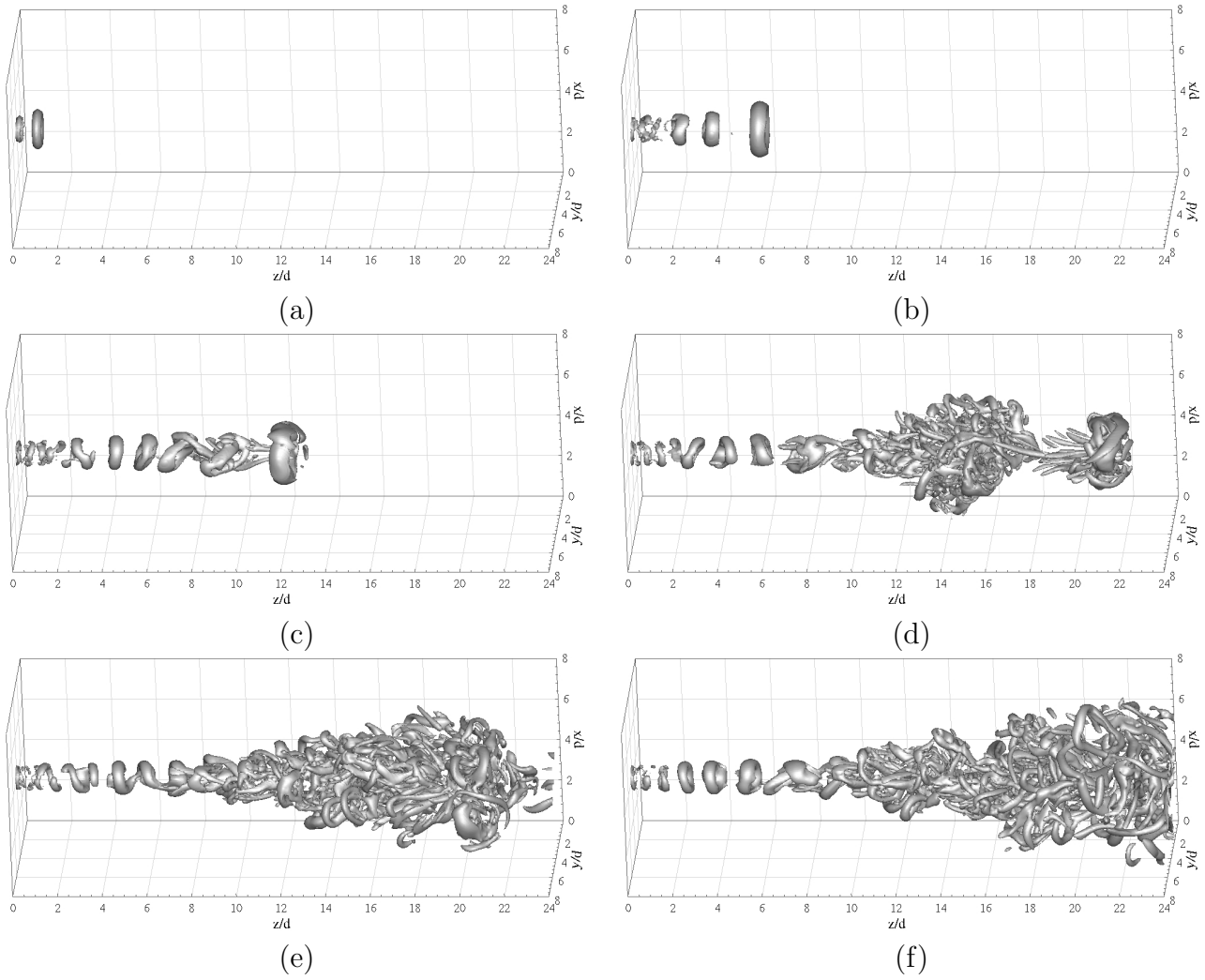

Figure 2.3: Temporal evolution of $Q = 0,1\ [s^{-1}]$ isosurfaces: (a) t=0.1 [s],(b) t=5 [s], (c) t=10 [s],(d) t=20 [s], (e) t=30 [s] e (f) t=40 [s]. (MOREIRA, 2011).

Moreira (2011) developed a methodology which allows the simulation of a turbulent spatially developing jet with a full Fourier Pseudo Spectral Method. Such a methodology is based on the coupling of the Fourier pseudo-spectral (FPSM) (MARIANO, 2011), and immersed boundary methodologies (IBM) (LIMA-E-SILVA; SILVEIRA-NETO; DAMASCENO, 2003). A main characteristic of the FPSM is the high numerical accuracy associated to a relatively low computational cost, since solving the linear system of the pressure-velocity coupling is no longer necessary, at least in constant density flows. However, the FPSM methodology has its applicability restricted to problems with periodic boundary conditions only. The coupling of such a methodology with the IBM allowed to expand the range of prob-

lems to which the FPSM could be applied towards more complex problems. Figure (2.3) shows the temporal evolution of the criteria Q isosurfaces (JEONG; HUSSAIN, 1995) of a spatial developing jet at Re = 1,050. The first vortical structures of the Kelvin-Helmholtz instabilities are clearly identifiable.

So far, a brief overview of the literature concerning non-reactive free shear flows was presented. Before presenting how combustion chemical reactions may affect turbulent free shear flows, and how turbulent reactive flows have been treated in the scientific literature, an overview about the possible numerical methods that can be retained for simulating those kind of flows is given. The reason for this is due to the interest of the present thesis in flows that present non-negligible density variations, but are in a low-Mach number regime.

2.2 Compressible vs low Mach number approximations

An important non-dimensional parameter that characterizes a flow field is the Mach number $Ma{=}U/c$, where U is a characteristic velocity of the flow field, and c is the speed of sound. The incompressible limit is usually defined as the situation associated to Mach number values smaller than 0.3. Above this value the compressibility effects cannot be neglected any longer, and variations of density and pressure are coupled through an equation of state. For incompressible flows a partial decoupling between the equations of momentum and the energy equation is possible, and in such flows the pressure variations are typically very small. The possible density variations are not related to pressure variations, but to temperature and mixture composition variations. The pressure is often said to be thermodynamically constant, and its influence is only felt through the spatial derivatives that appear in the momentum transport equation.

In fact, there exists a fundamental difference between the behavior of the set of transport equations in an incompressible flow, with respect to compressible flows. In compressible flows featuring high Mach number values, the fluid velocity is of the same order of magnitude as the velocity of sound waves, i.e., $O(U) \approx O(c)$, and the mathematical system of governing

equations follows an hyperbolic behavior (ANDERSON, 1995), whereas in the low Mach number incompressible case, the velocity of sound waves are much higher than the fluid velocity, i.e., $O(U) \ll O(c)$. Such a disparity of magnitudes between the velocity of the flow and the speed of sound waves leads to a great stiffness in the system of balance equations. This severely hampers the accuracy and convergence of the numerical methods that rely on the consideration of density variations, i.e., density-based solvers (CHOI; MERKLE, 1993), which remain the most commonly used to perform the numerical simulations of compressible flows. In the case of incompressible flows such a disparity between the wave and flow velocities is also one of the major sources of numerical instability (NAJM; NAJIM; WYCKOFF, 1998; COOK; RILEY, 1996; RAUWOENS; VIERENDEELS; MERCI, 2007).

In the present work, the interest is focused on low velocity flows, i.e., in the incompressible regime, but featuring non negligible density variations, the so-called low Mach number flows. There are basically two broad classes of numerical methodologies to deal with this kind of flows: those relying on density-based solvers, i.e., based on methods usually retained for compressible flows, and those relying on pressure-based solvers, such as those retained to perform the numerical simulation of incompressible flows. The application of each one of these two methodologies to low Mach number flows requires the introduction of several modifications and improvements, that are briefly summarized below.

2.2.1 Density-based methods

The density-based methods represent a wide class of numerical schemes originally developed to study compressible flows (SILVA; AZEVEDO; KORZENOWSKI, 2000). Turkel, Radespiel and Kroll (1997) determined that the set of discretized equations retained for the numerical simulation of a compressible flows fails to provide an accurate solution for an incompressible flow. The simulations of incompressible flows based on the fully compressible method, with no modifications to reduce the disparity existing between the flow velocity and the speed of sound, are found impracticable due to the associated computational costs. In this case, temporal integration schemes, whatever they are explicit or implicit, are penalized. In the former case, the Courant-Friedrichs-Lewy (CFL) condition, that must be satisfied at

each time step to enforce the numerical stability of the numerical integration scheme, leads to prohibitively small time step values due to the prevailing influence of acoustic waves propagation. In the case of implicit methods such a disparity induces large differences in the characteristic eigenvalues of the algebraic system to be solved, which becomes ill-conditioned, leading therefore to extremely high-cost iterative solutions (ROLLER; MUNZ, 2000).

Two distinct sets of techniques have been proposed to achieve better convergence properties of density-based solvers, in the limit of low Mach number flows: preconditioning and perturbation methods. Both techniques strive to minimize the stiffness of the algebraic system that results from the discretization of the balance equations.

The first technique pre-multiplies the temporal derivatives by a preconditioning matrix, whose choice is determined according to the problem to be analyzed (CHOI; MERKLE, 1993), thus leading to a new set of equations. As a consequence, the initial (stiff) system is altered. The technique essentially aims at re-scaling the characteristic eigenvalues with respect to the original system, so that eigenvalues of similar orders of magnitude can be obtained, leading to a better conditioned system (TURKEL; RADESPIEL; KROLL, 1997; TURKEL, 1992). The major drawback associated with preconditioning methods is that the governing equations are modified in terms of their mathematical nature due to the incorporated transient term. The modified system of equations has only the steady-state solution in common with the original system and becomes, therefore, devoid of any physical transients. A second limitation is the failure of this methodology, in terms both of efficiency and robustness, in the vicinity of stagnation points, where the characteristic eigenvectors become almost parallel (DARMOFAL; SCHMID, 1996). Furthermore, the design of general purpose pre-conditioners adequate for a large variety of physical problems remains far from being straightforward.

The second set of techniques is associated to perturbation methods, or asymptotic analysis. In this case, a perturbed form of the equations is used to reduce the stiffness of the algebraic system of equations. A Taylor expansion is performed, in terms of the Mach

number, thus decoupling the acoustic waves from the equations, and replacing them with a set of pseudo-acoustic forms, where the wave velocities become the same order of magnitude as the fluid velocity. Such a procedure alters the velocity of the acoustic waves in order to allow the numerical integration to be performed with larger time steps (CHOI; MERKLE, 1993; ROLLER; MUNZ, 2000).

Other methodologies have been also developed for the purpose of considering density variations, such as the artificial compressibility methods, and the PGS (Pressure Gradient Scaling). The first, described, for instance in Ferziger and Peric (1996), has been successfully applied to the numerical simulation of reactive flows and, in particular, to describe the propagation of a planar turbulent premixed flame (DOURADO; BRUEL; AZEVEDO, 2004). The PGS method (RAMSHAW; O'ROURKE; STEIN, 1985; AMSDEN, 1989; WANG; TROUVé, 2004; PAPAGEORGAKIS; ASSANIS, 1999) displays certain similarities to the perturbation methods, and it also acts on the pressure term that appears in the momentum equation. In this method the pressure gradient is multiplied by a factor $1/\alpha_{PGS}^2$, where α_{PGS} is a constant that amplifies the pressure variations. As a consequence, since the velocity of acoustic waves is decreased by a factor α_{PGS}, the pressure variations are amplified by a factor α_{PGS}^2, thus, improving the robustness of the numerical method as the Mach number tends towards zero (AMSDEN, 1989). Finally, it is worth adding that one reason for the use of the last two methods rely in the fact that they can be easily implemented within existing compressible solvers.

2.2.2 Pressure-based methods

In contrast to the methodologies discussed above, that are based on density variations, pressure-based methods have been initially proposed to solve fully incompressible flows, retaining the pressure as one of the primary variables. Such numerical schemes that are often referred to as pressure-corrections methods, or projection methods, evaluate the pressure and velocity fields in a segregated manner (CHORIN, 1968). In pressure-based methods, the pressure does not play a thermodynamic role, but ensures the incompressibility condition, which leads to a discretization scheme based on a separation of operators (splitting method).

In a first step, momentum equations are solved to obtain an estimated velocity field, based on a previous evaluation of pressure. The velocity field should be solenoidal, and this property is enforced by a subsequent projection step within the subspace of divergence-free vectorial fields. Such projection, which defines the corrector step, relies on the Hodge decomposition theorem (CHORIN; MARSDEN, 1993). The pioneering works in this field (CHORIN, 1968; PATANKAR, 1980) have provided the basis for the development of several projection schemes that are still currently used. More specifically, the work of Patankar (1980), has led to a family of methodologies referred to as the SIMPLE (Semi-Implicit Pressure Linked Equations) approach, which undoubtedly remains the most widely used to obtain the solution of incompressible flows.

As previously mentioned, in the low Mach number regime, the compressibility effects have a negligible influence on the momentum transport and the pressure is only a weak function of density. To prevent significant inaccuracies when performing the evaluation of pressure, it is usually divided into two distinct components:

$$P(\mathbf{x},t) = P_o(t) + P'(\mathbf{x},t), \tag{2.1}$$

where P_o is a reference pressure level[2], with $P_o(t)/P_o = O(1)$, and $P(\mathbf{x},t)/P_o = O(Ma^2)$. It is worth noting that $P_o(t)$ is often referred to as the thermodynamic pressure, whereas $P'(\mathbf{x},t)$ is called the dynamic pressure since it is directly related to modifications of the velocity field.
Using such a decomposition, the thermodynamic pressure appears in the equations of state and energy conservation only, vanishing in the momentum equation. Since its gradient is zero everywhere, only the gradient of the dynamic pressure component remains. It is worth noting that this procedure significantly accelerates the convergence only if the pressure fluctuations remain sufficiently small.

Since one of the objectives of the present work is to provide guidelines for verification

[2]Since the interest of the present thesis lies in gaseous flow fields, the effects of gravity are not considered, hence $P_o(t)$ is a function of the time only.

and cross-checks of a recently developed incompressible code, the most natural choice for an extension to variable density flows is a formulation based on pressure variations, i.e., to extend a mathematical and numerical model proposed for fully incompressible flows to handle density variations.

A wide class of numerical methods that remains used to perform such simulations of low Mach number flows, is based on predictor-corrector methods. Several works, (NAJM; NAJIM; WYCKOFF, 1998; COOK; RILEY, 1996; RAUWOENS; VIERENDEELS; MERCI, 2007; COLELLA; PAO, 1999; KARKI; PATANKAR, 1989; LIMA-E-SILVA; SILVEIRA-NETO; DAMASCENO, 2003; BELL, 2005a; LESSANI; PAPALEXANDRIS, 2006a; KNIO; NAJM; WYCKOFF, 1999) share such pressure-velocity coupling. Rider et al. (1998) report an extensive discussion about robust projection methods applied to variable density low Mach number flows. The details of the algorithm retained for the present study will be presented in Chapter 4. In the next sections a brief review on the modeling of turbulent combustion is presented.

2.3 Turbulent premixed combustion modeling

Under many circumstances of applied interest, combustion proceeds in mixtures in which reactants have been fully mixed prior to chemical reaction. In many practical applications premixed combustion is turbulent (MERCI; MASTORAKOS; MURA, 2010), and well known examples can be outlined: in the field of propulsion, they include spark ignitions engines and jet engines, for instance. In the safety field, another important example are vapor clouds explosions, associated with the leakage of fuel in the atmosphere, where it mixes with air and may subsequently ignite. A more common example of turbulent premixed combustion is the flame above a Bunsen burner, where the flow of premixed reactants is turbulent due the high velocity of the mixture in the feeding tube or due to a turbulence-generating grid. In the following sections, a brief review is presented of LES and combustion models usually retained to perform the numerical simulation of premixed turbulent reactive flows.

2.3.1 Large Eddy Simulation

As mentioned in the introduction of this thesis, the solution of the balance equations (mass, momentum, energy, species mass fractions, etc.) is deemed sufficient to represent the evolution of a multi-component gas-phase mixture in either laminar or turbulent flow, provided that the continuum hypothesis holds, and once suitable constitutive equations for the fluids of interest are specified (HAWORTH, 2010a). The full solutions of this set of equations is, however, far from being straightforward, specially under turbulent conditions. To solve each and every scale of a turbulent reactive flow, i.e., to perform a Direct Numerical Simulation of a turbulent reactive flow with the computational power available today still remains out of reach for problems of engineering interest, see for instance Pope (2000). Since all length and timescales must be resolved, the computational cost of a DNS increases proportionally to Re^3, where Re is the Reynolds number (POPE, 2000).

The highly non-linear set of PDE's is extremely sensitive to small variations of initial and boundary conditions. If the simulation of an actual combustion device is of interest, information on the boundary conditions is seldom available with the required level of accuracy. Moreover, the mesh required for the DNS simulation of reactive flows must be fine enough to resolve the inner structure of the flame, which, in many cases, is much smaller than the so-called Kolmogorov scales of the flow (POINSOT; VEYNANTE, 2005; HAWORTH, 2010a).

To give an idea of the computational cost of a DNS, Poinsot and Veynante (2005) present the results of a DNS of a premixed flame front at atmospheric pressure interacting with isotropic turbulence. The mesh adopted in a such simulation contains approximately two million grid points and the corresponding computational domain is a cubic box of size $5 \times 5 \times 5\ mm^3$. Finally, even if a computation of full set of PDE's of a turbulent reactive flow is computationally possible, the large amount of data generated is too cumbersome to be dealt with for most practical purposes.

Directly opposed to the completeness of Direct Numerical Simulations description, the

Reynolds Averaged Navier Stokes (RANS) or Unsteady Reynolds Averaged Navier Stokes (URANS) computations provide the temporal average of the flows properties of interest. Still largely adopted in turbulent combustion (POINSOT; VEYNANTE, 2005; FOX, 2003; HAWORTH, 2010a; YILMAZ, 2008), these methods consist on the application of a temporal average operator on the transport equations. Such a process results in averaged equations, with unclosed terms where some sort of closure is needed. These unclosed terms are the Reynolds stresses and the turbulent scalar fluxes, and the averaged chemical reaction term. Although indisputably much less expensive than DNS, providing mean values only precludes a RANS model from predicting turbulent structures that can influence the flame front, specially in shear flows, such as mixing layers, boundary layers and jets (LIBBY; WILLIAMS, 1994).

The URANS methods also involve models for the unclosed terms in the turbulent transport equation for the scalar fields, such as the mass fractions and chemical reaction. The modeling of such terms in a URANS methodology is more complicated, due to the possible occurrence of counter-gradient diffusion (LIBBY; BRAY, 1981).

Counter gradient diffusion can occur when the flow near the flame front is dominated by the acceleration induced by the thermal expansion due to the chemical reactions, whereas gradient diffusion occurs when turbulence dominates the flow field near the flame front.

URANS models are usually based on gradient transport assumptions. This is an acceptable hypothesis in constant density flows, but in variable density flows, such an important phenomena, i.e. the counter gradient diffusion, cannot be accounted for within the framework of turbulent diffusion transport (YOSHIZAWA et al., 2009).

The modeling (closure) of the chemical reaction term based on the direct application of the same averaging procedure applied to the other terms of the transport equations is incorrect, due to the high non-linearity of the expressions that describe the chemical kinetics based on the Arrhenius law (POINSOT; VEYNANTE, 2005). As a consequence of such difficulty, phenomenological models are largely used. Two examples of such modeling are the Eddy Break-Up model of Spalding (1971) and the BML of Bray, Libby and Moss (1985).

Large Eddy Simulations (LES) can be thought as an intermediate methodology between the DNS and URANS. The large scales of the turbulent flows are explicitly calculated, whereas the non-linear interactions between large scales and subfilter scales are modeled using subfilter (or subgrid) closure models. The balance equations for large eddy simulations are obtained by filtering the instantaneous transport equations. LES can determine the instantaneous position of a "large scale" resolved flame front but a subgrid model is required to account for the effects of small turbulent scales on the combustion processes (POINSOT; VEYNANTE, 2005). Since large structures are explicitly computed in LES, instantaneous fresh and burnt gases zones, where turbulence characteristics are quite different, can be, most often, clearly identified, at least at the resolved scale. In comparison with a URANS methodology, LES could provide a better prediction of the turbulence/combustion interactions. Schumann (1989) was one of the first to conduct a LES of a reacting flow. Colucci et al. (1998a) argue however, that the assumption made in that work, simply to neglect the contribution of the SGS scalar fluctuations on the filtered reaction rate, needs to be justified for general applications. The importance of such fluctuations is well recognized in Reynolds averaged procedures in both combustion and chemical engineering problems (LIBBY; WILLIAMS, 1994), therefore, it is natural to believe that these fluctuations are also important in LES.

LES can be expected to have the greatest advantage over RANS in situations where large-scale flow dynamics are important (LESIEUR; MÉTAIS, 1996; LESIEUR; MÉTAIS; COMTE, 2005). This is the case, for example, when combustion instabilities in gas-turbine combustors or cycle-to-cycle variations in reciprocating-piston IC engines is of interest (HAWORTH, 2010a). However, there are significant differences between LES for non-reacting flows (where most of studies have been made) and LES for reacting flows (COOK; RILEY, 1996; POPE, 2000). In constant-density, high-Reynolds-number hydrodynamic turbulence, remote from walls and without chemical reactions, the rate-controlling processes are determined by the resolved large scales. In contrast, in turbulent combustion at high Reynolds and Damkhöler numbers, the essential rate-controlling processes of molecular mixing and chemical reaction occur at the smallest, usually unresolved, scales (POPE, 2004). For such

cases, the arguments in favor of LES may be less compelling over RANS approaches, since the modeling of rate-controlling combustion on LES processes requires the same modeling as in RANS. In fact, most LES combustion models, with proper modifications, are derived from RANS models (FOX, 2003; POPE, 2004).

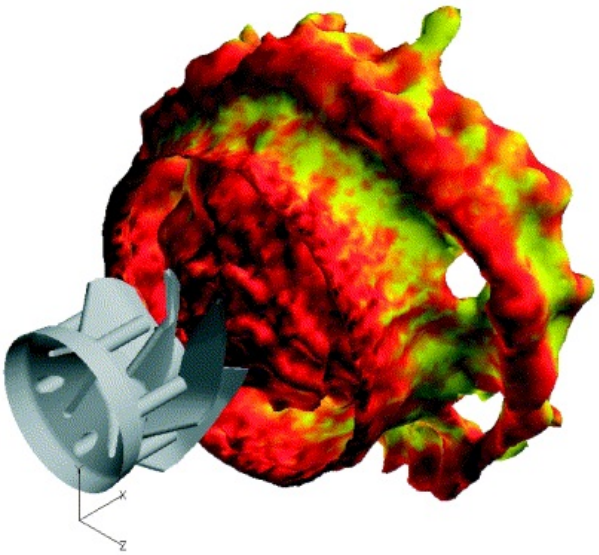

Figure 2.4: Axial swirler vanes and temperature iso-surface (T=1,000 K) colored by velocity modulus (SELLE et al., 2004).

It is important to underline, though, that LES may provide potentially more reliable turbulence models than RANS and its applicability on turbulent reactive flows has shown very promising results, hence its wide and rapid growth (POPE, 2000; PIERCE, 2001; PITSCH; LAGENESTE, 2002; WESTBROOK et al., 2005; POINSOT; VEYNANTE, 2005; COURTOIS, 2005; HAWORTH, 2010a; ANDRADE; SILVA; MURA, 2011; YILMAZ et al., 2011). The reason why LES provides substantial advantages for modeling turbulent combustion lies on the fact that the scalar mixing process is of paramount importance in chemical conversion. As an illustration of LES capability, Fig. (2.4) shows a three-dimensional visualization of the reacting flow inside of an industrial gas turbine burner. The isosurface of temperature at $T = 1,000$ K is shown. The wrinkling of the flame surface illustrates the turbulent nature of the flame/flow interaction. Pockets of fresh gases are periodically shed from the main flame zone and burnt downstream. A central core of hot gases is stabilized

along the burner axis by the recirculation zone induced by swirl (SELLE et al., 2004).

2.3.1.1 Characteristic turbulent time, velocity and length scales

Figure (2.5) shows the energy spectrum $[E(k)]$ of homogeneous isotropic turbulence at a sufficient high Reynolds number, as a function of the reciprocal of the eddy size, i.e., the wave number k. According to the Kolmogorov hypothesis (POPE, 2000), the energy transfer rate in the inertial subrange leads to a slope of $-5/3$.

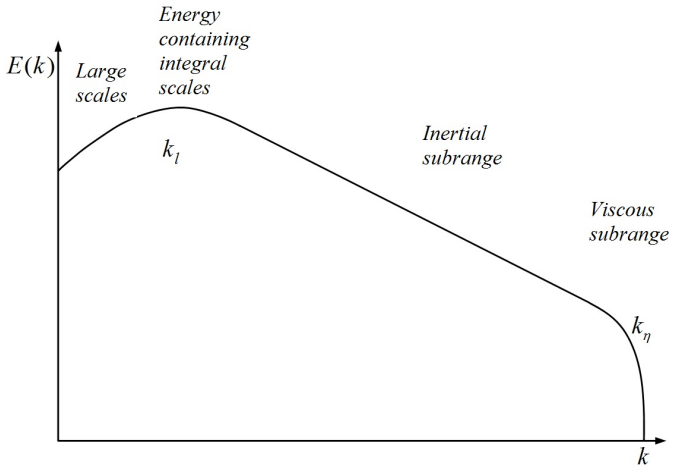

Figure 2.5: Energy spectrum of a homogeneous, isotropic turbulence. Kinetic energy, $[E(k)]$ as a function of wave number. Representation in a logarithmic scale.

Two important characteristic turbulent length scales bounding the inertial subrange can be identified in Fig. (2.5), the Kolmogorov length scale, η, and the integral length scale l. The Kolmogorov length scales denotes the scale of the smallest eddies. At these length scales, dissipation of the energy due to viscous forces occurs. Thus, the Kolmogorov length scale has to be a function of the kinematic viscosity, ν, and the kinetic energy dissipation, ε. In addition, the Kolmogorov time scale τ_η, can be defined as being proportional to the turnover time of a Kolmogorov eddy. By dimensional analysis, the Kolmogorov length, time and velocity scales can be defined as,

$$\eta = \left(\frac{\nu^3}{\varepsilon}\right)^{1/4}, \quad \tau_\eta = \sqrt{\frac{\nu}{\varepsilon}}, \quad v_\eta = \left(\nu^3 \varepsilon\right). \tag{2.2}$$

The relevant turbulent and chemical time and length scales for laminar premixed combustion

are presented in the following sections. Such laminar parameters are important since, when compared to those of a turbulent flow in a flow regime diagram, the different regimes of premixed turbulent combustion can be identified. In the following section the regimes of premixed turbulent flames are presented.

2.3.2 The laminar premixed flame

In a qualitative way, the characteristics of a premixed laminar flame are now described using Fig. (2.6). The fresh gases enters at the left hand side at a temperature T_u and are consequently burnt through the flame front. The burnt gases, at a temperature T_b, are convected to the outlet (right hand side) of the domain of interest. If the injection velocity of the fresh gases is the same as the laminar flame speed, S_l^0, such a flame front would appear fixed to an external observer.

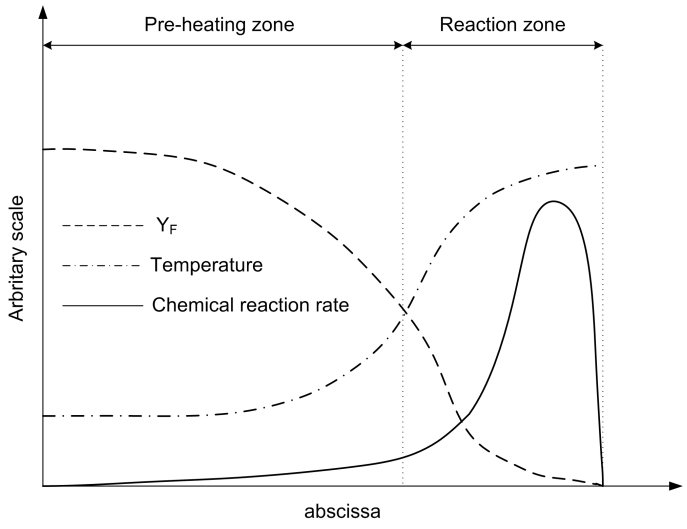

Figure 2.6: Evolution of the chemical reaction rate, temperature and mass fraction of fuel through a laminar flame front.

The flame front, with a thickness l_F can be separated in two zones: a pre-heating zone, and a reaction zone. In the pre-heating zone there is a temperature increase, without a strong presence of chemical reactions. The decrease of the reactants concentration is due the diffusion of species that mixes with part of the burnt gases before entering the reaction zone, where chemical reactions occurs. There is a strong decrease of the reactants concentration, which are progressively consumed. When no reactants are left, the chemical reaction stops, and the chemical reaction rate goes to zero.

2.3.2.1 Thickness and velocity of a laminar premixed flame

Based on a one-dimensional analysis of the Navier-Stokes equations, supposing a certain number of simplificative hypothesis (mainly supposing the flame as adiabatic and composed by gases with constant specific heat), Mallard and Chatelier (1883) proposed in 1883 to describe the laminar speed of a premixed flame as,

$$S_L \propto \left(\Gamma_k \overline{\dot{W}}_F\right)^{1/2}, \tag{2.3}$$

where $\overline{\dot{W}}_F$ is the mean reaction rate of fuel inside the flame front [3]. Supposing the chemical time, τ_c is of order $1/\overline{\dot{W}}_F$, and considering that $l_F \approx S_L \tau_c$, it is possible to show that,

$$l_F = \frac{\Gamma_k}{S_L}, \tag{2.4}$$

where, Γ_k is the molecular diffusivity of the chemical species k

2.3.3 Regimes and diagram of premixed turbulent flames

The understanding of the mechanisms by which turbulence and chemistry interact is essential prior to modeling of turbulent premixed combustion. Turbulent premixed reacting flows can be described by a wide range of characteristic time and length scales. The relevant turbulent and chemical time and length scales for laminar premixed combustion are important since, when compared to those of a turbulent flow in a flow regime diagram, the different regimes of premixed turbulent combustion can be identified. Borghi (1985) and Peters (1999), by analyzing experimental results of turbulent premixed flames, defined the possible modes of interaction between turbulent structures and flame structures. Such possible interactions are based on the relations between the turbulent and combustion time and length scales. Thus, the combustion regimes, could be represented graphically by a diagram known as Borghi diagram, illustrated, in a logarithmic scale, in Fig. (2.7).

[3] More precisely $\overline{\dot{W}}_F = \frac{1}{T_b - T_u} \int_{T_u}^{T_b} \dot{\omega}_F dT$, where $\dot{\omega}_F$, is the rate of fuel consumption.

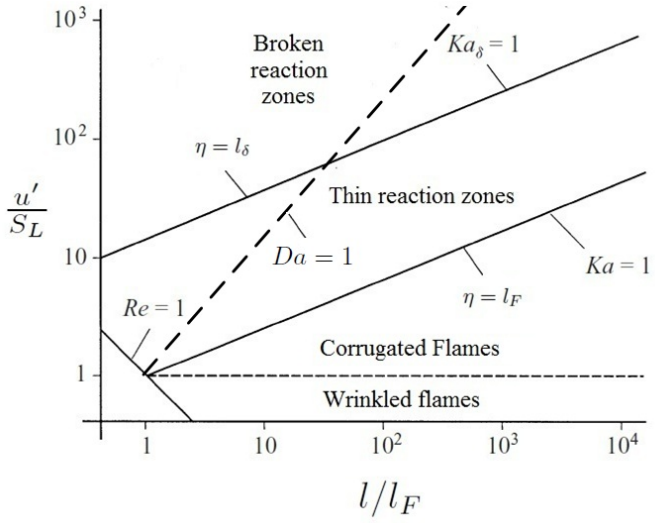

Figure 2.7: Regime diagram for premixed turbulent combustion, adapted from Peters (1999).

In the diagram presented in Fig. (2.7), the abscissa express the ratio l/l_F, which can be interpreted as a measure of the turbulent integral length scale, l, interacting with flames of thickness l_F, l_F being the total thickness of a laminar flame, proportional to the thickness of the pre-heating zone. The thickness of the internal layer, where the majority of the chemical reaction occurs, is called l_δ. The l_δ is approximately of order $0.1l_F$. The ordinate shows the ratio of u'/S_L, which is a measure of the turbulent intensity u', over the laminar flame speed S_L. The line $Re_T = 1$, with $Re_T = u'l/S_L l_F$, (BORGHI, 1985) delineates the turbulent combustion regime ($Re_T > 1$).

Considering the diagram shown in Fig. (2.7), at least four different turbulent premixed combustion regimes can be identified. They are outlined in the following.

1. Wrinkled flames regime: it is delimited by the condition of $u'/S_L < 1$. The laminar flame velocity is higher than the intensity of fluctuations and, therefore, governs the process flame-turbulence interaction. The turbulence practically does not wrinkle the flame front. Since turbulence is desired in a number of industrial applications, this kind of flame has few practical applications (ANDRADE, 2009);

2. Corrugated flames regime: it is delimited by the conditions $u'/S_L > 1$ and $Ka < 1$, where the Karlovitz number ($Ka = l_F^2/\eta^2 = \tau_c/\tau_\eta$), is the ratio between the chemical time scale and the Kolmogorov time scale (MERCI; MASTORAKOS; MURA, 2010;

PETERS, 1997). The characteristic turbulence intensity is higher than the laminar flame velocity, which induces the corrugation of the flame front. The smallest structures in the Kolmogorov scale however, are larger than the laminar flame thickness, thus not interfering with the internal structure of the flame;

3. Thin reaction zones: it is delimited by the conditions $Ka > 1$ and $Ka_\delta = l_\delta^2/\eta^2 < 1$. The first condition indicates that the Kolmogorov length scale, η, is smaller than the laminar flame thickness, l_F. The second condition indicates that η is larger than the inner layer of the laminar flame, l_δ. In this case the turbulence could alter the structure of the pre-heating layer of the flame and significatively modify the transport of the chemical species and energy. However, there still no interaction between the turbulence and the inner part of the flame;

4. Broken reaction zones or thickened flames: Above $Ka_\delta > 1$, with the Damkhöler number, i.e., the ratio of the integral turbulence time scale to a characteristic chemical time scale, $Da = \tau_t/\tau_c$, smaller than 1, the turbulent length scale is sufficiently small to penetrate the inner part of the laminar flame, l_δ. It can promote local extinctions of the chemical reaction due to heat and radicals losses in the pre-heating layer. In such a regime even a local extinction of the combustion is possible.

2.3.4 Effects of flame fronts on turbulence

The flame-turbulence interaction is a two-way mechanism. Turbulence not only affects the flame front, but the flame modifies the turbulent flow field also. An example of that occurs due the fact that when temperature changes along the flame front, kinematic viscosity and, therefore, the local Reynolds number changes as well. The kinematic viscosity of air, for instance, increases roughly as $T^{1.7}$, which means that for a flame in which the ratio $T_b/T_u = 8$, where T_b and T_u are the temperature of the burnt and fresh gases respectively, the local Reynolds number is about 40 times smaller in burnt than in the fresh gases. This results in the possibility of a relaminarization of the turbulent flow after it passes through a flame front (POINSOT; VEYNANTE, 2005).

Another effect that the combustion may induce on the turbulence is an increase of the turbulent kinetic energy associated with the flow acceleration through the flame front. For subsonic combustion, (POINSOT; VEYNANTE, 2005) show that the flow accelerates through a flame front from a velocity u_1 to $u_1 + S_L(\rho_u/\rho_b - 1) = u_1 + S_L(T_b/T_u - 1)$, where ρ_b and ρ_u are the density of the burnt and fresh gases respectively. This acceleration can be significant since it occurs in very thin regions, hence the turbulent flow field is altered. The vorticity can also be affected by the velocity and density changes leading to the so-called "flame-generated turbulence" (BORGHI; CHAMPION, 2000).

An important subject connected to turbulent premixed flames is the possible presence of the counter-gradient diffusion. In Veynante et al. (1997), Direct Numerical Simulations (DNS) are used to provide basic information on the modeling of the turbulent flux of the mean chemical reaction progress variable $\tilde{c}$, $\overline{\rho u_i' c'}$ and study the occurrence of counter-gradient transport. The configuration studied corresponds to two or three-dimensional premixed flames stabilized in an isotropic turbulent flow. The simulations, which correspond to various flame and flow conditions that are representative of flamelet combustion, reveal that different flames feature different turbulent transport properties. These differences can be related to basic dynamical differences in the flame flow interactions: counter-gradient diffusion occurs when the flow field near the flame is dominated by thermal dilatation due to chemical reaction, whereas gradient diffusion occurs when the flow field near the flame is dominated by the turbulent motions. By assuming infinitely fast chemical reactions, in the limit of high Damkhöler number values, Libby and Bray (1981), show that the turbulent transport of a reactive scalar, represented by the chemical reaction progress variable, can be determined by,

$$\overline{\rho u_i' c'} = \bar{\rho}\tilde{c}(1 - \tilde{c}) \left(\overline{u_k^b} - \overline{u_k^u} \right), \tag{2.5}$$

where $\overline{u_k^b}$ and $\overline{u_k^u}$ denote the conditional velocities in burned and unburned mixtures. Veynante et al. (1997) introduced the Bray number, N_B, a dimensionless parameter to qualitatively characterize the transition between gradient diffusion (GD) and counter-gradient

diffusion (CGD) scalar transport in turbulent premixed flames:

$$N_B = \frac{\tau S_L}{2\alpha\overline{u'}}, \tag{2.6}$$

where τ is the heat release parameter. The parameter α is an order-of-unity function that describes the ability of various sized eddies to affect the flame front (MERCI; MASTORAKOS; MURA, 2010). When $N_B > 1$, CGD takes place, whereas $N_B < 1$ correspond to GD.

The interaction between combustion-induced density changes and the pressure gradient plays a very important role in both flame-generated turbulence and counter-gradient diffusion. However, only in recent works on turbulent premixed combustion modeling is the considered conditional pressure gradients, (DOMINGO; BRAY, 2000; ROBIN; CHAMPION; MURA, 2008; MURA; CHAMPION, 2009). The next section provides a synthetic overview of the available models for turbulent premixed combustion.

2.3.5 Combustion models

As it will be seen in chapter 3, the filtering process of the transport equations yields a filtered chemical reaction rate term, $\overline{S}(c)$. The main difficulties in modeling this term are connected to the fact that the time and length scales of the flames are usually far smaller than the characteristics lengths of the mesh and time step size retained, at least concerning LES applications. Indeed, if considered the general dimensions of a combustion chamber, the size of the filters (which are related to the grid and time step size) retained in the simulations of turbulent flames are significantly larger than the thickness of a flame front. However, the chemical reaction rate, $\overline{S}(c)$, is connected to strong properties variations, such as temperature and mass fractions for instance. This renders that the determination, and consequently the modeling, of the contributions of the chemical reactions on the turbulent flow field quite challenging.

In this sense, many strategies have been developed during the last twenty years to tackle the modeling of turbulent premixed flames, more specifically the modeling for the

flamelet regime (MERCI; MASTORAKOS; MURA, 2010). Among them, the following approaches are highlighted: (a) Artificially thickened flames models (POINSOT; VEYNANTE, 2005), (b) G-equation based models, or level set models(WILLIAMS, 1985; PETERS, 1997, 1999; HERRMANN, 2006), (c) Flame surface density models (HAWKES; CANT, 2001), and (d) models based on probability density functions - PDFs. The first three approaches are based on the hypothesis of infinitely fast chemistry, i.e., flames in which the characteristic time scale of the chemical reactions are much smaller that the characteristic time scale of the turbulence, which correspond to very high Damkhöler numbers. In this situation, the flame front is seen as a extremely thin surface, constantly wrinkled and corrugated by the effects of turbulence. The literature is rich in information about those approaches, see for instance Bray, Libby and Moss (1985), Peters (1997), Pitsch and Lageneste (2002), Fox (2003), Poinsot and Veynante (2005), Pitsch (2006).

For finite rate chemistry, in the regime of thickened flames for instance, it is expected that the previous closures, developed for the fast chemistry limit, becomes less suitable, (MERCI; MASTORAKOS; MURA, 2010). In cases of finite rate chemistry the time scales of the chemical reactions have the same order of magnitude of the time scales of the turbulence, i.e., a close to unity Damkhöler number.

According to Mura, Galzin and Borghi (2003), the fourth approach "(d)", based on the probability density functions, allows modeling both fast chemistry and finite rate chemistry cases. Such a category of models are conceptually different from the models developed in the fast chemistry limit. While these are based on the dynamics and physical properties of the flames, thus being restricted to applications where laminar flames may be found, the PDF models are based on one-point statistical analysis of the flow (ANDRADE; SILVA; MURA, 2011).

There are two different ways to obtain the desired probability density function. A first one is to assume the PDF to have a particular shape that is parameterized by its first and second moments. These first and second moments are then solved using modeled transport

equations. Nevertheless, this approach may not account for the complex PDF distributions actually observed when complex chemistry effects are considered(FOX, 2003). A more powerful technique is to obtain the joint PDF of the scalars directly from their transport equations. This eliminates the need to specify PDF shapes, which almost always involves guessing and is therefore inaccurate. This method is referred to as the composition joint PDF method or "transported" PDF method.

Merci, Mastorakos and Mura (2010) argue that despite the great advantages of the transported PDF modeling, the resort to these models in premixed conditions remain relatively scarce. This is a result of the difficulty associated with the closure of the micro-mixing terms for reactive scalars (ANAND; POPE, 1987; MURA; GALZIN; BORGHI, 2003). The essential issue of premixed combustion in the PDF framework is that, it is mandatory to take into account the strong coupling between molecular diffusion and chemical reactions.Finally, Robin et al. (2007) provide robust methodologies based on the presumed PDF approach that are well-suited to deal with both wrinkled and thickened flames regimes, provided that a satisfactory closure is set forth to represent the mean scalar dissipation functions (MURA; ROBIN; CHAMPION, 2007; CHAKRABORTY; SWAMINATHAN, 2007).

In the transported PDF models (FOX, 2003), the main physical processes involved in a combustion, i.e., molecular diffusion, turbulent micro-mixing and thermal expansion due chemical reactions, which generally occur below the subfilter length scales, are analyzed by a statistical approach. The focus of the present work is on this approach, the models based on the transported probability density functions, or in a LES context the Filtered Density Function - FDF . Such an approach will be detailed in the following chapter.

CHAPTER III

MATHEMATICAL MODELING

In this chapter the mathematical framework retained for simulating turbulent reactive flows is presented. The method involves the numerical solution of partial differential equations and stochastic differential equations. A hybrid approach in which the LES methodology is coupled with the transport of the probability density function (PDF) is retained. From the LES approach the Eulerian filtered variables are evaluated, whereas stochastic differential equations are solved using Lagrangian particles that evolve in both physical and compositional space. The latter yields the full one point, one time statistics of filtered scalar fields and provides the LES solver with the filtered chemical reaction rate.

In the first part of the present chapter the balance equations that model the flows under consideration are presented, as well as the hypothesis adopted to proceed with their closures. Since the LES methodology is adopted, the filtering process of the balance equations is also described.

The second part of the chapter describes the main characteristics of the transported PDF method. The scalar PDF transport equation is presented and its equivalent system of stochastic differential equations is described. Finally, the chapter is concluded with a brief description of the coupling between the Eulerian and Lagrangian approaches (LES-PDF).

3.1 Governing equations

The main objective of the present work is to simulate turbulent reactive low Mach number flows. Considering a mathematical model suitable for variable density flows, in which the primary transported variables are the density $\rho(x_i, t)$, the three velocity components $u_i(\mathbf{x}, t)$ $(i = 1, 2, 3)$, the specific enthalpy h and the mass fractions Y_k of the K chemical species $(k = 1, \ldots, K)$, the balance equations for the cited variables in space, $(x_i, i = 1, 2, 3)$, and time, t, are summarized below along with an equation of state that relates the thermodynamic component of the pressure to density and temperature.

$$\frac{\partial \rho}{\partial t} + \frac{\partial \rho u_i}{\partial x_i} = 0, \tag{3.1}$$

$$\frac{\partial \rho u_i}{\partial t} + \frac{\partial \rho u_i u_j}{\partial x_j} = -\frac{\partial P}{\partial x_i} + \frac{\partial}{\partial x_j}\tau_{ij} + S_{ui}, \tag{3.2}$$

$$\frac{\partial \rho h}{\partial t} + \frac{\partial}{\partial x_j}\rho u_j h = \frac{\partial J_{hj}}{\partial x_j} + S_h, \tag{3.3}$$

$$\frac{\partial \rho Y_k}{\partial t} + \frac{\partial}{\partial x_j}\rho u_j Y_k = \frac{\partial J_{kj}}{\partial x_j} + S_k, \tag{3.4}$$

$$P = P_o(t) + P'(\mathbf{x}, t); \;\; P_o(t) = \rho R T; \tag{3.5}$$

in the above equations, τ_{ij} stands for the viscous strain rate tensor, S_{ui} represents the body forces, J_{hj} is the molecular flux of enthalpy in the j direction, S_h is the source term of enthalpy, J_{kj} is the molecular flux of the k chemical specie in the j direction, S_k is the chemical reaction rate of the k-th species, $P_o(t)$ is the thermodynamic pressure, a function of time only, $P'(\mathbf{x}, t)$ is the dynamic pressure, henceforth denoted only by p. Since the flows treated in this work operates in open domains, the thermodynamical pressure does not vary in time. Hence, $P_o(t)$ becomes a reference pressure, e.g. atmospheric pressure. $R^o = R\Sigma_{k=1}^{K} Y_k/\mathcal{M}_k$ is the mixture gas constant, with R being the universal gas constant. The molar mass of species is denoted by $\mathcal{M}_k$, and T is the temperature.

Considering a Newtonian fluid the viscous strain rate tensor is given by,

$$\tau_{ij} = \mu\left(\frac{\partial u_i}{\partial x_j} + \frac{\partial u_j}{\partial x_i}\right) - \frac{2}{3}\mu\frac{\partial u_k}{\partial x_k}\delta_{ij}, \tag{3.6}$$

where the bulk viscosity has been neglected and, μ is the fluid viscosity and δ_{ij} is the Kronecker delta tensor. In this work the molecular diffusion flux of species is based on the gradient transport hypothesis, and can be described by the Fick law. Neglecting the Soret effect, J_{kj} is given by,

$$J_{kj} = -\frac{\mu}{Sc_k}\frac{\partial Y_k}{\partial x_j}, \tag{3.7}$$

In Eq. (3.7) $Sc_k = -\nu/\Gamma_k$ is the Schmidt number of the k species; Γ_k is the molecular diffusivity of the chemical species k.

The molecular flux of enthalpy can be described by,

$$J_{hj} = -\frac{\mu}{Pr}\left[\frac{\partial h}{\partial x_j} + \sum_{k=1}^{K}\left(\frac{Pr}{Sc_k} - 1\right)h_k\frac{\partial Y_k}{\partial x_j}\right], \tag{3.8}$$

where the first term of the right hand side of Eq. (3.8) is the flux of enthalpy by molecular diffusion, and the second term stands for the flux of enthalpy induced by different diffusion coefficients of each chemical specie. The term representing the specific enthalpy associated to each chemical specie k, h_k, is the sum of the chemical and sensible enthalpies, i.e.,

$$h_k = h_k^0 + \int_{T_0}^{T} C_{p,k}dT, \tag{3.9}$$

where C_p is the mean specific heat at constant pressure of the mixture. Heat transport by radiation and Dufour effects [1], have been neglected in the present analysis.

The Prandtl number, ratio of momentum and thermal diffusivity is given by,

$$Pr = \frac{\mu C_p}{\lambda}, \tag{3.10}$$

where λ stand for the thermal conductivity of the fluid.

The ratio of Schmidt and Prandtl numbers i.e., the Lewis number, that describes the ratio between the thermal and mass diffusivity of each chemical species k is given by $Le_k = Sc_k/Pr = \lambda/(\rho C_p \Gamma_k)$. Assuming Lewis number values equal to unity, i.e., equivalent thermal

[1] diffusion of enthalpy due the gradient of mass fractions of chemical species

and mass diffusivity coefficients, and also assuming $\Gamma_k = \Gamma$, the molecular flux of enthalpy is given by,

$$J_{hj} = -\rho\Gamma\frac{\partial h}{\partial x_j}. \tag{3.11}$$

The source term of sensible enthalpy S_h of Eq. (3.3) can be written,

$$S_h = \frac{Dp}{Dt} + \frac{\partial \tau_{ij} u_i}{\partial x_j}, \tag{3.12}$$

where the term Dp/Dt represents the effects of compressibility, and the term $\partial(\tau_{ij}u_i)/\partial x_j$ stands for the energy dissipation due the action of viscous forces. The decomposition of the pressure shown in Eq. (3.5) is reinforced here. In the work of Lessani and Papalexandris (2006b) it is recalled that there are basically three considerations to be addressed when dealing with the time derivative of pressure: (i) the system is open, (ii) the system is closed and (iii) the system is semi-open so that there is a restricted opening (for example, a crack) between the flow domain and its exterior. In the present work the flows of interest are flows with open boundaries, in which p_o is constant, and therefore Dp/Dt can be neglected. For closed and semi-open systems, Lessani and Papalexandris (2006b) present alternatives for modeling Dp/Dt. Concerning the energy dissipation due the action of viscous forces, with the assumption of low Mach number flow, this term is neglected.

With the simplifying assumptions retained above, Eqs. (3.3) and (3.4) present equivalent forms, thus a general transport equation for a scalar field Φ composed by $\sigma = K + 1$ species, where $\phi_k = Y_k; k = 1, ..., K$, and $\phi_\sigma = h$, can be derived.

Based on the assumptions and hypothesis retained, the system of equations to be solved can finally be written,

$$\frac{\partial \rho}{\partial t} + \frac{\partial \rho u_i}{\partial x_i} = 0, \tag{3.13}$$

$$\frac{\partial \rho u_i}{\partial t} + \frac{\partial \rho u_i u_j}{\partial x_j} = -\frac{\partial p}{\partial x_i} + \frac{\partial \tau_{ij}}{\partial x_j}, \tag{3.14}$$

$$\frac{\partial \rho \phi_\alpha}{\partial t} + \frac{\partial \rho u_j \phi_\alpha}{\partial x_j} = \frac{\partial}{\partial x_j}\left(\rho\Gamma_\alpha\frac{\partial \phi_\alpha}{\partial x_j}\right) + S_\alpha, \tag{3.15}$$

$$\rho = \rho(\phi_\alpha) \tag{3.16}$$

As it will be seen in section 3.1.6, through some additional assumptions concerning the chemical kinetics and the Mach number of the flow, it is possible to further simplify Eq. (3.15) to a transport equation of a single scalar, called progress variable, denoted by c. The evaluation of this progress variable determines the influence of the combustion process on the flow by governing density variations. In this case the density and the scalar source term, S_α, are exclusive functions of c, i.e. $\rho = \rho(c)$ and $S_\alpha = S(c)$. It is noteworthy that the effects of the eventual variations of temperature on the molecular viscosity are also taken into account using the Sutherland's law (SCHLICHTING, 1951).

3.1.1 Filtered transport equations

The main idea behind the LES methodology is to compute the largest structures of the flow field, typically larger then the computational grid, whereas the non-linear interaction between large and sub-grid scales must be modeled. This methodology has been widely used with success for non-reacting flows, see in Pope (2000), Lesieur and Métais (1996), Germano et al. (1991), Lilly (1992), Silveira-Neto et al. (1993). In combustion modeling however, the application of LES still remains its early stages (POINSOT; VEYNANTE, 2005).

In LES, the dependent variables can be filtered in spectral space, where components greater than a given cut-off frequency are suppressed, (DA-SILVA, 2001) or in physical space (weighted average over a given volume). In the present work a box filter in physical space is adopted. These types of LES filters have been discussed, among others, in Pope (2000). A filtered quantity f is defined as,

$$\overline{f}(\mathbf{x}) = \int f(\mathbf{x}')F(\mathbf{x} - \mathbf{x}')d\mathbf{x}', \tag{3.17}$$

where F is the LES filter, defined as:

$$F(\mathbf{x}) = F(x_1, x_2, x_3) = \begin{cases} 1/\Delta^3 & if\ |x_i| \leq \Delta,\ i = 1, 2, 3 \\ 0 & otherwise \end{cases}, \tag{3.18}$$

where (x_1, x_2, x_3) are the spatial coordinates of the vector $\mathbf{x}$, and $\Delta = \sqrt[3]{V_c}$ is a cubic box of size equivalent to that of the finite-volume grid retained for discretizing the transport equations in the eulerian field, and V_c is the volume of a mesh element. It is worth noting that the filter used in the present work is implicit, i.e., the process of filtering is implicitly performed based on the fact that the actual process of discretization of the transport equations is, intrinsically, a filtering process in space and time. Thus, the characteristic length of the box in Eq. (3.18) is equivalent to the characteristic length of the finite volume grid adopted in the solution of the discretized system of equations and the temporal band width is associated with the size of the time step used in the simulations.

In variable density flows it is useful to define the mass-weighted Favre filtering:

$$\overline{\rho}\tilde{f}(\mathbf{x}) = \int \rho f(\mathbf{x}')F(\mathbf{x}-\mathbf{x}')d\mathbf{x}'. \tag{3.19}$$

The filtered quantities $\overline{f}$ and/or $\tilde{f}$ are computed by the numerical simulations. The fluctuations $f' = f - \overline{f}$ are the unresolved, subgrid scale part of the quantity f. With such a definition it is possible to perform the filtering of the transport equations. This procedure, however, must be done with care, once, contrary to RANS averaging for instance, in LES we have $\overline{f'} \neq 0$. Filtered and double filtered values are not equal neither ($\overline{\overline{f}} \neq \overline{f}$).

The filtered transport equations can be written,

$$\frac{\partial \overline{\rho}}{\partial t} + \frac{\partial \overline{\rho}\tilde{u}_i}{\partial x_i} = 0, \tag{3.20}$$

$$\frac{\partial \overline{\rho}\tilde{u}_i}{\partial t} + \frac{\partial \overline{\rho}\tilde{u}_i\tilde{u}_j}{\partial x_j} = -\frac{\partial \overline{p}}{\partial x_i} + \frac{\partial \bar{\tau}_{ij}}{\partial x_j} - \frac{\partial \tau_{ij}^{SGS}}{\partial x_j}, \tag{3.21}$$

$$\frac{\partial \overline{\rho}\tilde{\phi}_\alpha}{\partial t} + \frac{\partial \overline{\rho}\tilde{u}_i\tilde{\phi}_\alpha}{\partial x_j} = \frac{\partial}{\partial x_j}\left(\overline{\rho}(\overline{\Gamma})\frac{\partial \tilde{\phi}_\alpha}{\partial x_j}\right) - \frac{\partial Q_{\alpha j}}{\partial x_j} + \overline{S_\alpha}, \tag{3.22}$$

where, $\tau_{ij}^{SGS} = (\widetilde{\overline{\rho}u_i u_j} - \overline{\rho}\tilde{u}_i\tilde{u}_j)$ and $Q_{\alpha j} = \left(\widetilde{\overline{\rho}u_i\phi_\alpha} - \overline{\rho}\tilde{u}_i\tilde{\phi}_\alpha\right)$ are the subgrid scale (SGS) stress tensor and the SGS scalar fluxes, respectively. For non-reacting flows the SGS closure is associated with τ_{ij}^{SGS} and $Q_{\alpha j}$ only. In reacting flows, an additional model is required for

the filtered reaction rate $\overline{S}(\alpha)$.

In the next section the modeling approaches adopted in the present work for the terms τ_{ij}^{SGS} and $Q_{\alpha j}$ are described.

3.1.2 Subgrid closure: the Smagorinsky Model

Most of the subgrid models assume that the smallest turbulent scales are approximately isotropic and homogenous, exhibiting a "universal" character, whereas the largest, more energetic structures, are dependent on the flow characteristics. The universal character of the smallest scales should render them more amenable to modeling, i.e., such an universal behavior should make these structures more predictable. The most popular subgrid scale model is the Smagorinsky model (SMAGORINSKY, 1963). The unresolved momentum flows are expressed according to the Boussinesq assumption (FERZIGER; PERIC, 1996; POINSOT; VEYNANTE, 2005),

$$\tau_{ij}^{SGS} - \frac{\delta_{ij}}{3}\tau_{kk}^{SGS} = \mu_{SGS}\left(\frac{\partial\tilde{u}_i}{\partial x_j} + \frac{\partial\tilde{u}_j}{\partial x_i} - \frac{2}{3}\frac{\partial\tilde{u}_k}{\partial x_k}\delta_{ij}\right) = 2\mu_{SGS}\left(\tilde{S}_{ij} - \frac{\delta_{ij}}{3}\tilde{S}_{kk}\right), \tag{3.23}$$

where μ_{SGS} is the subgrid (or turbulent) viscosity and $\tilde{S}_{ij}$ is the strain rate tensor of the resolved field (FERZIGER; PERIC, 1996). Note, however, that the isotropic part of the residual stress does not need to be modeled separately when pressure is decoupled from thermodynamic variables, because it may then be lumped together with the pressure. In the present study, acoustic interactions and compressibility effects are not considered, so in the interest of computational efficiency, this term is not actually computed.

In the Smagorinsky model the eddy viscosity μ_{SGS} is obtained by assuming that the small scales are in equilibrium, so that energy production and dissipation are in balance. This yields,

$$\mu_{SGS} = 2\bar{\rho}(C_s\Delta)^2|\tilde{S}| = 2\bar{\rho}(C_s\Delta)^2\left(2\tilde{S}_{ij}\tilde{S}_{ij}\right)^{1/2}, \tag{3.24}$$

where C_s is known as Smagorinsky constant. Its value is chosen, in such a way that lo-

cal equilibrium is maintained, between 0.1 to 0.25 (GERMANO et al., 1991; POPE, 2000). Although its successful application in numerous cases, the Smagorinsky model is restricted, with several limitations. Among then, it can be cited: (i) the model does not prevent vanishing small values of the turbulent viscosity in cases when re-laminarization of the flow occurs, an important effect that may occur in reactive flows, once the thermal expansion can locally lead to flow laminarization, (ii) by assuming the equilibrium hypothesis, the model fails in regions where such equilibrium is not maintained, for instance, the model does not allow the energy transfer from the smallest to the largest structures, which is known as backscattering (LILLY, 1992), (iii) for simulations where grid elements are highly anisotropic, the models tends to be excessively diffusive, and the accuracy of the numerical methods retained is compromised (SCOTTI; MENEVEAU; LILLY, 1993), (iv) it is known that the Smagorinsky model can be excessively dissipative, especially near walls. One possible solution to circumvent this last drawback is to diminish the value of C_s near walls, thus limiting the near-wall eddy viscosity.

In this respect Ferziger and Peric (1996) present the van Driest damping function,

$$C_s = C_{so}\left(1 - e^{-n^+/A^+}\right)^2, \tag{3.25}$$

where n^+ is the distance from the wall in viscous wall units, $n^+ = nu_\tau/\mu$, the shear velocity $u_\tau = \sqrt{\tau_\omega/\rho}$ and τ_ω is the shear stress at the wall. A^+ is a constant, usually taken as 25. C_{so} is the initial value of the Smagorinsky constant. Ferziger and Peric (1996) argue that although this modification of C_s produces the desired result, it is difficult to justify its use within the LES context. The SGS model should only depend on the local properties of the flow, and a distance to a wall is not a flow property.

3.1.3 Subgrid closure: the dynamic Smagorinsky Model

Large eddy simulation has been developed and studied as a prediction tool for turbulent flows during the past forty years, with significant advances with the development of the dynamic Smagorinsky model (GERMANO et al., 1991), with the modifications proposed by (LILLY, 1992). Based also on the Boussinesq hypothesis, with the dynamic procedure, model

coefficients are automatically computed using information contained in the resolved turbulent scales, thereby eliminating possible uncertainties associated with tunable parameters. On great advantaged of the dynamic model is that in the modeling of flows with presence of walls, the turbulent viscosity tends to zero automatically once the tensor L_{ij}, which depends only on the velocity field, tends to zero at the walls. This fact makes the use of damping functions, like the van Driest damping function showed above, no longer necessary.

Several authors have been using the dynamical Smagorinsky model in a wide range of applications, see for instance Lesieur, Métais and Comte (2005), Meneveau, Lund and Cabot (2006), Moin (2008). Moin et al. (1991) applied the dynamic procedure to scalar transport and subgrid kinetic energy models for compressible turbulent flows using Favre filtering. Pierce (2001) using a progress-variable approach and a presumed beta PDF for a conserver scalar, applied the dynamic model in the prediction of the lift-off in non-premixed combustion. In the context of simulation of turbulent premixed combustion, Knudsen and Pitsch (2008), using a level-set approach, presented a dynamic model for describing the turbulent burning velocity in the context of LES. They applied such a model in a simulation of a turbulent premixed Bunsen flame studied experimentally by Chen et al. (1996).

Similarly to the Smagorinsky model, the subgrid viscosity is given by,

$$\mu_{SGS} = \bar{\rho} C_s \Delta^2 |\tilde{S}| = \bar{\rho} C_s \Delta^2 \left(2\tilde{S}_{ij}\tilde{S}_{ij}\right)^{1/2}. \tag{3.26}$$

In the dynamic Smagorinsky model the constant C_s is evaluated using the dynamical procedure. Adopting the nomenclature used in the work of Pierce (2001), the following notation for density-weighted test filtering is retained:

$$\breve{\tilde{u}} = \frac{\widehat{\bar{\rho}\tilde{u}}}{\widehat{\bar{\rho}}}. \tag{3.27}$$

In dynamic modeling, the test filter width is denoted by $\widehat{\Delta}$ and is usually taken to be twice the width of the grid filter, Δ. For the subgrid turbulent stress model, Eq. (3.23), the

dynamic procedure gives,

$$C_s = \frac{\mathcal{L}_{ij}\mathcal{M}_{ij}}{2\mathcal{M}_{ij}\mathcal{M}_{ij}}, \tag{3.28}$$

where,

$$\mathcal{L}_{ij} = -\widehat{\overline{\rho}\tilde{u}_i\tilde{u}_j} + \overline{\rho}\check{\tilde{u}}_i\check{\tilde{u}}_j, \tag{3.29}$$

and,

$$\mathcal{M}_{ij} = \widehat{\overline{\rho}}\widehat{\Delta}^2\check{\tilde{S}}_{ij}|\check{\tilde{S}}| - \widehat{\overline{\rho}\Delta^2\tilde{S}_{ij}|\tilde{S}|}. \tag{3.30}$$

It is noteworthy that subgrid models are generally valid for predicting statistical properties of the subgrid scales but usually cannot account for instantaneous subgrid scale fluctuations (PIERCE, 2001). For the dynamic procedure to be applicable, the quantity to be modeled must vary substantially between the grid and test filter scales; otherwise, the difference between the values of a property in the test filter and in the grid filter will not be significant and therefore may not be used for modeling subgrid-scale quantities. Examples of quantities that cannot be modeled dynamically are dissipation and chemical reaction rates, because these phenomena occur almost exclusively at the smallest scales, which are always unresolved in LES. The resort to transported PDF methods, like the one explained in the further sections, is due to the fact that such a method may provide closed solutions for at least one of the aforementioned quantities.

3.1.4 Subgrid closure: the scalar flux

Following the closure retained for the subgrid stress tensor, the SGS scalar flux can be represented using a gradient-diffusion model (FOX, 2003),

$$Q_{\alpha j} = -\bar{\rho}\Gamma_{SGS}\frac{\partial\tilde{\phi}_\alpha}{\partial x_j}, \tag{3.31}$$

where $\tilde{\phi}_\alpha$ is the resolved scalar field and Γ_{SGS} is the subgrid diffusion coefficient. Γ_{SGS} is evaluated as (ANDRADE, 2009),

$$\Gamma_{SGS} = \frac{2\bar{\rho}(C_s\Delta)^2}{Sc_{SGS}}|\tilde{S}| = \frac{\mu_{SGS}}{Sc_{SGS}}, \tag{3.32}$$

where Sc_{SGS} is the subgrid turbulent Schmidt number that controls the magnitude of the SGS turbulent diffusion.

3.1.5 Chemical reaction rate

The accurate determination of the filtered chemical reaction rate $\overline{S}_\alpha$ remains one of the most important challenges in Large Eddy Simulations. The main difficulties are due to the characteristic size of the spatial and temporal scales of the chemical phenomena, whose order is usually smaller than grid size. Therefore, the modeling of the filtered chemical reaction rate is a crucial step.

Among the basic requisites of the models that intend to represent $\overline{S}_\alpha$ is the one to encompass regimes of premixed combustion, as well as the basic chemical kinetics mechanisms. In the present thesis, a formulation based on statistical representations of the subgrid effects is retained. Such methodology is based on the transport of a probability density function, and, in principle, allows the modeling of the filtered chemical source term independent of the Damköhler number.

According to Mura, Galzin and Borghi (2003), the basic equations for PDFs are of general validity, but the so-called micro-mixing model, needed for the closure of the turbulent transport in the compositional space, and the turbulent diffusion model that are adopted in the modeled equations do restrict the applicability domain of such equations.

The closure assumptions and the mathematical modeling of the PDF equation are the subject of section 3.2. In the next subsection, the focus is to define an expression for the chemical reaction rates.

3.1.6 Simplifying assumptions of the chemical kinetics

In order to proceed with the mathematical modeling of the chemical source term, it is presented here a description of the chemical kinetics mechanisms and the simplifying assumptions adopted in order to obtain a non-dimensional reaction the rate for a single, global and irreversible chemical reaction. The equations here presented are inspired in the work of Orbegoso (2007) and Orbegoso and Silva (2009).

First, the fundamental equations of the chemical kinetics are presented. Considering a chemical system composed by K chemical species, reacting through M elementary chemical reactions,

$$\sum_{k=1}^{K} v'_{km}\mathcal{N}_k = \sum_{k=1}^{K} v''_{km}\mathcal{N}_k, \qquad m = 1, ..., M, \tag{3.33}$$

where $\mathcal{N}$ is the chemical symbol of the specie k, v'_{km} and v''_{km} are, respectively, the stoichiometric coefficient of the k-th species in the reactants and products of the m-th reaction. The mass conservation equation can be written as,

$$\sum_{k=1}^{K} v'_{km}\mathcal{W}_k = \sum_{k=1}^{K} v''_{km}\mathcal{W}_k, \qquad m = 1, ..., M, \tag{3.34}$$

where $\mathcal{W}_k$ is the molar mass of the k-th species. Eq. (3.34) can also be written,

$$\sum_{k=1}^{K} v_{km}\mathcal{W}_k = 0, \qquad m = 1, ..., M, \tag{3.35}$$

with $v_{km} = v'_{km} - v''_{km}$.

The production rate of the k-th chemical species, S_k, is the result of the sum of the productions rates of this species in each of the M reactions,

$$S_k = \sum_{m=1}^{M} S_{km} = W_k \sum_{m=1}^{M} v_{km}q_m, \qquad k = 1, ..., K, \tag{3.36}$$

where q_m is the velocity of the m-th reaction. The sum of the production rates of the K

species is,

$$\sum_{k=1}^{K} S_k = \sum_{k=1}^{K} \left[\mathcal{W}_k \sum_{m=1}^{M} v_{km} q_m \right] = \sum_{m=1}^{M} \left[q_m \sum_{k=1}^{K} v_{km} \mathcal{W}_k \right] = 0. \tag{3.37}$$

The velocity of the m-th reaction, q_m, is given by,

$$q_m = k_m^f \prod_{k=1}^{K} [X_k]^{v'_{km}} - k_m^r \prod_{k=1}^{K} [X_k]^{v''_{km}}, \tag{3.38}$$

where $[X_k]$ is the molar concentration of the k-th species, k_m^f and k_m^r are, respectively, the direct and inverse reactions rates of the m-th reaction. The molar concentrations are,

$$[X_k] = \frac{\rho Y_k}{\mathcal{W}_k} = \frac{\rho_k}{\mathcal{W}_k} = \frac{\rho}{\overline{\overline{\mathcal{W}}}} X_k, \tag{3.39}$$

where Y_k, X_k and ρ_k are, respectively, the mass fraction, the molar fraction and the partial density of the k-th species. The quantities k_m^f and k_m^r are important factors in the modeling of the chemical processes and can be described by the use of the empirical law of Arrhenius,

$$k_m^f = A_m T^{\beta_m} exp(-E_m/RT). \tag{3.40}$$

A_m, β_m and E_m are the pre-exponential constant (frequency factor), the temperature exponent and the activation energy of the m-th chemical reaction, respectively. The velocity k_m^r can be evaluated from k_m^f together with the equilibrium constant of the k-th elementary reaction, K_{cm} (WILLIAMS, 1985).

Once defined the fundamental equations of chemical kinetics, simplifying assumptions are made in order to obtain non-dimensional reaction rate of a single, global and irreversible chemical reaction. These assumptions are:

1. Combustion of a single, global ($m = 1$) irreversible ($k_m^r = 0$) reaction, i.e.,

$$C + rO \rightarrow (1 + r)P, \tag{3.41}$$

where C represents the fuel, O the oxidizer, P the combustion products and r the mass of oxidizer necessary to react a unity of mass of fuel,

2. The fuel C is the minor species reactant, i.e., $[X_C] \ll [X_O]$. As a consequence,

$$Y_O = \frac{\dot{m}_O}{\dot{m}_O + \dot{m}_C} \approx 1 = cte, \tag{3.42}$$

3. The molecular diffusivity of the fuel and the thermal diffusivity of the mixture are equivalents, i.e.,

$$Le = \frac{\lambda}{\rho c_p \Gamma} = 1, \tag{3.43}$$

4. Low Mach number flow, $Ma \ll 1$,

5. The exponent of temperature of the Arrhenius law is null ($\beta_1 = 0$)

Under those hypothesis, the velocity of the unique global equations lies,

$$q = [X_C][X_O]A_\tau exp(-E/RT). \tag{3.44}$$

where A_τ becomes the frequency factor of the unique global irreversible chemical reaction.

Applying the equalities Eq. (3.39) in Eq. (3.44) it is possible to write,

$$q = \left(\frac{\rho}{\overline{\overline{\mathcal{W}}}}\right)^2 X_C X_O A_\tau \exp\left(-E/RT\right). \tag{3.45}$$

The characteristic time of the chemical reactions is defined as,

$$\tau_c = \left[\frac{\rho}{\overline{\overline{\mathcal{W}}}} X_C|_o X_O|_o A_\tau \exp\left(-E/RT_b\right)\right]^{-1}. \tag{3.46}$$

where $X_C|_o$, $X_O|_o$ are values of the molar fractions of fuel and oxidizer in the fresh mixture,

respectively. T_u is the temperature of the fresh gases. Combining Eq. (3.45) and Eq. (3.46),

$$q = \frac{1}{\tau_c}\frac{X_C}{X_C|_o}\frac{X_O}{X_O|_o}\exp\left(-\frac{E}{RT}+\frac{E}{RT_b}\right). \tag{3.47}$$

The chemical reaction progress variable is defined as,

$$c = 1 - \frac{X_C}{X_C|_o} = \frac{T - T_u}{T_b - T_u}, \tag{3.48}$$

where T is the temperature, T_u is the temperature of unburnt (fresh) gases and T_b is the temperature of the burnt gases. A value of $c = 0$ is associated to fresh gases, and $c = 1$ corresponds to burnt gases.

Under the assumptions used in this section, once given the parameters $\tau = (T_b - T_u)/T_b$ and $\beta = \tau(T_a/T_b)$, where $T_a = E_a/R$ is the activation temperature, E_a is the activation energy and R is the universal constant of gases, the structure of a stationary premixed flame depends on the "flame parameter" Λ (POINSOT; VEYNANTE, 2005).

$$\Lambda = \frac{\alpha A_\tau T_u^{\beta_1}}{S_L^2}\exp^{-\frac{\beta}{\tau}}, \tag{3.49}$$

Such a parameter contains information like heat diffusivity, $\alpha = \lambda/(\rho C_p)$, rate parameters, A_τ, laminar flame speed S_L. According to Poinsot and Veynante (2005) various asymptotic analysis techniques have been developed to solve Eq. (3.49). The first one is due to Zeldovich, Frank Kamenetski and von Karman (ZKF) and gives:

$$\Lambda = 0.5\beta^2, \tag{3.50}$$

A more precise result, developed by Williams (1985), and retained in the present work is:

$$\Lambda = 0.5\beta^2\left[1 + \frac{2}{\beta}(3\tau - 1.344)\right], \tag{3.51}$$

The chemical reaction rate, $S(c)$, is related to the rate of progress of the single, global

reaction, q, and the non-dimensional chemical rate of production, $\dot{\mathcal{S}}$, by the expression,

$$S(c) = A_\tau \rho \dot{\mathcal{S}}, \tag{3.52}$$

where the pre-exponential constant can be calculated as $A_\tau = \Lambda S_L^2 / \left[\alpha e^{(-\beta/\tau)}\right]$ and $\dot{\mathcal{S}} = (1-c)\exp\left[-\frac{\beta(1-c)}{1-\tau(1-c)}\right]$,.

It is noteworthy that the term $S(c)$ presents a strongly non-linear dependency on β, τ and of the progress variable c.

Based on the definitions given in this subsection, the mathematical background required to describe the method of the transported PDF can readily be obtained. This is the objective of the next section.

3.2 Turbulent combustion modeling using a Hybrid LES/PDF computational model

Probability density function (PDF) methods offer compelling advantages for modeling chemically reacting turbulent flows (HAWORTH, 2010a). In particular, they provide an effective resolution to the closure problems that arise from averaging or filtering the highly nonlinear chemical source terms, and other terms that correspond to one-point physical processes in the instantaneous governing equations (FOX, 2003). The closure of the chemical source term represents a challenge, since the derived representations of the mean chemical source term must be consistent with known theoretical constraints and experimental observations, without the direct knowledge of sub-grid scalar fields[2]. This characteristic implies that, in principle, even complex chemical kinetics schemes can be treated without closure difficulties by a transported PDF-based method. Another reason is that statistical moments of first and second order, associated to RANS or LES models, can be easily evaluated.

On the other hand, since PDF models determine one-point statistics only, terms that thus involve gradient of properties cannot be resolved explicitly, hence important effects, such as molecular diffusion and dissipation of scalar fields must be modeled. Indeed, most of the

[2]Actually, such an information would be available in a DNS simulation, however, DNS simulations for turbulent reacting flows are not easily tractable with the present computational power.

developments in the past years have been devoted to the improvement of the physical realism of such models, known as micro-mixing models (MURA; GALZIN; BORGHI, 2003).

The joint scalar-velocity PDF equation is a multidimensional transport equation that involves both independent variables and geometrical dimensions of the velocity vector and the mixture composition. Such an equation contains classical evolution terms in physical space, such as transient and advective transport of the PDF; pressure fluctuations, viscous dissipation and other terms that describe the PDF evolution in composition space, such as the molecular diffusion conditioned to the scalar field; mean pressure gradient and a term connected to the rate of chemical reaction.
In the present work a formulation based on a PDF transport equation of the filtered scalar field is retained. However such a formulation does not contain information on the evolution of the velocity field and turbulence time and length scales. As a consequence, it is necessary to model the transport of these flow properties separately. In the present work that coupling is achieved by means of a hybrid LES-PDF approach.

In contrast with classical algorithms that are commonly retained to perform the numerical simulation of a set of partial differential equations, i.e, finite-difference or finite-volume methods, the modeled PDF transport equation has a rather different structure. It is a high-dimensional scalar transport equation, and it is less amenable for finite-volume or finite-difference methods. From early on times in the development of PDF methods, Monte Carlo techniques, in which the PDF is represented by an ensemble of stochastic particles, have been employed (POPE, 1985). Stochastic differential equations (SDEs) are constructed to model the particle properties, e.g., velocity, composition, and frequency, such that the particles exhibit the same PDF as in the turbulent flows.

3.2.1 Transport of the Probability Density Function

In this subsection the mathematical formulation of the transported Probability Density Function method is detailed. First, the joint velocity-composition PDF equation is derived, from the general form of such an equation, the joint composition PDF is demonstrated and

the closures hypothesis retained are presented.

3.2.1.1 Joint velocity-scalar PDF

Considering a vector field $\Phi(\mathbf{x},t) = [\mathbf{u}(\mathbf{x},t), \mathbf{Y}(\mathbf{x},t), \mathbf{h}(\mathbf{x},t)]$ as an ensemble of the velocity field, of the mass fractions of the chemical species and the enthalpy, its one point, one time joint probability density function $P_\Phi(\Psi;\mathbf{x},t) = P_{\mathbf{u},\mathbf{Y},\mathbf{h}}(\mathbf{V},\psi,H;\mathbf{x},t)$ is defined as the probability of an event where the random fields of velocity $\mathbf{u}(\mathbf{x},t)$, mass fraction $\mathbf{Y}(\mathbf{x},t)$ and enthalpy $\mathbf{h}(\mathbf{x},t)$ in a point $\mathbf{x}$ and in a instant of time t are within a differential neighborhood of the values $\mathbf{V},\psi,H$, i.e.,

$$\begin{aligned} P_\Phi(\Psi;\mathbf{x},t)d\Psi &\equiv Prob\left\{\Psi \leq \Phi(\mathbf{x},t) < \Psi + d\Psi\right\} \\ &\equiv Prob\left\{\mathbf{V} \leq \mathbf{u}(\mathbf{x},t) < \mathbf{V} + d\mathbf{V}\right\} \cap \\ &\quad Prob\left\{\psi \leq \mathbf{Y}(\mathbf{x},t) < \psi + d\psi\right\} \cap \\ &\quad Prob\left\{H \leq \mathbf{h}(\mathbf{x},t) < H + dH\right\}. \end{aligned} \tag{3.53}$$

The transport equation of the joint velocity - mass fraction - enthalpy PDF can be written as (DOPAZO; O'BRIEN, 1974; POPE, 1985):

$$\begin{aligned} \frac{\partial \rho(\Psi) P_\Phi(\Psi;\mathbf{x},t)}{\partial t} + \frac{\partial \rho(\Psi) u_j P_\Phi(\Psi;\mathbf{x},t)}{\partial x_j} = &-\frac{\partial}{\partial \mathbf{V}_j}\left[\rho(\Psi)\langle A_j|\Phi\rangle P_\Phi(\Psi;\mathbf{x},t)\right] \\ &-\frac{\partial}{\partial \psi_k}\left[\rho(\Psi)\langle C_k|\Phi\rangle P_\Phi(\Psi;\mathbf{x},t)\right] \\ &-\frac{\partial}{\partial H}\left[\rho(\Psi)\langle C_h|\Phi\rangle P_\Phi(\Psi;\mathbf{x},t)\right], \end{aligned} \tag{3.54}$$

where the conditional fluxes $\langle A_j|\Phi\rangle$, $\langle C_k|\Phi\rangle$, and $\langle C_h|\Phi\rangle$ are related to the instantaneous transport equations as follows:

$$\rho\frac{Du_i}{Dt} = \rho A_i, \qquad \text{where,} \quad \rho A_i(\mathbf{x},t) = -\frac{\partial p}{\partial x_i} - \frac{2}{3}\mu\frac{\partial u_k}{\partial x_k}\delta_{ij} + \mu\left(\frac{\partial u_i}{\partial x_j} + \frac{\partial u_j}{\partial x_i}\right) + F_i, \tag{3.55}$$

$$\rho\frac{DY_k}{Dt} = \rho C_k, \qquad \text{where,} \quad \rho C_k(\mathbf{x},t) = -\frac{\partial}{\partial x_j}\left(-\rho\Gamma_k\frac{\partial Y_k}{\partial x_j}\right) + S_k, \tag{3.56}$$

The assumptions here are those put forth in section (3.1), i.e., thermal and mass diffusivity coefficients are equal (unity Lewis number), and assuming equality of the molecular

diffusivity among species, i.e. $\Gamma_k = \Gamma$,

$$\rho\frac{Dh}{Dt} = \rho C_h, \qquad \text{where,} \quad \rho C_h(\mathbf{x},t) = -\frac{\partial}{\partial x_j}\left(-\rho\Gamma\frac{\partial h}{\partial x_j}\right) + S_h. \tag{3.57}$$

Eqs. (3.55-3.57) show that the instantaneous state of a fluid particle in any position is completely described by the three velocity components $(u_i, i = 1, 2, 3)$, by an ensemble of k mass fractions of chemical species $\mathbf{Y} = (Y_1, ..., Y_k)$, by the enthalpy and by the pressure. Thus, a complete description of a reactive turbulent flow can be done by the use of a joint PDF of the fields of velocity, mass fraction and enthalpy.

From Eq. (3.54), the PDF evolves in physical space, $\mathbf{x}$, due to the velocity field, u_j, in the velocity sample space due to the conditional acceleration term $\langle A_j|\Phi\rangle$, in the mass fractions sample space due to the conditional diffusion/reaction term $\langle C_k|\Phi\rangle$, and in the enthalpy sample space due to the conditional diffusion/source term $\langle C_h|\Phi\rangle$.
Under the previous set of simplifying hypothesis, that has been retained to describe [3] the joint PDF transport equations of species mass fractions and enthalpy becomes:

$$\begin{aligned}\frac{\partial\rho(\Psi)P_\Phi(\Psi;\mathbf{x},t)}{\partial t} + \frac{\partial\rho(\Psi)u_jP_\Phi(\Psi;\mathbf{x},t)}{\partial x_j} &= \\ -\frac{\partial}{\partial\mathbf{V}_j}\left[\rho(\Psi)\langle A_j|\Phi\rangle P_\Phi(\Psi;\mathbf{x},t)\right] &- \frac{\partial}{\partial\psi_\alpha}\left[\rho(\Psi)\langle\Theta_\alpha|\Phi\rangle P_\Phi(\Psi;\mathbf{x},t)\right],\end{aligned} \tag{3.58}$$

where ψ_α represents the sample space variable and $\langle\Theta_\alpha|\Phi\rangle$ stands for the mean conditional diffusion/source term,

$$\rho(\Psi)\langle\Theta_\alpha|\Phi\rangle = \left\langle\left[\frac{\partial}{\partial x_j}\left(\rho\Gamma\frac{\partial h}{\partial x_j}\right)\right]\middle|\Psi\right\rangle + S_\alpha(\psi). \tag{3.59}$$

The main advantage of the formulation presented above is that, once the distribution of the PDF of the velocity and scalar fields $\rho(\Psi)P_\Phi(\Psi;\mathbf{x},t)$ are known, the m-th central

[3] The following simplifying assumptions are recalled: (a) fluid is considered as Newtonian, (b) body forces, heat transport by radiation, Soret and Dufour effects are neglect, (c) the model is developed for low Mach number flows (d) unity Lewis number and equal molecular diffusion coefficient for all species .
In the case of reactive flows the following assumptions regarding the chemical kinetics mechanisms are also retained: (i) global, single step and irreversible chemical reactions, (ii) fuel is the deficient reactant, and (iii) null temperature exponent β of Arrhenius expression.

statistical moment, μ_m, of any function $Q(\Phi)$ of the random variables Φ can be evaluated by integration:

$$\mu_m = \langle Q'^m(\Phi)\rangle = \int_{-\infty}^{-\infty} [Q(\Psi) - \langle Q(\Phi)\rangle]^m P_\Phi(\Psi;\mathbf{x},t))d\Psi. \tag{3.60}$$

Using Eq. (3.60) the statistical moments, usually associated to the conventional URANS modeling of turbulent reactive flows, such as the mean velocity $\langle\mathbf{u}\rangle$, mean value of the scalar ϕ_α, $\langle\phi_\alpha\rangle$, the Reynolds stress tensor components $\langle u_i u_j\rangle$, scalar fluxes $\langle u_i\phi'_\alpha\rangle$, the second order covariance $\langle\phi'_\alpha\phi'_\beta\rangle$ and the mean chemical reaction term $\langle S_\alpha(\phi_\alpha)\rangle$ and high order statistical correlations, for instance the triple velocity correlations $\langle u_i u_j u_k\rangle$, can be readily evaluated.

A drawback of the formulation described above is that mean values of non-linear functions of velocity and/or scalar gradients appear in a unclosed form and, therefore, require closure. This is the case of the terms corresponding to effects of viscous dissipation and pressure fluctuations.
It is possible, under certain hypothesis that will be discussed further on, to obtain a simpler set of equations can be obtained from the joint velocity-scalar PDF, in which the conditional acceleration term is integrated over the velocity sample space. In this case a joint scalar PDF transport equation is obtained, retaining the advantage of maintaining the closed form of the chemical reaction term. Such a formulation is based on a joint scalar PDF and will be presented in the next section.

3.2.1.2 Joint scalar PDF

If the velocity field, and characteristic time and length scales of turbulence are known, it is possible to adopt a joint PDF description of the scalar field $P_\phi(\psi,\mathbf{x},t)$, instead of the joint velocity-scalar PDF $P_{\mathbf{u}\phi}(V,\psi,\mathbf{x},t)$. Since, in the present work, the variables related to the velocity field are obtained by an LES model, the joint scalar PDF transport equation can be used to evaluate the statistical moments of the scalar field and the chemical reaction term.

The transport equation for the joint scalar PDF can be obtained from the integration of the joint velocity-scalar PDF transport equation over the sample space of velocities:

$$P_\phi(\psi, \mathbf{x}, t) = \int_{-\infty}^{-\infty} P_{\mathbf{u}\phi}(V, \psi, \mathbf{x}, t) dV. \tag{3.61}$$

Integrating Eq. (3.61), and separating the contributions of the conditional diffusion and chemical reaction terms the PDF of the scalar field can be written as:

$$\begin{aligned} &\frac{\partial \rho(\psi) P_\phi(\psi; \mathbf{x}, t)}{\partial t} + \frac{\partial}{\partial x_j}\left[\rho(\psi)\langle u_j|\psi\rangle P_\phi(\psi; \mathbf{x}, t)\right] \;=\; \\ &-\frac{\partial}{\partial \psi_\alpha}\left[\rho(\psi)\left\langle\left[\frac{\partial}{\partial x_j}\left(\Gamma\frac{\partial \phi}{\partial x_j}\right)\right]\middle|\psi\right\rangle P_\phi(\psi; \mathbf{x}, t)\right] \;-\; \frac{\partial}{\partial \psi_\alpha}\left[S_\alpha(\psi) P_\phi(\psi; \mathbf{x}, t)\right]. \end{aligned} \tag{3.62}$$

In Eq. (3.62) the PDF of the scalar field evolve under the influence of the convective transport due to the conditional velocity $\langle u_j|\psi\rangle$, the transport in the sample space due to the conditional molecular mixing (first term in the right hand side of Eq. (3.62)), and due to the chemical reaction term $S_\alpha(\psi)$. According to Colucci et al. (1998b), the conditional velocity can be decomposed into a filtered contribution and a subgrid contribution:

$$\langle u_j|\psi\rangle P_\phi(\psi; \mathbf{x}, t) = \tilde{u}_j P_\phi(\psi; \mathbf{x}, t) + \left[\langle u_j|\psi\rangle - \tilde{u}_j\right] P_\phi(\psi; \mathbf{x}, t), \tag{3.63}$$

where the first term in the right hand side stands for the effect of advection of the PDF due the resolved velocity field provide by the LES, and the second term stands for the effects of the turbulent diffusion of the PDF in the subgrid scales. It is noteworthy that the latter must be modeled.

A widely used closure for the turbulent transport of the PDF, in the context of Large Eddy Simulation, is based on the diffusion gradient transport (COLUCCI et al., 1998b):

$$\left[\langle u_j|\psi\rangle - \tilde{u}_j\right] P_\phi(\psi; \mathbf{x}, t) = \Gamma_{SGS}\frac{\partial P_\phi(\psi; \mathbf{x}, t)}{\partial x_j}, \tag{3.64}$$

where Γ_{SGS} is the subgrid diffusion coefficient, evaluated by an LES model.

The conditional molecular mixing term can also be decomposed into two contributions

(COLUCCI et al., 1998b):

$$\frac{\partial}{\partial\psi_\alpha}\left[\rho(\psi)\left\langle\left[\frac{\partial}{\partial x_j}\left(\Gamma\frac{\partial\phi}{\partial x_j}\right)\right]\middle|\psi\right\rangle P_\phi(\psi;\mathbf{x},t)\right] = \frac{\partial}{\partial x_j}\left(\rho(\psi)\Gamma\frac{\partial P_\phi(\psi;\mathbf{x},t)}{\partial x_j}\right) - \frac{\partial^2}{\partial\psi_\alpha^2}\left[\left\langle\rho(\psi)\Gamma\frac{\partial\phi_\alpha}{\partial x_j}\frac{\partial\phi_\alpha}{\partial x_j}\middle|\psi\right\rangle P_\phi(\psi;\mathbf{x},t)\right], \tag{3.65}$$

The first term on the right hand side of Eq. (3.65) represents the effects of molecular diffusion on the PDF transport in physical space, whereas the second term is the micro-mixing term, which represents the effects of the scalar dissipation rate on the PDF transport in the scalar field sample space.

The micro-mixing term must be modeled, and the search for physically realistic models has been an important subject of researches in the field of turbulent combustion modeling for the past few years (MURA; GALZIN; BORGHI, 2003; MURA; BORGHI, 2003; SABEL'NIKOV; GOROKHOVSKI; N, 2006). This is due to the fact that the interaction between these terms and the chemical source term exerts a controlling role in the evolution of the turbulent combustion, therefore, the choice of micro-mixing is paramount to the success of the flow field predictions.

One of the earliest mixing models for particle PDF methods is the coalescence and dispersion (CD) model by Curl (1963), which was developed to describe mixing of colliding droplets with different concentrations in a two-liquid suspension. Therefore, this model can easily be integrated into a stochastic particle framework, as used for PDF simulations. Other early approaches are summarized by Dopazo and O'Brien (1974) and Janicka, Kolbe and Kollmann (1979). The basic idea behind this model is mixing pairs of particles in the sense that the mixing intensity is random for each particle pair. The mixing rate is adjusted through the number of pairs that mix per unit of time. The main disadvantage of these models is that the PDF of an inert scalar does not become Gaussian in the homogeneous turbulence limit. Furthermore, the particle trajectories in scalar space are not continuous over time and hence, these models are not local even in a weak sense (MEYER; JENNY, 2009).

The most widely used mixing model was proposed by Villermaux and Devillon (1972) and it is known as interaction by exchange with the mean (IEM) mixing model (also known as the linear mean-square estimation (LMSE) model (DOPAZO; O'BRIEN, 1974)). This model is based on the simple fact that molecular mixing should reduce scalar fluctuations and thus draw instantaneous scalar values towards their local mean. If the IEM model correctly predicts inert scalar variance decay in homogeneous turbulence, the model is not able to describe the evolution of the scalar PDF appropriately, i.e., the shape of the initial PDF is preserved and it does not tend to a Gaussian distribution. Using the IEM-LMSE closure yields,

$$\left\langle \Gamma_\alpha \frac{\partial \phi_\alpha}{\partial x_j}\frac{\partial \phi_\alpha}{\partial x_j}\middle| \psi \right\rangle P_\phi(\psi;\mathbf{x},t) = \Omega_m(\psi_\alpha - \langle\psi_\alpha\rangle)P_\phi(\psi;\mathbf{x},t), \tag{3.66}$$

where $\Omega_m = C_\omega(\Gamma + \Gamma_{sgs})/\Delta^2$ is the turbulent frequency determined by LES, C_ω is a mechanical-to-scalar time-scale ratio, which is assumed to be constant. The standard value, 2.0, is based on the local equilibrium assumption between production and dissipation of variance in isotropic turbulence (RAMAN, 2004).

Using the presented the strategies for the closure of the open terms of the transported PDF, the joint PDF of the scalar field can be written as:

$$\begin{aligned}\frac{\partial \rho(\Psi)P_\Phi(\Psi;\mathbf{x},t)}{\partial t} + \frac{\partial \rho(\Psi)u_j P_\Phi(\Psi;\mathbf{x},t)}{\partial x_j} &= \frac{\partial}{\partial x_j}\left[(\Gamma+\Gamma_{SGS})\frac{\partial P_\phi(\psi;\mathbf{x},t)}{\partial x_j}\right] \\ &+ \frac{\partial}{\partial \psi_\alpha}\left[\Omega_m(\psi_\alpha - \langle\phi_\alpha\rangle)P_\phi(\psi;\mathbf{x},t)\right] \\ &- \frac{\partial}{\partial \psi_\alpha}\left[S_\alpha(\psi)P_\phi(\psi;\mathbf{x},t)\right].\end{aligned} \tag{3.67}$$

The Eq. (3.67) evolves in physical space due to the effects of convection and diffusion, and in sample space of scalars due to the contributions of micro-mixing and chemical reaction. It is noteworthy that Eq. (3.67) may be integrated in the scalar sample space thus yielding the statistical moments of the scalar field. The resulting integrated equations are statistically equivalent to those obtained by a LES filtering procedure. However, it is important to

remember that within the PDF transport equation the chemical reaction term appears in a closed form, thus eliminating the difficulties associated to its modeling.

The equations presented in the previous sections are based on a eulerian frame of reference and describe the statistics of the filtered field at a given point $\mathbf{x}$ and time t. These equations exhibit a high-dimensionality, since the PDF transport equation contains a large number of independent variables, $V, \psi, \mathbf{x}$ and t. As a consequence, the numerical solution by the using standard methods like Finite-Volumes or Finite-Differences, is feasible only in the simplest cases. As previously indicated, one way of circumventing such limitation is to use Lagrangian approaches, which is the subject of the next section.

3.2.2 Lagrangian Monte Carlo approach

In the Lagrangian approach the joint scalar PDF the flow properties is represented by an ensemble of notional particles (FOX, 2003). It is possible to consider each stochastic notional particle as a realization of the turbulent reactive flow, which is a discrete representation of the eulerian PDF. Each of these particles transports its own ensemble of independent variables, i.e., position in the physical space and composition of the scalar field. Each particle is also subjected to stochastic differential equations (SDE). Given a sample of particles, the results obtained from the statistical moments are by construction of the SDEs equivalent to those that would be obtained with the solution of the eulerian PDF. A general framework for the construction of SDEs that are equivalent to the PDF transport equation is given in Gardiner (2009).

Using such a framework, the differential stochastic equations that govern the trajectory of the particles in the physical space $\mathbf{x}$, and in the sample space of the scalar field, Φ, can be written as:

$$d\mathbf{x} = [\tilde{u}(\mathbf{x}, t) + \langle \mathbf{u}' | \Phi, \mathbf{x} \rangle] dt, \tag{3.68}$$

$$d\Phi = \langle \Theta | \Phi, \mathbf{x} \rangle dt, \tag{3.69}$$

where $\tilde{u}(\mathbf{x},t)$ is the filtered velocity field, evaluated by a LES model, $\langle \mathbf{u}'|\Phi,\mathbf{x}\rangle$ is the conditional velocity fluctuation, that appears in a open form and, therefore, needs to be modeled. $\langle \Theta|\Phi,\mathbf{x}\rangle$ is the conditional mean diffusion flux and chemical reaction, given by Eq. (3.59). The equivalent lagrangian PDF transport equation of the scalar field, $P^*_\phi(\psi,\mathbf{x})$, is given by:

$$\frac{\partial \rho(\psi) P^*_\phi(\psi,\mathbf{x})}{\partial t} + \frac{\partial \rho(\psi)(\tilde{u}_j + \langle u'_j|\psi\rangle) P^*_\phi(\psi,\mathbf{x})}{\partial x_j} = -\frac{\partial}{\partial \psi_\alpha}\left[\rho(\psi)\langle \Theta_\alpha|\psi\rangle P^*_\phi(\psi,\mathbf{x})\right]. \quad (3.70)$$

The conditional term of velocity fluctuation,$\langle \mathbf{u}'|\Phi,\mathbf{x}\rangle$, is closed analogously as the eulerian version of the eulerian PDF transport equation, i.e., it is modeled based on the gradient diffusion assumption of the PDF in the physical space,

$$\begin{aligned}\langle u'_j|\psi\rangle P^*_\phi(\psi,\mathbf{x}) &= -\Gamma_{SGS}(\mathbf{x},t)\frac{\partial P^*_\phi(\psi,\mathbf{x})}{\partial x_j} \\ &= \left(\frac{\partial \Gamma_{SGS}}{\partial x_j}\right) P^*_\phi(\psi,\mathbf{x}) - \frac{1}{2}\left[\frac{\partial}{\partial x_j}\left(2\Gamma_{SGS}\right) P^*_\phi(\psi,\mathbf{x})\right]. \end{aligned} \quad (3.71)$$

Substituting Eq. (3.71) in Eq. (3.68) it is possible to obtain the final form of the stochastic differential equation that describes the trajectory of the particles in physical space $\mathbf{x}$:

$$d\mathbf{x} = \left[\tilde{\mathbf{u}}(\mathbf{x},t) + \frac{\partial(\Gamma_{SGS})}{\partial x_i}\right] dt + (2\Gamma_{SGS})^{\frac{1}{2}} d\mathbf{W}(t). \quad (3.72)$$

The evolution of each notional particle occurs according to statistically independents increments $d\mathbf{W}(t)$. It is worth noting that the subgrid diffusion coefficient is evaluated by a LES model. The shortcomings of such an approach are discussed by Haworth (2010b) The conditional diffusion/chemical reacting flux term, $\langle \Theta_\alpha|\psi,\mathbf{x}\rangle$, contains contributions of the molecular diffusion and chemical reaction rate. The molecular diffusion term in the lagrangian PDF transport equation can also be modeled as the eulerian PDF, e.g., by using the IEM micro-mixing model.

The final form of the stochastic differential equation that describes the trajectory of particles in the sample space of scalar field, Φ, is given by:

$$\frac{d\phi}{dt} = -\left[\Omega_m\left(\phi - \langle\phi\rangle\right)\right] + S(\phi). \quad (3.73)$$

3.2.3 Coupling of the hybrid model solvers

It is important to note that due the simplifying hypothesis retained in the present work concerning the transport equations and chemical kinetics, the effects of the chemical reaction on the flow are exclusively noted by the density variations generated by the thermal expansion. In the Eulerian field it is possible to solve a transport equation for the filtered progress variable $\tilde{c}$,

$$\frac{\partial \overline{\rho}\tilde{c}}{\partial t} + \frac{\partial \overline{\rho}\tilde{u}_j\tilde{c}}{\partial x_j} = \frac{\partial}{\partial x_j}\left(\overline{\rho}(\Gamma + \Gamma_{SGS})\frac{\partial \tilde{c}}{\partial x_j}\right) + \overline{S}(c). \tag{3.74}$$

where Γ_{SGS} is evaluated from Eulerian quantities through Eq. (3.32) and the filtered chemical reaction rate term $\overline{S}(c)$ is evaluated in the Lagrangian framework.

As commented in the subsection (3.2.1.1), another advantage of adopting a Lagrangian approach is that the central statistical moments of the progress variable, c, can be readily recovered by the Monte Carlo simulation retained for the solution of the system generated by Eqs. (3.72) and (3.73).

It will be seen in section (4) that the filtered progress variable, $\tilde{c}$, can be evaluated from the first central moment of c. In the case of the second central moment, i.e., the variance of the filtered progress variable its modeled transport equation is given by,

$$\frac{\partial \overline{\rho}\,\widetilde{c''^2}}{\partial t} + \frac{\partial \overline{\rho}\,\tilde{u}_i\,\widetilde{c''^2}}{\partial x_i} = \underbrace{\frac{\partial}{\partial x_i}\left[\overline{\rho}(\Gamma + \Gamma_{SGS})\frac{\partial\,\widetilde{c''^2}}{\partial x_i}\right]}_{\text{turbulent transport}} + \underbrace{2\overline{\rho}\,(\Gamma + \Gamma_{SGS})\,\frac{\partial \tilde{c}}{\partial x_i}\frac{\partial \tilde{c}}{\partial x_i}}_{\text{production}} - \underbrace{2\,C_\Omega \Omega_m \widetilde{c''^2}}_{\text{dissipation}} + \underbrace{2\overline{(c-\tilde{c})}\;\overline{S}(c)}_{\text{reaction}}. \tag{3.75}$$

The turbulent transport, production, dissipation and reaction terms in the equation for the variance of the progress variable, c Eq. (3.75) are modeled in the same way as in the RANS framework. It noteworthy also that the molecular diffusion terms becomes negligible, once the flows of interest are classified as having characteristic high Reynolds number, and as will be seen in the results chapter, the mesh adopted for the simulations performed have a sufficiently large local Reynolds number, e.g., the mesh size adopted has at least ten times

the size of the Kolmogorov length scale.

The importance of Eq. (3.75) is based on the fact that, the Eulerian and Lagrangian approaches must be equivalent. This is a matter of validation of the Lagrangian approach and will be further discussed.

CHAPTER IV

NUMERICAL MODELING

In this section, the numerical procedures retained to obtain the solution of the transport equations presented in chapter 3 are described.

The solution of an equation originally proposed in the continuum, once expressed in a discrete domain, invariably leads to a loss of information. However, it is possible to minimize such losses, by choosing appropriately the numerical methods retained to solve the equations. Important factors that directly impact the performance of a numerical method that seeks to solve the Navier-Stokes equations are: (i) the choice of the variables arrangement in the computational grid, (ii) the type and order of accuracy of the numerical scheme retained to perform the discretization in space of both viscous and advective terms, and (iii) the type and order of accuracy of the method chosen to perform the temporal integration. These factors are important in the numerical solution of the stochastic differential equations as well. Moreover, further care must be accounted for regarding the evaluation of the chemical reaction term.

In general lines, the numerical method chosen for solving the variable density momentum, scalars and Poisson equations is based on a three-dimensional, conservative, staggered, finite-volume discretization. The central difference scheme (CDS) is applied to express the diffusive contributions of the transport equations. For the advective contributions both

CDS and Deferred Correction (FERZIGER; PERIC, 1996) approaches were implemented and are available in the numerical code developed. A fully implicit approach is adopted, and the resulting linear systems are solved using the MSIP - Modified Strongly Implicit Procedure (SCHNEIDER; ZEDAN, 1981) for velocity components, the Eulerian equation for the chemical reaction progress variable and its variance, Eqs. (3.74) and (3.75), respectively. Since the numerical code developed adopts a pressure-based approach, an algorithm for pressure-velocity coupling is needed. Here, a projection method based on the fractional steps technique is retained, resulting in a variable-coefficient Poisson equation which is solved with the Bi-Conjugate Gradient Stabilized, BICGSTAB (VORST, 1981) solver.

Concerning the organization of the present chapter, first, the numerical schemes retained to solve the transport equations in the Eulerian domain are described, followed by the pressure velocity coupling, and the development of a physically consistent constraint, which is used to substitute the divergence of the velocity field in the right hand side of the variable-coefficient Poisson equation. Further on, the Monte Carlo method, which is used to obtain the solution of Eqs. (3.72) and (3.73) is described in details. Finally, in the case of transport of a passive scalar, the equivalence between the Eulerian and Lagrangian approaches is discussed and verified.

4.1 The finite volume method

If the discretization relies on a finite-volume (FV) approach, it is necessary to evaluate vectorial fields coupled to scalar fields, as it is the case when the Navier-Stokes equations are considered. The issue associated to the positioning of the primary variables in the computational grid must be carefully accounted. There are several options and they may be classified into two principal groups: staggered, in which the vectorial variables are stored in the control volume (CV) faces, while the scalars are stored in the center of the CV, or co-located grids arrangements, in which the vectorial and scalar quantities are stored in the same location, see Fig. (4.1). In the former case, the vectorial and scalar variables are positioned at different locations. In the latter, all physical variables, and specially the pressure

and the velocity components are evaluated at the same location. This is the simplest choice for implementation, in particular when distributed computing strategies are to be applied. However, in incompressible (and low Mach number) flows, if the velocity and pressure are positioned in the same location, decoupling instabilities, often referred to as checkerboard patterns can arise (ANDERSON, 1995; FERZIGER; PERIC, 1996; KARKI; PATANKAR, 1989). The discretization procedure retained for the momentum equation is basically iden-

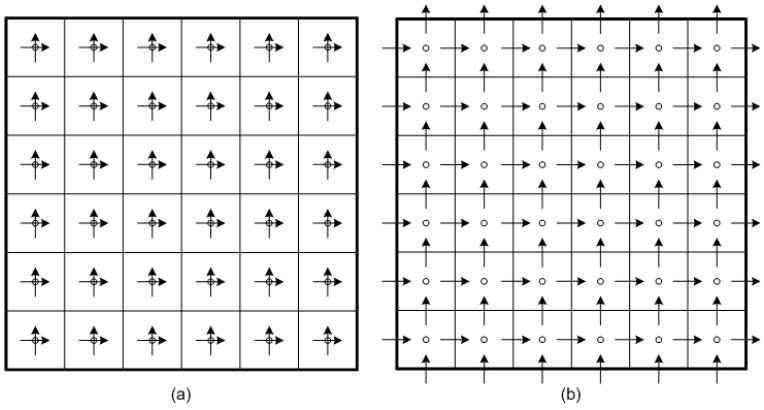

Figure 4.1: Schematic representation of variable arrangement in a grid, (a) collocated, (b) staggered. The arrows stand for the vectorial variables, and the circles represent the scalars.

tical for both the staggered and the co-located arrangements. Nevertheless, with the latter, the velocity components, positioned at the center of the control volumes must be interpolated to their faces. The most common procedure is to use the Rhie-Chow interpolation (RHIE; CHOW, 1983). Shen, Michelsen and Sorensen (2001) underline that the Rhie-Chow interpolation produces excellent results when steady-state solutions are sought for, and large time steps used, but pressure field oscillations may arise for small time step values and during transient simulations. Versteeg and Malalasekera (2007), and Ferziger and Peric (1996), argue that there is no intrinsic physical requirement that all variables share the same location. For cartesian grids, the concept of staggered grid was introduced in Harlow and Welch (1965). If second order of accuracy schemes are retained for spatial discretization, such an arrangement does not require additional interpolations, which otherwise would be necessary for a co-located grid. Finally, the major advantages of the staggered variable arrangement is that the pressure terms are naturally discretized by second order accuracy central differences scheme, without any resort to interpolation rules, and the evaluation of mass fluxes at the

faces of control volumes is straightforward, which leads to a strong coupling between pressure and velocity, thus avoiding the birth of spurious instabilities in the calculated pressure field.

In transient flows the transport equations must be integrated in time as well, which requires the choice of a suitable time marching procedure and brings an important issue associated to the simulation of transient flows: the stability of the numerical scheme. This is the subject of the next subsection.

4.1.1 Temporal approximations and numerical stability

In Large Eddy Simulations (LES) of turbulent reactive flows, the size of the time step necessary to capture the smallest resolved scales can be very restrictive. Therefore, the temporal integration method must be chosen carefully. Explicit schemes exhibit numerical stability issues when using CFL (Courant Friedrich Lewy) numbers values larger than unity. In order to restrict the size of the time step necessary to maintain numerical stability, the following stability criteria can be defined:

$$\Delta t = C \left(\frac{1}{t_{adv}} + \frac{1}{t_{dif}} + \frac{1}{t_{ther}} \right)^{-1}, \tag{4.1}$$

where C is a numerical factor ranging between 0 and 1. $t_{adv}, t_{dif}, t_{ther}$ stand for, respectively, the advective, the diffusive and the thermal maximum allowable size of time step. For a given flow,

$$t_{adv} = \left(\frac{\Delta x}{|u|_{max}} + \frac{\Delta y}{|v|_{max}} + \frac{\Delta z}{|w|_{max}} \right), \tag{4.2}$$

$$t_{dif} = \left(\frac{\Delta x^2}{\nu} + \frac{\Delta y^2}{\nu} + \frac{\Delta z^2}{\nu} \right), \tag{4.3}$$

$$t_{ther} = \left(\frac{\Delta x^2}{\alpha} + \frac{\Delta y^2}{\alpha} + \frac{\Delta z^2}{\alpha} \right), \tag{4.4}$$

where Δx, Δy and Δz denote, respectively, the mesh discretization length in the x, y and z directions, $\alpha = \lambda/\rho C_p$ is the thermal diffusivity and $\nu = \mu/\rho$ is the kinematic viscosity. $|u|_{max}$, $|v|_{max}$ and $|w|_{max}$ are the maximum values of the norm of velocity u, v and w.

If an explicit treatment for both advective and diffusive terms is retained, the above set of equations gives a size of time step of order of $\mathcal{O}(\Delta x^2)$, essentially due to the diffusive term (FERZIGER; PERIC, 1996).
Such a numerical limitation does not apply to implicit or semi-implicit discretizations. The main advantage of implicit and semi-implicit methods, despite the more complicated implementation, is its higher stability. With the implicit treatment of the diffusive terms, the temporal restriction of order $\mathcal{O}(\Delta x^2)$ is removed, becoming of order $\mathcal{O}(\Delta x)$ (VILLAR, 2007).

Ferziger and Peric (1996) provide an introduction to several types of classical temporal integration methods. Examples of semi-implicit approaches can be found in Ceniceros and Roma (2007) and Villar (2007). A detailed evaluation of various semi-implicit schemes has been reported in Ascher, Ruuth and Wetton (1995). The temporal integration schemes retained in the present work are fully implicit.
Considerations on the evolution of the time step size has yet to be made. Note that the choice of constant or variable time step sizes may have a strong influence on the stability of a numerical simulation.

4.1.2 Variable time step size approach

The solution of partial differential equations with different characteristic time scales, e.g., flows that rapidly vary in some regions of the domain, while slowly change in other regions, variable time step size schemes are often essential to obtain computationally efficient and accurate results. Standard temporal integration methods, such as the Backward Difference Formula or Crank-Nicolson methods, are designed for constant time step sizes. When dealing with problems where it is desirable for time step size to vary, modifications to recover a more general form of the methods must be accounted for.

Wang (2005) presents a general formulation for variable time step size implicit-explicit methods (VSIMEX) for time-dependent partial differential equations (PDE)[1]. In his work a

[1]In IMEX approaches are semi-implicit approaches in which only the diffusive part of the PDE is treated implicitly. The advective contribution still remain processed explicitly

semi-discretized arrangement is proposed in such a way that any differential equation could be temporally integrated using second order semi-implicit schemes:

$$\frac{1}{\Delta t_{n+1}} \sum_{j=0}^{2} \alpha_{j,n+1} U^{n+j} = \sum_{j=0}^{1} \beta_{j,n+1} \zeta(U^{n+j}) + \sum_{j=0}^{2} \theta_{j,n+1} \epsilon(U^{n+j}), \tag{4.5}$$

where $\zeta(U^{n+j})$ and $\epsilon(U^{n+j})$ stand for, respectively, diffusive and advective contributions to the differential equation and $n+1$ represents the current time level. The values of $\alpha_{j,n+1}$, $\beta_{j,n+1}$ and $\theta_{j,n+1}$ are:

$$\begin{aligned}
\alpha_{0,n+1} &= \frac{(2\gamma-1)\omega_{n+1}^2}{1+\omega_{n+1}}, \\
\alpha_{1,n+1} &= (1-2\gamma)\omega_{n+1} - 1, \\
\alpha_{2,n+1} &= \frac{1+2\gamma\omega_{n+1}}{1+\omega_{n+1}}, \\
\beta_{0,n+1} &= -\gamma\omega_{n+1}, \\
\beta_{1,n+1} &= 1+\gamma\omega_{n+1}, \\
\theta_{0,n+1} &= \frac{c}{2}, \\
\theta_{1,n+1} &= 1-\gamma-\left(1+\frac{1}{\omega_{n+1}}\right)\frac{c}{2}, \\
\theta_{2,n+1} &= \gamma+\frac{c}{2\omega_{n+1}},
\end{aligned} \tag{4.6}$$

where $\omega_{n+1} = \Delta t_{n+1}/\Delta t_n$ is the ratio between two consecutive time steps. A family of numerical schemes involving the two parameters γ and c can be derived. For instance, if the size of the time step is kept constant, Eq. (4.6) takes the form (ASCHER; RUUTH; WETTON, 1995):

$$\begin{aligned}
\frac{1}{\Delta t}\left[\left(\gamma+\frac{1}{2}\right)u^{n+2} - 2\gamma u^{n+1} + \left(\gamma-\frac{1}{2}\right)u^{n}\right] &= (\gamma+1)\zeta(u^n) - \gamma\zeta(u^{n-1}) \quad + \\
&\left[\left(\gamma+\frac{c}{2}\right)\epsilon\left(u^{n+2}\right) + (1-\gamma-c)\,\epsilon\left(u^{n+1}\right) + \frac{c}{2}\epsilon\left(u^{n}\right)\right].
\end{aligned} \tag{4.7}$$

Depending on the values retained for constants γ and c in Eq. (4.7), different time integration schemes can be obtained (ASCHER; RUUTH; WETTON, 1995; WANG, 2005):

- Crank-Nicolson Adams-Bashfort (CNAB): $(\gamma, c) = (0.5, 0.0)$;
- Modified Crank-Nicolson Adams-Bashfort (MCNAB): $(\gamma, c) = (0.5, 0.125)$;

- Crank-Nicolson Leap Frog (CNLF): $(\gamma, c) = (0.0, 1.0)$;
- Semi-Backward Difference Formula (SBDF): $(\gamma, c) = (1.0, 0.0)$.

In the present work, instead of a semi-implicit, a fully implicit scheme is adopted. However, the organization allowed by Eq. (4.5) remains very attractive, since it includes the possibility of (i) describing several methods of temporal discretization within the same formulation and, hence, (ii) retaining the more adequate for a given problem.
Using the same values for the constants γ and c, Eq. (4.5) can be adapted within a fully implicit framework as follows:

$$\frac{1}{\Delta t_{n+1}} \sum_{j=0}^{2} \alpha_{j,n+1} U^{n+j} = \sum_{j=0}^{2} \theta_{j,n+1} (\zeta(U^{n+j}) + \epsilon(U^{n+j})). \tag{4.8}$$

As previously commented, in the present work a fully implicity approach is retained for the transport equations, i.e., all the transport equations solved on the Eulerian domain are discretized according to the temporal integration described here. For instance, applying Eq. (4.8) to Eq. (3.14) and re-arranging the different terms, the momentum equation, once discretized in time, takes the following form:

$$\begin{aligned} \frac{\alpha_{2,n+1}(\rho u_i)^{n+1} + \alpha_{1,n+1}(\rho u_i)^{n} + \alpha_{0,n+1}(\rho u_i)^{n-1}}{\Delta t} = & -\frac{\partial p^{n+1}}{\partial x_i} \\ & + (\theta_{2,n+1}) m_2 + (\theta_{1,n+1}) m_1 + (\theta_{0,n+1}) m_0, \end{aligned} \tag{4.9}$$

where $\theta_{0,n+1}$, $\theta_{1,n+1}$ and $\theta_{2,n+1}$ are taken from Eq. (4.6), and,

$$m_{k+1} = \left(\frac{\partial \tau_{ij}^{n+k}}{\partial x_j} - \frac{\partial \rho^{n+k} u_i^{n+k} u_j^{n+k}}{\partial x_j} \right), k = -1, 0, 1 \tag{4.10}$$

It is worth recalling that Eq. (3.14) and consequently Eq. (4.9), are filtered transport equations, ready to be used in a Large Eddy Simulation. The variables are shown without the filtering notation ($\bar{}$) or ($\tilde{}$) only for the sake of conciseness, and these concise representation will be dropped out hereafter, unless explicitly mentioned in the text.

As mentioned above, if retained a constant size of time step, the choice of the constant values γ and c, allows to recover the Crank-Nicolson method $(\gamma, c) = (0.5, 0.0)$, the Modified

Crank-Nicolson $(\gamma, c) = (0.5, 0.125)$, the Leap Frog method $(\gamma, c) = (0.0, 1.0)$ and the Backward Difference Formula - BDF, $(\gamma, c) = (1.0, 0.0)$. In the present work, the above temporal integration methods can be also recovered, but with the advantage of allowing the adoption of a variable size of time step, calculated by Eq. (4.1). Finally, it is worth to point out that, through Eq. (4.9), the fully implicity framework retained here requires the numerical resolution of a large algebraic system for each discretized equation.

4.1.3 Spatial discretization of the transport equations

As commented in the introduction of the present chapter, the central difference scheme (CDS) is applied to express the diffusive terms of the transport equations whereas, for the advective contributions, both CDS and Deferred Correction (FERZIGER; PERIC, 1996) approaches are available. To illustrate the discretization of a derivative using the CDS approach, consider the control volume of lengths $\Delta x \times \Delta y \times \Delta z$, shown in Fig. (4.2). In such figure, the capital letters stand for the center of the control volumes, whereas the lower case letters represent the faces of the control volume. The letters e, w, n, s, t and b and its capital forms, are respectively the faces in the directions east, west, north, south, top and bottom.

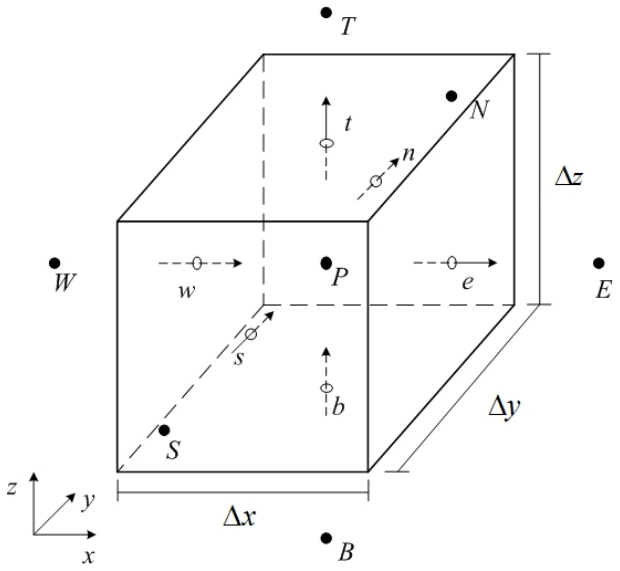

Figure 4.2: Elementary control volume retained for the discretization of transport equations.

The advective term of Eq. (4.9) in time $k+1$, x direction and for $i = 1$ and $j = 1$,

can be approximated, using the finite volume method, as:

$$\frac{\partial \rho u u^{k+1}}{\partial x} = [(\rho u u)_e - (\rho u u)_w]\Delta x \Delta y, \tag{4.11}$$

The structure adopted for the computational grid can be uniform or non-uniform, so it is necessary to perform interpolations to discretize any spatial derivatives. In the case of non-uniform grids, it is important that such interpolations are obtained using distance-weighted rules (FERZIGER; PERIC, 1996). To determine the value of each scalar property, θ, on a face e, the following expression is used: $\theta_e = \theta_E \Lambda_e + \theta_P(1 - \Lambda_e)$, where:

$$\Lambda_e = \frac{(\delta x)_e^-}{(\delta x)_e}. \tag{4.12}$$

As can be seen in Fig. (4.3), the indexes P, E and e, denotes, respectively, the center of the current control volume, the center of the left control volume, and the position of the face of the control volume centered in P, that lies between P and E.

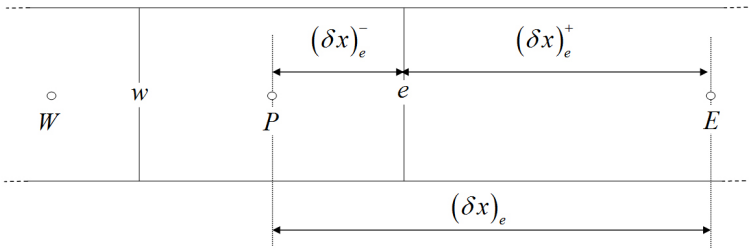

Figure 4.3: Non-uniform finite-volume grid and distances associated to the face e.

The discretization of the advective term of the transport equations is a crucial point for accuracy and stability of numerical schemes. Ferziger and Peric (1996) argue that some iterative solvers can fail to converge when applied to the algebraic equation systems where the CDS approach is used in the approximations, mainly because the matrices may not be diagonally dominant. A technique to circumvent this difficulty is to use the deferred correction approach. In this technique the advective term evaluated in a face e is expressed

as:

$$(\rho u u)_e^{k+1} = (\rho u u)_{e,UDS}^{k+1} + \left[(\rho u u)_{e,CDS} - (\rho u u)_{e,UDS}\right]^k \tag{4.13}$$

where the subscript UDS stands for a discretization of the advective term using the upwind scheme ((FERZIGER; PERIC, 1996; VERSTEEG; MALALASEKERA, 2007)). The term inside the brackets is evaluated using values calculated in the previous iteration. At convergence, the UDS contributions cancel and a CDS solution is recovered. It is worth recalling that in Eq. (4.13) only the density must be interpolated to the face e, once a staggered grid is adopted and therefore, the velocity component u is already stored in the face e.
A deeper discussion about the accuracy and order of convergence of CDS and deferred correction approaches will be made in the chapter 6, devoted to the verification of the developed numerical code.

Finally, boundary conditions must be provided in order to solve the set of transport equations. In the developed numerical code, it is possible to choose between periodicity, Dirichlet, Neumann, or advective boundary conditions (ORLANSKI, 1976) for each boundary of the computational domain. Particular care is taken when LES are performed on open domains. In this case, not only the mean velocities, but also experimental turbulence stress tensors profiles, if available, can be used for more realistic representations of a flow of interest. In the present work, different methods for generating turbulent inflow data are implemented and assessed in both non-reactive and reactive flows. Such methods, as well as the assessment are shown in Chapter 7.

Within the pressure based approach adopted in the present work, once discretized the transport equations, the pressure velocity coupling must be enforced. This is the subject of the next section.

4.2 Pressure velocity coupling

Since a fully implicit fractional step method is used in the present work, a Poisson type equation must be solved to apply a pressure correction to both velocity and pressure fields. To provide such an equation, the Eq. (4.9) is re-written, with the pressure derivative evaluated at time level n as:

$$\frac{\alpha_{2,n+1}(\rho u_i^*)^{n+1} + \alpha_{1,n+1}(\rho u_i)^n + \alpha_{0,n+1}(\rho u_i)^{n-1}}{\Delta t} = -\frac{\partial p^n}{\partial x_i} + (\theta_{2,n+1})m_2 + (\theta_{1,n+1})m_1 + (\theta_{0,n+1})m_0, \tag{4.14}$$

where u_i^{*n+1} stands for the estimated velocity field. Subtracting Eq. (4.14) from Eq. (4.9). Is is noteworthy that the discretization of the temporal derivative of the last equation can be achieved by any of the methods shown in subsection (4.1.3). Defining $Q = p^{n+1} - p^n$, and rearranging the different terms, it is possible to obtain:

$$\frac{\rho^{n+1}\alpha_{2,n+1}}{\Delta t}\left(u_i^{*n+1} - u_i^{n+1}\right) = \frac{\partial Q}{\partial x_i}, \tag{4.15}$$

proceeding classically by taking the divergence of Eq. (4.15):

$$\frac{\alpha_{2,n+1}}{\Delta t}\left(\frac{\partial u_i^{*n+1}}{\partial x_i} - \frac{\partial u_i^{n+1}}{\partial x_i}\right) = \frac{\partial}{\partial x_i}\left(\frac{1}{\rho^{n+1}}\frac{\partial Q}{\partial x_i}\right). \tag{4.16}$$

In situations where the density can be considered constant, at least along a streamline, the second derivative at the LHS of Eq. (4.16) is zero due the incompressibility condition. However, when density variations arise from temperature (and/or composition) variations as encountered, for instance, in reactive flows, the corresponding term can no longer be neglected. Thus, an approximation must be made regarding its closure.

4.2.1 A physically consistent constraint over the velocity field

In the low Mach number reactive flows under consideration, the density is solely determined by the temperature and thermodynamic pressure fields. The energy equation plays the role of an additional constraint on the velocity field, which is enforced by the dynamic

pressure. This constraint acts onto the flow field divergence, and it is related to the total derivative of the density field, which involves - through the equation of state Eq. (3.5) - the total derivatives of both pressure and temperature. Re-writing the energy equation Eq. (3.3) in the temperature form it is possible to obtain,

$$\frac{\partial \rho T}{\partial t} + \frac{\partial \rho u_j T}{\partial x_j} = \mathcal{A}, \tag{4.17}$$

where,

$$\mathcal{A} = \frac{1}{C_p}\left(\frac{\partial J_{hj}}{\partial x_j} + S_h\right). \tag{4.18}$$

Applying the chain rule to the left hand side of Eq. (3.19), it yields,

$$\rho\frac{\partial T}{\partial t} + T\frac{\partial \rho}{\partial t} + \rho u_j\frac{\partial T}{\partial x_j} + \rho T\frac{\partial u_j}{\partial x_j} + Tu_j\frac{\partial \rho}{\partial x_j} = \mathcal{A}. \tag{4.19}$$

Rewriting Eq. (3.5) in the form $P_o^*(t) = \rho T$, and substituting it in the derivatives of T at the left hand side of Eq. (4.19),

$$\rho\frac{\partial}{\partial t}\left(\frac{P_o^*(t)}{\rho}\right) + T\frac{\partial \rho}{\partial t} + \rho u_j\frac{\partial}{\partial x_j}\left(\frac{P_o^*(t)}{\rho}\right) + \rho T\frac{\partial u_j}{\partial x_j} + Tu_j\frac{\partial \rho}{\partial x_j} = \mathcal{A}. \tag{4.20}$$

Re-arranging the terms of Eq. (4.20),

$$\rho\left[\frac{\partial}{\partial t}\left(\frac{P_o^*(t)}{\rho}\right) + u_j\frac{\partial}{\partial x_j}\left(\frac{P_o^*(t)}{\rho}\right)\right] + T\frac{\partial \rho}{\partial t} + \rho T\frac{\partial u_j}{\partial x_j} + Tu_j\frac{\partial \rho}{\partial x_j} = \mathcal{A}. \tag{4.21}$$

Applying the chain rule to in the derivatives inside the brackets of Eq. (4.21), and reorganizing the different terms yields,

$$\begin{aligned}\rho\left(-\frac{P_o^*(t)}{\rho^2}\frac{\partial \rho}{\partial t} + \frac{1}{\rho}\frac{\partial P_o^*(t)}{\partial t} - \frac{u_j P_o^*(t)}{\rho^2}\frac{\partial \rho}{\partial x_j} + \frac{u_j}{\rho}\frac{\partial P_o^*(t)}{\partial x_j}\right) & \\ +T\frac{\partial \rho}{\partial t} + \rho T\frac{\partial u_j}{\partial x_j} + Tu_j\frac{\partial \rho}{\partial x_j} &= \mathcal{A}.\end{aligned} \tag{4.22}$$

Recalling the assumption made in the present work regarding the thermodynamic pressure, which does not vary in space nor in time,

$$-\frac{P_o^*}{\rho}\frac{\partial \rho}{\partial t} - \frac{u_j P_o^*}{\rho}\frac{\partial \rho}{\partial x_j} + T\frac{\partial \rho}{\partial t} + \rho T\frac{\partial u_j}{\partial x_j} + Tu_j\frac{\partial \rho}{\partial x_j} = \mathcal{A}. \tag{4.23}$$

Dividing Eq. (4.23) by P_o^* leads to,

$$-\frac{1}{\rho}\frac{\partial \rho}{\partial t} - \frac{u_j}{\rho}\frac{\partial \rho}{\partial x_j} + \frac{T}{P_o^*}\frac{\partial \rho}{\partial t} + \frac{\rho T}{P_o^*}\frac{\partial u_j}{\partial x_j} + \frac{Tu_j}{P_o^*}\frac{\partial \rho}{\partial x_j} = \frac{\mathcal{A}}{P_o^*}. \tag{4.24}$$

Through the use of the equation of state Eq. (3.5), it is possible to obtain an equation that connects the divergence of velocity with the energy equation,

$$\frac{\partial u_j}{\partial x_j} = \frac{\mathcal{A}}{P_o^*}. \tag{4.25}$$

Under the assumptions made regarding the chemical kinetics and flows of interest of the present work, detailed in Chapter 3, The term $\mathcal{A}$ can be simplified to,

$$\mathcal{A} = \left[\frac{\partial}{\partial x_j}\left(\rho\Gamma\frac{\partial T}{\partial x_j}\right)\right]. \tag{4.26}$$

Adopting a formulation based on the consideration of a single progress variable of chemical reaction, the Eq. (4.26) can be written,

$$\mathcal{A} = \left\{\frac{\partial}{\partial x_j}\left[\rho\Gamma\frac{\partial}{\partial x_j}(c(T_b - T_u) + T_u)\right]\right\} = (T_b - T_u)\left[\frac{\partial}{\partial x_j}\left(\rho\Gamma\frac{\partial c}{\partial x_j}\right)\right]. \tag{4.27}$$

Hence, the final form of the constraint is written as,

$$\frac{\partial u_j}{\partial x_j} = \frac{(T_b - T_u)}{P_o^*}\left[\frac{\partial}{\partial x_j}\left(\rho\Gamma\frac{\partial c}{\partial x_j}\right)\right]. \tag{4.28}$$

The equation for pressure correction, for low Mach number flows simulations may, therefore, be written as:

$$\frac{\partial}{\partial x_i}\left(\frac{1}{\rho^{n+1}}\frac{\partial Q}{\partial x_i}\right) = \frac{\alpha_{2,n+1}}{\Delta t}\left\{\frac{\partial u_i^{*n+1}}{\partial x_i} - \frac{(T_b - T_u)}{P_o^*}\left[\frac{\partial}{\partial x_j}\left(\rho\Gamma\frac{\partial c}{\partial x_j}\right)\right]\right\}. \tag{4.29}$$

Once the pressure correction is evaluated, the velocity field can be updated:

$$u_i^{n+1} = u_i^{*n+1} - \left(\frac{\Delta t}{\alpha_2 \rho^{n+1}}\right) \frac{\partial Q}{\partial x_i}. \tag{4.30}$$

The constraint given by Eq. (4.28) in variable density flows has been previously discussed, among others, by Bell (2005b) and Nicoud (2000). Moreover, an inner iterative process can be used to enhance both stability and convergence of the solution process. Further considerations about such a procedure and the associated effects on the numerical convergence are deferred to the chapter devoted to the code verification using low Mach number manufactured solutions. Finally, it is worth recalling that, for constant density, non-reactive flows simulations, the constraint presented above is not necessary.

4.3 Numerical modeling of the system of stochastic differential equations

Methods based on Monte Carlo solutions of the transport equation for the joint probability density function (PDF) are among the most general and promising approaches to describe turbulent reactive flows. For the treatment of convection and diffusion two approaches to describe turbulent transport are well established, i.e., the Eulerian and the Lagrangian points of view. According to Möbus (2001), roughly speaking, the former is computationally less expensive, but also less accurate, than the latter one.

In the Eulerian approach each notional particle represents a fraction of the PDF of its host elementary volume. Particles do not have specific locations within this volume. The number of particles remains constant in time, and particles have identical statistical significance. Due to the transport processes, fractions of the PDF are replaced by the PDF's of neighboring elementary volumes. Interpreted in the sense of Monte Carlo schemes, this implies that a number of particles of a given volume is replaced by particles from surrounding volumes that are selected at random. In the Lagrangian point of view, stochastic particles move through physical space independently of each other. They are assigned spatial coordinates and transport mass. Due to the stochastic nature of motion, the number of particles present in a given elementary volume, or cell, changes in time. As can be derived

for constant density flows, the average number of particles per unit volume is proportional to the cell volume if particle masses are equal. In order to prevent particle accumulations in large computational cells and to keep small computational cells from running empty, particles are ascribed a relative weight, which may vary throughout the domain and, as a consequence of movement, among the particles within a cell (ZHANG; HAWORTH, 2004). The particles are transported in such a way that the evolution of their PDF is identical to that of the transport equation. The stochastic particles therefore need not necessarily behave as fluid particles. In fact, each notional particle represents a single realization of the turbulent flow (MöBUS, 2001).

4.3.1 Method of fractional steps applied to the solution of SDE's

From a general point of view, for a system described by N thermochemical variables evolving in three spatial dimensions with temporal variations, the joint scalar PDF is a function of $(N + 3)$ variables and time. As a consequence, the use of either a standard finite difference (FD) or finite-volume (FV) numerical scheme is found to be impracticable. Therefore, to solve the Eulerian PDF transport equation, an equivalent particle system is defined such that the particles evolve using SDE's in time and space, relying on the used of a Monte Carlo technique in which the PDF is represented by stochastic particles, dubbed as notional particles also.

The solutions for the discrete Stochastic Differential Equations are obtained from a time-step procedure. Pope (1985) shows that, from a numerical point of view it is convenient to treat the transport of the particles in physical and composition spaces sequentially, instead of simultaneously. Such procedure of solution is called the fractional step method.

In order to demonstrate the numerical methods implemented in the developed numerical code, the Eq. (3.72) can be rewritten as,

$$dx_i = A(X(t))dt + B(X(t))dW_i(t). \tag{4.31}$$

The stochastic nature of Eq. (4.31) is associated to the Wiener process W_i, that corresponds

to the Brownian motion of each particle (GARDINER, 2009). The increments of the Wiener process, $dW_i(t+\Delta t) = W_i(t+\Delta t) - W_i(t)$, with $i = 1, ..., N_w$, where N_w is the number of independent processes that influence the evolution of the particle in physical space. Numerically, ΔW_i corresponds to a gaussian random variable with zero mean and variance Δt. According to the model used here, the drift, $A(X(t))$, and diffusion coefficients, $B(X(t))$, are functions defined as,

$$A(X(t)) \equiv \left[\tilde{u}_i + \frac{\partial(\Gamma + \Gamma_{SGS})}{\partial x_i}\right], \tag{4.32}$$

and,

$$B(X(t)) \equiv [2(\Gamma + \Gamma_{SGS})]^{\frac{1}{2}}. \tag{4.33}$$

The most widespread procedure of discretizing Eq. (4.31) is the Euler-Maruyama method (GARDINER, 2009). Given a size of time step Δt, the transport of the notional particles in physical space can be expressed by,

$$X_{n+1} = X_n + A(X_n, t_n)\Delta t + B(X_n, t_n)\Delta W_n, \tag{4.34}$$

where X_n and X_{n+1} are the position of the particle in physical space in the current time step n, and in the subsequent time step $n+1$ respectively. t_n is the current time step.

The Euler-Maruyama method is characterized by presenting a strong order of convergence $\gamma_s = 0.5$ and weak order of convergence $\gamma_w = 1.0$. In the present work, it is adopted the definitions of strong and weak order of convergence of numerical methods applied to the solution of stochastic differential equations. This is based on the work of Higham (2001) and it will be briefly summarized here.

A numerical method has a strong order of convergence equal to γ_s if there is a constant

K_s such as,

$$E|X_N - X(t_N)| \leq K_s \Delta t^{\gamma_s} \tag{4.35}$$

where E stands for mean value of the error committed in the discretization, X_N is the approximation of $X(t_N)$ at the time step t_{end} after N uniformly spaced time steps Δt.
The strong order of convergence gives the rate with which the "average error" of the numerical method decays when $\Delta t \to 0$.
Another error measure adopted is the decay of the "mean error" known as the weak order of convergence. A numerical method has a weak order of convergence equal to γ_w if there is a constant K_w for any function f such that,

$$|Ef(X_N) - Ef[X(t_N)]| \leq K_w \Delta t^{\gamma_w} \tag{4.36}$$

where the function f is smooth and polynomial (HIGHAM, 2001). The function f is usually chosen as a very simple function, e.g., $f(X) = X$.

The method of Euler-Maruyama in its explicit formulation,(Eq. 4.34), exhibits a strong restriction to the size of the time step due to stability issues. In fact the method is stable only when the drift and diffusion coefficients of Eq. (4.31) are almost linear, i.e. when the coefficients $A(X(t))$ and $B(X(t))$ are almost constant (ORBEGOSO, 2007). In most practical situations that is not the case and thus, the use of numerical methods presenting higher order of convergence, both weak and strong, is recommended (KLOEDEN; PLATEN, 2000).
The numerical method retained for the simulations carried-out in the present work, Milstein scheme (GARDINER, 2009; KLOEDEN; PLATEN, 2000), has a strong and weak order of convergence equal to one. Applying the Milstein scheme in Eq. (3.72), the final form of the discretized stochastic differential equation that describes the particles trajectories in physical space reads:

$$dx_i = A(X(t))\Delta t + B(X(t))\Delta W_i + 0.5\, B'(X(t))B(X(t))((\Delta W_i)^2 - \Delta t), \tag{4.37}$$

where $B'(X(t))$ is the first derivative of $B(X(t))$ with respect to time. Note that numerical stability considerations also restrict the value of the maximum time step that can be envisaged. Resorting to implicit SDE discretization techniques, which do not exhibit such restrictions has been attempted seldom (ORBEGOSO; SILVA, 2009).

4.3.2 Operator splitting

Once the stochastic particles have been transported in the physical space, the transport of the particles in composition space, given by Eq. (3.73), uses an operator splinting technique (FOX, 2003), in such a manner that the micro-mixing term and the chemical reaction source term are evaluated separately. This is possible only in the cases where the micro-mixing model is deterministic. If the mixing process is described by a Langevin equation, the use of such a splitting technique requires special attention (GARDINER, 2009).

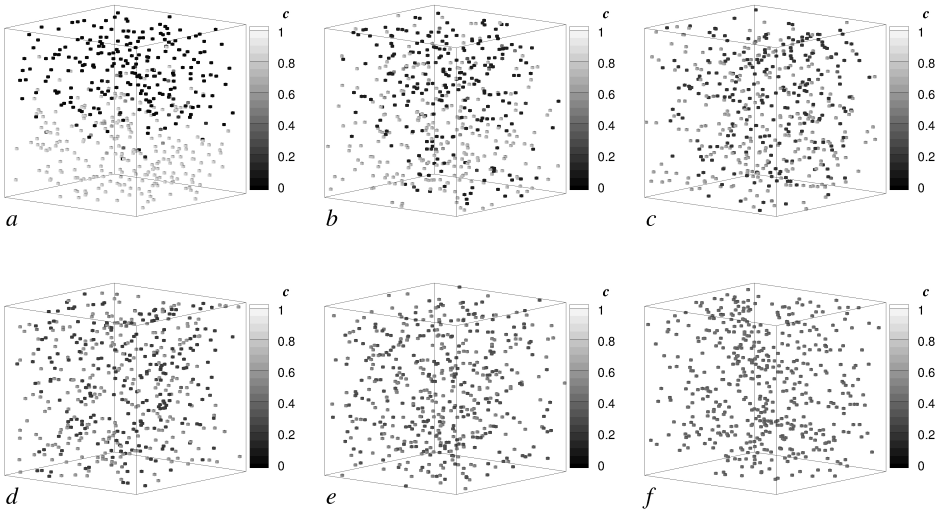

Figure 4.4: Evolution in physical and scalar sample spaces of notional particles are subject to Eqs. (3.72) and (3.73).

Concerning the micro-mixing modeling, as mentioned in Chapter 3, the IEM model is adopted to model the scalar dissipation rate in the joint PDF transport equation of a reactive scalar. Recalling that the IEM model assumes a linear relaxation of the scalars towards the average value and that the IEM model does not contain information of the scalar gradients the original PDF shape is always preserved. In order to illustrate the above statement, Fig.

(4.4) shows the evolution in space and time of notional particles subjected to Eqs. (3.72) and (3.73). In such a figure, sub-figure "a" shows the initial condition, whereas sub-figure "f" stands for the final stage of the mixing.

In this illustrative example, 1000 particles are randomly arranged in a closed cubic box with rigid walls in its boundaries, in such a way that initially, half one assigned with a scalar value one (dark gray), whereas the other half corresponds to a zero value of c (the scalar). As time evolves, i.e., from Fig. (4.4) a to f. The movement of the particles in physical space, due Eq. (3.72), is clearly noted. The figure also illustrates the mixing of the scalar variable c, promoted by Eq. (3.73).

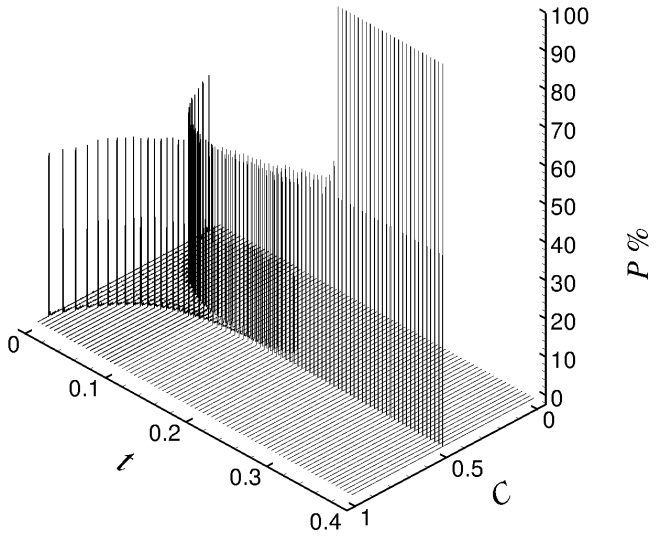

Figure 4.5: Evolution of the PDF of a illustrative case with particles subjected to Eq. (3.72) and Eq. (3.73).

The fact that the IEM model leads the scalar variable to relax toward to the average value, without, however, accounting for scalar gradients, is exemplified in Fig. (4.5). In this figure the shape of the scalar PDF is shown for different discrete times. At $t = 0$ it can be noted that the PDF exhibits two peaks along the c axis, around zero, and one, which corresponds to the condition a of Fig. (4.4). These two peaks correspond to a probability of 50% of particles with $c = 0$ and 50% of particles with $c = 1$. Again, as time evolves, the distance between the two peaks begins to decrease and the probability of having particles

with intermediate values of c between 0 and 1 increases, indicating that the mixing is over the particles, forcing the values of all particles to tend towards 0.5, and finally the probability to obtain this values achieves 100%, the case shown in Fig. (4.4)-f.

Although the IEM model presents the aforementioned shortcomings, in this work it is adopted because of its low computational cost. However it is expected that results obtained with the use of such a simple model will not be influenced strongly by the choice of micro mixing models. This is due to the fact that, in the flows of interest in the present work, the scalar gradients are essentially controlled by the turbulent mixing, in such a way that the chemical reactions influence can be determined explicitly. These are characteristics of flames with low Damköhler number, and of distributed wrinkled flames.

The explicit treatment of the the chemical reaction source term, given by the empirical Arrhenius expression, Eq. (3.52), can lead to extremely small time step sizes due to its high non-linearity and stiffness. Moreover the solution of the chemical reaction source term requires a stiff Ordinary Differential Equations - ODE solver. Stiff ODE solvers typically uses implicit methods, which require an inversion of a Jacobian matrix. In the present work both explicit and implicit methods are retained and compared for solving the stiff part of Eq. (3.73). The computational implementation of the former is quite straightforward since the Euler method has been retained. The stiff ODE solver adopted in the present work was developed by Brown, Byrne and Hindmarsh (1989).

4.3.3 Treatment of initial and Boundary conditions

Analogous to the situation in the Eulerian domain, where boundary conditions must be specified for solving the system of partial differential equations. Boundary conditions must also be applied at the limits of the flow domain during a Monte Carlo simulation. The four most common types are outflow, inflow, symmetry, and a zero-flux wall (FOX, 2003).

At an outflow boundary, the mean velocity vector will point out of the flow domain. Thus, there will be a net motion of particles in adjacent grid cells across the outflow boundary. In this case, these particles are simply eliminated. When symmetry boundaries or

zero-flux-walls are the boundary conditions, particles may attempt to leave the flow domain across the boundary and the common procedure is to reflect the particle position back into the flow domain. Reflecting the particles does not change the particle composition (in the case of non-catalytic walls), but may affect their temperature if the wall is non adiabatic (STROZZI et al., 2008).

At an inflow boundary, the mean velocity vector will point into the flow domain. Denoting the component of the mean velocity normal to the inflow surface (S_{in}) by U_{in}, then the total mass entering each computational volume at each time step Δt is:

$$\Delta m_{in} = \rho S_{in} U_{in} \Delta t, \tag{4.38}$$

The initial composition of the new particle must correspond to the inflow compositions. The initial position of particles in the physical space are randomly defined in directions Y and Z inside the finite volume cell of the inlet, and the position in X direction, based on the Courant criteria is evaluated as:

$$X^{(i)} = U_{in} \Delta t \xi, \tag{4.39}$$

where ξ is a random number ranging between 0 and 1.

4.3.4 Numerical aspects associated to the lagrangian Monte Carlo approach

The LES and PDF solvers are coupled by means of a feedback mechanism that exchanges information at each integration time step. At the beginning of the simulations the flow field is initialized and the stochastic particles are uniformly distributed in the whole 3-D Cartesian mesh. Balance equations for the mass and momentum are first solved within the finite volume (FV) framework. The filtered velocity components, the turbulence frequency and the diffusion coefficients are provided to the Lagrangian solver, so that the particles evolution can be determined according to the stochastic differential equations. The filtered reaction rate term is evaluated using the Lagrangian representation, then fed to the Eulerian

progress variable transport equation. As a next step, the transport equation of the progress variable, is solved, so the temperature field is determined by means of Eq. (3.48), and the new density field is calculated from an equation of state. This procedure is repeated at each integration time step until the end of the simulations.

Some other numerical aspects are relevant to the use of the lagrangian Monte Carlo method. This concerns, among others, the initialization of the particle field, the procedures of interpolation of the mean field variables to the particles, the particles weighting control and the mean values estimations are examples of some of those aspects, which will be addressed in the forthcoming subsections.

4.3.4.1 Initialization of the particle field

The number of particles within each control volume is prescribed to be initially uniform. However, a given stochastic weight (evaluated through Eq. 4.38) is attributed to the particles in such a manner that the particle mass and density fields are consistent with the finite-volume mass and density values. As described above, the particles initial positions are randomly distributed within each control volume, and the associated properties, such as scalar values for instance, are also prescribed consistent with the corresponding Eulerian initial values.

4.3.4.2 Interpolation of average eulerian quantities to the particle field

In order to model the transport of the particles in the physical space, it is necessary to interpolate the mean velocity field, given by the Large Eddy Simulation, to the particles positions. This is accomplished by, first, interpolating the velocities from the control volume faces to the nodes of the finite-volume grid, following the procedure described in Subsection (4.1.3). Once the velocity components at each node of a given control volume are known, a method of interpolation based on the distance weighting is used to interpolate the velocities components from the nodes to the particles positions (VINCOVIK, 2005).

In this interpolation method, the velocity of a particle that lies within a control volume

is weighted by the inverse of the square of the distance between the particle and the nodes, i.e,

$$\tilde{u}_{ip} = \frac{\sum_{No=1}^{8} (\tilde{u}_{i,No}/\mathcal{D}_{No})}{\sum_{No=1}^{8} (1/\mathcal{D}_{No})}, \tag{4.40}$$

where $\tilde{u}_{ip}$ is the i-th component, $i = 1, 2, 3$ of the velocity vector interpolated at the particle p, $No = 1, ..., 8$, is an index associated to a node in a finite-volume hexahedral grid, and $\mathcal{D}_{No}$ is the square of the distance between the particle and a node No, given by,

$$\mathcal{D}_{No} = (x_p - x_{No})^2 + (y_p - y_{No})^2 + (z_p - z_{No})^2, \tag{4.41}$$

where, x_p, y_p and z_p are the coordinates of a particle p in the x, y and z directions respectively, and x_{No}, y_{No} and z_{No} are the positions of the nodes of the considered control volumes. The nodes No, distances $\mathcal{D}_{No}$ and the particle p are illustrated in the Fig. (4.6).

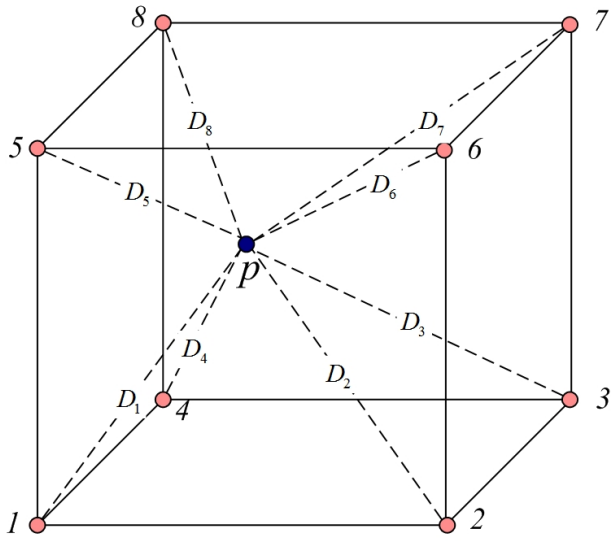

Figure 4.6: Weighted interpolation scheme. The solid lines represent the control volume edges, and the dashed lines connects the nodes and a particle p.

4.3.4.3 Particles weighting control

Due to the stochastic nature of the method of Monte-Carlo and to the turbulent motions, the number of particles present in a given cell may significantly change in time. As can

be derived for constant density flows, the average number of particles per cell is proportional to the cell volume if all particle masses are equal. In order to prevent particle accumulations, particles are ascribed a relative weight, which may vary throughout the computational domain and even among the particles within a single computational cell (ZHANG; HAWORTH, 2004). The particles evolve in such a manner that the evolution of the joint PDF is equivalent to PDF in the physical transport equation. The stochastic particles therefore need not necessarily to behave as fluid particles, i.e., they can have mass for instance, but not inertia. In fact each of them represents a single realization of the turbulent flow (MöBUS, 2001).

To maintain an acceptable distribution of particles as they move in physical space, particle *cloning* and *annihilation* algorithms are employed (ZHANG; HAWORTH, 2004). Particles are cloned in control volumes having less particles than a pre-determined value by splitting a particle of mass m into two particles each having mass $m/2$ and each having the same properties as the original particle. Thus the highest-mass particles in each element may be cloned. Haworth (2010b) argues that cloning does not modify the local PDF of particle properties.

Particles are annihilated in elements having more particles than a pre-determined quantity by collapsing three particles of masses m_1, m_2, m_3 and properties c_1, c_2 and c_3, selected at random (with a bias given to low-mass particles) into two particles of masses $m_1^* = m_2^* = (m_1 + m_2 + m_3)/2$ in a manner that preserves the particle mass, the mean particle properties exactly and, also, the second central statistical moments of the particle properties. This is achieved by taking the mean value ($\widetilde{c_{123}}$) and the variance ($\widetilde{c_{123}^{"2}}$) of these three particles and, then, by applying Eqs. (4.42) and (4.43) to the two new particles.

$$c_1^* = \widetilde{c_{123}} + \sqrt{\widetilde{c_{123}^{"2}}}, \tag{4.42}$$

$$c_2^* = \widetilde{c_{123}} - \sqrt{\widetilde{c_{123}^{"2}}}, \tag{4.43}$$

This particle weighting control algorithms preserve the first and second statistical moments. However, the behavior higher order moments is unknown beforehand. Since

the accuracy of the Monte-Carlo methods depends directly on the number of particles in a given computational cell, in the present work these algorithms act only where the number of particles is 80% smaller than the number of particles initially distributed and in cells where the number of particles is 1.5 times higher than the initial number of particles. It is important to note that the consideration of a group of particles large than 3 may allow more moments to be preserved, however, this is deemed unpractical in the present work.

4.3.4.4 Estimation of average quantities from particle fields

A fundamental issue in hybrid Monte Carlo-Finite Volume methods is the estimation of average quantities from noisy data. In the present thesis this is the case of the properties such as the chemical reaction progress variable, the density and the chemical reaction rate evaluated at each particle. The mean values of the last two quantities are directly used in the transport equations.

Since each particle has its own mass it is natural to use an average weighted by the mass of the particles. Considering a Lagrangian property Q, the weighted average $\langle Q \rangle$ in a given control volume n is given by,

$$\langle Q \rangle_n = \frac{\sum_{l=1}^{N_p^n} m^{(l)} Q}{\sum_{l=1}^{N_p^n} m^{(l)}}, \tag{4.44}$$

where N_p^n is the total number of particles in a given control volume n, and $m^{(l)}$ is the mass of each particle l.

The quality of the implemented Monte Carlo scheme will be estimated by comparing the density of the fluid evaluated from the chemical reaction progress variable field, and the density evaluated from the particle masses. This is the subject of the next section.

4.4 Equivalence between Eulerian and lagrangian approaches

In this section, it is presented the verification of a fundamental pre-requisite of a hybrid LES-PDF method, the equivalence between the Eulerian and Lagrangian approaches.

The model of transported PDF retained in the present work is based on the hypothesis that the stochastic differential equations, Eqs. (3.72) and (3.73), give statistically equivalent results to the solution of the Eulerian equation of transport of the scalar field PDF, Eq. (3.74), when solved over a sufficient large number of Lagrangian particles using the Monte Carlo method.

In this sense, a requirement for the use of the transported PDF model, coupled with a finite-volume model is the verification of the statistical equivalence between the two approaches, based on Eulerian and Lagrangian referentials, respectively. The verification procedure is performed by simulating non reactive cases, where statistical central moments of first and second orders are evaluated and compared quantitatively using both approaches. Another important verification test performed is to ensure the consistency, i.e., the distribution of particle mass in physical space is not arbitrary and it must remain consistent with the fluid mass, or volume, distribution.

A general idea to ensure mass conservation is to devise a system of *notional* particles whose evolution yields the same one-point, one-time PDF as the real fluid particle system (HAWORTH, 2010b). Each notional particle represents a specified mass of fluid $m^{(i)}$ (given by eq. 4.38) of an assembly of N_p particles. The expected value of the mass of particles in each finite-volume cell should be equal to the mass of fluid in the finite volume cell. The mass of fluid in a finite-volume cell of volume V_c is $m_{FV} = \overline{\rho} V_c$, and the mass of particles in that same volume is $m_{pc} = \sum_{n=1}^{N_{pc}} m^{(n)}$, where the sum applies over all particles in the cell. The requirement then is: $\langle m_{pc} \rangle = m_{FV}$. The rules associated with the particle *cloning* and *annihilation* algorithms are used precisely for this purpose: ensure mass conservation.

4.4.1 Scalar field results for constant-density flows

In this section, the equivalence between the Eulerian and Lagrangian is assessed through the simulations of a high speed mixing layer, based in the work of Magre et al. (1988). The computational domain retained is a box with dimensions $(800 \times 2 \times 100)$ mm, in the x, y and z direction respectively. It is discretized in a finite volume mesh of $320 \times 1 \times 100$

control volumes. No-slip conditions are imposed along the z direction and periodicity is used in y direction. An advective boundary condition, (ORLANSKI, 1976), is used as outflow condition. The mean velocity profile used at the inlet is represented by a hyperbolic function:

$$\overline{u}(z) = \frac{\overline{u}_q + \overline{u}_p}{2} + \frac{\overline{u}_q - \overline{u}_p}{2} \tanh\left(\frac{2h(z)}{\delta_m} - \frac{2h_p}{\delta_m}\right), \tag{4.45}$$

where, $\overline{u}_q$ and $\overline{u}_p$ are respectively the velocities of the auxiliary burner (lower part) and of the main duct (upper part); h_p is the height of auxiliary duct. δ_m is the width of the mixing layer. The main duct incoming flow is characterized by a mean longitudinal velocity of 55 m/s. The auxiliary duct incoming flow presents a mean longitudinal velocity of 110 m/s. The Reynolds number, based on the initial width of the mixing layer, $\delta_m = 5mm$, the mean velocity between the two flow streams $U_r = 97.5$ m/s and the value of the kinematic viscosity in air at $600K$ is $Re = 3075$. Over that mean velocity profile, in the x direction, random fluctuations, based on white noise, corresponding to 8% of the mean velocity are superimposed. In the Z direction, the random fluctuations are of 4% of the mean velocity.

The same form of the hyperbolic function used in Eq. (7.21) is kept for the mean value of the progress variable,

$$\overline{c}(z) = \frac{\overline{c}_q + \overline{c}_p}{2} + \frac{\overline{c}_q - \overline{c}_p}{2} \tanh\left(\frac{2h(z)}{\delta_m} - \frac{2h_p}{\delta_m}\right), \tag{4.46}$$

where, $\overline{c}_q$ and $\overline{c}_p$ are respectively the mean values of the progress variable of the auxiliary burner ($\overline{c} = 1$; $T_b = 2000$ K) and of the main duct ($\overline{c} = 0$; $T_u = 560$ K); h_p is the height of auxiliary duct. Concerning the Monte Carlo simulation, an average of 50 particles per control volume are used and the Milstein scheme has been employed for the numerical integration of Eqs. (3.72) and (3.73).

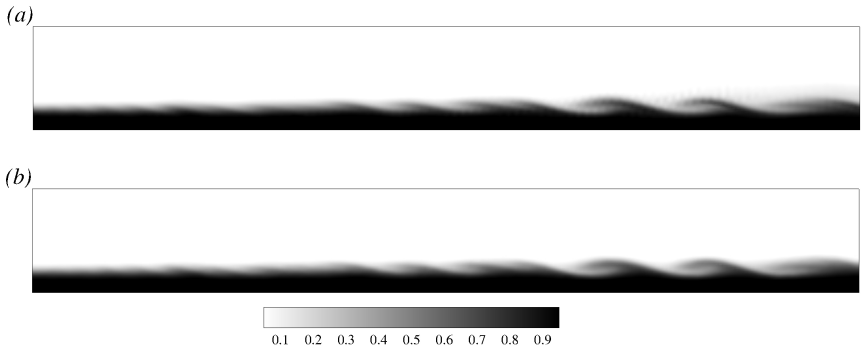

Figure 4.7: Distribution of the progress variable $\tilde{c}$ in the plane xz at $t = 0.03$ s (3000 iterations) (a) Finite Volume method (b) Monte Carlo method.

Figure (4.7) shows the qualitative comparison of an instantaneous field of the progress variable, evaluated by the finite volume method and by the Monte Carlo method. It is noteworthy that both fields are very similar, even in regions where the presence of eddies are more pronounced. Concerning the variance, displayed in Fig. (4.8) the agreement between both methodologies is very satisfactory also.

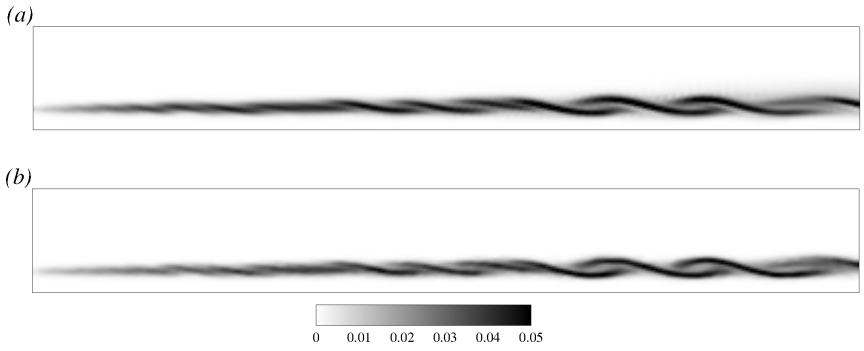

Figure 4.8: Distribution of the variance of the progress variable $\tilde{c}$ in the plane xz at $t = 0.03$ s (3000 iterations) (a) Finite Volume method (b) Monte Carlo method.

Although the developed numerical code is suitable to simulate low Mach number flows, the results presented in this section concern constant density flows. Nevertheless, the consistency test is still of fundamental importance. Fig. (4.9) is a quantitative comparison in terms of time-averaged, denoted by brackets, and instantaneous values of a longitudinal

probe of the density field evaluated by the transport of particles in physical space. The probe is placed along the x axis and at $z = 0.02$m, exactly the position of the splitter plate.
In that case the highest value of the error between the eulerian value of density and the mean values of the density evaluated from particle data is less than 0.1%.

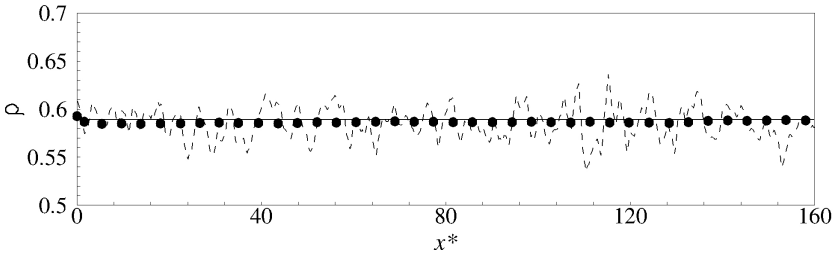

Figure 4.9: Assessment on the consistency of the particle scheme: Solid line stands for the Eulerian (constant) density. The dashed line represents the instantaneous value of the density evaluated from the particle density control algorithm, and the dots are the time-averaged value of the density evaluated by such algorithm.

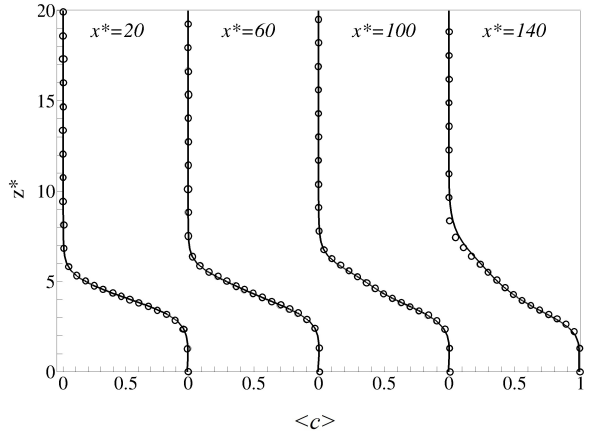

Figure 4.10: Equivalence between the method of finite volumes and the Monte Carlo method. Time-averaged value of the mean value of the progress variable for different positions along the computational domain. $z^* = z/\delta_m$ is non-dimensionalized based on the initial width of the mixing layer.

Figures (4.10)-(4.11) present quantitative comparisons of the first and second central statistical moments of the scalar at different positions along the x axis. It is possible to

verify that there is an excellent agreement between the methodologies. For the variance of the passive scalar, for instance, the maximum difference between the finite-volume and Monte-Carlo methods is about 6%.

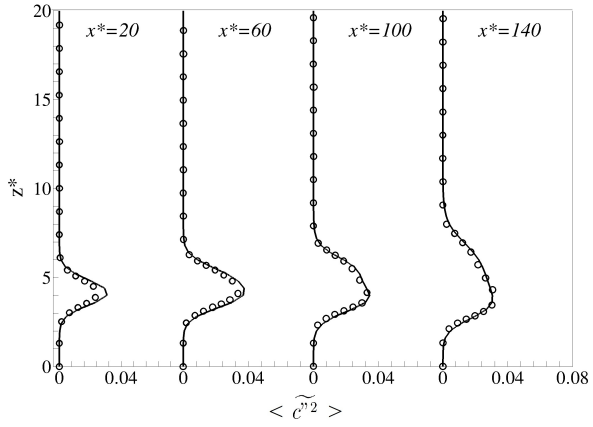

Figure 4.11: Equivalence between the method of finite volumes and the Monte Carlo method. Time-averaged value of the mean value of the variance of the progress variable for different positions along the computational domain.

4.4.2 Scalar field results for variable-density flows

In order to demonstrate the equivalence between the Eulerian and Lagrangian schemes in variable density flows, a temporal mixing layer involving transport of a passive scalar quantity c featuring increasing values of the density ratio is studied. The governing equations for such a variable are the same transport equations that govern the chemical reaction progress variable, however it is important to note that in the present section there is no chemical reaction, i.e., $S(c) = 0$. The flow configuration consists of two co-flowing streams traveling in opposite directions with the same reference velocity $U_r = \Delta U/2$ where ΔU denotes the velocity difference across the layer.

The flow variables reported below are normalized with respect to a reference length scale L_r equal to half the initial vorticity thickness, i.e., $L_r = \delta_v(t = 0)/2$. The corresponding flow is dominated by the growth of large scale coherent Kelvin Helmholtz type structures. In the retained representation, x and y denote the streamwise, and the cross-stream directions,

respectively. The temporal mixing layers are initiated by a hyperbolic-tangent velocity profile, i.e., $u = U_r \tanh(y/L_r)$, with free stream conditions as $u_1 = U_r = 1$ and $\phi_1 = 1$ on the top and $u_2 = -U_r = -1$ and $\phi_2 = 0$. A weak white noise random perturbation is superimposed on the initial velocity field in the rotational region. Simulations are conducted at $Re = U_r L_r/\nu = 500$ for three different values of the density ratio $s = 2, 4, 8$, where s is the characteristic density contrast defined as $s = \rho_1/\rho_2$; $\rho_1 = \rho(c_1)$ and $\rho_2 = \rho(c_2)$ denote the values of the density in the top and bottom streams, respectively.

The computational mesh features homogeneous grid spacings $\Delta x = \Delta y = \Delta z = \Delta$, and the number of grid points is set to $n_x = 2L_x/\Delta = 140$ in the longitudinal direction, $n_y = 2L_y/\Delta = 1$ in the streamwise direction and $n_z = 2L_z/\Delta = 140$ in the cross-stream direction. For all simulations presented in this subsection the size of the time step is allowed to be variable, however the security factor presented in Eq. (4.1) is fixed in 0.25. Concerning the Monte-Carlo approach, the simulations have been carried-out retaining $N_p = 50$ and $N_p = 250$ particles per control volume.

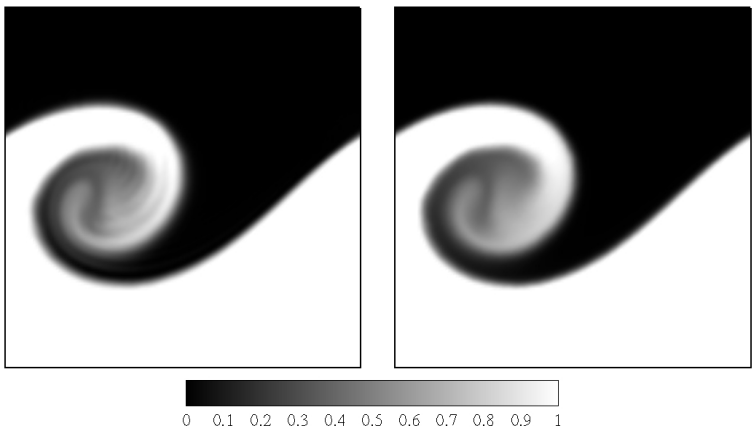

Figure 4.12: Two-dimensional temporal mixing layer simulation results for a density ratio $s = 2$ at $t^* = tU_r/L_r = 54$. Contours of the scalar c. The figure in the right hand side presents results for the simulation using the finite volume scheme. In the left hand side, results of the Monte-Carlo simulation.

In Figs. (4.12) and (4.13) are reported snapshots at $t^* = tU_r/L_r = 50$ of the scalar and variance fields in the case where 250 particles per control volume are initially distributed

to perform such simulation. With values of $c = 0$ in the bottom and $c = 1$ in the top streams, both figures show a moment in the flow where a single vortex is presented in the computational domain. Figs. (4.12) and (4.13) provide a simple visual evidence of the equivalence between the Eulerian and Lagrangian approaches for the transport of a passive scalar.

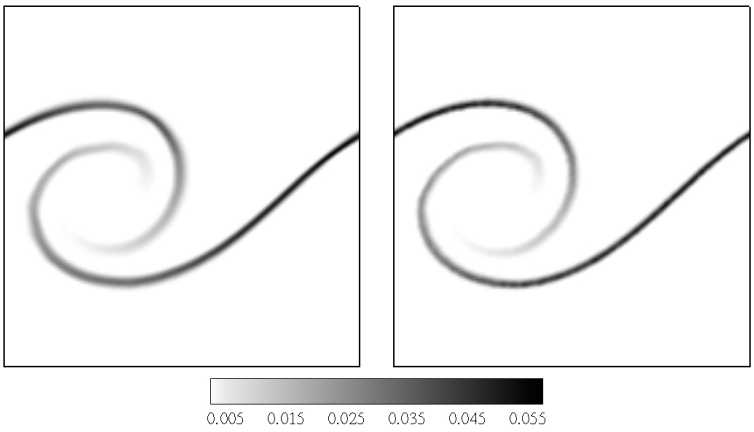

Figure 4.13: Two-dimensional temporal mixing layer simulation results for a density ratio $s = 2$ at $t^* = tU_r/L_r = 50$, where t is the physical time. Contours of the variance of the scalar c. The figure in the right hand side presents results for the simulation using the finite volume scheme. In the left hand side, results of the Monte-Carlo simulation.

The number of particles in the Monte-Carlo simulations affect directly the accuracy of the results. In order to evaluate its influence in the time average results of the two dimensional mixing layer, Fig. (4.14) shows the results of a probe placed at the position $x^* = x/L_r = 0.3$, along the z^* axis. The time-averaged values of the mean values of the scalar variable and its variance are obtained over an average of 2500 iterations (time steps). It is worth recalling that since the numerical code developed is capable of adapt the size of the time step, thus, it is important that the time-average variables are evaluated by taking into account the "distances" in time where samples are taken.

In the present work, the time-averaged value of any variable θ, $\langle\theta\rangle$ is given by,

$$\langle\theta\rangle = \frac{\sum_{i=t_{ini}}^{t_{end}} (\langle\theta\rangle + \Delta t\theta)}{\sum_{i=t_{ini}}^{t_{end}} \Delta t}, \tag{4.47}$$

where, t_{ini} is the first time step the average procedure begins, t_{end} is the time until the procedure will keep averaging the variable θ, and Δt is the size of the time step that can be variable. It is noteworthy that although the mean values of scalar quantity c seems to be independent of the number of particles retained, the variance of the scalar variable displays a higher sensitivity to the number of particles initially retained.

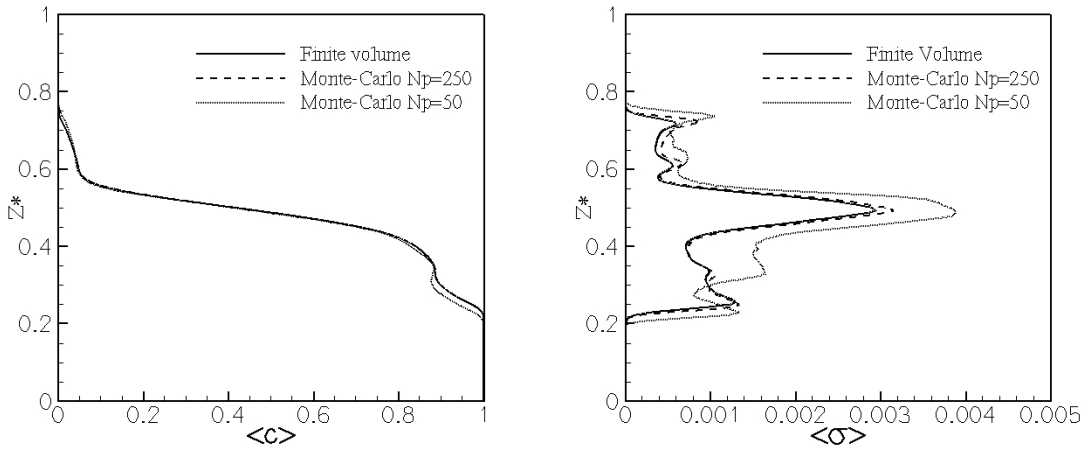

Figure 4.14: Time average results for the two-dimensional temporal mixing layer simulation for a density ratio $s = 2$ for number of particles per control volume N_p equal to 50 and 250. Left hand side: scalar quantity c, right hand side: its variance.

The verification of the equivalence between the Eulerian and Lagrangian approaches is completed with a set of simulations conducted for different values of the density ratio s. Fig. (4.15) (a), (b) and (c) stand, respectively, for quantitative comparisons of simulations carried out with density ratios $s = 2$, $s = 4$, and $s = 8$. In these figures are reported the scalar quantity value, the variance of the scalar, and as a measure of mass conservation of the Lagrangian scheme, the density evaluated from the scalar value (through the equation of state Eq. 3.5), and evaluated from the particle weights.

The data used to build Fig. (4.15) have been obtained from probes positioned in such a manner that they measure the core of the main vortex of the flow. Since the featured results represent different simulations with different flows characteristics, it is natural that

the probes are positioned in different positions in both time and space. For the Fig. (4.15)-(a), the probe is placed at the position $x^* = 0.3$, at $t^* = 50$. For the Fig. (4.15)-(b) the probe is placed at the position $x^* = 0.9$, at $t^* = 50$. Finally, for the Fig. (4.15)-(c) the probe is placed at the position $x^* = 0.7$, at $t^* = 56$. All probes are taken along the z^* axis. Since all comparisons are made based on two-dimensional simulations, the position of the probes along the y-axis is fixed at $L_y/2$.

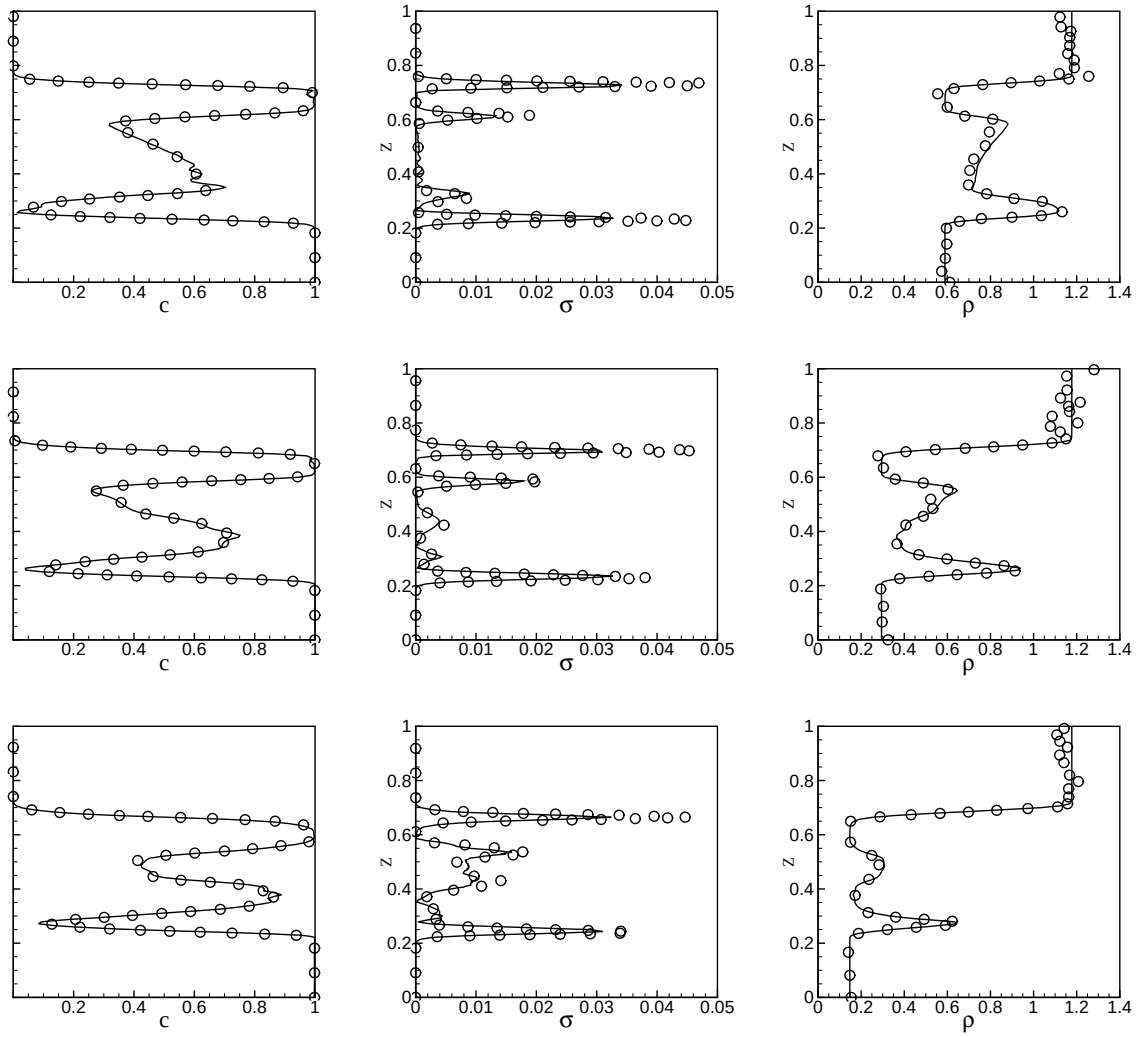

Figure 4.15: Instantaneous probes characterizing the equivalence between the Eulerian and Lagrangian approaches for different ratios of density Top to bottom: $s = 2$, $s = 4$ and $s = 8$. From left to right: the value of the scalar quantity, its variance and the density variations along the z^* axis.

Despite the differences that exist between the numerical algorithms retained for the

transport of a single passive scalar in either constant or variable density flows both the Eulerian and the Lagrangian fields agree very well and feature negligible differences. It confirms, at least, that the transport equations for the scalar have been well implemented, ensure mass conservation and evaluates satisfactorily the first two central statistical moments.

Once the equivalence of the numerical methods adopted in the present work is verified, it is important to address another important numerical issue of the numerical code developed: the capability of performing parallel distributed computations. The corresponding parallelization strategy relies on a three-dimensional cartesian topology of domain decomposition, its detailed description is the subject of the next chapter.

CHAPTER V

PARALLEL APPROACH

One of the main limitations faced by computational simulations of complex physical systems is that associated to the required computational resources. The use of parallel computers, i.e., a set of Central Processing Units - CPUs, that cooperatively solve a computational problem, is each day more affordable. However, the applications designed for serial machines are not readily portable to parallel computers, and require the retained algorithms to be parallel as well.

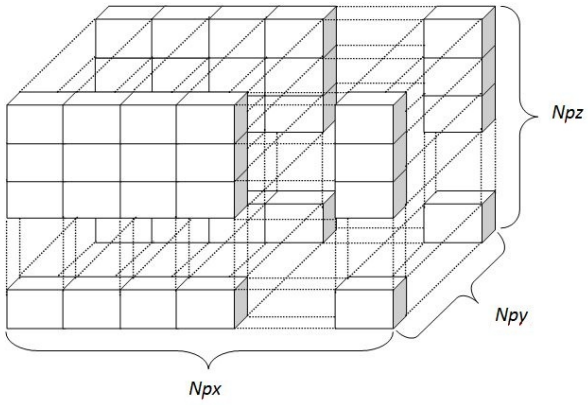

Figure 5.1: Domain decomposition in a three-dimensional cartesian topology. Np_x, Np_y and Np_z stand for, respectively, the number of processes in the x, y and z directions

There are different levels of parallelization that can be adopted in the development of a numerical code. If parallelization is performed at the loop level, which is the case with auto-

parallelizing compilers, achieving a high efficiency in a distributed memory parallel computer is difficult, since the portion of the code that cannot be parallelized has to be very small. A second type of parallelization involves performing some instructions in parallel, e.g., if a product vector-matrix is the most time consuming part of an algorithm, such operation may be treated with aid of other processors, whereas the remaining parts of the algorithm are executed sequentially.

According to Ferziger and Peric (1996), an approach more suitable to fluid dynamics problems is to subdivide the solution domain in sub-domains and assign each of them to one processor (or core). Figure (5.1) exemplifies this approach. In this case, the same code runs on all processors (cores), each one with its own data. Each sub-domain must exchange data with the neighbors, to allow for derivatives to be computed. This is the parallel computing paradigm retained in the present work. The communication between different sub-domains is performed by the using the Message Passing Interface - MPI library (GROPP; THAKUR; LUSK, 1999).

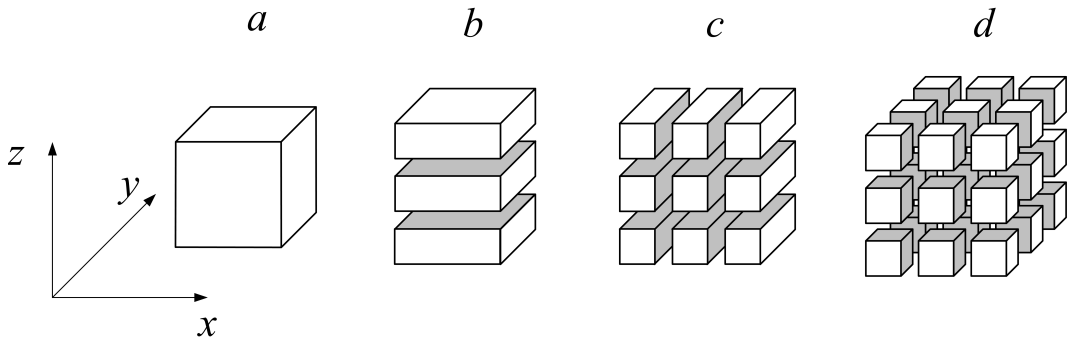

Figure 5.2: Domain decomposition in a cartesian topology. *a*) Original (serial) domain, *b*) one-dimensional decomposition, *c*) two-dimensional and *d*) domain decomposition in the three cartesian directions.

An important aspect in the domain decomposition approach is how the domains are partitioned, more specifically, the topology of parallelization adopted. The topology of parallelization can be unstructured, normally used in numerical codes based on non-structured

grids. Alternatively, as is the case of the code developed in the present thesis, such topology can be structured, more specifically, cartesian. The domain partition strategy in a cartesian topology can vary from one-dimensional to three-dimensional, as shown in Fig. (5.2). In the one-dimensional topology the message exchange proceeds in one direction only, for the two and three-dimensional types of topology the algorithm of message exchange occurs in two and three coordinate axis, respectively.

In Fig. (5.2)-*a*, the original domain has been decomposed in the three different directions. For example, in Fig. (5.2)-*b* the original domain is decomposed into three sub-domains along the z axis, whereas Fig. (5.2)-*c* shows a decomposition along the directions x and z, resulting in 9 sub-domains. Finally, Fig. (5.2)-*d* displays a domain decomposition along the three coordinate directions. It is important to underline that, since the three-dimensional topology was implemented in the computational code developed in the present work, the types of decomposition shown in Figs. (5.2)-*b* and *c*, are also available. Another important fact about the choice of the three-dimensional topology is that, despite its more complicated implementation, when the number of sub-domains is increased (to hundreds for instance), the three-dimensional topology is expected to yields better results, in terms of both speed-up and efficiency, due to an improved volume of calculated data $\times$ amount of data exchanged relation (CAMPREGHER, 2005).

As stated previously in the present manuscript, a hybrid finite volume-Monte Carlo method is among the most promising options to simulate turbulent reactive flows from a general point of view. It should be noted however, that due to the inherent numerical differences between the Eulerian and Lagrangian approaches, its parallel algorithms, although both based on domain decomposition, display significant differences. In the forthcoming sections the main characteristics of such algorithms will be given.

5.1 The finite-volume method parallelization

Concerning the spatial discretization of the transport equations, described in Chapter 4, it is essential to ensure that information is available at every grid point of the stencil used to discretize a derivative. Since, in the present work, a second order approximation is adopted, at least three points are needed to perform such a discretization. When considered the limits of the computational domain, the prescription of boundary conditions may require an extra control volume[1]. When a sub-domain is considered, boundary conditions must be applied in all computational boundaries as well, but differently of a classical boundary condition, e.g., Neumann or non-slip conditions, in the overlapping area[2], the prescribed data comes from others sub-domains.

Still concerning the prescription of the boundary conditions on the overlapping cells, it is important to underline that the storage mode of scalar and vectorial variables in a computational grid also affects the message exchange algorithms. For instance, the choice of a collocated grid simplifies the data exchange algorithms, since all the data structures that are passed from one sub-domain to another have the same size, i.e., the faces exchanged have the same number of control volumes, regardless of scalar or vectorial variables. On the other hand, since the type of grid arrangement may affect the pressure-velocity coupling in incompressible and low-Mach number regimes, the use of a staggered grid is desirable. In this case, the size of the arrays used for the storage of vectorial and scalar variables are different, hence, different messages sizes must be transmitted across the sub-domains. In the case of the numerical code developed in the present work, four different grids are used, one for each component of velocity, and a fourth for the scalar variables (pressure, density, viscosity, chemical reaction progress variable and its variance).
The exchange of this set of variables is done before the evaluation of the coefficients of each linear system to be solved in the projection method retained, and the communication between subdomains of a single variable is performed inside the linear system solver, i.e.,

[1] In the present work it is adopted the nomenclature of ghost cells for the extra cells retained to enforce the correct boundary conditions.

[2] Region where two ghost cells occupy the same position in space

since the solvers used in the present work are iterative, the variable to be solved within the linear system solver must be updated after each iteration.

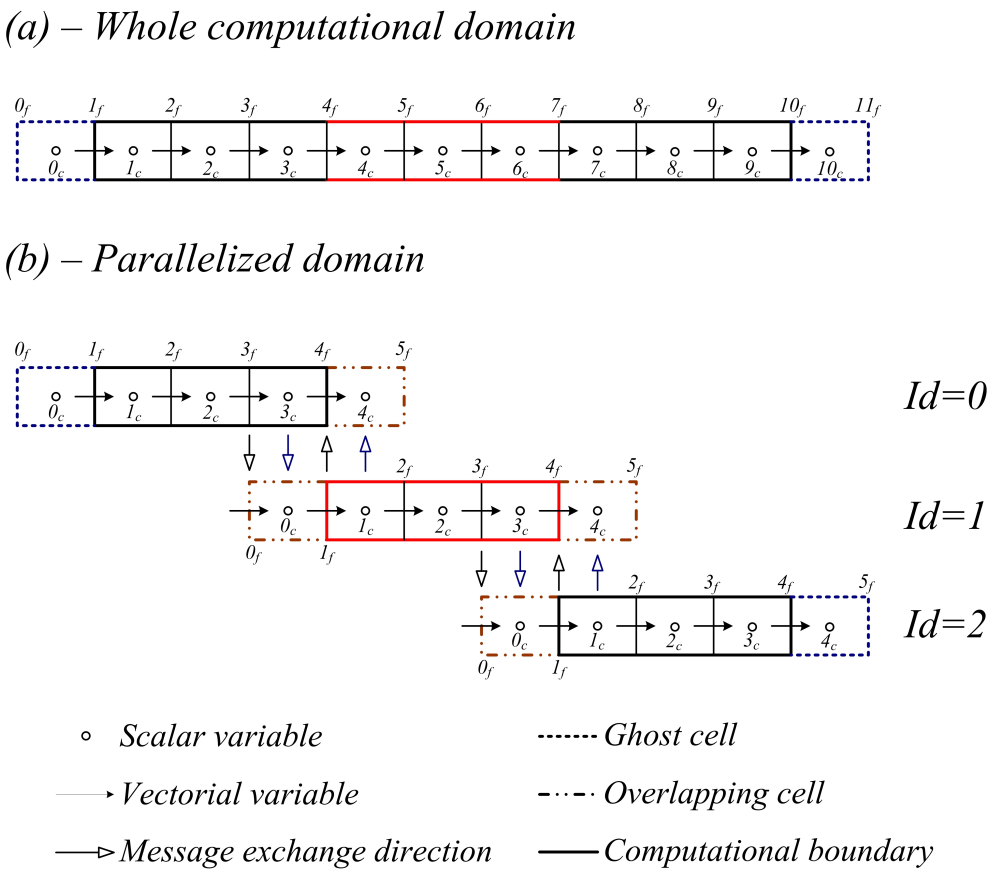

Figure 5.3: Domain decomposition in a one-dimensional cartesian topology and data exchange scheme for vectorial and scalar variables.

To illustrate the procedure of data exchange in the finite-volume method, Fig. (5.3)-a shows an one-dimensional domain which is decomposed in three sub-domains. To each sub-domain an ID is attributed, thus, in this example, there are IDs from 0 to 2. The vectorial and scalar variables are positioned in a staggered way. Consider first the vectorial variable, Fig. (5.3)-a shows that a ghost cell is not needed at the limits of the domain, i.e., classical boundary conditions can be prescribed at faces 1_f and 10_f. In Fig. (5.3)-b, for the IDs 0 and 2, such classical boundary conditions can also be prescribed at faces 1_f and 4_f, with respective IDs 0 and 2. However, at face 4_f of ID 0, the value of the vectorial variable should come from the ID 1, face 1_f.

In order to evaluate such face at ID 1, the value of the variable at its left neighbor 0_f is

required, which, is determined from the face 3_f of ID 0. The same procedure is performed at the end of ID 1 and at the beginning of ID 2 and so forth.

The data exchange procedure for the scalar variables is similar to that retained for the vectorial variables, however, ghost cells are needed to ensure that the three points stencil, required by the second order discretization, is always available. In this sense each sub-domain must have its own ghost cells. The communication procedure also follows the same algorithm as the communication of vectorial variables, i.e., in order to calculate the value of a scalar variable at point 1_c of ID 1, it is necessary to transport the value of point 3_c of ID 0, to cell 0_c of ID 1. Analogously, to evaluate the scalar at cell 3_c of ID 0, the ID 1 must send the value of the scalar at 1_c to cell 4_c of ID 0.

Finally, if a periodic boundary condition is required, regardless the position of the ID in relation to the computational domain, the data exchange procedure treats the sub-domain as an "internal" sub-domain. In this case, all ghost cells become overlapping cells along the periodicity direction. Considering the above example, if periodicity is applied, the data contained in faces 3_f and 4_f of ID 2 must be exchanged with the faces 0_f and 1_f of ID 0. Similarly, the data of cells 3_c and 4_c of ID 2 are exchanged with the data of cells 0_c and 1_c of ID 0.

5.2 Parallelization of the Lagrangian approach

In the case of a Monte Carlo simulation, each particle can move, under Eq. (3.72), across different sub-domains. Since each particle carries information that must be preserved across the sub-domains, e.g., the value of the scalar, such information must be transferred across the processors as well. As stated in the previous paragraphs, the number of particles in a given simulation can easily be of the order of several millions. Moreover, the number of particles present within each sub-domain at a given time in unknown, as is the number of particles that cross the faces of the sub-domains. Such indetermination governs the choice of the particle data structure, which should be suited for dynamic data. For the Lagrangian

approach, in the present work is adopted a linked list data structure, which is now outlined.

5.2.1 Data structure and linked lists

Blevins (2009), defines a linked list as a list containing a series of individual node elements, where each node contains a data member and one pointer that points to the next node in the list. In the present work a second pointer that points to the previous node in the linked list is implemented. The first node, known as head of the list, points to the next node, but its pointer indicating the previous node is null. The contrary characterizes the last node, i.e., the pointer known as the tail of the linked list. A schematic view of the used linked list is given in Fig. (5.4),

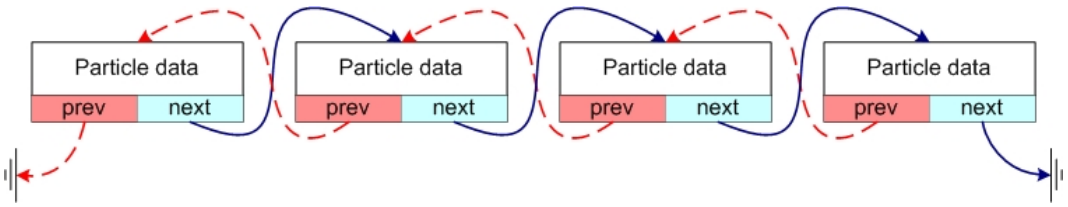

Figure 5.4: Schematic view of the linked list. The arrows departing for the pointers "prev" and "next" indicate the previous and next data members.

The data contained in a given data member can be as complex as needed. In the the present work, each node of the linked list represents a notional particle, thus, each data member contains the velocity components, scalars arrays, logical arguments and integers variables grouped in a Fortran-90 type structure (PRESS et al., 1992). The main advantage of the linked list is that the list can grow and shrink by simple point operations of linking applied on the pointers, thus avoiding the need of allocating or deallocating great amount of data, as it would be the case if regular arrays were used.

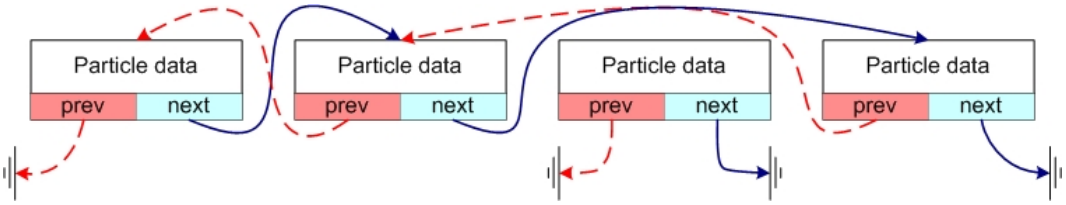

Figure 5.5: Reallocation of pointers in the process of deleting an node in a linked list. The arrows departing for the pointers "prev" and "next" indicate the previous and next data members.

The shrinking operation, i.e., the act of deleting a particle from the linked list, can be explained with aid of Fig. (5.5). First, consider that a particle is no longer necessary in the linked list. In the present example, the third particle from the left to the right in Fig. (5.5). The first operation is to nullify the "prev" and "next" pointers of such a particle.
Then, the "next" pointer of the previous particle is redirected to the next particle after the one that is to deleted, whereas, the "prev" pointer of the next particle is redirected to the previous one. The process of redirecting the pointers isolates the particle to be deleted from the linked list, which allows for easy deallocation.
The procedure of adding a new particle in the linked list is simpler. In this case, it is sufficient to add the new particle at the end of the linked list, reconnecting the "next" pointer of the old tail in the actual tail, and connecting the "prev" pointer of the actual tail to the old tail. In the next subsection the algorithm developed to exchange particle data between sub-domains will be explained.

5.2.2 Data exchange between sub-domains

Since a three-dimensional cartesian topology of parallelization is adopted, the particles within each sub-domain may move across its boundaries in any direction. Moreover, considering again Fig. (5.1), it is possible to note that, given the structure of the domain decomposition, particles from a given sub-domain may be transported to different destinations (sub-domains) at a given time. This requires a mapping, in which for each sub-domain is computed the number of particles that leave its boundaries, the corresponding destination,

and consequently, how many particles each sub-domain receives from every possible origin.

Such a map is constructed by identifying each particle with an integer variable, that gives the actual ID of the particle, i.e., the identity of the sub-domain the particle lies within at the time step considered. The ID of the particle is set by verifying if the coordinates of the particle lies between the boundaries of a given sub-domain, or if the coordinates of a particle shows that such a particle must be transported to another sub-domain, the value of the integer variable will be the destination ID.
It is worth noting that such operation must be done at each time step. However this is not a costly operation since it is necessary only an *if* statement to verify the ID of each particle, and this statement can be positioned inside a loop for the numerical solution of Eq. (3.72).

Once determined the data that must be sent and received by each sub-domain, the procedures of sending and receiving data are performed. A careful design of this exchange procedure is required in order to ensure a good efficiency and speed-up of the overall computational code.
Before discussing the possible data exchange algorithms it is important to introduce a few communication paradigms, more specifically those related to the send and receive functions of the MPI library. The point-to-point communication is basically composed of two operations: send and receive, each of which may be classified as synchronous or asynchronous, blocking or non-blocking operations.

The communication operation is synchronous or asynchronous if it completes, or not, before the corresponding receive operation has been initiated. Thus, synchronous sends complete only when the corresponding message is handled by some receiving process, whereas, asynchronous sends completes as soon as the corresponding message has been delivered to the communication buffer. It is possible to understand the above statements with a simple example: a fax message or registered mail is a synchronous operation. The sender can find out if the message has been delivered, for its turn, a post card is an example of an asynchronous message. The sender only knows that it has been put into the post-box but has no

idea if it ever arrives unless the recipient sends a reply.

Another classification is related to the blocking or non-blocking nature of the communication, which relate the completion time of a communication operation to the procedure that initiate that particular communication operation. Blocking procedures only return when the corresponding communication has completed, whereas non-blocking procedures return immediately and allow the process to proceed to perform other work. Note that, at some later time, the process may verify for the completion of the corresponding communication. It is important to point out that non-blocking operations demand careful implementations, since they are usually associated to the overload risks or dead-lock problems, however, non-blocking communication is generally faster than its blocking counterpart.

Different approaches are possible for transporting particle data between domains. Once defined the target-sub-domain of a particle, the first approach is to send particle by particle separately for its destination, i.e, one operation of send and receive for each particle transported. This can be made using blocking or non-blocking communication. For the applications of interest, blocking communication has a prohibitive cost, but independently of the form of communication it was found that use a send-receive for each particle is costly and the risk of having a overload of communication when increasing the number of particles is high.

In the algorithm proposed in the present work, the number of particles that crosses the sub-domain boundaries is determined before entering the send-receive procedures by the mapping algorithm commented in the above paragraphs, thus it is natural to group the particles which have a common destination in a package and send the package of particles, instead of single particles. For a small number of sub-domains, usually 2 or 3 in a one-dimensional topology of parallelization, the use of blocking communication has presented the same computational cost as that of non-blocking communication. However, the blocking communication cost rapidly degrades as the number of sub domains grows. Note that when N_p sub-domains are considered, in principle one has N_p^2 communication possibilities, hence,

the resort to fully blocking communication is no longer affordable.

The approach developed in the present work uses non-blocking sends and blocking receives. The receiving routine is capable of distinguishing different incoming data, and yet be able of be aware of the completeness of the message arrived, because, for each message sent, there is a particular control code. That control, based on the mapping of the communication, works like a tag for the message, avoiding that the same sub-domain receives messages from a same "origin" sub-domain more than once. Moreover, the receive function uses a blocking form in order to ensure that the particles transfer process is correctly done and that at the end of the operation, no particle were "lost", i.e, every particle that needed to be transported, has been transported, and has arrived correctly in its destination.

Finally, the received particles must be inserted in the linked list of its corresponding sub-domain. This is made by adding the recently arrived particles at the end of the linked list. The particles positions in the linked list at the originating domains, are deleted using the procedure given in the subsection (5.2.1).

5.3 Performance assessment on the parallel approach implemented.

The performance analysis of a parallel code can be measured by the *speed-up* factor and the *efficiency*, defined respectively as (FERZIGER; PERIC, 1996):

$$S_n = \frac{t_s}{t_n}, \tag{5.1}$$

and,

$$E_n^{tot} = \frac{t_s}{nt_n}, \tag{5.2}$$

where t_s is the execution time for the best serial algorithm on a single processor, and t_n is the execution time for the parallelized algorithm using n processors. It is important to point-out that $t_s \neq t_1$, i.e., the time of the best serial algorithm is not necessarily the same

as the parallel code executed in one processor only. Indeed, in the present work, the value of t_s is not available, therefore, the speed-up factor and efficiency results here presented are evaluated as,

$$S_n = \frac{t_1}{t_n}, \tag{5.3}$$

and,

$$E_n^{tot} = \frac{t_1}{nt_n}. \tag{5.4}$$

As will be seen in the Chapter 6, it is possible to propose analytical solutions to the transport equations, in such a manner that a thorough verification of the numerical code is achieved. Through the prescription of known source terms, it is possible to compare the results of the numerical scheme against analytical solutions. The solution that will be used here to verify the data exchange procedures is:

$$u_e = sin^2(2\pi x + 2\pi y + 2\pi z + t), \tag{5.5}$$

$$v_e = -cos^2(2\pi x + 2\pi y + 2\pi z + t), \tag{5.6}$$

$$w_e = 2cos^2(2\pi x + 2\pi y + 2\pi z + t), \tag{5.7}$$

$$p_e = cos^2(2\pi x + 2\pi y + 2\pi z + t), \tag{5.8}$$

$$c_e = cos^2(2\pi x + 2\pi y + 2\pi z + t). \tag{5.9}$$

In these equations t is the time, and x, y and z are the coordinate directions. The subscript e stands for the manufactured solutions of the primary variables, i.e., the three velocity components, pressure and chemical reaction progress variable. This solution, when substituted in the transport equations for velocity and chemical reaction progress variable generates source terms. Once solved the transport equations with such source term incorporated, the resulting velocity and chemical reaction progress variable fields are compared to the exact values given by Eqs. (5.5) to (5.9). More details about the use of analytical functions in the

verification of numerical codes will be given in Chapter 6.

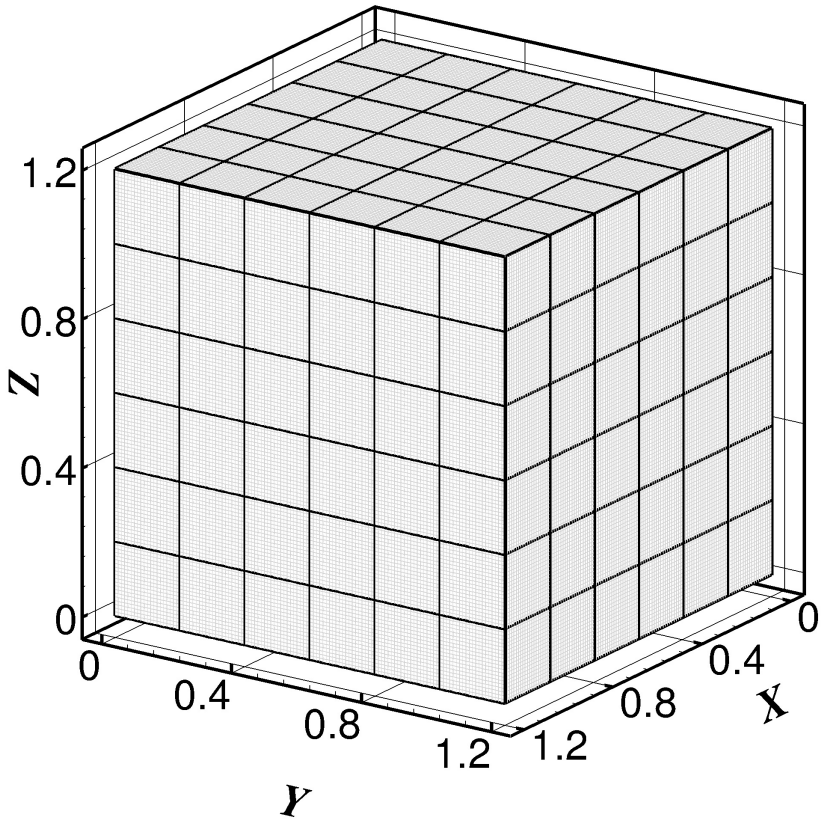

Figure 5.6: Original domain sub-divided in 216 sub-domains. Each cubic box of the assembling is assigned to a processor (core).

For the assessment of the parallel implementation, it is considered an incompressible non-reactive flow, in which, variable "c" is considered to be a passive scalar. The computational domain is a periodic, cubic, box with dimensions $1.2 \times 1.2 \times 1.2$ m^3, discretized in a computational mesh of 120^3 control volumes. The density and dynamic viscosity are set to 1 $kg\,m^{-3}$ and 0.1 $kg\,m^{-1}\,s^{-1}$, respectively. The simulations carried-out are already performed with the coupling of the finite-volume and Monte Carlo methods. For all simulations, 10 particles are initially assigned per control volume, totalizing about 17 million of particles in the original (serial) domain. Such a domain is then sub-divided in 8, 27, 64, 125 and 216 sub-domains, always maintaining an uniform three-dimensional topology of parallelization. A view of the domain sub-divided in 216 sub-domains can be seen in Fig. (5.6). In such figure, the original domain is divided in 6 slices per direction, within each one of the 216

sub-domains, the resulting grid is of 20^3 control volumes.

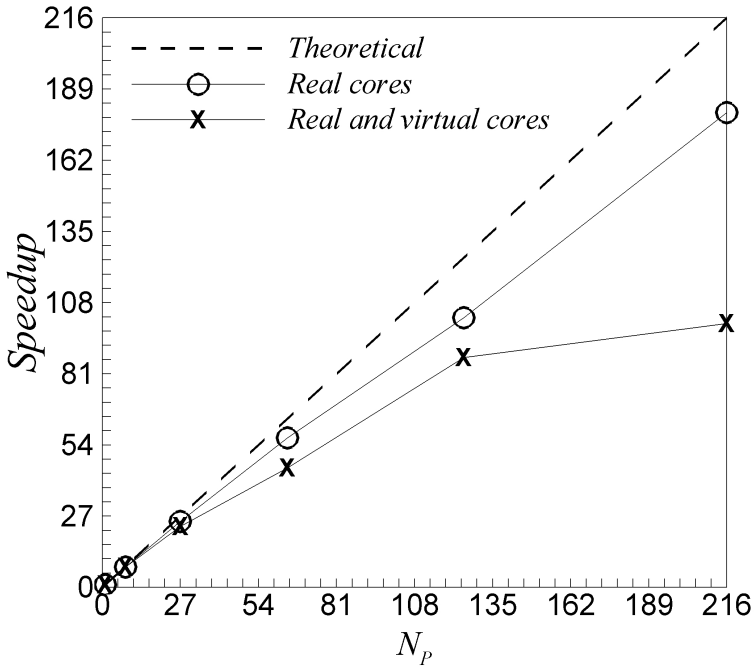

Figure 5.7: Speed-up evaluation for the hybrid finite-volume Monte-Carlo method.

For all simulations, a high-performance SGI/Altix XE1300 Linux cluster consisting of 30 Intel Xeon processors (26 processors E5650 2.67GHz and 4 E5520 2.27GHz, resulting in 344 cores), which are connected via an Infiniband IB QDR / 10GigE interconnect is used. One of the characteristics of such a class of processors is the capability of the use of the hyper-thread technology. Hyper-threading is an Intel-proprietary technology used to improve parallelization of computations. Roughly speaking, for each processor core that is physically present, the operating system addresses two virtual processors, or cores, and shares the workload between them when possible. Considering the cluster presently used for the speed-up and efficiency evaluation, the 344 real cores would become 688 cores.

The simulations were first performed using the full capacity of the system, i.e., with all real and virtual cores requested by the numerical code, and, then, a second set of simulations, using only real cores. The differences between the speed-up curves for the cases where real cores are used instead of real and virtual cores, are shown in the Fig. (5.7). In all

simulations where virtual nodes were used, the speed-up factor was worse than when only real cores were requested. This can be due to several causes, e.g., the computer nodes were overloaded, since each core, besides the numerical code, has also to maintain the operational system, putting eventually the numerical code in a wait status, or even by the non-optimized use of the cache L2 memory. In the last case, if two processes tries to access the L2 memory at the same time, but there is not enough space, one of the process must be put on hold.

It is noteworthy that, when more than 27 processors are used, there is a decrease in the speed-up factor when virtual and real cores are used simultaneously. Such a performance penalty increases when the number of sub-domains is increased, for 216 sub-domains, for instance, the maximum speed-up achieved is 100, whereas when only real cores are requested, the speed-up factor is 181. The difference between the theoretical speed-up factor, 216 and obtained one, 181, could be explained by the communication increase among the sub-domains, specially due the Monte-Carlo method. For example, when eight sub-domains are used, the average amount of particles exchanged among all sub-domains per iteration is about 70,000, whereas for 216 sub-domains, this number increases to 252,000.
Tab. 6.5 displays the overall characteristics of the cases simulated, as well as the values of efficiency and speed-up factor, calculated from Eqs. (5.3) and (5.4).

Table 5.1: Numerical efficiency and speed-up factor evaluation for various topologies of parallelization.

Topology of parallelization $Np_x \times Np_y \times Np_z$ $[Total]$	Grid per Sub-domain	Particles per Sub-domain	Theoretical speed-up factor	Speed-up factor obtained (real cores only)	Numerical efficiency (in %)
$1 \times 1 \times 1\,[1]$	120^3	17,280,000	1	1.00	100.0
$2 \times 2 \times 2\,[8]$	60^3	2,160,000	8	7.66	95.8
$3 \times 3 \times 3\,[27]$	40^3	640,000	27	24.8	91.7
$4 \times 4 \times 4\,[64]$	30^3	270,000	64	56.7	88.6
$5 \times 5 \times 5\,[125]$	24^3	138,240	125	102.3	81.8
$6 \times 6 \times 6\,[216]$	20^3	80,000	216	181	83.8

For large reactive simulations the parallel performance is expected to increase for two reasons. First, with increasing number of control volumes and of particles, for a given number of processors, the relative communication effort reduces. The second reason is connected to the evaluation of the Arrhenius law reaction source terms, which is the single, most expensive operation responsible for increasing the workload.

Concerning the overall efficiency of the parallel approach retained, Fig. (5.8) shows that the numerical code developed presents an acceptable efficiency. The less than two percent of increase in the efficiency between the cases with 125 and 216 sub-domains may be due the fact that, since the amount of data sent to the cache L2 is lower in the case with 216 sub-domains, such lower amount of memory requested could fit the L2 memory, i.e., the size of the memory sent to the processor may fit in the size of the L2 memory, avoiding extra communication between the L2 memory and the RAM memory, consequently reducing the computational time.

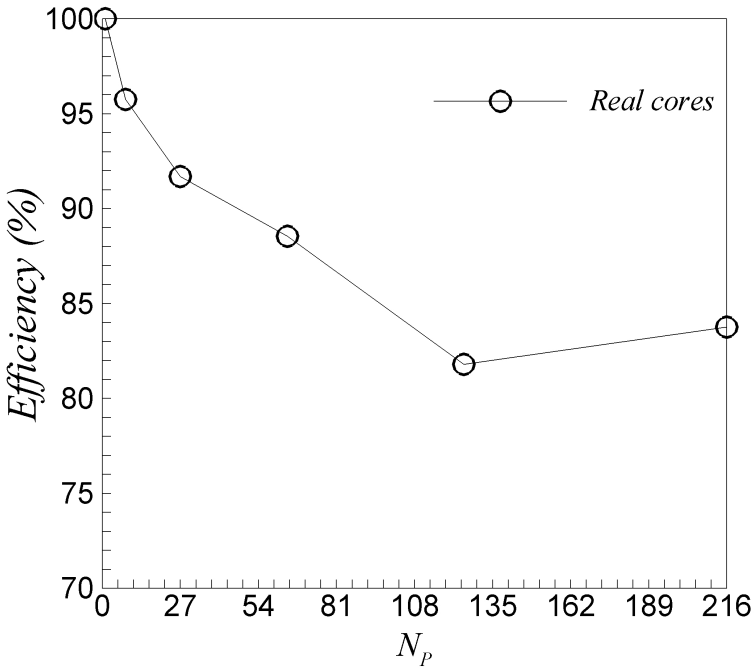

Figure 5.8: Efficiency of the parallel implementation of the hybrid finite-volume Monte-Carlo method.

CHAPTER VI

CODE VERIFICATION

As aforementioned, the solutions of the balance equations (mass, momentum, energy, species mass fractions, etc.) are sufficient to represent any flows irrespective of their characteristic velocity, provided that the continuum hypothesis holds, and once suitable constitutive equations for the fluids of interest are provided. However, when dealing with discrete approaches for solving such a system of balance equations, the numerical techniques do involve, invariably, errors. These errors have different sources, spanning from unavoidable roundoff errors to mere programming mistakes (bugs), hence emphasizing the crucial need for well defined procedures to evaluate the numerical accuracy. Moreover, it is of fundamental importance to be able to characterize the capabilities of a numerical approach, i.e., it is imperative to determine whether (or not) the retained mathematical / numerical scheme is suitable to cope with the problem of interest.

An important step in the development of a new numerical tool is the process of verification and validation of the numerical code. In the present work, the Method of Manufactured Solutions (MMS) is used to to verify the accuracy and the convergence rate of the numerical methods implemented. A noteworthy characteristic of such a method is the capability of identifying the eventual presence of implementation bugs. The resort to the Method of Manufactured Solutions is progressively becoming a classical and well-accepted methodology retained in the framework of a numerical code verification (STEINBERG; ROACHE, 1985).

There is an undeniable interest in the use of such a method to quantify, accurately, numerical capabilities before using computational programs to perform the simulation of complex physical systems.

The MMS consists in developing *a priori* known analytical solutions for the system of governing equations. These manufactured solutions require the addition of a source term to the original differential model, such as those presented in Eqs. (3.2), (3.3) and (3.74), for instance. It is worth recalling that, in this chapter, the analysis of the accuracy and convergence rate are made by considering the Eulerian set of equations only. Therefore, no chemical reaction is present in the manufactured solutions. The variable c, called chemical reaction rate should be understood as an passive scalar herein. As a consequence, in this chapter, the source term of the chemical reaction progress variable in Eq. (3.74), represents the analytical source term used in the Method of Manufactured Solutions.

In order to construct the manufactured solution, a set of almost arbitrary functions are selected and substituted into the considered system PDEs, thus allowing to solve its derivatives analytically. The result of such a substitution is the "source term". To avoid errors in the symbolic manipulation of this source term, which can be composed of hundreds of terms, algebraic manipulation softwares, like the Maplesoft 12.0, for instance, may be used. The source term is then considered as an input to the numerical code, which allows reproducing the manufactured solution. The pioneering works that make use of manufactured solutions with the objective of verifying the accuracy and the convergence rate of a given numerical code can be assigned to Steinberg and Roache (1985), Roache (1998b) and Roache (1998a). A recent application of such a method can be found in Vedovoto et al. (2011).

The arbitrary nature of the analytical functions must satisfy, at least, the following conditions:

- They must be continuous smooth functions of independent variables. Problems involving discontinuities are generally dealt using lower order algorithms due to stability issues;

- The solution must be continuously differentiable up to the order required by the cor-

responding terms in the governing equations;

- To avoid numerical difficulties, manufactured solutions should respect positiveness for quantities that are physically defined as positive semi-definite, e.g., density, molecular viscosity;

- If periodic boundary conditions are chosen, the solution must be periodic as well to avoid the development of discontinuities.

In the case of verification of a numerical code devoted to simulating fluid flows, it may be interesting for the analytical solution to satisfy the continuity equation at least. With a null source term in the continuity equation, most algorithms retained for the solution of fluid flow problems do not need to be modified excepted for the source terms. For instance, if the continuity equation is obeyed by the analytical velocity field, i.e., the divergence of the analytical velocity field is null, the algorithm used for solving the pressure-velocity coupling does not need to be modified, otherwise, it would be necessary to add new source terms in the Poisson equation for instance. Salari and Knupp (2000) provide well documented guidelines for creating manufactured solutions as well as the procedures for obtaining the corresponding source terms and performing the analysis of the obtained results.

In general lines, to evaluate the convergence rate of the developed numerical implementation, a quantitative metric of the error is chosen, and successive grid refinements are performed. As the error metric decays with the grid refinement, it is evaluated as a function of the characteristic mesh size, h.

For a given level of resolution, $\Phi^h_{(i,j,k)}$ is defined as the discrete value of any variable Φ of interest, e.g. the density, velocity components, pressure or chemical reaction progress variable, at any point (i, j, k) of the discrete computational domain, and $\Phi^e_{(i,j,k)}$ is the corresponding value of the manufactured solution. The first step of the verification procedure requires to define a metric of the numerical error, denoted Ψ_h in the following, in order to subsequently quantify the error decay rate obtained, for decreasing values of the characteristic grid mesh size h.

In this work, it is adopted the L_2-norm as the relevant metric of the numerical error,

$$\Psi_h = L_2\left(\Phi^h_{(i,j,k)}\right) = \sqrt{\frac{1}{N}\sum_{i,j,k}\left(\Phi^h_{(i,j,k)} - \Phi^e_{(i,j,k)}\right)^2}, \tag{6.1}$$

where N denotes the total number of grid points.

The error decay ratio is defined as,

$$r_e = \log\left(\frac{\Psi_{2h}}{\Psi_h}\right), \tag{6.2}$$

with Ψ_{2h} the value of the error metric obtained on a grid with characteristic mesh size $2h$.

Following the nomenclature retained in Salari and Knupp (2000), the convergence rate q is defined as:

$$q \approx \frac{r_e}{log(2)}. \tag{6.3}$$

Using Eq. (6.3), it is possible to verify that the characteristic error decay ratio, using grids with characteristics mesh sizes $2h$ and h, for methods of convergence rate $q = 1$, 2 and 3, must be, 2, 4 and 8, respectively. It is worth noting that, although possible, the value of r_e does not always converges monotonically as the mesh is progressively refined, and it may exhibit oscillations.

The process of verification presented herein is divided into two distinct parts. First, the numerical code is tested using a manufactured solution that aims at verifying the convergence rate for an incompressible solution, i.e., the zero Mach number limit. This is performed using solutions based on sine and cosine functions, built in such a manner that the velocity divergence is zero. The two different approaches for the discretization of the advective terms in the transport equations are also assessed, as well as the effects of adopting homogeneous and non-homogeneous boundary conditions. A second set of tests aims at mimicking the propagation of a corrugated flame front that separates heavy from light gases. The application of the method of manufactured solutions still remains more scarce for such low Mach number situations. If excepted for the expression of the equation of state, the expression adopted

to perform this analysis is the same as the one previously considered by Ham (2007), and Shunn and Knupp (2007). This second set of tests clearly aims at evaluating the numerical capabilities of the developed code to deal with variable density flows as those encountered in combustion problems.

6.1 Verification of an incompressible solution

The set of functions reported below is retained as a solution for velocity components, pressure and chemical reaction progress variable, respectively, in the limit of a zero Mach number scheme:

$$u_e = sin^2(\alpha_s \pi x + \beta_s \pi y + \gamma_s \pi z + \delta_s t), \tag{6.4}$$

$$v_e = -cos^2(\alpha_s \pi x + \beta_s \pi y + \gamma_s \pi z + \delta_s t), \tag{6.5}$$

$$w_e = \frac{\alpha_s}{\gamma_s} cos^2(\alpha_s \pi x + \beta_s \pi y + \gamma_s \pi z + \delta_s t) + \frac{\beta_s}{\gamma_s} cos^2(\alpha_s \pi x + \beta_s \pi y + \gamma_s \pi z + \delta_s t), \tag{6.6}$$

$$p_e = cos(\alpha_s \pi x + \beta_s \pi y + \gamma_s \pi z + \delta_s t), \tag{6.7}$$

$$c_e = cos(\alpha_s \pi x + \beta_s \pi y + \gamma_s \pi z + \delta_s t). \tag{6.8}$$

The subscript e stands for the manufactured solutions of the primary variables, i.e. the three velocity components, pressure and chemical reaction rate; t is the time. It is observed that, if it is taken the divergence of Eqs. (6.4)-(6.6), the incompressibility condition is verified. The above set of equations is written as a function of the constant parameters α_s, β_s, γ_s and δ_s. Such parameters allow to apply the Method of Manufactured Solutions within a wide range of numerical verifications. For example, if δ_s is set to zero, only the spatial derivatives influence the convergence rate of the scheme. On the other hand, if α_s, β_s and γ_s are set to zero, only the temporal scheme is tested.

One advantage of the Method of Manufactured Solutions if the capability of testing a numerical implementation by parts, i.e., if is desired to test Eq. (3.2) without the pressure term, it is enough to suppress the pressure contribution from the MMS source term, and, of course, to remove the pressure contribution of the transport equations. If, for any reason,

the convergence rate is not achieved in a fully coupled system, such a procedure of testing the implementation by parts, facilitates the search for the eventual bugs. Throughout the development of the present thesis, every term of each transport equation is separately verified, prior to being assessed in a fully coupled algorithm. For the sake of conciseness, only the results of the fully coupled algorithms are presented. However, it is important to underline that, if there were residual bugs in the implemented algorithm, the expected convergence rate would not be achieved.

6.1.1 Convergence rate analysis

The computational domain considered for the present numerical simulations is a cube of dimensions $[0,1] \times [0,1] \times [0,1]$, in x, y and z directions respectively. The time step is controlled by Eq. (4.1), in such a manner that the factor C of Eq. (4.1) is set to 0.25. The parameters α_s, β_s and γ_s are set to 2, and $\delta_s = 1$. The constant values of density and viscosity are set to unity and 0.01, respectively. The variable coefficient Poisson solver is used, however, no constraint is enforced for such incompressible solution. Concerning the temporal integration scheme, the Backwards Difference Scheme - BDF, is retained.

The simulations carried-out for the verification of the accuracy and the convergence rate of the developed numerical code are divided in four groups: first, Dirichlet boundary conditions are set to all boundaries of the computational domain, and CDS approach is assessed. The second set of simulations retain the Dirichlet boundary conditions, but the deferred-correction approach is used. To verify the influence of the type of boundary conditions on the convergence rate, the last two set of simulations are carried-out with mixed boundary conditions: periodicity in the y direction, and Dirichlet boundary conditions in x and z directions. Again, the CDS and deferred-correction approaches are tested with such a mixed boundary conditions.

Table (6.1) reports the grid refinement, the decay of L_2 norm and the resulting convergence rate q for homogeneous boundary conditions (Dirichlet), and the CDS approach for the discretization of the advective term of the transport equations. It is worth noting that at least a convergence rate equals to two is obtained for all transported variables.

Table 6.1: Obtained convergence rates for Dirichlet boundary conditions and CDS approach for the spatial discretization of the advective terms.

Domain	L_2u	q	L_2v	q	L_2w	q	L_2p	q	L_2c	q
16^3	0.03730		0.03730		0.07090		0.06400		0.06260	
32^3	0.00837	2.15	0.00839	2.15	0.01610	2.13	0.01540	2.06	0.01290	2.28
64^3	0.00199	2.07	0.00200	2.07	0.00390	2.04	0.00380	2.02	0.00300	2.10
128^3	0.00048	2.05	0.00049	2.01	0.00094	2.05	0.00095	2.00	0.00073	2.04

Depending on the class of flows simulated, some iterative solvers may fail to converge when applied to the system of algebraic equations derived from central differencing of the advective fluxes. This behavior is associated to grid-to-grid oscillations that are not solved by central finite-difference schemes, and hence, should be removed because they may lead to numerical instabilities (BOGEY; BAILLY, 2004). Practically, the elimination of these spurious short waves is obtained by introducing artificial dissipation through additional damping terms in the equations (JAMESON; SCHMIDT; TURKEL, 1981) or, more efficiently, through filtering procedures (BOGEY; BAILLY, 2004), without affecting the physical long waves. It is possible, yet, to apply the deferred correction approach on the advective terms of the balance equations. Such approach, implemented in the present work, is designed to improve the numerical stability, however, it can adversely affect the convergence rate (FERZIGER; PERIC, 1996).

Table 6.2: Obtained convergence rates for Dirichlet boundary conditions and deferred-correction approach for the discretization of the advective terms.

Domain	L_2u	q	L_2v	q	L_2w	q	L_2p	q	L_2c	q
16^3	0.03410		0.03410		0.06490		0.05950		0.057330	
32^3	0.00763	2.16	0.00760	2.16	0.01468	2.14	0.01420	2.07	0.011800	2.28
64^3	0.00180	2.08	0.00185	2.04	0.00351	2.06	0.00348	2.03	0.002765	2.09
128^3	0.00043	2.06	0.00045	2.04	0.00083	2.08	0.00094	1.89	0.000660	2.07

In the tests performed in the present work, as can be seen in Tab. (6.2), it is verified that the deferred correction approach maintains a convergence rate equals to two for all

variables tested, excepted for the pressure in the last grid refinement. In this case, the convergence rate from the refinement of the 64^3 mesh to the mesh of 128^3 is found to be 1.89. Figure (6.1), graphically represents the results shown in Tabs. (6.1) and (6.2). In this figure, N stands for the number of grid points in each of the coordinates directions.

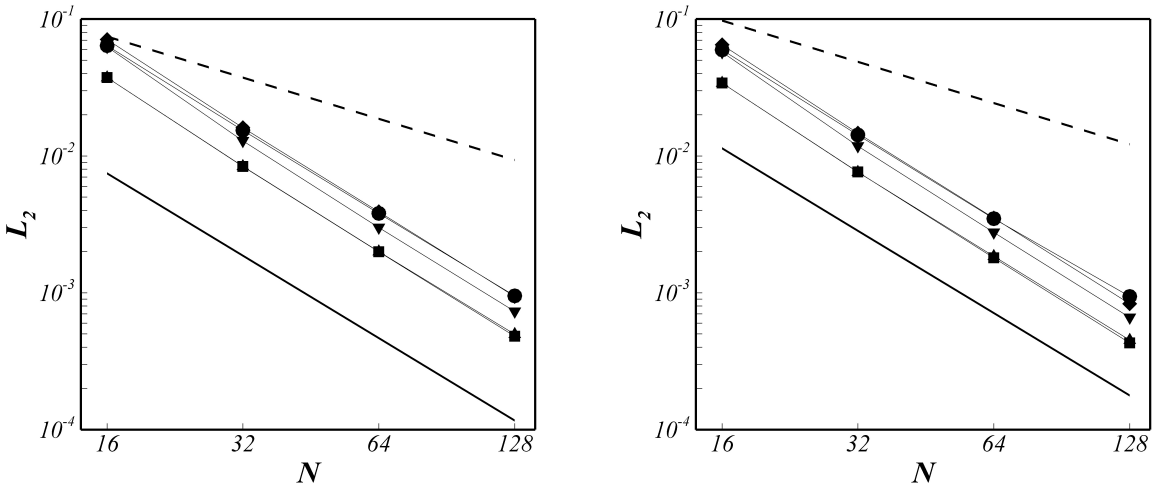

Figure 6.1: Decay of the L_2 norm for the zero Mach number manufactured solution with Dirichlet boundary conditions. ■: u, ▲: v, ♦: w, ▼: c, •: p. The solid line stands for the second order decay rate, and the dashed line stands for first order decay rate. Left figure: CDS approach; right: deferred correction approach.

The results of the convergence rate analysis for the incompressible scheme, when mixed boundary conditions are retained, is shown in Tabs. (6.3) and (6.4) for, respectively, the discretization based on the CDS and deferred correction approaches for the discretization of the advective terms in the transport equations. In both cases, a convergence rate equals to two is achieved.

Table 6.3: Obtained convergence rates for mixed boundary conditions and Central differencing scheme for the advective terms.

Domain	L_2u	q	L_2v	q	L_2w	q	L_2p	q	L_2c	q
16^3	0.03240		0.051900		0.063100		0.05110		0.0582	
32^3	0.00722	2.16	0.011300	2.19	0.014100	2.16	0.01184	2.10	0.0122	2.25
64^3	0.00174	2.05	0.002700	2.06	0.003490	2.01	0.00292	2.02	0.0029	2.07
128^3	0.00043	2.01	0.000655	2.04	0.000863	2.01	0.00074	1.98	0.0007	2.05

Table 6.4: Obtained convergence rates for mixed boundary conditions and deferred-correction differencing scheme for the advective terms.

Domain	L_2u	q	L_2v	q	L_2w	q	L_2p	q	L_2c	q
16^3	0.02969		0.04821		0.05746		0.047100		0.05337	
32^3	0.00659	2.17	0.01050	2.20	0.01294	2.15	0.010770	2.13	0.01112	2.26
64^3	0.00158	2.06	0.00250	2.07	0.00312	2.05	0.002640	2.03	0.00262	2.08
128^3	0.00039	2.02	0.00060	2.06	0.00076	2.04	0.000669	1.98	0.00062	2.08

The results gathered in Tabs. (6.3) and (6.4) are illustrated in Figure (6.2). For the incompressible solution, the numerical code is shown to yield at least second order in the convergence rate for velocity. Finally, concerning the pressure, it is possible to note a continuous decrease of the convergence rate as the computational mesh is refined, however, its value does not exceed 1.98.

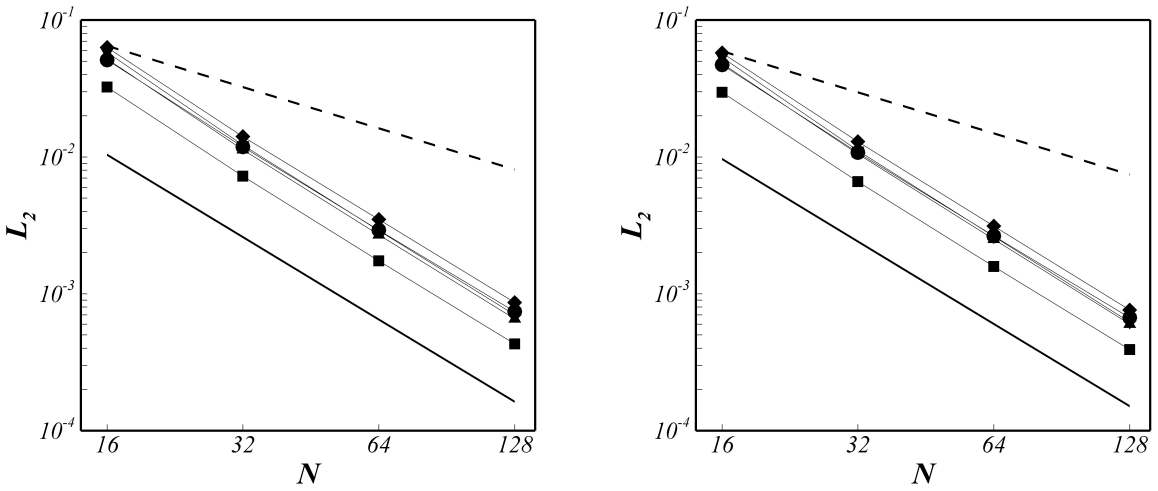

Figure 6.2: Decay of the L_2 norm of the zero Mach number manufactured solution with mixed boundary conditions. ■: u, ▲: v, ♦: w, ▼: c, •: p. The solid line stands for the second order decay, and the dashed line stands for first order decay. Left figure: CDS approach; right: deferred correction approach.

Such an analysis of the incompressible solution under consideration clearly demonstrates that, in terms of numerical accuracy, the numerical code developed is a good candidate to perform Large Eddy Simulations of constant density turbulent flows that require at

least a convergence rate equals to two.

The preliminary key step associated with the verification of the numerical code being performed for an incompressible regime, the verification of the numerical code developed is now assessed for variable density flows.

6.2 Verification of the low-Mach number solution

The set of manufactured solutions retained in the present section are similar to those introduced by Shunn and Knupp (2007) and Ham (2007). However, it is used here with a different equation of state, which involves a different pressure-velocity coupling. It is also worth mentioning that, in the present work the interest is in density ratio variations representative of those encountered in flames, which are significantly smaller than those considered in the study conducted by Ham (2007).

The manufactured solutions are not necessarily related to an expected physical solution. However, a solution that attempts to represent some relevant features of a given problem, is both, a tool to assess the convergence rate, and provide a pertinent preview of the behavior of the numerical code, when applied to situations of interest. In this sense, the set of analytical functions reported below gathers some interesting features of a propagative combustion front.

$$c_e = \frac{1 + \tanh[b\hat{x}\exp(-\omega t)]}{\left(1 + \frac{\rho_0}{\rho_1}\right) + \left(1 - \frac{\rho_0}{\rho_1}\right)\tanh[b\hat{x}\exp(-\omega t)]}, \tag{6.9}$$

$$\rho_e = \frac{P_o}{c_e}, \tag{6.10}$$

$$u_e = \frac{\rho_1 - \rho_0}{\rho_e}\left\{-\omega\hat{x} + \frac{\omega\hat{x} - u_f}{\exp[2b\hat{x}\exp(-\omega t)] + 1} + \frac{\omega\log[\exp(2b\hat{x}\exp(-\omega t)) + 1]}{2b\exp(-\omega t)}\right\}, \tag{6.11}$$

$$v_e = v_f, \tag{6.12}$$

$$w_e = 0, \tag{6.13}$$

$$p_e = 0, \tag{6.14}$$

where, $\hat{x} = u_f t - x + a\cos[k_2(v_f t - y)]$ and a, b, k_2, ω, u_f, v_f and P_o are constant parameters, given in Tab (6.5).

To proceed with the analysis of the order of a accuracy of the numerical scheme for variable density flows, different sets of numerical simulations are performed, increasing values of the density ratio $s = \rho_0/\rho_1$. It is important to stress that the manufactured solution must be compatible with the full set of equations that govern the evolution of the system under consideration, and this also includes the equation of state. Equations (6.9 - 6.14) satisfy the mass balance equation with a null source term, however, non-zero source terms also appear in momentum and chemical reaction progress variable transport equations.

Table 6.5: Values of the constant parameters for the variable density numerical simulation.

parameter	value	parameter	value
P_o	101.325	a	1/5
C_p	1000	b	20
u_f	0.5	k_2	4π
v_f	0	ω	3/2
w_f	0	μ	10^{-4}

Figure (6.3) displays the temporal evolution of the density field. It is noteworthy that, as the time evolves, the front is simultaneously advected and diffused. The computational domain is a box of $[-1, 2] \times [-0.5, 0.5] \times [-h/2, h/2]$. Five different grids are used, from: $150 \times 50 \times 1$, up to, $2400 \times 800 \times 1$. These grids are henceforth denoted, respectively, by: $4h$, $2h$, h, $h/2$ and $h/4$. For velocity components, chemical reaction progress variable and density, Dirichlet boundary conditions are set at $x = 0$, $y = -1/2$ and $y = 1/2$. A Neumann boundary condition is used in the outlet $x = 2.0$. Regarding the pressure, Neumann boundary conditions are applied at $x = 0$, $y = -1/2$ and $y = 1/2$. At the outlet a Dirichlet condition is retained. For all variables, periodicity is assumed in spanwise direction, z. Similarly to the incompressible tests, the BDF scheme is used in the simulations presented in the present section.

The procedure of cycling some parts of the algorithm may be used to enhance convergence and stability of the numerical scheme. Such a procedure is based on the recent work

of Ham (2007), but with some modifications. First, as noted above, a different equation of state is used, second, a constraint on the divergence of the velocity field is added herein, as a part of the strategy retained to solve the Poisson problem.

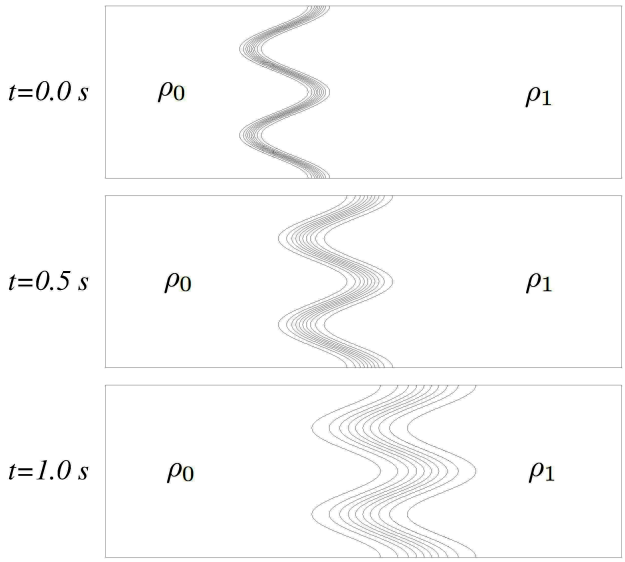

Figure 6.3: Evolution of the density field. The isolines stand for equally spaced density levels.

6.2.1 Convergence rate analysis

In this section, are presented and discussed the results of a convergence rate analysis, performed for the low Mach number MMS case. All the simulations presented below have been carried out with a constant value of time-step size set to 0.01. Four different density ratios are studied, $s = 2$, 5, 7 and 10. Tables (6.6), (6.7) and (6.8) display the convergence rate, and the value of the L_2 norm obtained for velocity, density and chemical reaction progress variable for the first three ratios. These values of error and convergence rate are measured at $t = 1.0$, following the procedure adopted by Ham (2007).

As commented at the beginning of the present chapter, although the analytical solution manufactured can be somewhat arbitrary, there are some desirable characteristics that will improve the tests for verifying the convergence rate.

Table 6.6: Obtained convergence rates for low Mach number solution, $s = \rho_0/\rho_1 = 2$.

Domain	L_2u	q	L_2v	q	L_2p	q	L_2c	q	$L_2\rho$	q
$4h$	7.63E-02		1.21E-02		1.14E-01		3.62E-02		1.61E-02	
$2h$	1.73E-02	2.14	1.09E-02	0.15	3.53E-02	1.69	1.21E-02	1.58	6.57E-03	1.29
h	3.00E-03	2.53	1.64E-03	2.73	9.22E-03	1.93	3.09E-03	1.97	1.87E-03	1.81
$h/2$	6.69E-04	2.16	1.20E-04	3.77	2.28E-03	2.01	7.61E-04	2.02	4.65E-04	2.01
$h/4$	1.63E-04	2.04	8.21E-06	3.87	5.60E-04	2.02	1.90E-04	2.00	1.17E-04	1.99

Table 6.7: Obtained convergence rates for low Mach number solution, $s = \rho_0/\rho_1 = 5$.

Domain	L_2u	q	L_2v	q	L_2p	q	L_2c	q	$L_2\rho$	q
$4h$	5.15E-02		1.27E-02		3.70E-02		5.90E-02		4.70E-02	
$2h$	2.17E-02	1.25	7.72E-03	0.72	9.75E-03	1.92	1.65E-02	1.84	1.70E-02	1.47
h	7.20E-03	1.59	1.38E-03	2.48	3.73E-03	1.39	3.94E-03	2.07	4.80E-03	1.82
$h/2$	1.93E-03	1.90	1.18E-04	3.55	1.00E-03	1.90	9.75E-04	2.01	1.20E-03	2.00
$h/4$	4.90E-04	1.98	7.61E-06	3.95	2.70E-04	1.89	2.43E-04	2.00	3.00E-04	2.00

Table 6.8: Obtained convergence rates for low Mach number solution, $s = \rho_0/\rho_1 = 7$.

Domain	L_2u	q	L_2v	q	L_2p	q	L_2c	q	$L_2\rho$	q
$4h$	6.08E-02		2.77E-02		4.35E-02		7.00E-02		6.00E-02	
$2h$	2.73E-02	1.15	1.92E-02	0.53	2.70E-02	0.69	1.73E-02	2.02	1.90E-02	1.66
h	9.44E-03	1.53	2.75E-03	2.80	8.69E-03	1.63	3.80E-03	2.18	5.60E-03	1.76
$h/2$	2.50E-03	1.92	2.00E-04	3.78	2.34E-03	1.89	9.00E-04	2.08	1.43E-03	1.97
$h/4$	6.50E-04	1.94	1.31E-05	3.93	5.90E-04	1.99	2.20E-04	2.03	3.50E-04	2.03

The manufactured solution adopted for the low-Mach number tests, has the great advantage of be capable of reproducing some simplified features of a reactive flow. Moreover, the fact of the manufactured solution retained respect the mass conservation equation, allows a profound verification of the algorithm implemented. However, such a manufactured solution displays some limitations. The fact that the analytical solutions for v_e, w_e and

p_e are constants, does not says much about the behavior of the decay of the L_2 norm and convergence rate of such variables. Again, despite that, the information gathered from the analysis of order of accuracy for the u component of velocity, density and chemical reaction progress variable is highly valuable.

It is possible to observe that for a density ratio $s = 2$, the convergence rate for the u-component of velocity achieves at least two. Unlike the convergence rate analysis conducted for the incompressible solution, where the values of the L_2 norm decrease with a constant convergence rate, the present results show that, as the grid is refined, not only the magnitude of the L_2 norm decreases, but also the convergence rate increases. Such a trend is even more pronounced for density and chemical reaction progress variable. The decays of the L_2 norm obtained for the primary variables, corresponding to the results gathered in Tables (6.7) and (6.8), are illustrated in Fig. (6.4).

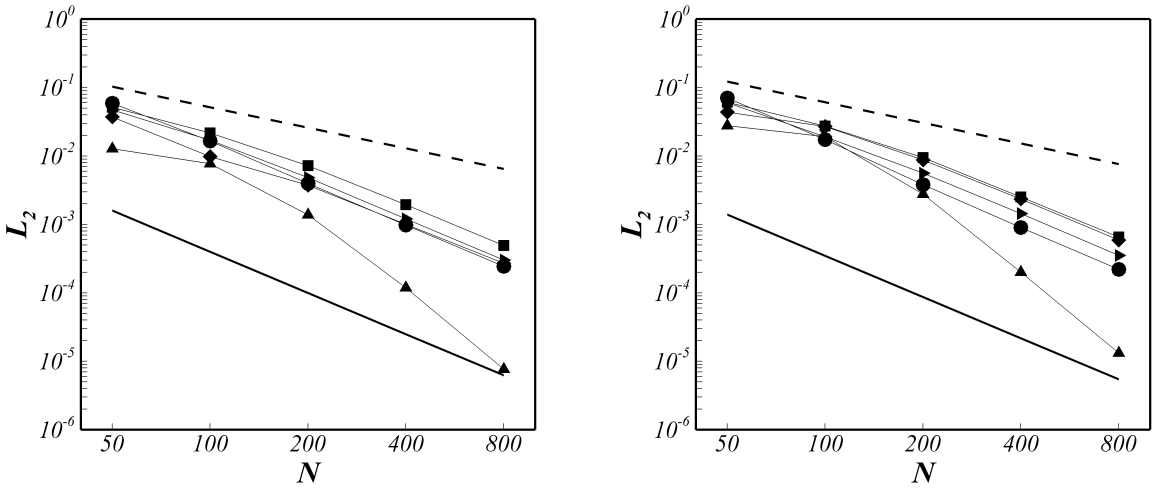

Figure 6.4: Evolution in time of the L_2 norm. . Left figure: $s = 5$; right: $s = 7$. ■: u, ▲: v, ♦: p, ●: c, ►:ρ. The solid line stands for the second order decay, and the dashed line stands for first order decay.

Increasing the density ratio to 5 and 7, the convergence rate for density and chemical reaction progress variable follows the same behavior as the one described in the above paragraph, however a slight decrease in the convergence rate is observed for the u-component of

velocity. Specially when coarser meshes are considered. As aforementioned, not much can be said about the accuracy and convergence rate of the v-component of velocity and the pressure, since the analytical functions used are constants. However, the observed accuracy and convergence rates for such a variables, corroborates with the conclusions obtained above in the analysis of the convergence rate for an incompressible solution, i.e, an increasing of convergence rate with the refinement of the grid suggests, at least, a correct computational implementation of the transport equations.

In order to examine the effects of the number of cycles on the convergence rate, a density ratio $s = 10$ is considered. The results of the convergence rate analysis are shown in Tab. (6.9). A convergence rate equals to two is difficult to obtain for the chemical reaction progress variable, for the u-component of velocity and for the density, the achieved convergence rate is lower than the expected.

Table 6.9: Obtained convergence rates for low Mach number solution, $s = \rho_0/\rho_1 = 10$.

Domain	L_2u	q	L_2v	q	L_2p	q	L_2c	q	$L_2\rho$	q
$4h$	1.05E-01		8.26E-02		8.38E-02		1.10E-01		1.00E-01	
$2h$	3.60E-02	1.54	3.17E-02	1.38	5.05E-02	0.73	1.69E-02	2.70	2.23E-02	2.16
h	1.22E-02	1.56	4.27E-03	2.89	1.40E-02	1.85	3.40E-03	2.31	6.44E-03	1.79
$h/2$	3.30E-03	1.89	3.00E-04	3.83	3.69E-03	1.92	8.40E-04	2.02	1.63E-03	1.98
$h/4$	8.54E-04	1.95	1.89E-05	3.99	9.37E-04	1.98	2.10E-04	2.00	4.09E-04	1.99

As commented above, the procedure of cycling some parts of the algorithm can be used to enhance convergence and stability of a numerical scheme. To verify that, a convergence rate analysis is made by cycling two times the pressure-velocity coupling before advancing the numerical simulation in time. The obtained results are gathered in Tab. (6.10). As it can be noted, the process of cycling twice the pressure-velocity algorithm has some positive aspects on both the L_2 norm and convergence rate of the whole algorithm. For instance, for the u-component of velocity, the smallest value of the convergence rate is found to be 2.4. A graphical comparison between the numerical simulations using either one or two cycles is presented in Fig. (6.5).

Table 6.10: Obtained convergence rates for low Mach number solution, $s = \rho_0/\rho_1 = 10$, two cycles per iteration.

Domain	L_2u	q	L_2v	q	L_2p	q	L_2c	q	$L_2\rho$	q
$4h$	9.90E-02		6.25E-02		8.32E-02		1.30E-01		1.46E-01	
$2h$	1.88E-02	2.40	3.30E-02	0.92	4.90E-02	0.76	1.13E-02	3.52	9.28E-03	3.97
h	3.46E-03	2.44	4.91E-03	2.74	1.40E-02	1.80	1.44E-03	2.97	1.53E-03	2.60
$h/2$	4.80E-04	2.89	4.00E-04	3.67	3.95E-03	1.82	1.40E-04	3.36	2.44E-04	2.64
$h/4$	7.17E-05	2.74	2.69E-05	3.89	1.00E-03	1.98	1.38E-05	3.34	2.48E-05	3.30

Finally, although undeniable gains in terms of convergence rate can be obtained by resolving twice the pressure-velocity coupling per time step, it is important to keep in mind that such an artifice must be used carefully, since it significantly impacts the computational costs, i.e., cycling twice the pressure-velocity coupling means solving again all the linear systems, hence, twice the CPU time spent.

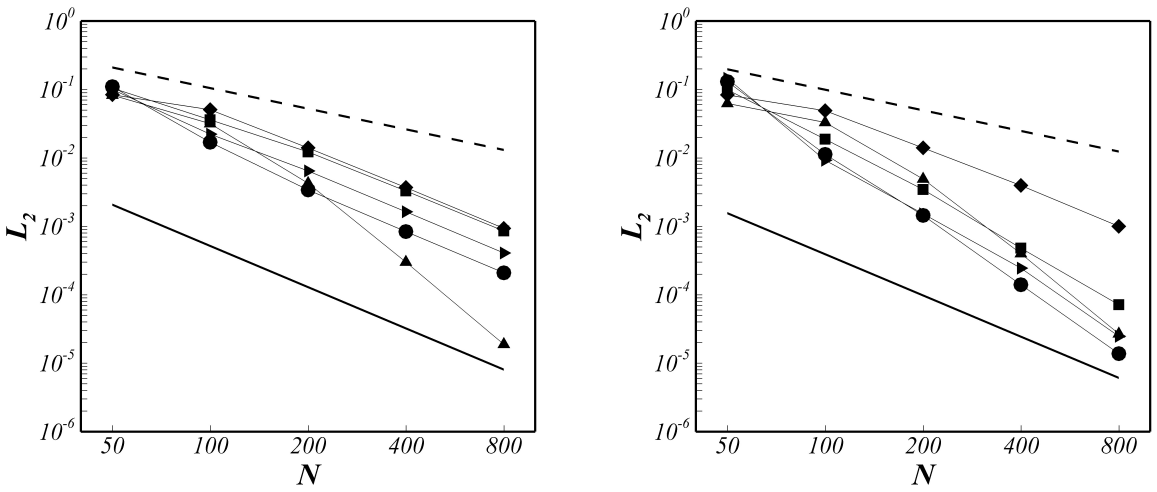

Figure 6.5: Evolution in time of the L_2 norm, $s = 10$. Single cycle (left), Two cycles (right). ■: u, ▲: v, ♦: p, ●: c, ►:ρ. The solid line stands for the second order decay, and the dashed line stands for first order decay.

Although not fully physically consistent - since the MMS is more a mathematical exercise rather than a real attempt of reproducing a real life experiment or physical problem

- the procedure of verification allows to gain more insights into the capabilities and limitations of a numerical code devoted to simulate complex flows, such as those of interest of the present thesis. Moreover, since large eddy simulations of turbulent reactive flows is one of the ultimate objectives of the present work, one of the required characteristics desirable of a numerical code suitable to that, which is a convergence rate at least equals to two, is verified. Thus, it allows us to proceed with other requirements, such as the prescription of correct and realistic boundary conditions.

CHAPTER VII

TURBULENT INLET CONDITIONS

It is well known that a subject of great importance in the numerical simulation of fluid flows is the prescription of correct and realistic boundary conditions, specifically for the inflow and outflow. For the latter, it appears that the use of a buffer zone (BODONY, 2006) or an advective boundary condition (ORLANSKI, 1976), or even a combination of both may adequately describe several flow conditions of practical interest. More elaborated boundary conditions can be used to avoid reflection of pressure waves, see Poinsot and Lele (1992). The specification of the inflow boundary conditions can be more problematic. Most flows encountered in real applications are spatially developing turbulent flows. Hence, they pose a great challenge for numerical simulation approaches due to the need to prescribe time-dependent turbulent inflow data at the upstream boundary. For steady RANS simulations, simple analytical or experimental profiles for the mean velocities and turbulent variables are usually retained. For LES or DNS simulations however, where the flow at the inlet is turbulent, the inflow data should consist of an unsteady fluctuating velocity signal representative of the turbulence field (even residual) at the inlet.

A basic technique to generate such a turbulent inflow data is to take a mean velocity profile with a superimposed random fluctuations. The major drawback of such a methodology is that the inflow data generated do not exhibit spatial and/or temporal correlations. The energy generated is also uniformly spread over all wave numbers and, due to a lack of

large scale energy-containing structures, the “turbulence” is quickly dissipated (JARRIN et al., 2009).

In principle, it may be possible to predict turbulence via a LES technique by starting from a quiescent flow or with the mean flow values of velocities obtained from RANS simulations. Unfortunately, a very long time is required for a turbulent flow to develop spatially and temporally (SMIRNOV; SHI; CELIK, 2001). Ideally, the simulation of the upstream flow entering a computational domain would provide realistic inlet conditions to the main simulation. However, due to the computational cost, the domain cannot be extended upstream indefinitely, and so approximate turbulent inlet conditions must be specified.

There are several ways to remedy this situation, however, the existing methods described in the literature tend to fall in two basic categories: *recycling methods*, in which some sort of turbulent flow is pre-computed, prior to the main calculation, and introduced in the domain inlet, and *synthetic turbulence methods*, in which some form of random fluctuation is generated and combined with the mean flow at the inlet.

This chapter is organized as follows: first a brief description of recycling methods is provided. Further, synthetic turbulence generators are focused, and the two methods retained in the present work are detailed, the method proposed by Klein, Sadiki and Janicka (2003) and the *Random Flow Generator - RFG*, proposed in Smirnov, Shi and Celik (2001). As part of the process of implementation and verification of both methods, an assessment of the routines written to generate the inflow data is made. The main desired characteristics are the capability of generating a turbulent signal whose energy spectra is similar to the one associated with a fully developed turbulent flow spectra, and the capability of reproducing a given stress tensor. The latter means that the inflow data generator should be able of reproducing an anisotropic turbulent flow at the inlet.
Concerning the application of the implemented methods in simulations of turbulent flows, in the final part of the present chapter, the results of a simulation of a high speed non-reactive and reactive mixing layers experimented by Moreau and Boutier (1977) and Magre et al.

(1988) are presented.

7.1 Recycling methods

The most accurate method to specify turbulent fluctuations for either LES or DNS would be to run a precursor simulation which has the purpose to provide the main simulation with accurate boundary conditions. However, such a procedure can be retained only when the turbulence at the inlet can be regarded as fully developed or spatially developing boundary layer, and therefore lacks generality. In this case periodic boundary conditions in the mean flow direction can be applied to the precursor simulation. Instantaneous velocity fluctuations in a plane at a fixed streamwise location are extracted from the precursor simulation and prescribed at the inlet of the main simulation at each time step.

In general, the flow in the precursor simulations is initiated with a mean velocity profile perturbed with a few unstable Fourier modes. As mentioned above, periodic boundary conditions can only be used to generate inflow conditions for homogeneous flows in the streamwise direction, which restricts their applications to simple fully developed flows.
A more flexible technique to generate inlet conditions, also based on the procedure of recycling the velocities in a plane located several boundary layer thicknesses downstream of the inlet, is proposed by Lund (1998). In this case, the velocity field at the re-scaling station, (Fig. 7.1), is decomposed in mean and fluctuating parts; scaling is applied to the mean and to the fluctuating parts in the inner and outer layers separately to account for the different similarity laws that govern these two regions. The re-scaled velocity is then finally re-introduced as a boundary condition at the inlet of the computational domain. The use of such a methodology results in a spatially evolving boundary layer simulation that is capable of generating its own inflow data.

Bodony (2006) noted that the method introduced by Lund, i.e., random uncorrelated fluctuations superposing a mean velocity profile, is very sensitive to the initialization of the flow field. Bodony (2006) also states that the generation of fully developed turbulence was not

obtained and hence, proposed a more robust variant of the original method of Lund, where the flow field is initialized using synthetic turbulence with a prescribed energy spectrum and shear stress profile.

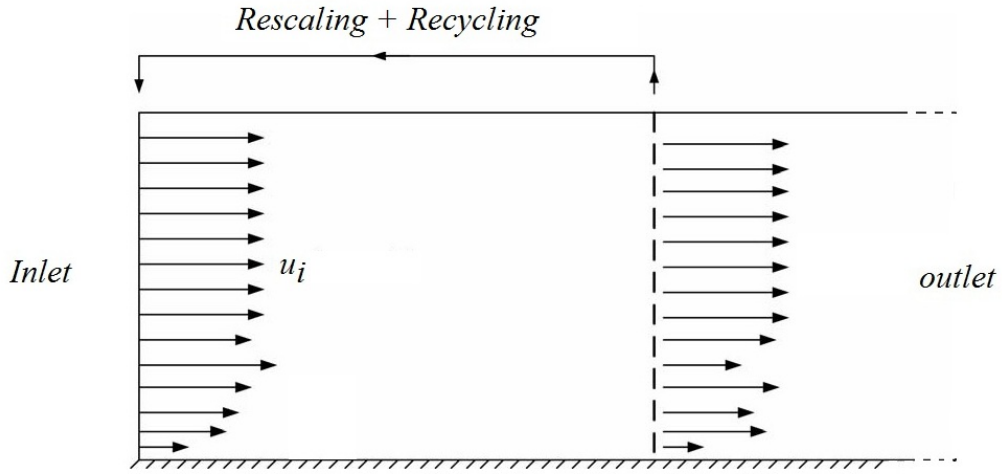

Figure 7.1: Sketch of the rescaling/recycling method of Lund et al. (1998) (LUND, 1998) to generate inlet conditions for a zero pressure gradient boundary layer.

Li, Balaras and Piomelli (2000) propose a procedure to reduce the storage requirement as well as the computational cost associated to a precursor simulation prior to the main simulation. A spatially developing turbulent mixing layer, originating from the mixing of a low and high-speed boundary layer at the end of a splitter plate is simulated in the LES context. Instead of running the precursor boundary layer simulations with the mixing layer simulation, only a time series of instantaneous velocity planes with duration approximately equal to the integral time scale of the flow is extracted from the boundary layer simulation. This signal is converted into a periodic one using a classic windowing technique, see (LI; BALARAS; PIOMELLI, 2000), and is re-used as many times as required to obtain converged statistics in the main simulation. This is beneficial both from computational and storage points of view, since the precursor simulation is run only over a short duration and the data used to generate the inflow data correspond only to a few integral time scales of the flow. In the case of the mixing layer, the periodicity involved by the inflow decays rapidly in about 25% of the domain. However, Li, Balaras and Piomelli (2000) reported that the resort to this procedure for wall-bounded flows, where destabilizing effects are relatively weak, might

require a longer transition region to weaken the periodicity involved in the inflow hence interfering in it with low-frequency flow dynamics.

7.2 Synthetic turbulence generators

Methods which do not rely on a precursor simulation or re-scaling of a database obtained from a precursor simulation synthesize inflow conditions using some sort of stochastic procedure. These stochastic procedures make use of random number generators to construct a random velocity signal similar to those obtained in turbulent flows. This is possible based on the assumption that a turbulent flow can be approximated by reproducing a set of low order statistics, such as mean velocity, turbulent kinetic energy, Reynolds stresses, two-point and two-time correlations. However, it is important to emphasize that the synthesized turbulence represents a crude approximation to real turbulence only. From a statistical point of view, the crucial quantities, such as the terms in the Reynolds stresses balance (the dissipation rate, the turbulent transport or the pressure-strain term) are usually not well reproduced. Additionally, the synthesized turbulence might have a structure that differs from the one of the real flow (JARRIN et al., 2009), and, as a result, the dynamics of the turbulent eddies are not accurately reproduced, and the synthesized flow may undergo the transition to turbulence.

7.2.1 White noise based synthetic turbulence generators

The most straightforward approach to generate synthetic fluctuations is to generate a set of independent random numbers $\mathcal{R}$ between 0 and 1 which once multiplied by a factor $\mathcal{C}_{\mathcal{R}}$, can "mimic" the turbulence intensity at the inlet, e.g. 10% of the mean inflow velocity,

$$u_i = \tilde{u}_i + \tilde{u}_i \mathcal{C}_{\mathcal{R}} \mathcal{R}. \tag{7.1}$$

If the turbulent kinetic energy k is available, it is possible to re-scale a random signal $\mathcal{R}_{u,i}$ which has a zero mean and unity variance, in such a manner that the fluctuations have

the correct turbulent kinetic energy k; which, when added to the mean velocity $\tilde{u}_i$, yields:

$$u_i = \tilde{u}_i + \mathcal{R}_{u,i}\sqrt{\frac{2}{3}k}, \tag{7.2}$$

where the $\mathcal{R}_{u,i}$ is taken from independent random variables for each velocity component at each time and point of the grid at the inlet. This procedure generates a random signal capable of reproducing mean velocity and the turbulent kinetic energy. However, the signal generated presents no two-point nor two-time cross-correlations. If the Reynolds stresses tensor (R_{ij}) is available, Lund (1998) shows that it is possible to apply a transformation (a_{ij}), based on the Cholesky decomposition, that will reconstruct correlated velocity components.

$$u_i = \tilde{u}_i + \mathcal{R}_{u,i}a_{ij}, \tag{7.3}$$

where (a_{ij}) is

$$a_{ij} = \begin{pmatrix} \sqrt{R_{11}} & 0 & 0 \\ R_{21}/a_{11} & \sqrt{R_{22} - a_{21}^2} & 0 \\ R_{31}/a_{11} & (R_{32} - a_{21}a_{31})/a_{22} & \sqrt{R_{33} - a_{31}^2 - a_{32}^2} \end{pmatrix}. \tag{7.4}$$

This procedure allows the basic random procedure to reproduce the target cross-correlations (R_{ij}) between velocity components i and j.

Although the methods presented above are capable of reproducing characteristics such as the anisotropy present in turbulent flows, they still exhibit no correlations either in time or in space. Therefore, these random fluctuations have energy uniformly spread over all wave numbers and, as stated before, the energy is quickly dissipated.

A more valuable approach for generating synthetic turbulence involves creating entirely random number data which can then be processed using digital filters, so that the data presents desired statistical properties, such as spatial and temporal correlations (KLEIN; SADIKI; JANICKA, 2003; KLEIN, 2003; LUND, 1998). In order to generate anisotropic turbulence, further transformations can be applied to the data in order to reproduce, for

instance, a specified Reynolds stress tensor.

7.2.2 Digital filters based synthetic turbulence generator

Klein, Sadiki and Janicka (2003) proposed a digital filtering procedure to remedy the lack of large-scale dominance in the inflow data generated through a random method. In one dimension the velocity signal $u'(j)$ at a point j is defined by a convolution (or a digital linear non-recursive filtering) as.

$$u'(j) = \sum_{k=-N}^{N} b_k \mathcal{R}_{j+k}, \tag{7.5}$$

where $\mathcal{R}_{j+k}$ is a series of random data generated at point $(j+k)$ with $\overline{\mathcal{R}_m} = 0$, $\overline{\mathcal{R}_m \mathcal{R}_m} = 1$ and b_k are the filter coefficients. N is connected to the support of the filter. The relation between the filter coefficients and the two-point velocity correlation function is given by:

$$\frac{\overline{u'(j)u'(j+m)}}{\overline{u'(j)u'(j)}} = \frac{\sum_{k=-N+m}^{N} b_k b_{k-m}}{\sum_{k=-N+m}^{N} b_k^2}. \tag{7.6}$$

This procedure is extended to the time-dependent generation of synthetic velocity field on a plane (Oyz) by generating a three-dimensional random field $\mathcal{R}_m(i,j,k)$ for each velocity component m. The indices i, j, and k represent the direction x (or time t by the Taylor hypothesis), the direction y and the direction z, respectively. A three-dimensional filter b_{ijk} is obtained by the convolution of three one-dimensional filters:

$$b_{ijk} = b_i b_j b_k. \tag{7.7}$$

This is used to filter the random data $\mathcal{R}_m(i,j,k)$ in the three directions x, y and z,

$$U_m(1,j,k) = \sum_{i'=-N_x}^{N_x} \sum_{j'=-N_y}^{N_y} \sum_{k'=-N_z}^{N_z} b(i',j',k') \mathcal{R}_m(i', j+j', k+k'). \tag{7.8}$$

In order to generate fluctuations that reproduce exactly the targeted two-point correlations $\overline{u'(j)u'(j+m)}$, the filter coefficients b_k should be computed by inverting Eq. (7.6). Since the two-point autocorrelation tensor is seldom available, Klein, Sadiki and Janicka

(2003) assumed a Gaussian shape depending on one single parameter, the length scale $L = n\Delta x$. The coefficients can then be computed analytically, without inverting Eq. (7.6),

$$b_k \approx \frac{\tilde{b}_k}{\left(\sum_{j=-N}^{N} \tilde{b}_j^2\right)}; \qquad \tilde{b}_k := \exp\left(-\frac{\pi k^2}{2n^2}\right). \tag{7.9}$$

Once the processed random signal is evaluated in Eq. (7.8), the final inflow velocity can be written as,

$$u_i = \tilde{u}_i + U_m(1, j, k)a_{ij}. \tag{7.10}$$

An algorithm for generating inflow data on-the-fly may be the one presented below. According to (KLEIN; SADIKI; JANICKA, 2003), it is also possible to generate a large volume of data, store it and convect it through the inflow plane by applying Taylor's hypothesis.

1. Choose for each direction corresponding to the inflow plane a length scale, $L_x = n_x\Delta x$, $L_y = n_y\Delta y$, $L_z = n_z\Delta z$, and a filter width according to condition $N_\alpha \geq 2n_\alpha, \alpha = x, y, z$.

2. Initialize and store three random fields $R_\alpha, \alpha = x, y, z$, of dimensions $[-N_x : N_x, -N_y + 1 : M_y + N_y, -N_z + 1 : M_z + N_z]$, where $M_y \times M_z$ denotes the dimensions of the computational grid at the inflow plane, i.e., at $x = 0$.

3. Calculate the filter coefficients b_{ijk} according to Eqs. (7.7) and (7.9).

4. Apply Eq. (7.8) for $j = 1, ..., M_y$, $k = 1, ..., M_z$, which yields two-dimensional arrays of spatially correlated data $U_\alpha, \alpha = x, y, z$.

5. Perform the coordinate transformation, tensor a_{ij}, resulting in $u_\alpha(j, k)$

6. Copy u_α to the inflow plane

7. Discard the first y, z plane of R_α and shift the whole data: $R_\alpha(i, j, k) = R_\alpha(i + 1, j, k)$. Fill the plane $R_\alpha(N_x, j, k)$ with new random numbers.

8. Repeat steps 4-7 for each time step.

It should be noted that the main parameter retained to evaluate the method of (KLEIN; SADIKI; JANICKA, 2003) is the choice of the length scales L_x, L_y and L_z, which

are directly connected to the size of the support of the filter N_x, N_y and N_z, and the dimensions, Δ_x, Δ_y and Δ_z of the control volume. Thus, given an experimental length scale, it is possible to reproduce such length scale by correctly choosing the size of the support of the filter and the dimensions of the control volumes. However, as will be shown in the sub-section (7.2.4.2), the size of the length scales and, consequently, the size of support of the filter strongly impacts on the computational cost of the method. Since a fixed computational grid is used here for the simulations carried-out to assess the different methods of generating turbulent inflow data, the parameters to the evaluation of the method of (KLEIN; SADIKI; JANICKA, 2003) are the sizes of support, N_x, N_y and N_z, only.

Tabor and Baba-Ahmadi (2010) state that, since turbulence is often analyzed by decomposition of a basis set of harmonic functions, i.e., Fourier analysis, the fluctuations can be more efficiently represented by resorting to a linear sum of sine and cosines functions, with the coefficients representing the energy contained in each mode.

7.2.3 Synthetic turbulence generators based on Fourier techniques

Kraichnan (1970) was the first to use a Fourier decomposition to generate a synthetic flow field. In Kraichnan's work, the flow domain is initialized with a three-dimensional homogeneous and isotropic synthetic velocity field to study the diffusion of a passive scalar. Since the velocity fluctuations are homogeneous in the three dimensions x, y and z, it can be decomposed in Fourier space,

$$\mathbf{u}'(\mathbf{x}) = \sum_{\mathbf{k}} \hat{\mathbf{u}}'_{\mathbf{k}} e^{-i\mathbf{k}.\mathbf{x}}, \tag{7.11}$$

where $\mathbf{k}$ is a three-dimensional wave number. Each complex Fourier coefficient $\hat{\mathbf{u}}'_{\mathbf{k}}$ defines an amplitude evaluated from a prescribed isotropic three-dimensional energy spectrum $E(|\mathbf{k}|)$ and a random phase $\theta_{\mathbf{k}}$, taken uniformly in the $[0, 2\pi]$ interval (ROGALLO, 1981). The synthesized velocity field is thus given by,

$$\mathbf{u}'(\mathbf{x}) = \sum_{\mathbf{k}} \sqrt{E(|\mathbf{k}|)} e^{-i(\mathbf{k}.\mathbf{x}+\theta_{\mathbf{k}})}. \tag{7.12}$$

Several adaptations of the Kraichnan's method were proposed throughout the years, among them, Lee, Lele and Moin (1992) proposed one that allowed for the application of the Kraichnan's method to spatially evolving turbulent flows. They showed that it is possible to generate a synthesized turbulent signal along time, in which the prescription a phase shift between different time steps allows to obtain a synthesized velocity field at the inlet with correct temporal correlations. One advantage of the method of Lee, Lele and Moin (1992) is that the generation of the turbulent signal can be performed by using a *Fast Fourier Transform - FFT* algorithm, which is computationally very efficient.

The capability for generating an anisotropic random signal was introduced by Le, Moin and Kim (1997). Based on the method of (LEE; LELE; MOIN, 1992), an isotropic turbulent synthesized signal is generated and then it is re-scaled using Eq. (7.4). In this way the reconstructed fluctuations match a prescribed Reynolds stress tensor. If one is interested in initializing the whole computational domain with the procedure proposed by Le, Moin and Kim (1997), the method has some drawbacks, since the method of (LEE; LELE; MOIN, 1992) is based on direct and inverse transforms using a FFT algorithm, therefore, its application in non-uniform grids is only possible in the inlet plane, which considerably reduces its interest for practical applications.

Smirnov, Shi and Celik (2001) proposed some modifications of the original method of (LE; MOIN; KIM, 1997) in such a manner that it would be possible to obtain a turbulent velocity field by requiring only statistical information. The method proposed by Smirnov, Shi and Celik (2001) is capable of synthesizing non-homogeneous turbulence in a general framework. It relies on Fourier decomposition, with Fourier coefficients computed from spectral data obtained at different locations across the flow based on local turbulent time and length scales (JARRIN et al., 2009). The method presented by (SMIRNOV; SHI; CELIK, 2001), called henceforth *Random Flow Generation - RFG* method, is different from the method originally proposed in (LEE; LELE; MOIN, 1992) since it does not use Fourier transforms, being based on scaling and coordinate transformation operations only, which, in non-uniform grids, are much more efficient than the original method of Lee, Lele and Moin (1992).

The RFG computational routines retained in the present work were developed by (SMIRNOV, 2004), and incorporated in the numerical code developed during the course of this thesis. In the following a brief description of the procedure of generating the turbulent inflow data is given. According to the Smirnov, Shi and Celik (2001) method, a transient flow field in a three-dimensional domain, $[v_i(x_j,t)]_{i,j=1,2,3}$ can be generated from,

$$v_i(x_j,t) = \sqrt{\frac{2}{N}} \sum_{n=1}^{N} \left[p_i^n \cos(\tilde{k}_j^n \tilde{x}_j + \omega_n \tilde{t}) + q_i^n \sin(\tilde{k}_j^n \tilde{x}_j + \omega^n \tilde{t}) \right], \tag{7.13}$$

where the following non-dimensional quantities have been introduced,

$$\tilde{x}_j = \frac{x_j}{l_t};\;\; \tilde{t} = \frac{t}{\tau_t};\;\; c = \frac{l_t}{\tau_t};\;\; \tilde{k}_j^n \tilde{x}_j = k_j^n \tilde{x}_j \frac{c}{c_{(j)}}, \tag{7.14}$$

where,

$$p_i^n = \varepsilon_{ijm} \zeta_i^n k_m^n;\;\; q_i^n = \varepsilon_{ijm} \xi_i^n k_m^n \tag{7.15}$$

with,

$$\zeta_i^n, \xi_i^n, \omega_n \in N(0,1),\;\; k_i^n \in N(0,1/2). \tag{7.16}$$

In the non-dimensional expressions, l_t and τ_t are the length and time scales of turbulence, respectively. ε_{ijk} is the permutation tensor used in the vector product operation, $c_i (i = 1, 21, 3)$[1] are the fluctuating velocity components u_i', in a new system of coordinates, which is obtained after the application of the transformation tensor a_{ij}. $N(M,\sigma)$ is a normal distribution with mean value M and standard deviation σ. The numbers k_j^n, ω^n represent a sample of n wave-number vectors and frequencies of the modeled turbulence spectrum:

$$E(k) = 16 \frac{2}{\pi}^{1/2} k^4 \exp(-2k^2). \tag{7.17}$$

[1] In the description of the RFG method, according to the nomenclature retained in (SMIRNOV; SHI; CELIK, 2001), repeated subindexes imply summation, whereas parentheses around indexes preclude summation

The final form of the flow field generated is obtained by the operations of scaling and orthogonal transformation of the flow field v_i,

$$u_i = a_{ij} w_j, \tag{7.18}$$

where $w_j = c_{(j)} v_{(j)}$. It is important to note that the tensor a_{ij} is such that,

$$a_{mi} a_{nj} R_{ij} = \delta_{mn} c^2_{(n)}, \tag{7.19}$$

$$a_{ik} a_{kj} = \delta_{ij}, \tag{7.20}$$

where R_{ij} is a prescribed velocity correlation tensor, e.g., the Reynolds stress tensor.

It is worth noting that the above procedure requires specifying the characteristic integral length and time scales of turbulence, and the correlation tensor R_{ij} of the flow intended to be simulated. These quantities can be obtained from either RANS simulations or experimental data.

7.2.4 Assessment of the capability for reproducing prescribed Reynolds stress tensors

As stressed in the beginning of the present chapter, it is important to verify that the procedures retained for generating the turbulent inflow data are capable of reproducing a random signal in which the energy spectra distribution correspond to more energetic scales in the smallest wave numbers, and to less energetic scales in the higher wave numbers. Moreover, the capability of reproducing a prescribed Reynolds stress tensor is paramount.

The methods developed by Klein, Sadiki and Janicka (2003) and Smirnov, Shi and Celik (2001) have adjustment factors that directly impact both the accuracy in reproducing the characteristics of the flows of interest and the associated computational cost. For the former, this factor is the size of the support retained for the filter, and for the latter, i.e., method of Smirnov, Shi and Celik (2001) the factor is the number of Fourier modes retained in Eq. (7.13).

In order to assess the influence of such parameters, a numerical code is developed. Given a set of initial conditions, e.g., mean velocity distribution, size and number of control volumes of the computational domain at the inlet, Reynolds stress tensor, characteristic length and time scales of a flow, the algorithm applies the initial conditions to the turbulent inflow routines until it is possible to recover the statistics of the variables of interest by regular ways, i.e., by an averaging procedure of the velocity for instance. For all the cases presented in this subsection, such number of iterations was set to 5000. Even if the computational routines available in (SMIRNOV, 2004) offer the possibility of generating both isotropic and anisotropic inflow data, in the present work, due to a lower computational cost, an isotropic signal is generated, and then Eq. (7.4) is applied to the signal in order to obtain the desired level of anisotropy. It is important to point out that the overall flow solution is not involved at the moment. The results presented here are obtained only from the application of an averaging process to the signal generated using the different methods described above.

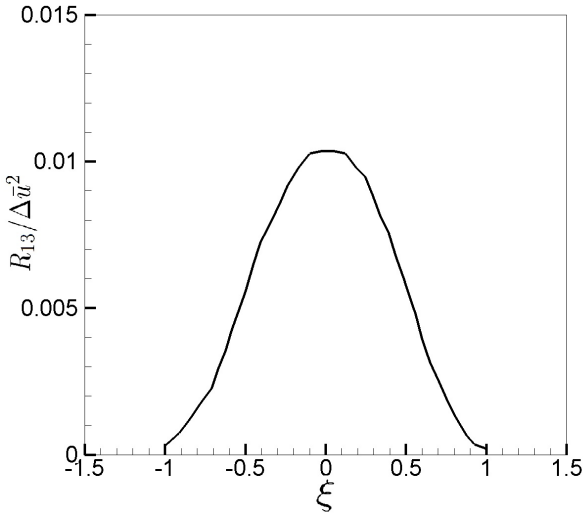

Figure 7.2: R_{13} component of the Reynolds stress tensor as a function of the non-dimensional width of the mixing layer ξ, (BRUCKER; SARKAR, 2007).

The experimental stress tensor profile, mean velocity and computational domain characteristics retained for testing the turbulent inflow generators are based on the early work conducted by Moreau and Boutier (1977). The experimental test section presented in details

in (MOREAU; BOUTIER, 1977) contains a turbulent high speed mixing layer within a combustion chamber, where a premixed air-methane flow is ignited and stabilized by a parallel flow of combustion products. Profiles of mean velocity, turbulence intensity and velocity fluctuations are given for both reactive and non-reactive flows.

In the work of Moreau and Boutier (1977), only the R_{11} component of the Reynolds stress tensor is given. Andrade (2009), when simulating the same experimental configuration, assumed that the R_{22} and R_{33} components are approximately half of the R_{11} component. The components $R_{12} = R_{21}$ and $R_{32} = R_{23}$ are taken as zero. Since no information is given about the cross component R_{13}, and such component plays a crucial role in the shear layer spreading rate, it is important to satisfactorily approximate such a quantity. Brucker and Sarkar (2007) provide a relation in which the non-dimensional width of the shear layer, $\xi = h/\delta_m$, with h varying between $[-\delta_m < h < \delta_m]$, is correlated to the non-dimensional quantity $R_{13}/\Delta\bar{u}^2$ in self-similar mixing layers. Once defined the velocity difference between two streams, $\Delta\bar{u}^2$, and the width of the mixing layer, the component $R_{13} = R_{31}$ can be evaluated from Fig. (7.2),

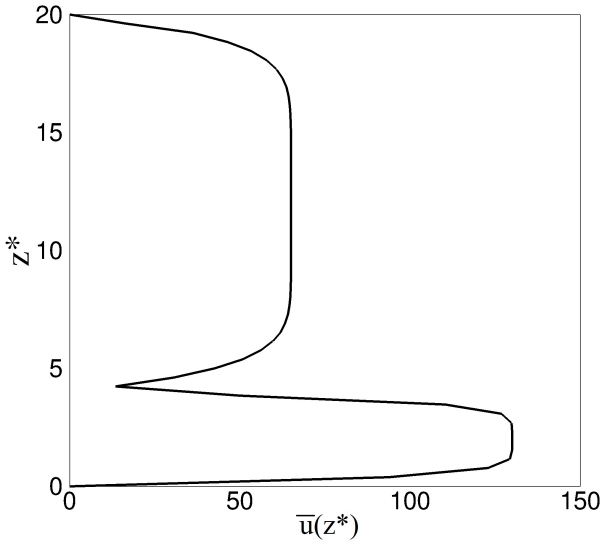

Figure 7.3: Mean velocity profile imposed. $z^* = z/\delta_m$, δ_m is the initial width of the mixing layer

The combustion chamber is a channel with dimensions 800 × 100 × 100 mm in the directions x, y and z respectively. The inlet is divided into two separated ducts by a splitter plate: the main duct where the fresh gases are injected at 65 m/s and an auxiliary duct for the hot gases, with mean velocity of 130 m/s. Since, for the present test, the variables of interest are evaluated only at the inlet plane, the two-dimensional grid is divided in 50 points in the y direction and 50 in z direction. The mean velocity profile used at the inlet is represented by a combination of two developed flows at different exit velocities. The analytical function adopted for generating the mean velocity profile as a function of the coordinate z, $\overline{u}(z)$, can be satisfactorily approximated through,

$$\overline{u}(z) = C_{in}\left[1 - \left(\frac{z - (a/2 + h)}{a/2}\right)^{\gamma_{in}}\right], \tag{7.21}$$

where C_{in} is the mean value of the velocity in the duct, a is the position of the bottom part of the duct in the z direction, h is the height of the duct, and γ_{in} is a constant that fix the thickness of the shear layer. The values of the above constants and the ducts dimensions of the corresponding experiment are given in Table (7.1). Such a combination of velocity profiles can be seen in Fig. (7.3), where the z axis is made non-dimensional using the initial width of the mixing layer, i.e, $z^* = z/\delta_m$.

Table 7.1: Constant values used for mean velocity profile.

Duct	C_{in} [m/s]	h [m]	a [m]	γ_{in}
Main duct	65	0.02	0.08	6.0
Auxiliary duct	130	0.00	0.02	8.0

7.2.4.1 White noise generator

The first method to be evaluated in the present work, and the simplest one, is the superimposition of a white noise over the mean velocity profile given by Eq. (7.21). In this case, a random signal with zero mean and unity variance is adjusted to imposed fluctuations representing 20% of the mean velocity profile determined by Eq. (7.21) in the x direction of the flow, i.e., the u-component of velocity. In the y and z directions, the fluctuations are set to 10% of the same mean profile of velocity. The fact that the energy is spread over

all the energy spectra, whatever the frequency of the fluctuation, contradicts the classical $-5/3$ behavior expected for fully developed turbulence. The energy spectra of a noise noise is illustrated in Fig. (7.4).

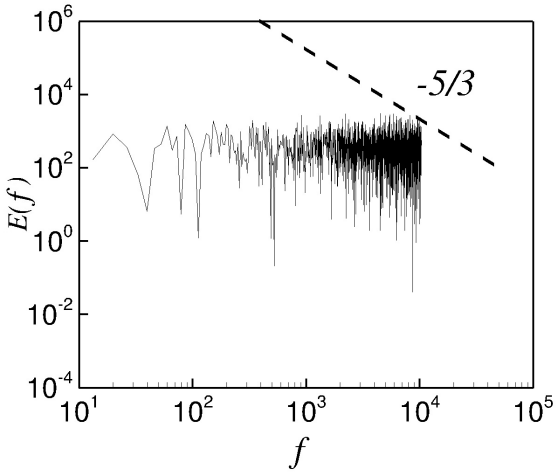

Figure 7.4: Energy spectra associated to a white noise.

As expected, the lack of any spatial or temporal correlations, added to the fact that the white noise considered is isotropic, leads to poor results when the experimental stress tensor is compared with the components of stress tensor evaluated from the averaging process of the inlet signal. Such a result is evidenced in Fig.(7.5). Therefore, it can be foreseen that the use of the white noise technique will lead to poor results when applied to the simulation of the mixing layer.

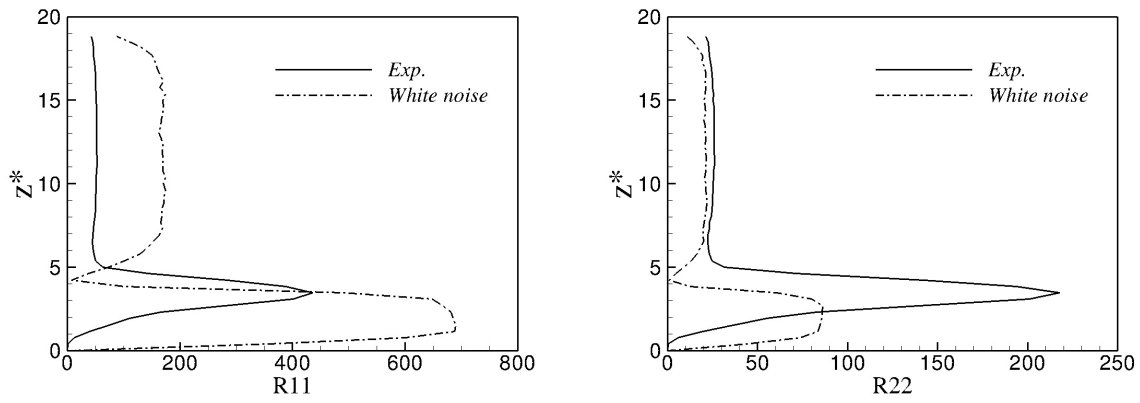

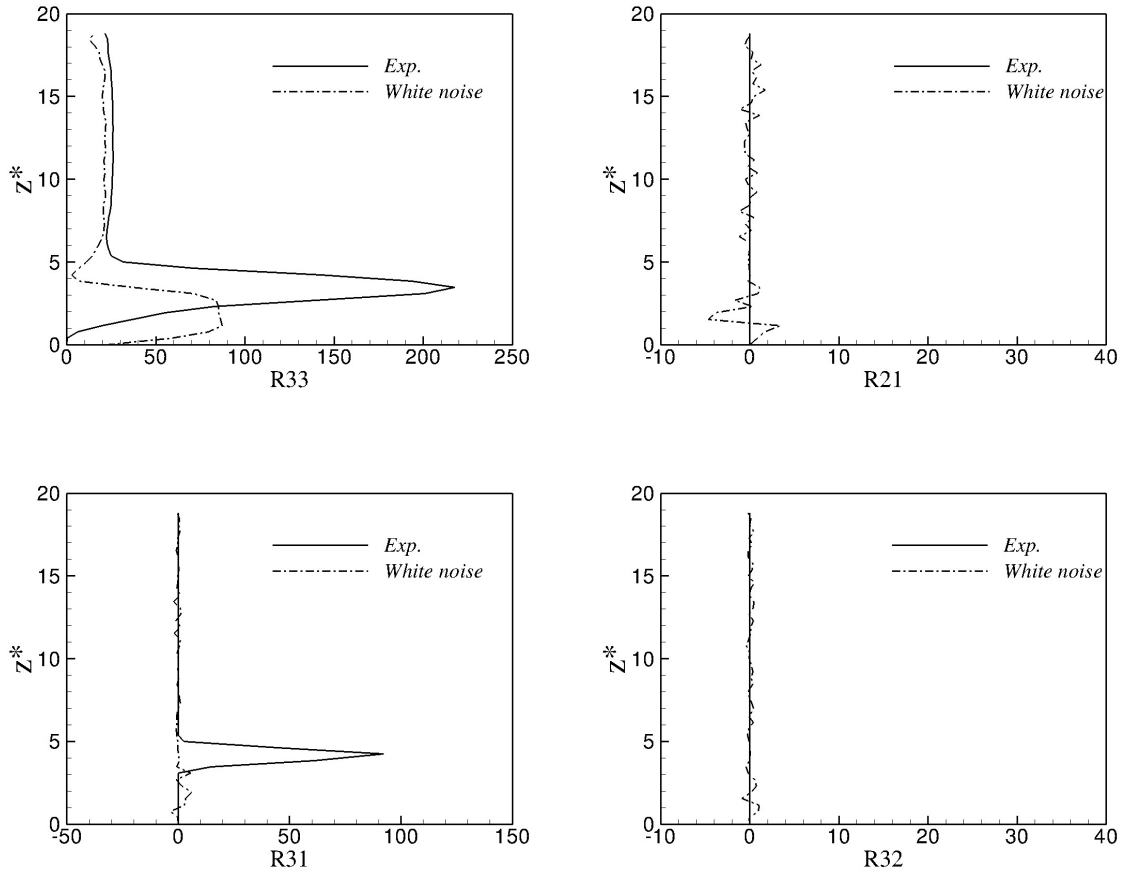

Figure 7.5: Stress tensor components evaluated from the superposition of white noise over the mean velocity profile.

7.2.4.2 The method of Klein, Sadiki and Janicka (2003)

Concerning now the method of Klein, Sadiki and Janicka (2003), there is a strong dependency on the size of the support of the filter, and once the support of the filter is directly connected to the number of grid points retained at the inlet, the computational cost associated to number of points in the support becomes an important issue. As can be seen in Fig. (7.6) as the size of the support of the filter grows, the energy spectra becomes more representative of a fully developed turbulent flow. For $N = 1$, for instance, the energy spectra exhibits little difference from a white noise spectra. The differences are more pronounced for sizes of support equal 5, 10 and 20. The last support dimension, i.e., 20, describes significantly well the energy cascade in a turbulent flow. As mentioned previously the section (7.2.2) it is important to keep in mind that, when the size of the support of

the filter changes, the turbulent length scale provided to the method of digital filtering also changes, thus, it is natural to obtain an energy spectra which is richer in structures.

Concerning the computational cost of the method of Klein, Sadiki and Janicka (2003), in the tests carried out to evaluate the sensitivity of the method with respect to number of points within the support of the filter, for $N = 1$, for instance, the code spent approximately one minute with a Intel (R) Xeon (TM) 3.00GHz CPU with 4 gigabytes of RAM memory to perform the 5000 iterations required to evaluate the statistics, whereas for $N = 20$, for the same number of iterations, in the same computer, approximately 14 hours and 30 minutes were necessary.

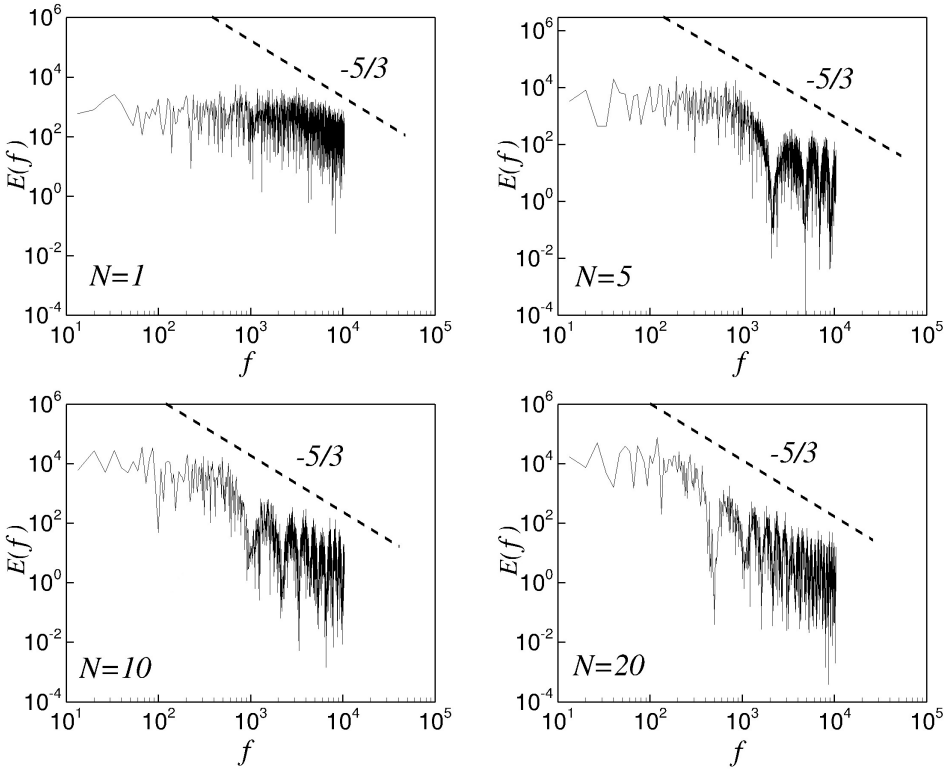

Figure 7.6: Comparison of the effects of size of the support (N) on the energy spectra in the method of Klein, Sadiki and Janicka (2003).

Such a disparity can be easily understood using a very simple example. For $N = 5$, a cubic box of dimensions $5 \times 5 \times 5$ is created for each point at the inlet. Since in the present configuration the inlet is composed by a grid of 50×50 points in y and z

directions respectively, the total number of points where the filtering process is performed is $50 \cdot 50 \cdot (5 \cdot 5 \cdot 5)$, or, $312,000$ points. For $N = 20$ this number is increased to 2^7 points, i.e., an increase of more than 60 orders of magnitude.

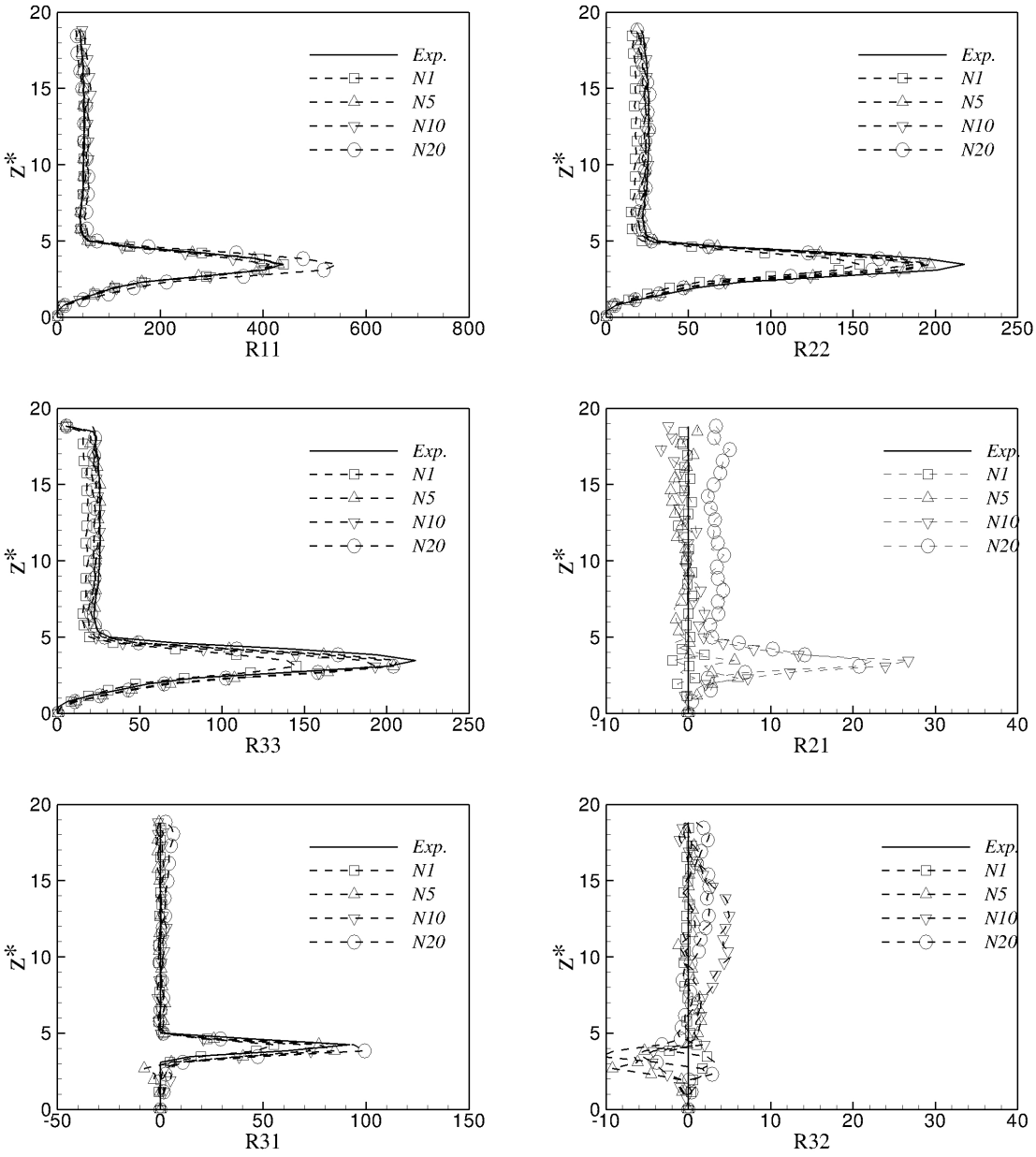

Figure 7.7: Stress tensor components evaluated from the method of Klein, Sadiki and Janicka (2003), for different sizes of filter support.

Concerning the capability of the method of Klein, Sadiki and Janicka (2003) in reproducing anisotropic stress tensors, it can be seen in Fig. (7.7) that the influence of the size of the support of the filter is less noteworthy than its effects evidenced previously in the energy

spectra. It is observed in such a figure that for a support of filter higher than 10 points, the gain in reproducing the stress tensor given has not shown great improvements. Based on the that, and considering the way that energy spectra alters its shape while increasing of the size of the filter support, in the present work a support size of 10 is suggested for the numerical simulation of the mixing layer.

7.2.4.3 The method of Smirnov, Shi and Celik (2001)

For the tests retained in the present section, the method proposed by Smirnov, Shi and Celik (2001) is found less sensitive to the number of Fourier modes retained both, in terms of capability of reproducing the prescribed stress tensor, and the shape of the turbulent spectra, as can be seen in Figs. (7.8) and (7.9), respectively.

It was mentioned in the introduction of the present chapter, when a decomposition of a turbulent flow is made in terms of Fourier modes, each mode can be understood as a particular turbulent scale. In Fig. (7.8), it is possible to note that even for a small number of Fourier number retained, there is a reasonable reproduction of the prescribed stress tensor. Above 500 Fourier modes the differences with respect to the experimental data become negligible.

Concerning the shape of energy spectra, it can be noted in Fig. (7.9) that, as the number of Fourier modes is increased, the energy spectra becomes more representative of the one associated to a high Reynolds number turbulent flows. Moreover, it is observed in Fig. (7.9) that little difference exist for a number of Fourier modes higher than $1,000$.

It is found that obtaining turbulent inflow data featuring representative energy spectra is computationally cheaper using the method of Smirnov, Shi and Celik (2001) than the method of Klein, Sadiki and Janicka (2003). For instance, the time spent to perform the 5000 iterations required by the RFG method, with $1,000$ Fourier modes for obtaining the statistics to be compared with the experimental data, was equivalent to the time consumed by the method of Klein, Sadiki and Janicka (2003), with a size of support $N = 5$, i.e.,

approximately five minutes in the same Intel (R) Xeon (TM) 3.00GHz CPU with 4 gigabytes of RAM memory.

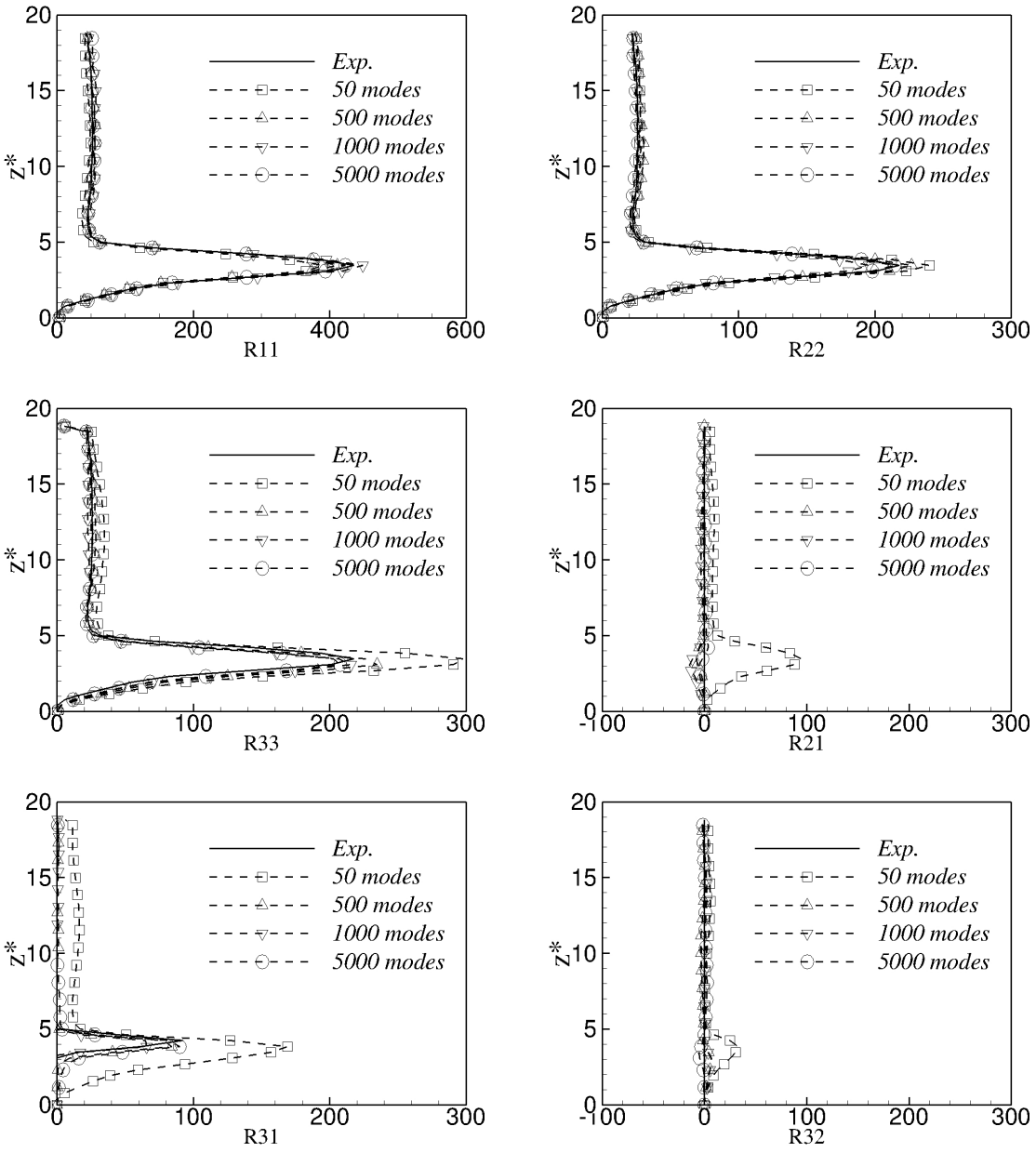

Figure 7.8: Stress tensor components evaluated using the method of Smirnov, Shi and Celik (2001), for different numbers of Fourier modes.

For the simulations of the experimental configuration studied by Moreau and Boutier (1977), the number of Fourier modes is set to $1,000$. In the next section, a comparison between the three methods of generation of turbulent inflow data in a three-dimensional simulations are provided.

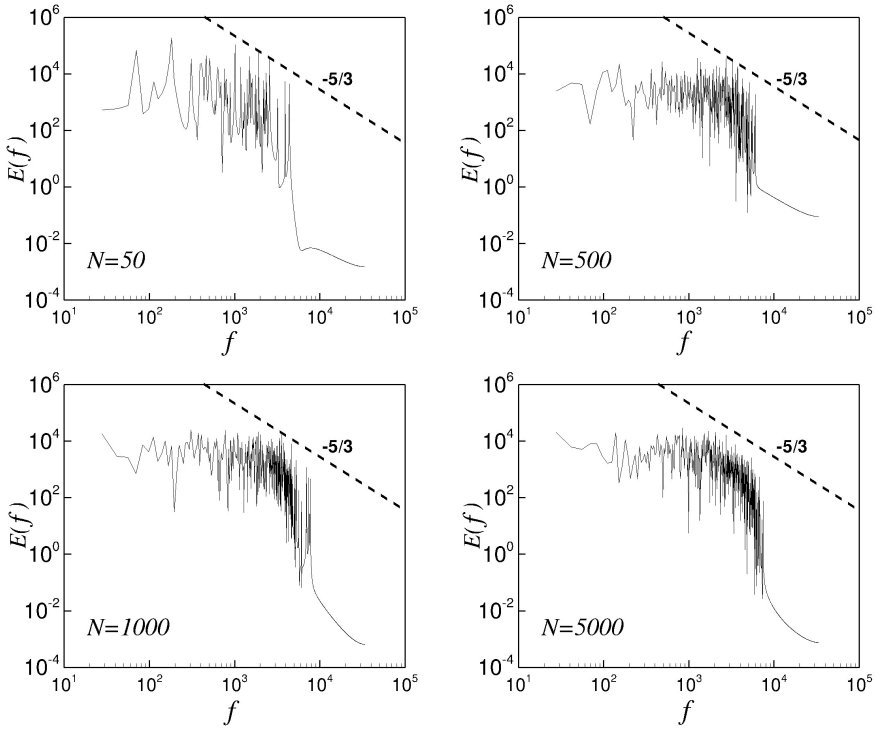

Figure 7.9: Comparison of the effects of number of Fourier modes in the energy spectra in the method of Smirnov, Shi and Celik (2001).

7.2.5 Non-reactive flow simulations

In order to assess the influence of the generation methods of inflow data retained, three-dimensional simulations of a high speed mixing layer are now performed. The obtained results are compared with the work of Moreau and Boutier (1977). The computational domain is a three-dimensional box with dimensions $(800 \times 100 \times 100)$ mm^3, discretized with a finite volume mesh of $320 \times 100 \times 100$ control volumes in the x, y and z directions, respectively. No-slip boundary conditions are imposed over the y and z directions. An advective boundary condition is used as outflow. The Smagorinsky constant is set to 0.18 (Eq. 3.24), and the Van-Driest damping function is used at the walls (Eq. 3.24). The Reynolds number, based on the initial width of the mixing layer, $\delta_m = 5$ mm, the mean velocity difference between the two flow streams $U_r = 97.5$ m/s and the value of the kinematic viscosity for air at 600 K is $Re = 3075$. The computational domain, as well as its dimensions in the directions x, y and z and a sketch of the u-component velocity profile are displayed in Fig.

(7.10).

For the simulation with white noise, a fluctuation level of 20% is imposed over the $\bar{u}$ mean component of velocity, whereas 10% fluctuations are set for the components in the y and z directions ($\bar{v}$ and $\bar{w}$, respectively). For the simulations with the method of Klein, Sadiki and Janicka (2003) the size of the support of the filter is set to 10 whereas $1,000$ Fourier modes were used for the simulations based on the method of Smirnov, Shi and Celik (2001). The mean velocity profile in given by Eq. (7.21). The Backward Difference Scheme is retained and the size of the time step is evaluated by (Eq. 4.1), with the constant C set to 0.5. The advective terms of the transport equations were discretized with the CDS approach. Since the numerical code developed has the capability of performing distributed computing, the computational domain was divided into 40 sub-domains.

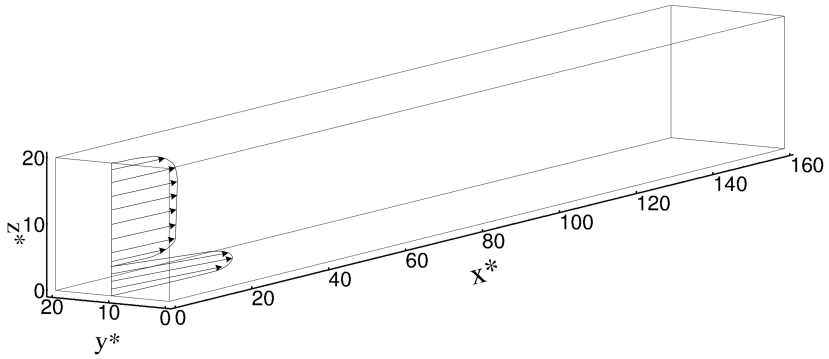

Figure 7.10: Computational domain used for the simulations of the non-reactive flows.

A first step of the analysis carried out is to verify the capability of the implemented methods of reproducing its respective energy spectra in a Navier-Stokes solver, i.e, the methods retained for the generation of turbulent inflow data should still provide a signal in which the energy spectra is representative of a fully developed turbulent flow. To verify that, a probe is positioned immediately downstream of the inlet in such a manner that it is kept at the first control volume in the x direction, $y^* = 10$ and $z^* = 4.6$. The results captured by the probe of the $u^* = u/U_r$-component velocity along time, $t^* = t^* U_r/\delta_m$, is shown in Fig. (7.11). The characteristic energy spectra, based on the velocity signals generated by the three different methods is shown in Fig. (7.12).

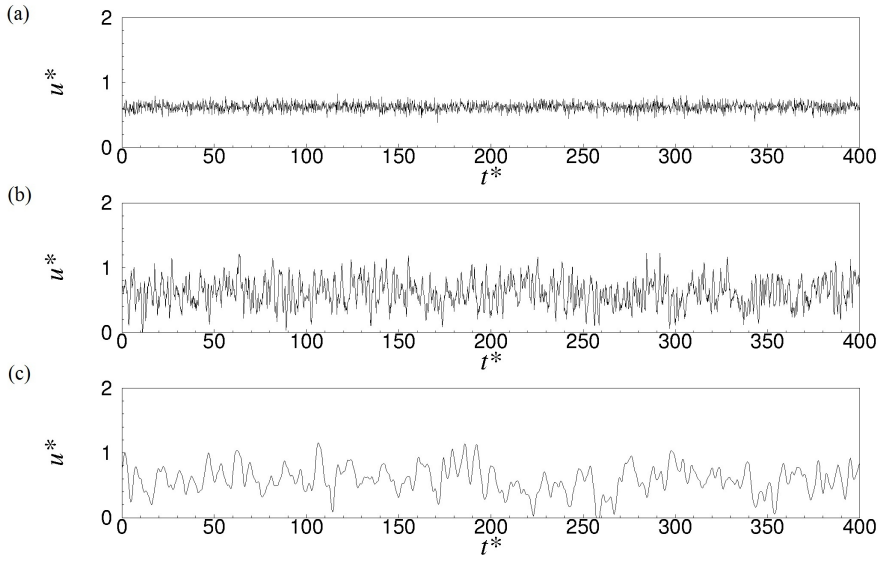

Figure 7.11: Temporal evolution of the u component of velocity immediately downstream of the flow inlet; (a) White noise, (b) method of Klein, Sadiki and Janicka (2003) and (c) method of Smirnov, Shi and Celik (2001).

In Fig. (7.11) the presence of high frequency structures appears to be more pronounced for the white noise, being less evidenced for the velocity signal evaluated from the method of Klein, Sadiki and Janicka (2003). That fact that in Fig. (7.11) - (c) there is almost no high frequencies is explained by the lack of energy observed at the small scales in the decaying part of the energy spectra.

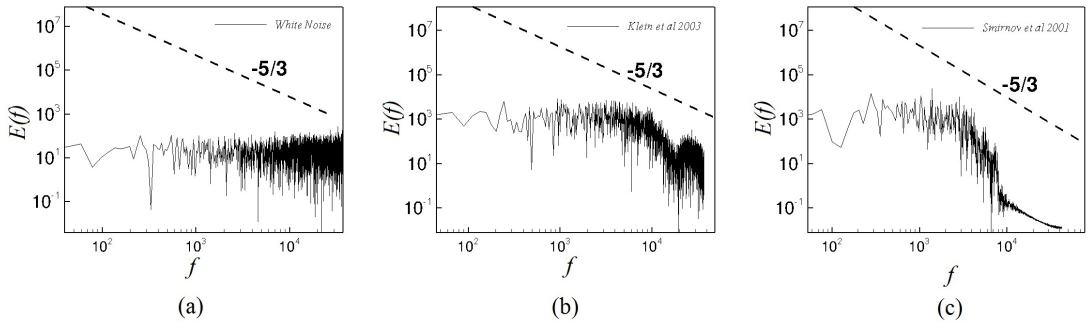

Figure 7.12: Turbulent spectra of a velocity probe for different methods of generation of turbulent inflow data; (a) White noise, (b) method of Klein, Sadiki and Janicka (2003) and (c) method of Smirnov, Shi and Celik (2001).

Fig. (7.13) shows a slice of the computational domain at $y^* = 10$, for the three different inflow generating methods. The field shown is the RMS of u', i.e., the square root of the component R_{11} of the Reynolds stress tensor. The statistics are obtained by time averaging of the filtered field over 4 flowthrough (residence) times, resulting in approximately $15,000$ iterations. It is worth recalling that since the numerical code developed adopts a variable time-step size, special care must be taken in the averaging process, considering always the size of the time step in the between the samples, see Eq. (4.47), section (4.4.2). It is noteworthy that the use of an adequate method of generation of turbulent inflow data drastically changes the flow field structure. In Fig. 7.13-(a) the values of $\sqrt{R_{11}}$ become significant only after half of the total length of the computational domain in the x direction, whereas for the methods of Klein, Sadiki and Janicka (2003) and Smirnov, Shi and Celik (2001), respectively the sub-figures (b) and (c) of Fig. 7.13, the flow resembles more to the one observed and discussed by Moreau and Boutier (1977). In this flow, due the high turbulent intensity in the incoming ducts that inject fresh and burnt gases into the combustion chamber, the turbulence at the inlet is fully developed.

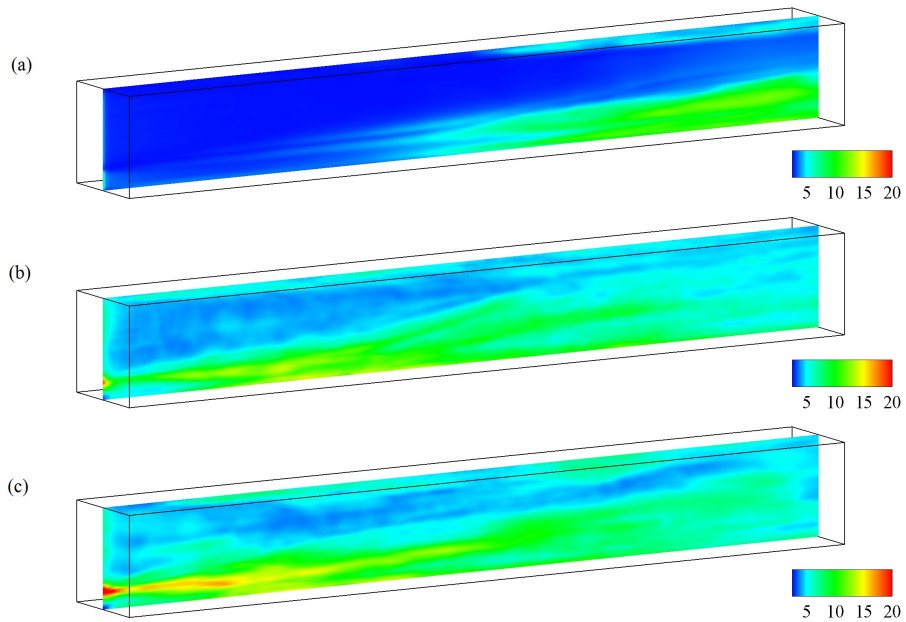

Figure 7.13: Fluctuations of $\sqrt{R_{11}}$ for the simulations carried-out with: (a) White noise, (b) method of Klein, Sadiki and Janicka (2003) and (c) method of Smirnov, Shi and Celik (2001).

The time-averaged filtered turbulent kinetic energy, evaluated from the trace of the Reynolds stress tensor, $(k = 0.5\delta_{ij}(\widetilde{\rho u_i'' u_i''}/\bar{\rho}) = 0.5(R_{11} + R_{22} + R_{33})$, is also compared, in Fig. (7.14), for the three methods retained to generate the inflow. Corroborating the behavior presented in Fig. 7.13, it is possible to verify that the turbulent kinetic energy for the methods of Klein, Sadiki and Janicka (2003) and Smirnov, Shi and Celik (2001) are also higher at the entrance of the computational domain. Again, although a transition to turbulence is observed when the white noise generator is used, practically all velocity fluctuations entering the computational domain are almost instantaneously dissipated close to the inlet boundary condition. The firsts coherent structures are observed only after the first half length of the domain, along the x direction.

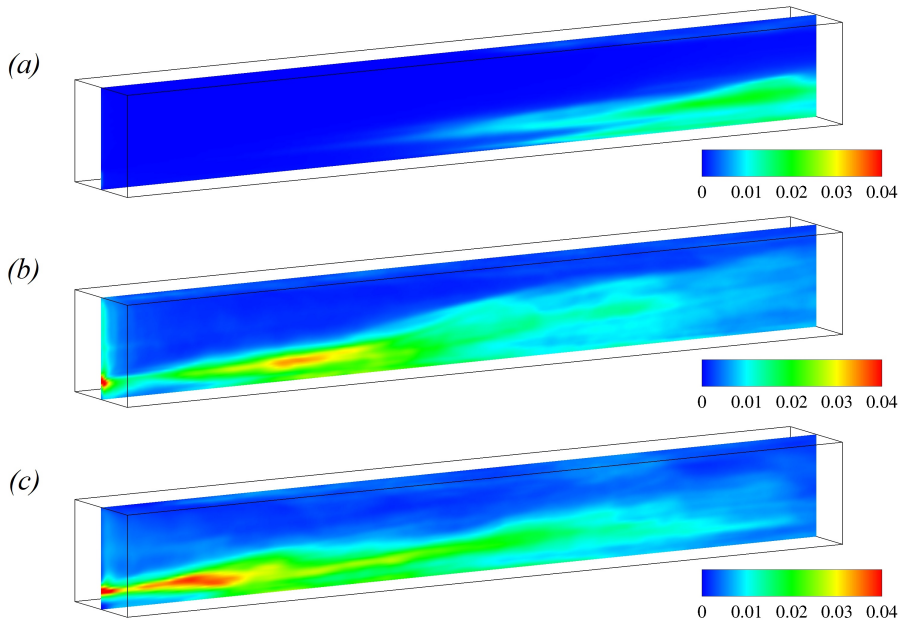

Figure 7.14: Turbulent kinetic energy, $k^* = k/U_r^2$, for the simulations carried-out with the method: (a) White noise, (b) , method of Klein, Sadiki and Janicka (2003) and (c) method of Smirnov, Shi and Celik (2001).

An instantaneous field of effective turbulent viscosity $\mu_{ef} = (\mu + \mu_{SGS})$, normalized by the molecular viscosity, $\mu_{ef}^* = \mu_{ef}/\mu$ is shown in Fig. (7.15) at $t^* = 586$. It is clearly shown in such a figure that the inflow turbulence is higher in sub-figures (b) and (c). It can thus be concluded, that, since the Smagorinsky model is employed, and such model relies on the evaluation of resolved strain rate to quantify the sub-grid viscosity, the values of strain rate

that enters the computational domain is also higher, when retaining the methods of Klein, Sadiki and Janicka (2003) and Smirnov, Shi and Celik (2001) than when the white noise is considered.

Figure (7.15) also provides an interesting illustration of the behavior of the Smagorinsky model. It is commonly agreed that the Smagorinsky model is highly dissipative, specially regarding the smallest turbulence structures. This is one of the reasons why the turbulence based on a white noise generator imposed at the inlet may be destroyed very rapidly, however, it can be seen in Fig. (7.15) - (a) that, provided that an adequate method is retained to generate the inflow turbulence, the largest scales introduced in the domain are not quickly dissipated, even with the use of the Smagorinsky model.

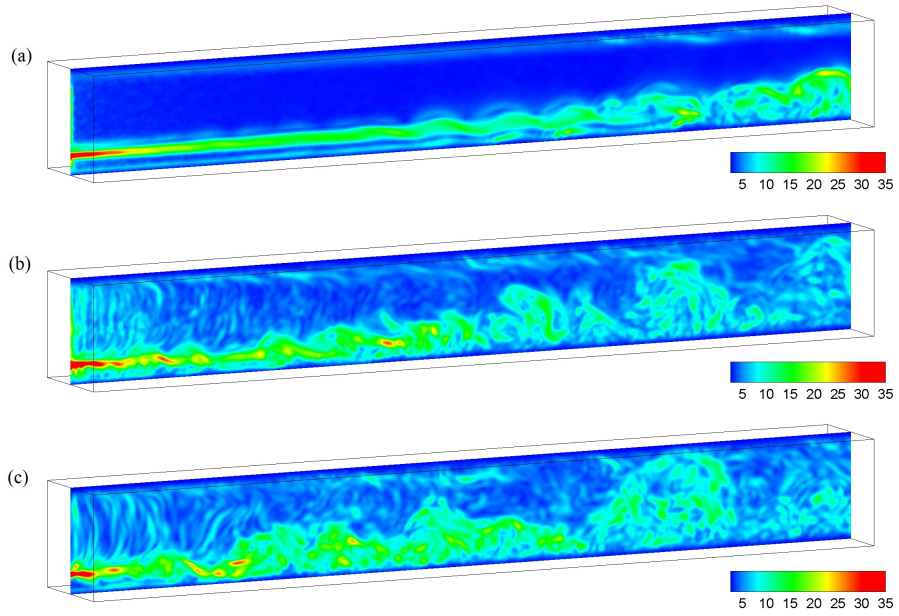

Figure 7.15: Snapshot of the normalized effective turbulent viscosity μ^*_{effec} at $t^* = 586$, for the simulations carried-out with the method: (a) White noise, (b) method of Klein, Sadiki and Janicka (2003) and (c) method of Smirnov, Shi and Celik (2001).

Instantaneous snapshots obtained from the three dimensional simulations of the flow described above are reported in Fig. (7.16). The property Q offers an interesting way to evidence the flow field coherent structures (JEONG; HUSSAIN, 1995). For a flow of uniform density, the corresponding quantity, i.e., the second invariant Q of the velocity-gradient tensor $\partial u_i/\partial x_j$, is related to the Laplacian of the pressure field, and positive iso-values

of Q are often used to characterize low pressure tubes that are generally associated with coherent structures. In Fig. (7.16) the isosurface of the property $Q = 2^6$ is displayed. The high value retained in this case results from the fact that the flow is a high velocity, high Reynolds number, confined flow. Moreover, it is noteworthy in Fig. (7.16), Kelvin-Helmholtz structures that are characteristic of the mixing layers dynamics can be recognized downstream of the computational domain inlet.

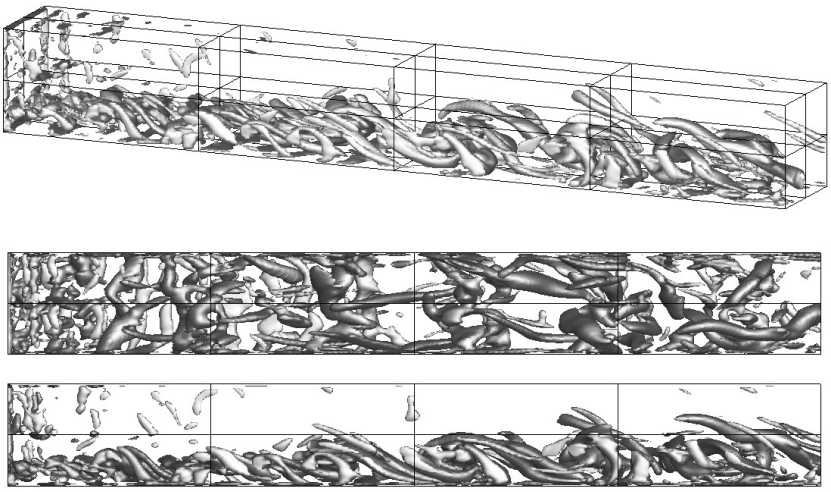

Figure 7.16: Perspective, top and lateral views of the isosurface of the second invariant of the velocity-gradient tensor $Q = 2^6$, at $t = 0.020$ s. The method of Klein, Sadiki and Janicka (2003) was used.

In order to quantify and validate the methods implemented, Fig. (7.17) shows comparisons for the average u-component of the velocity field at four locations along the computational domain, and $y^* = 10$. It can be noted in such a figure that all methods provide an acceptable agreement with experimental data concerning the mean velocity. However for the RMS of the velocity fluctuation the use of a adequate turbulent inflow generator becomes clear. It can be seen in Fig. (7.18) that the superposition of white noise over the mean velocity profile does not represent the experiment in at least in the first half of the computational domain along the x direction, which agrees with the work of Andrade (2009). The results obtained with the methods of Klein, Sadiki and Janicka (2003) and Smirnov, Shi and Celik (2001), however, display a good agrement with respect to experimental data, specially the latter.

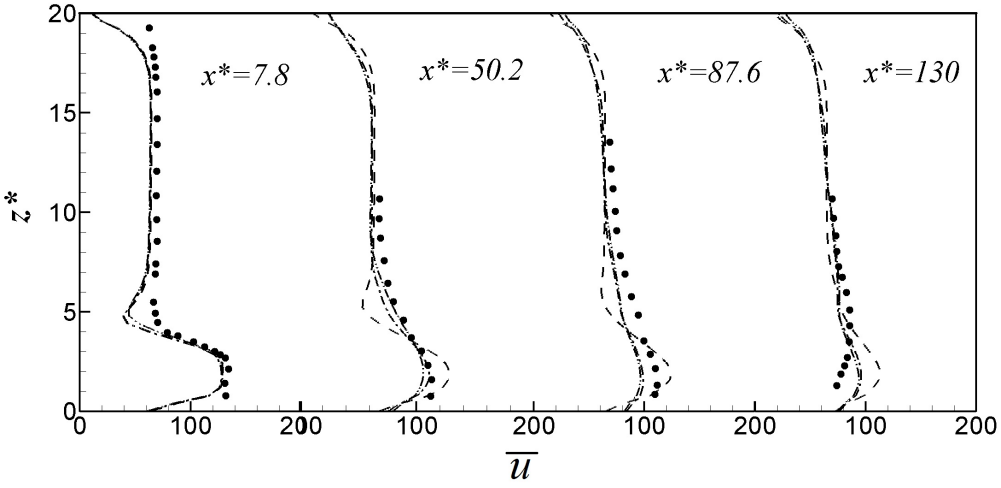

Figure 7.17: Mean longitudinal velocity profiles. (•): Moreau and Boutier (1977); method of Smirnov, Shi and Celik (2001) (- - -); method of Klein, Sadiki and Janicka (2003) ($-\cdot-$); white noise ($-\cdot\cdot-$).

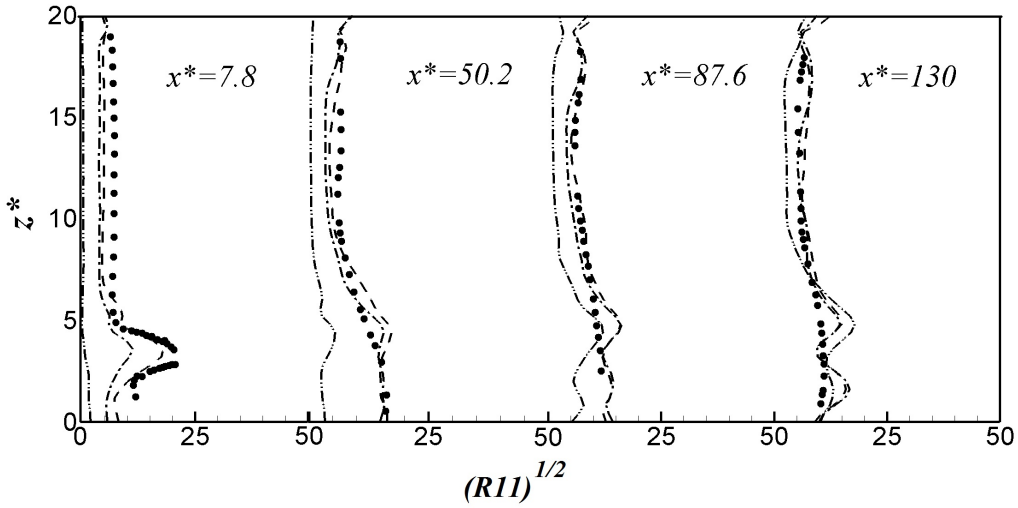

Figure 7.18: $\sqrt{R_{11}}$ stress tensor component. (•): Moreau and Boutier (1977); method of Smirnov, Shi and Celik (2001) (- - -); method of Klein, Sadiki and Janicka (2003) ($-\cdot-$); white noise ($-\cdot\cdot-$).

Although no experimental data on the turbulent kinetic energy is provided by Moreau and Boutier (1977), Fig. (7.19) shows that the different methods of generation of inflow turbulent data affects differently the turbulent kinetic energy throughout the computational

domain. The method of Smirnov, Shi and Celik (2001) provides the higher values of such quantity, while, as expected since the turbulence has to be practically generated from the inlet, the white noise procedure is associated with the lowest values.

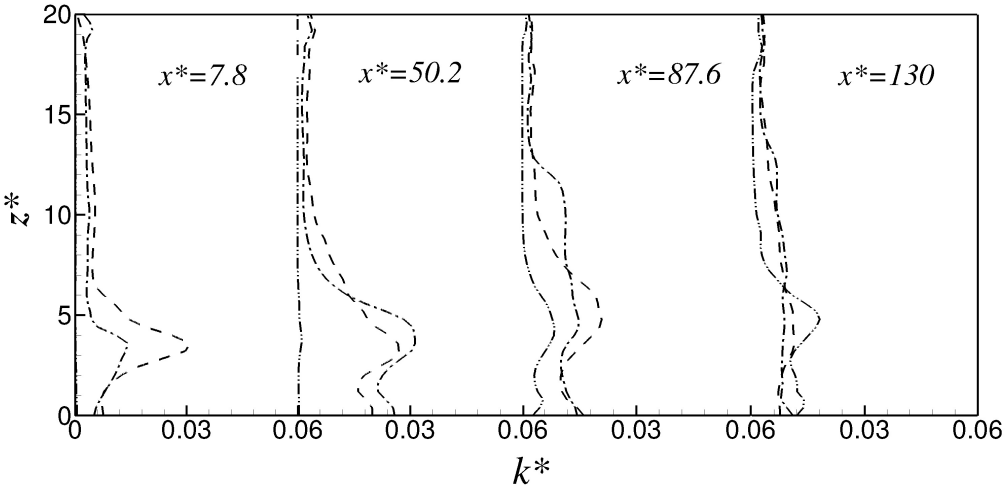

Figure 7.19: Turbulent kinetic energy. Method of Smirnov, Shi and Celik (2001) (- - -); method of Klein, Sadiki and Janicka (2003) ($-\cdot-$); white noise ($-\cdot\cdot-$).

Concerning the computational cost, it is worth recognizing that the better quality of the results provided by the methods of Klein, Sadiki and Janicka (2003) and Smirnov, Shi and Celik (2001) demand a higher CPU time than the method associated with the superimposition of a white noise on the mean velocity inlet profile. However, for the tests carried-out both the simulations with the methods of Klein, Sadiki and Janicka (2003) and Smirnov, Shi and Celik (2001) correspond to approximately the same computational cost, i.e., about 25% more than the simulation conducted with the white noise superposition.
Nevertheless, there are two crucial differences between the methods of Klein, Sadiki and Janicka (2003) and Smirnov, Shi and Celik (2001). The first does not present temporal correlations whatsoever. Only spatial correlations are guaranteed. Moreover, the method of Klein, Sadiki and Janicka (2003), does not generate a divergence free velocity field at the inlet.

In the next section, the effects of the turbulent inflow data generator will be assessed for reactive turbulent flows.

7.2.6 Application to reactive flows simulations

Although there is some literature on the importance of realistic turbulent inflow data prescription on non-reactive flows, an analysis of the effects of quality of the turbulent inflow data is much less common in the context of reactive flow simulations. Indeed, during the development of the present study, it was noted that, even if there is a concern in reproducing the correct Reynolds stress tensor, see for instance Yilmaz (2008), an assessment on the effects of retaining different methods of turbulent inflow generation has not yet been performed. In this subsection a set of two-dimensional simulations will be conducted to analyze these effects.

The procedure followed here is identical to that adopted when the turbulent inflow generators in non-reactive flows, i.e., a set of simulations was carried-out in order to evaluate the effects of the different methods for turbulent inflow generation: (*i*) superimposing white noise on the mean velocity profile at the inlet, (*ii*) using the method of Klein, Sadiki and Janicka (2003) and, finally, (*iii*) the method proposed by Smirnov, Shi and Celik (2001).

The computational domain is a three-dimensional box with dimensions $(800 \times 2 \times 100)$ mm^3, discretized with a finite volume mesh of $320 \times 1 \times 100$ control volumes in the x, y and z direction, respectively. Periodicity and no-slip boundary conditions are imposed along y the z directions respectively. An advective boundary condition is used as outflow. The Smagorinsky constant is set to 0.22 and the Van-Driest damping function is used. The Reynolds number, based on the initial width of the mixing layer, $\delta_m = 5$ mm, on the mean velocity difference between the two flow streams, $U_r = 82.5$ m/s, and on the value of the kinematic viscosity in air at 600 K, is $Re = 3,075$.

For the simulation with white noise, a fluctuation level of 20% is imposed over the u average component of velocity, whereas fluctuations of 10% are set for the average velocity component in the z direction (w). For the simulations with the method of Klein, Sadiki and Janicka (2003) filter support size is set to 10, whereas $1,000$ Fourier modes were used for

the simulations based on the method of Smirnov, Shi and Celik (2001). Magre et al. (1988) have provided a large amount of experimental data in the experimental set-up previously used by Moreau and Boutier (1977) in different flow conditions. Andrade (2009) presents a detailed study on the flow configuration used in the present section. The plausible range of the Karlovitz and Damköhler numbers, positions the flame studied by Moreau and Boutier (1977) in thin reaction zone regime within the premixed turbulent combustion diagram, Fig. (2.7).

The mean velocity profile has the same shape as that employed for the non-reactive flows, i.e., the velocity profile given by Eq. (7.21). However, to be consistent with the the values of the parameters used in Magre et al. (1988), the average values of inlet velocity are those given in Tab. (7.2). For the reactive flow simulations the Backward Difference Scheme is retained also, and the size of the time step is evaluated by Eq. (4.1), with the constant C set to 0.25. The advective terms of the transport equations are discretized with the CDS approach. Since the calculations presented herein are quasi two-dimensional, the computational domain is divided into 8 sub-domains only.

Table 7.2: Values for mean velocity profile retained for the simulation of reactive flows. See Eq. (7.21)

Duct	C_{in} [m/s]	h [m]	a [m]	γ_{in}
Main duct	55	0.02	0.08	6.0
Auxiliary duct	110	0.00	0.02	8.0

The initial and boundary condition for the mean value of the progress variable at $x^* = 0$, are given by the hyperbolic profile,

$$c(z) = \frac{c_q + c_p}{2} + \frac{c_q - c_p}{2} \tanh\left(\frac{2h(z)}{\delta_m} - \frac{2h_p}{\delta_m}\right), \tag{7.22}$$

where, c_q and c_p are the mean values of the progress variable of the auxiliary burner ($c = 1$; $T_b = 2000$ K) and of the main duct ($c = 0$; $T_u = 560$ K), respectively. The quantity h_p is the height of auxiliary duct, $\delta_m = 0.01$ is the initial width of the mixing layer. Such profile

can be seen in Fig. (7.20). Concerning the Monte Carlo simulation, 50 particles per control volume are used and the Milstein scheme is employed for the numerical integration of Eq. (4.31).

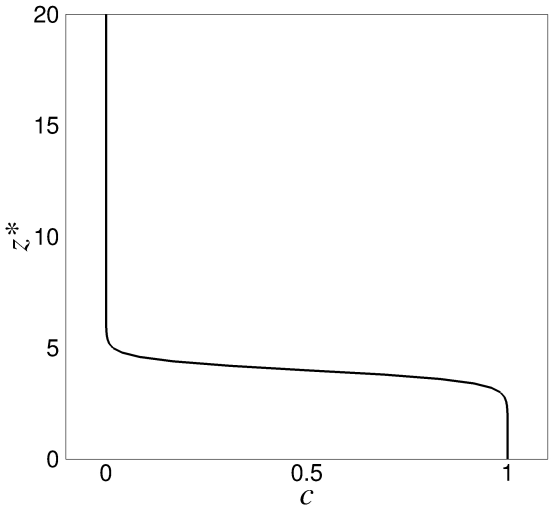

Figure 7.20: Prescribed average progress variable inlet and initial profile.

The assumption of a single, global and irreversible chemical reaction is retained for the chemical kinetics, together with that of a lean fuel/air mixture. Thus a single chemical reaction progress variable, c, can be retained. The methods and procedures adopted to describe the behavior of such variable are described in chapters 3 and 4. The DVODE algorithm of Byrne and Dean (1993) is employed to integrate the chemical reaction rate.

Another important effect assessed here, is the value of the activation energy, E_a, on the propagation of the turbulent flame. Three values are tested, to say, $E_a = 12,000 J/mole$, $E_a = 10,000 J/mole$ and $E_a = 8,000 J/mole$, which are representative of the CH_4/air combustion. When changing E_a the laminar flame speed, S_L, is kept constant, which leads to a modification of the pre-exponential frequency factor of the Arrhenius law according to Tab. (7.3), which describes the procedure adopted to evaluate the chemical reaction rate (POINSOT; VEYNANTE, 2005). Note that the characteristic laminar flame thickness varies with E_a, also.

Table 7.3: Procedure to evaluate the chemical source term.

[1]	*Prescription of the activation energy* E_a *and thus the activation temperature* $T_a = E_a/R$*;*
[2]	*Evaluation of* $\tau = (T_b - T_u)/T_b$ *and* $\beta = \tau T_a/T_b$*;*
[3]	*Evaluation of* Λ*:* $\Lambda = 0.5\beta^2\left[1 + \frac{2}{\beta}(3\tau - 1.344)\right]$ *(Considering* $\beta_1 = 0$*);*
[4]	*The pre-exponential constant can be calculated as* A_τ*:* $A_\tau = \Lambda S_L^2/\left[\alpha e^{(-\beta/\tau)}\right]$, *where* $S_L = 1.2$ *m/s (MAGRE et al., 1988);*
[5]	*Evaluation of the chemical reaction rate:* $S(c) = A_\tau \rho(1-c)\exp\left[-\frac{\beta(1-c)}{1-\tau(1-c)}\right]$.

Figure (7.21) shows the instantaneous fields of the chemical reaction progress variable c and the filtered chemical reaction rate $S(c)$ for the set of simulations performed for the characterization of the effects of activation energy of the method of generation of turbulent inflow data. When the activation energy is kept constant, the method of turbulent inflow data generation influences the shear layer spreading rate as well as the position of the instantaneous filtered flame front. For instance, when the subfigure (i) of Fig. (7.21) is considered, the longitudinal span of the flame when white noise is retained, is larger than when the other two methods are used. Moreover, another characteristic that is associated to the method of generation of turbulent inflow data is the presence of a range of length scales of the large eddies when the methods of Klein, Sadiki and Janicka (2003) and Smirnov, Shi and Celik (2001) are used.

Indeed such large eddies are responsible for increasing of the shear layer spreading rate and the wrinkling of the flame. The time-averaged field of the chemical reaction progress variable $\tilde{c}$ and the filtered chemical reaction rate $S(\tilde{c})$, presented in Fig. (7.22) show that increasing the activation energy always leads to a thicker and shorter flame brush, which is consistent with the corresponding higher degree of folding/corrugation of the instantaneous flame shown in Fig. (7.21). Concerning now the influence of the inlet boundary condition, it may be observed in Fig. (7.22) that accounting for a turbulence spectrum always leads to a shorter and thicker flame brush. Moreover, the influence of the inlet boundary condition is less pronounced as the activation energy is increased, which indicates that the flame dynamics plays a lesser role. Tab (7.4) gives the value of the length of the flame brush,

based on $\langle c \rangle = 0.9$ that does confirm such tendencies.

Table 7.4: Length of the 2D flame brush, based on $\langle c \rangle = 0.9$ in the x direction.

E_a [kJ/Mole]	White noise	Klein, Sadiki and Janicka (2003)	Smirnov, Shi and Celik (2001)
8	560 mm	543 mm	497 mm
10	434 mm	400 mm	370 mm
12	353 mm	330 mm	315 mm

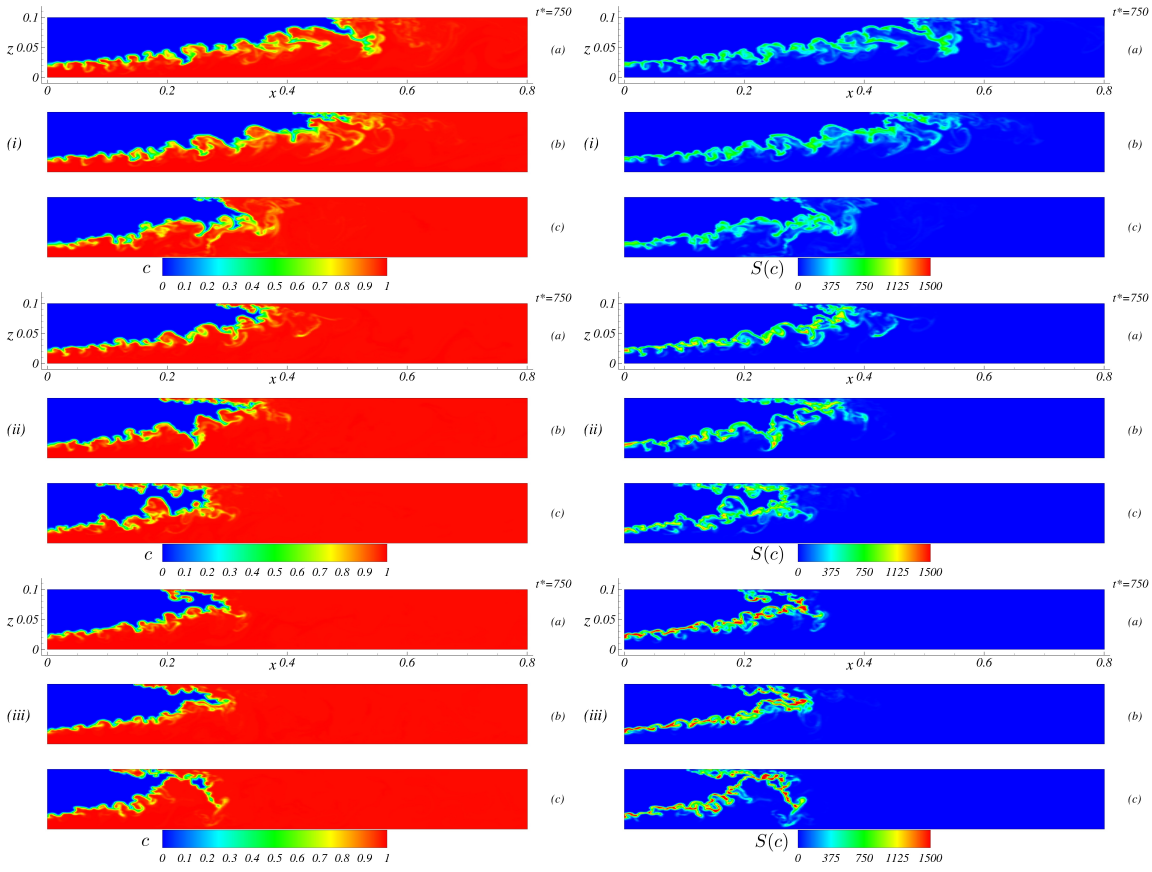

Figure 7.21: Instantaneous fields of chemical reaction progress variable c - left, and chemical reaction rate $S(c)$ - right. $(i) - E_a = 8,000$ J/mole; $(ii) - E_a = 10,000$ J/mole; $(iii) - E_a = 12,000$ J/mole. The subfigures (a), (b) and (c) are results of simulations with the respective inlet boundary condition methods: white noise superimposition; the method of Klein, Sadiki and Janicka (2003) and the method of Smirnov, Shi and Celik (2001)

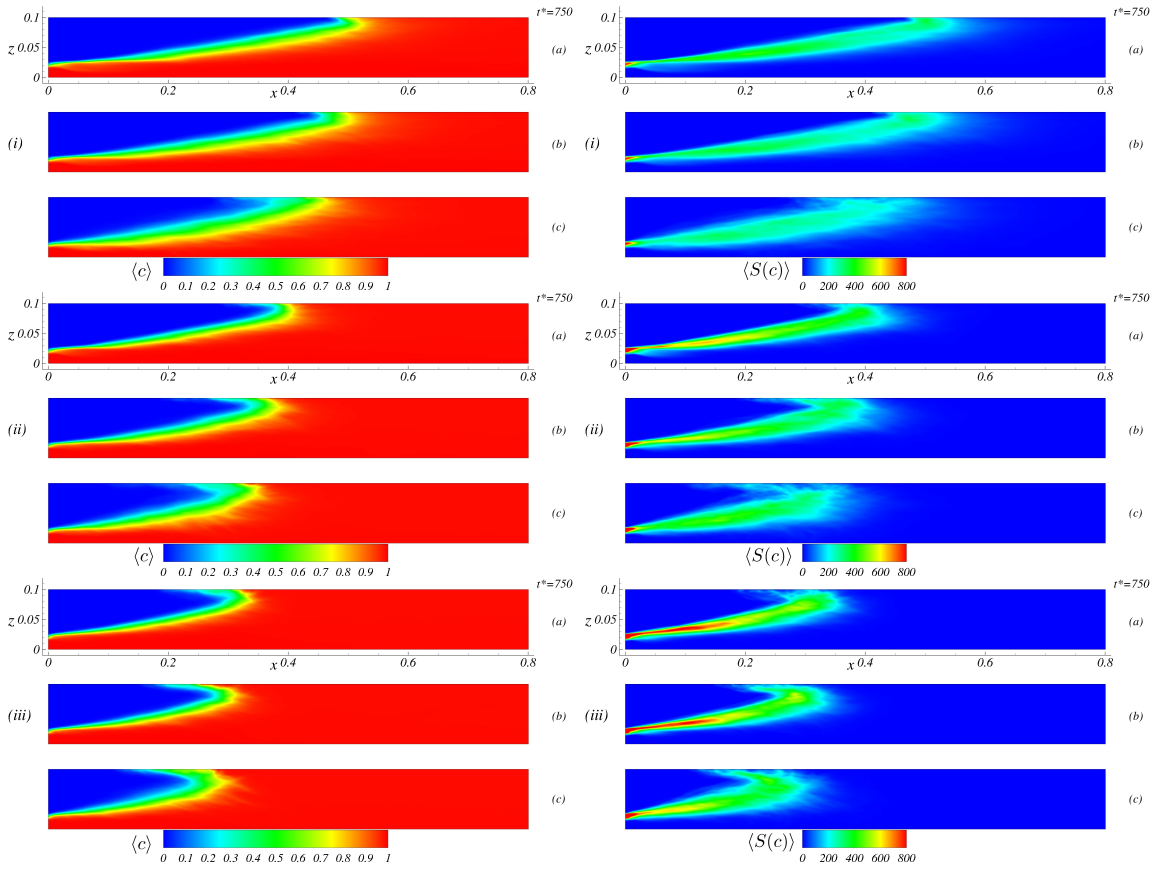

Figure 7.22: Average fields of chemical reaction progress variable c - left, and chemical reaction rate $S(c)$ - right. $(i) - E_a = 8,000$ J/mole; $(ii) - E_a = 10,000$ J/mole; $(iii) - E_a = 12,000$ J/mole. The subfigures (a), (b) and (c) are results of simulations with the respective inlet boundary condition methods methods: white noise superimposition; the method of Klein, Sadiki and Janicka (2003) and the method of Smirnov, Shi and Celik (2001)

An interesting point allowed by the present analysis is determining how the choice of the method of generation of turbulent inflow data affects the flame-turbulence interaction. To perform such an analysis, it is necessary to recall the definition of the Damköhler number, $Da = \tau_t/\tau_c$, which is the ratio of turbulent time scale, τ_t and the chemical time scale, τ_c. This number characterizes how turbulence interacts with chemical reactions. It should be noted that different methods of generating turbulent inflow data can lead to different Damköhler numbers. Indeed, as can be seen in Fig. (7.11) the characteristic time of turbulence varies strongly for the different methods of generation inflow data. It was observed, for the superimposition of white noise over the average velocity profile at the inlet, that the fluctuations

are in the range $1 - 20$ m/s, whereas, for the methods of Klein, Sadiki and Janicka (2003) and Smirnov, Shi and Celik (2001) the maximum value of fluctuations were about 60 and 40 m/s respectively. Given the grid size and the computational domain used in the present study, which provide a minimum length of the control volumes of 1 mm, the turbulent characteristic times for the white noise imposition, τ_{twn}, the method of Klein, Sadiki and Janicka (2003), τ_{tk} and the method of Smirnov, Shi and Celik (2001), τ_{ts} are $50\,\mu s$, $16\,\mu s$ and $25\,\mu s$, respectively. Considering that different activation energies may lead to different values of the computed chemical time scale, it may be expected for the Damköhler number to vary with the method of generation of turbulent inflow and activation energy. Table (7.5) shows that variation.

Table 7.5: Values of Damköhler number for the different values of activation energy and different methods of generation of inflow turbulent data.

E_a [kJ/Mole]	White noise	Klein, Sadiki and Janicka (2003)	Smirnov, Shi and Celik (2001)
8	0.11	0.03	0.053
10	0.19	0.06	0.097
12	0.33	0.10	0.1613

In the work of Magre et al. (1988) the postulated chemical time scale is $\tau_c = 1$ ms, and the characteristic turbulent time scale is $\tau_t = 0.01$ ms, which leads to a $Da = 0.01$. Based on the developments presented at the end of section 7.2.5, and considering that it is shown in Magre et al. (1988) that the flame stabilizes between the interval 0.322 - 0.422 m, approximately the position found in subfigures (ii) of Figs. (7.21) and (7.22), for the henceforth simulations presented in the present work the method used to prescribe turbulent inlet conditions is the method of Smirnov, Shi and Celik (2001).

7.2.6.1 Three-dimensional simulations

In this section it is presented the results obtained with a three-dimensional simulation of the case experimentally studied by Moreau and Boutier (1977) and Magre et al. (1988). The computational domain is a three-dimensional box with dimensions $(800 \times 50 \times 100)$ mm^3, discretized in a $320 \times 50 \times 100$ mesh in the x, y and z direction respectively. Periodicity and

no-slip boundary conditions are imposed over y the z directions respectively. An advective boundary condition is used as outflow. As the two-dimensional simulations presented above, the Smagorinsky constant is set to 0.22, the Van-Driest damping function is used and the profiles of mean velocity at the inlet is given by Eq. (7.22).
The activation energy retained is set to $E_a = 10,000$ J/Mole, and the method for generating the turbulent inflow data is the method of Smirnov, Shi and Celik (2001).

Figure (7.23) shows the instantaneous fields of chemical reaction rate (a) and chemical reaction progress variable (b). The isosurface presented in Fig. (7.23) correspond to a progress variable value $c = 0.5$. It is noteworthy that the flame front is established near the half-length of the computational domain, as expected from the experimental results.

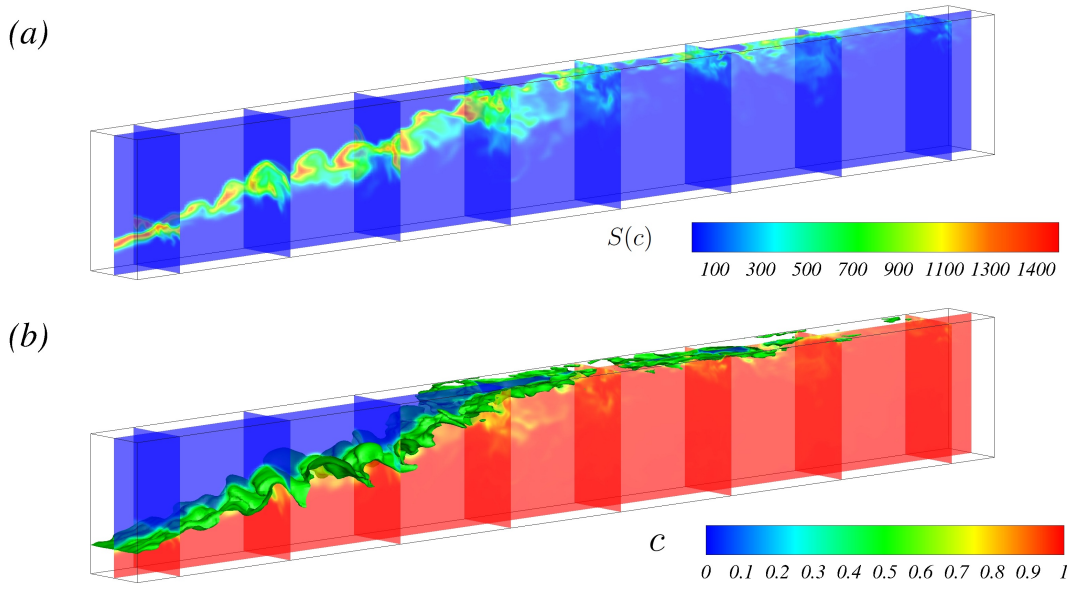

Figure 7.23: Instantaneous fields of chemical reaction rate (a) and chemical reaction progress variable (b). The isosurface presented in Fig. (7.23) is associated with a value of $c = 0.5$.

A quantitative analysis concerning the average velocity and its RMS if shown in Fig. (7.24). It demonstrates that the numerical code was able to capture reasonably well the RMS of the u component of velocity, but the mean velocity profile is not well reproduced, specially in the lower part of the computational domain. A reason for that may be an insufficient level of resolution of the mesh to simulate correctly the thermal expansion due the chemical

reactions. Moreover, it is important to point-out that in the present work the assumption of a unique, irreversible and global chemical reaction is made, therefore the chemical kinetics is rather poorly represented, and consequently important phenomena, like the transformation of CO in CO_2, which is very important in premixed CH_4/air combustion is neglected. As a suggestion for future work, the simulation of the present case, with both a finer mesh and a more accurate representation of the chemical kinetics may be needed.

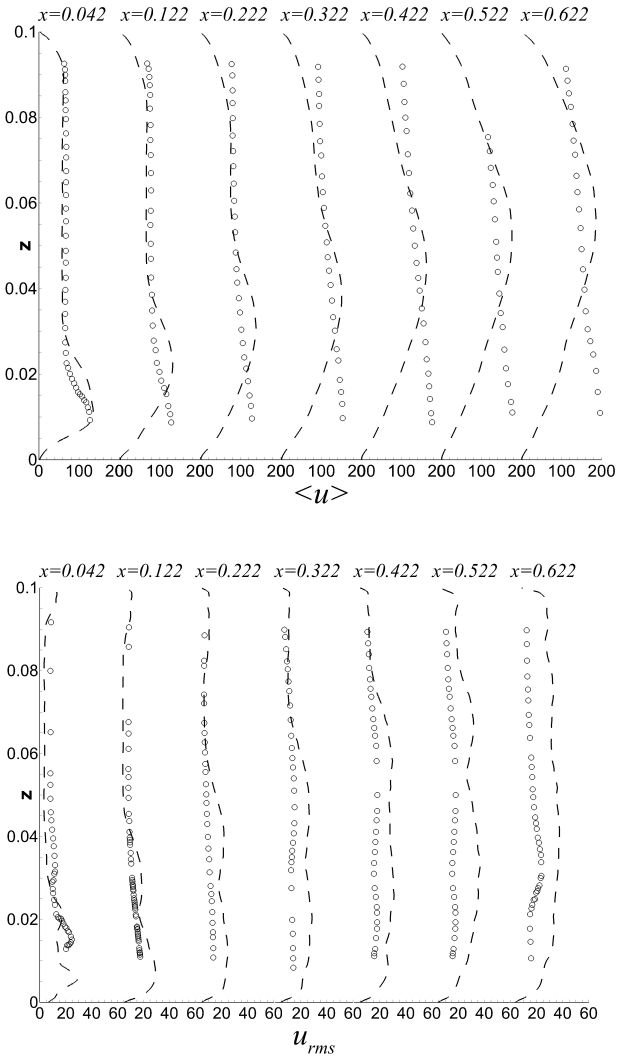

Figure 7.24: Evolution of the longitudinal average (top) and RMS (bottom) of the u-component of velocity at the centerline of the channel.

Comparing the temperature profiles obtained numerically with the experiment, it is possible to observe in Fig. (7.25) that a reasonable agreement is achieved. It is believed that

the residual differences are likely to be an outcome of the same limitations in the modeling of the chemical kinetics retained in the present work.

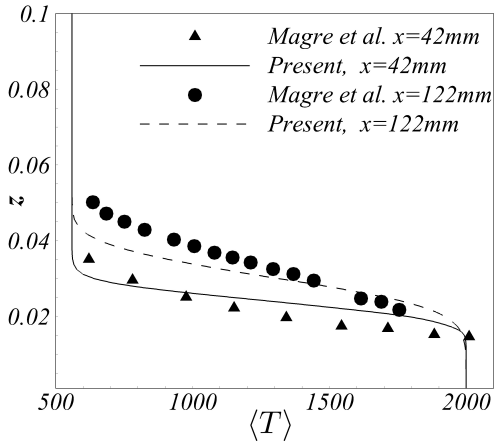

Figure 7.25: mean temperature profile at $x = 42$ and $x = 122$ mm.

CHAPTER VIII

APPLICATION TO NON-REACTIVE AND REACTIVE HIGH VELOCITY TURBULENT JET OF PREMIXED REACTANTS

In this chapter the methodologies described throughout this report are used to perform the numerical simulation of high velocity jets. The predictive capability of the developed solver is demonstrated via comparisons with experimental data associated with both non-reactive and reactive jet flows. Detailed experimental database of turbulent premixed combustion still remains seldom available when compared with non-premixed situations (MURA, 2002; ANDRADE, 2009). Indeed, there are still few experimental works that provide complete data base including measurements of both turbulence and combustion properties in geometrically simple flow configurations.

The flow considered in the present chapter is the piloted turbulent Bunsen burner investigated experimentally by Chen et al. (1996). The schematic diagram of the turbulent Bunsen Burner is reported in Fig. (8.1). The fuel/air mixture nozzle diameter, D, is 12 mm and the pilot stream issues through a perforated plate with an outer diameter of 6.8 mm. Chen et al. (1996) considered three stoichiometric premixed methane-air flames (namely F1 to F3) featuring a wide range of Reynolds and Damköhler number values.

This burner has been the subject of several numerical investigations. RANS simulations of flame F3 were conducted by Prasad and Gore (1999) using a flame surface density

model. Mura (2002) studied the three flames (F1 to F3) using RANS together with a prescribed PDF approach methodology, which relies on the joint PDF of progress and mixture variables. Herrmann (2006) also conducted RANS numerical simulations of the three flames using a level-set flamelet model. The prediction of the F3 flame based on a LES/Level-set approach is reported in Pitsch and Lageneste (2002). Finally, Yilmaz (2008) provides more recently a comprehensive study of the F3 flame using a LES/FDF methodology.

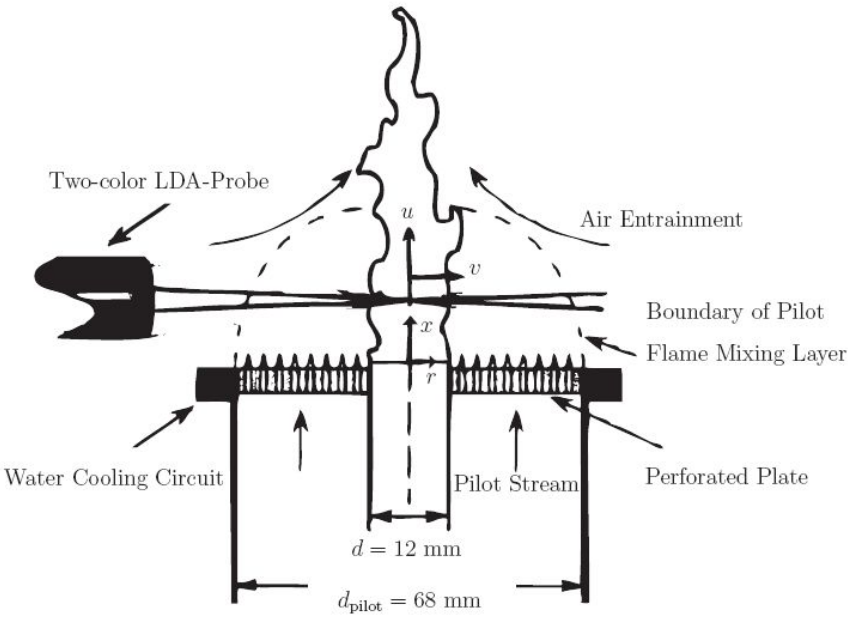

Figure 8.1: Experimental configuration of the turbulent bunsen burner of Chen et al. (1996).

As recalled in Chapter 2, in the flamelet regime the chemical time is the smallest time scale in the reactive flow field, and, thus, a decoupling between turbulence and chemical reactions is possible. For flames in the thin reaction zone regime, however, the interaction between turbulence and combustion is very important since, as aforementioned, turbulence can significatively alter the structure of the pre-heating layer of the flame, and thus, modifies the transport of the chemical species and energy.

The three flames studied in the work of Chen et al. (1996), although presenting different Reynolds and Damköhler numbers, have the characteristic of being situated in the thin

reaction zone regime. The location of these flames in the combustion regime diagram is shown in Fig (8.2). The F3 flame, with a mean nozzle exit velocity of 30 m/s, although positioned in the thin reaction zone regime is close to the flamelet regime. The flame F1, the fastest flame, with a mean nozzle exit velocity of 65 m/s, is positioned close to the region of broken reaction zones. The F2 flame, with a mean nozzle exit velocity of 50 m/s, is situated between F1 and F2.

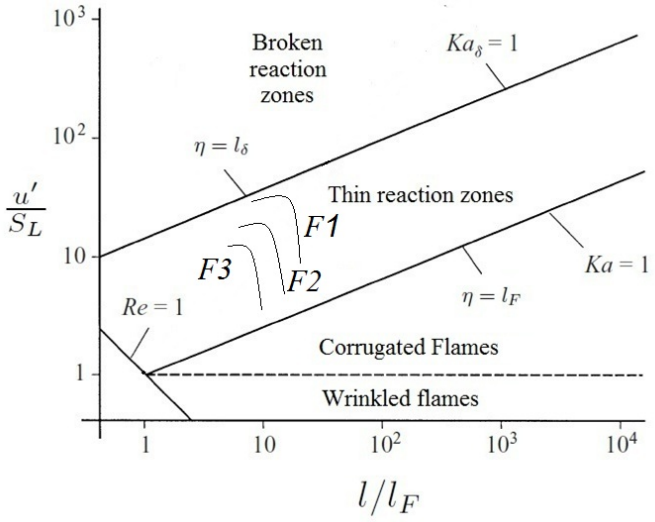

Figure 8.2: Location of the flames studied by Chen et al. (1996) in the combustion regime diagram (Borghi coordinates) for premixed turbulent combustion.

An interesting point that singles out the work of Chen et al. (1996) is that cold-flow characteristics and measurements are provided which allows for the preliminary validation of the developed numerical code in the flow configuration of interest, promoting valuable insights of the behavior of the numerical code in situations of high complexity. In the next section the cold-flow characteristics of the F3 flame is assessed.

8.1 Cold-flow characteristics

Jet flows are very dependent on inlet boundary conditions such as mean velocity profile and turbulence intensity and length scale at the nozzle exit. The mean velocity and the RMS profile retained in the simulations presented in the present work are shown in Fig. (8.3). For the analysis of the characteristics of the inert flow, only the configuration corresponding to the F3 flame is retained. To correctly represent the anisotropic RMS velocity profile depicted

in Fig. (8.3), the method of Smirnov, Shi and Celik (2001) is used, with the number of Fourier modes is set to $1,000$. The turbulent time scale, τ_t, necessary in such a method to evaluate temporal correlations of the velocity fluctuations is set to 1.1 ms (CHEN et al., 1996). The computational domain spans a region of 15D $\times$ 15D $\times$ 15D, in the x, y and z directions respectively. The number of control volumes retained in these respective directions is 225 $\times$ 180 $\times$ 180, which is approximately the number of control volumes adopted in the previous work of Yilmaz et al. (2011). A non-uniform computational grid is used in such a way that approximately 30 control volumes lie within the $fuel/air$ nozzle, in both the y and z directions, yielding the smallest length of cell size of 0.4 mm. The computational domain is divided into 144 sub-domains.

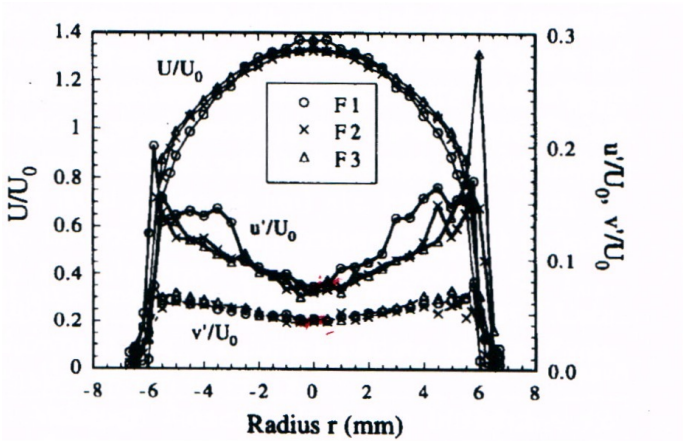

Figure 8.3: Normalized mean and RMS velocity profiles at the burner exit plane, from Chen et al. (1996).

It is worth noting that although there are no chemical reactions in the flow studied in the present section, the progress variable is solved as a passive scalar, with a mean profile at the inlet, $x = 0$, given by,

$$c(r) = 1 + \frac{c_q - c_p}{2} - \frac{c_q + c_p}{2} \tanh\left[\frac{1}{4}\frac{R_j}{\delta_j}\left(\frac{r}{R_j} - \frac{R_j}{r}\right)\right], \tag{8.1}$$

where, c_q and c_p are the mean values of the progress variable in the inner and outer parts of the jet, respectively, r is the radial coordinate, δ_j is the initial width of the shear layer and R_j is the radius of the jet. In Fig. (8.4) the inlet plane and the location of the nozzle in the

YZ plane are shown.

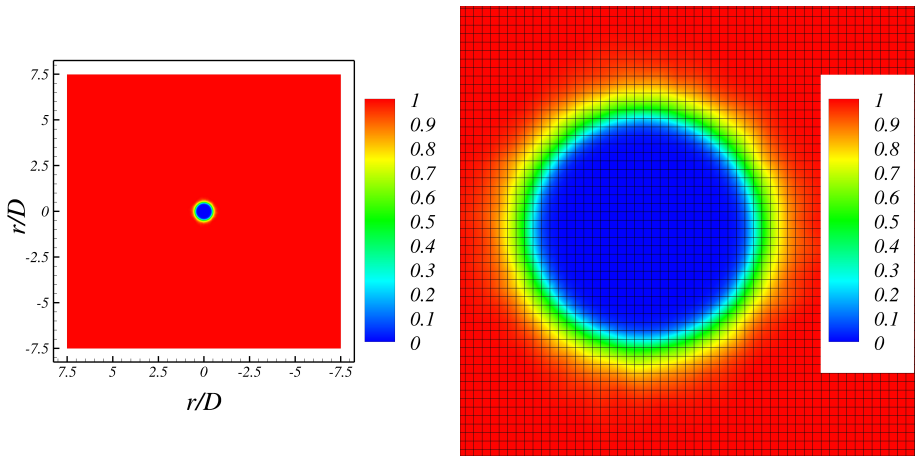

Figure 8.4: Scalar variable boundary condition at the computational inlet for the round jet. Global and detailed view of the jet region.

With a Reynolds number $Re = 22,400$ the jet F3 can be considered as a highly turbulent jet. The instantaneous flow field is dominated by the presence of high frequency structures, as can be seen in Fig. (8.5)-(a). In such a figure it is shown a snapshot of the scalar field c at $t^* = tU_0/D = 485$. The instantaneous scalar field averaged over approximately 10,000 time-steps is shown in Fig. (8.5)-(b). The different regions typically found in turbulent jets, such as the potential core, the shear layer and the zone of fully developed turbulence are clearly identifiable in this figure.

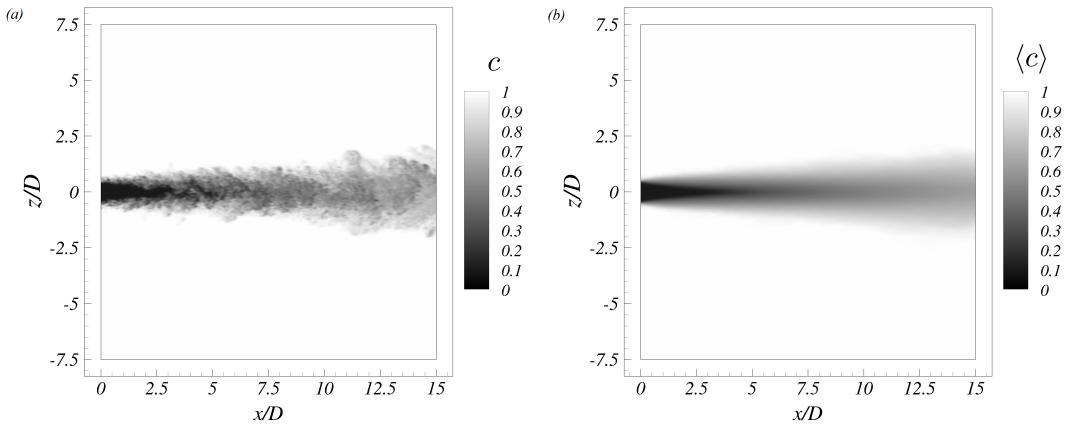

Figure 8.5: Scalar variable c for the cold jet: instantaneous (a) and averaged (b) fields.

An evaluation of the length of the potential core is often considered to provide a good indication of the quality of the results. According to Pope (2000) the length of the potential core ranges 3 to 5 nozzle diameters. In the present case, it is possible to note, with the help of Fig. (8.6), that the potential core length is approximately $4D$.

In order to quantitatively evaluate this inert flow, numerical simulations are conducted with different turbulence models are made. The Smagorinsky model, with two different values of the constant C_s, see Eq. (3.25), $C_s = 0.10$ and $C_s = 0.18$, and the dynamic Smagorinsky model are used. Figure (8.6) reports the longitudinal evolution of the mean axial velocity, non-dimensionalized by the mean velocity at the nozzle exit, and the turbulent kinetic energy, non-dimensionalized by the square of the mean velocity at the nozzle exit, along the axial direction at the centerline of the burner for the three modelings retained. The Smagorinsky model, with $C_s = 0.18$, is the model that provides the worst results. In this case, it is possible to note that a high value of C_s leads to a reduction of the size of the potential core, and to a decrease of the average velocity at the center line that is faster than the measured one, which is accompanied by an increase in the turbulent kinetic energy, which over predicts the maximum experimental value by almost 300%.

With a smaller value of the Smagorinsky constant, $C_s = 0.10$, there is an improvement in the results agreements with the experimental data. Nevertheless, the unexpected decrease of the average velocity, and the increase in turbulent kinetic energy are still notable. Moreover, the use of $C_s = 0.10$ led the computational code to present numerical stability issues in this case. In fact, for the results presented in Fig. (8.6), with $C_s = 0.10$, even with the resort to a variable time step size, which greatly improves the stability of the numerical code, the simulation is found to diverge after approximately 170 non-dimensional seconds [1].

The dynamic Smagorinsky model is the turbulence model that captures reasonably well the variations of the average velocity and turbulent kinetic energy along the centerline. The potential core length is correctly predicted, extending to approximately $x/D = 4.5$, where it

[1] In the present work, a simulation is said to diverge when the size of the time step continuously decreases from several orders of magnitude.

is possible to verify that the average velocity decreases as the jet expands along the radial direction. Nonetheless, the turbulent kinetic energy exhibits discrepancies for $x/D > 6$. The reason for that may be due to the fact the computational domain is too short to promote the full development of the jet and hence affecting adversely the developed turbulence zone of the jet. Further simulations, with a longer computational domain in the x direction may be performed in order to check this particular issue.

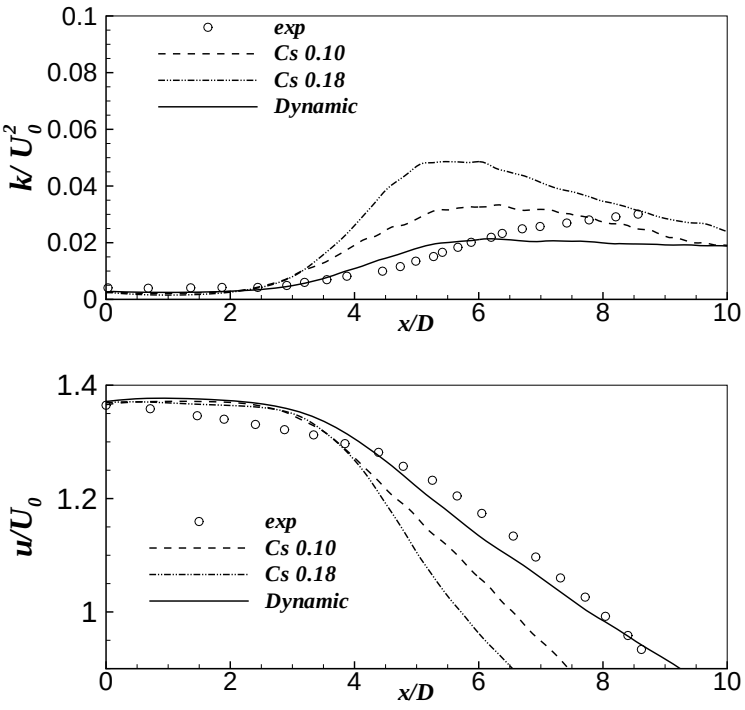

Figure 8.6: Streamwise evolution of average velocity and kinetic energy profiles for the cold jet.

Comparisons of the radial profiles of velocity and turbulent kinetic energy are presented in Fig. (8.7). Generally speaking, the results obtained for the cold flow confirm that the code is able to predict the experimental flow through a turbulent Bunsen burner, once the dynamic Smagorinsky closure is retained. Comparing the present results with the numerical results previously obtained by Yilmaz (2008), it is possible to observe that, specially concerning the turbulent kinetic energy, the predictions obtained by the present work are closer to

experimental data.

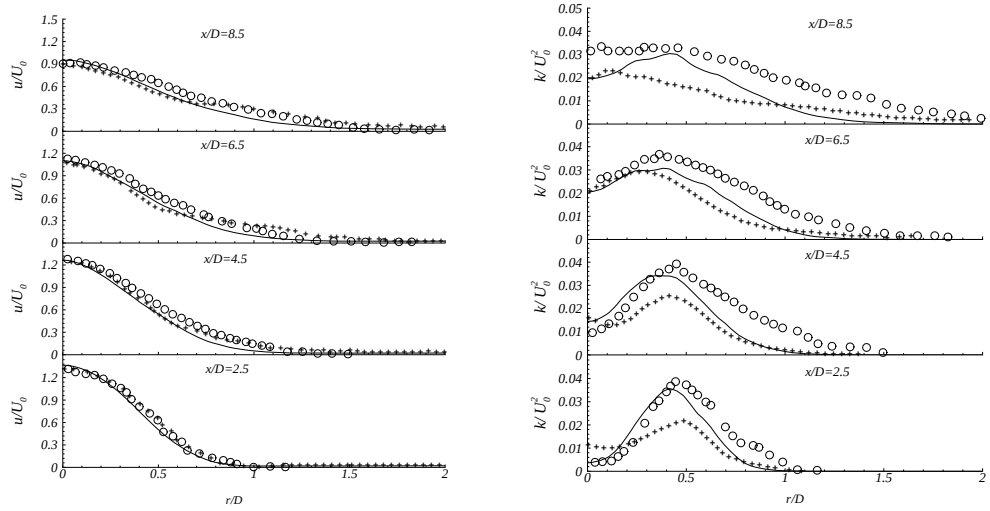

Figure 8.7: Radial variation of average velocity and kinetic energy profiles for the cold-flow F3 jet. The solid lines are results of the present thesis, the plus, (+), symbols are numerical results obtained by Yilmaz (2008) and the circles are experimental results of Chen et al. (1996).

The differences between the obtained radial turbulent kinetic energy profiles (shown in Fig. 8.7) and the experimental data, could be explained by the uncertainties in the prescription of the boundary conditions at the inlet. The RFG model (SMIRNOV, 2004), when retained for the generation of anisotropic turbulent inflow data requires two different characteristic scales: a length and a time scale. The first, given in the work of Chen et al. (1996) is evaluated from the experimental data. Nevertheless, in the work of Chen et al. (1996) the characteristic time scale at the inlet is given only for the reactive flow cases. For the simulations of the cold-flow presented here, the same turbulent time scale is adopted. Moreover, it is important to note that the turbulent inflow data is generated for the flow issuing from the nozzle only. Elsewhere the velocity fluctuations have been set to zero. In Fig (8.7) it is clear that for $r/D > 0.5$, i.e., in the outer region of the nozzle, the values of the turbulent kinetic energy are lower than the experimental data. This may be due to the lack of velocity fluctuations prescribed in this region, where the perforated plate is positioned. Considering the satisfactory results obtained for the non reactive flow field simulation, the

reactive flow F3 is now investigated in the next section .

8.2 The turbulent Bunsen flame F3

In principle, the transported PDF method allows the modeling of turbulent premixed flames whatever of the characteristic velocity of the chemical reactions. However, in the present work, due the assumptions retained to close the PDF transport equation, especially concerning the possible coupling between molecular diffusion and chemical reaction has been neglected, the closure implemented may not give good results in the flamelet regime. On the other hand, it is expected that near the broken reaction zone the method implemented may yield a better prediction of the flame. Despite the fact that the F3 flame is positioned close to the flamelet regime, as shown in Fig (8.2), the fact that it is actually in the thin reaction zone may allow a good prediction of such a flame.

For the study of the F3 flame of (CHEN et al., 1996), the computational domain in the x direction has the same dimensions of the computational domain retained in the simulations of its non-reactive counterpart presented above, i.e., the computational domain spans a region of 15D $\times$ 15D $\times$ 15D, into the x, y and z directions respectively. The number of control volumes retained in these respective directions is $225 \times 180 \times 180$. Such a computational domain is divided into 144 sub-domains. The method of Smirnov, Shi and Celik (2001) is retained for the generation of turbulent inflow data. The number of Fourier modes is kept to $1,000$. Concerning the turbulence modeling, for the simulation of the reactive jet flame, only the dynamic Smagorinsky model is retained. For the Monte-Carlo simulation, approximately 50 particles per control volume are set to the start the calculations. Using the particles weighting control described in Section 4.3.4.3, this number can vary between 40 and 150 particles.

For the F3 flame, the chemical reaction is also considered in the form of a single, global and irreversible step. The energy of activation, E_a is set in such a manner that respecting the laminar flame speed, $S_L = 0.4$ m/s, the range of temperature varying between $T_u = 300$

K for the fresh gases and $T_b = 2248$ K in the fully burnt gases, with a Damköhler number value approximately 0.25, we set $E_a = 10,000$ J/mole.

In Fig. (8.8)-(a) and (b) it is shown respectively, the chemical reaction progress variable c, and the chemical reaction rate for a slice taken along the x direction at $y^* = 0$, in such a manner that it is possible to evidence the instantaneous flame front. The solid line in Fig. (8.8)-b represents the limit of $S(c) = 0$. It is noteworthy that there are two regions where no chemical reactions occurs: inside the potential core of the jet, where only fresh gases are encountered, and in the region where only burnt gases are found, i.e, in the region outside the shear layer.

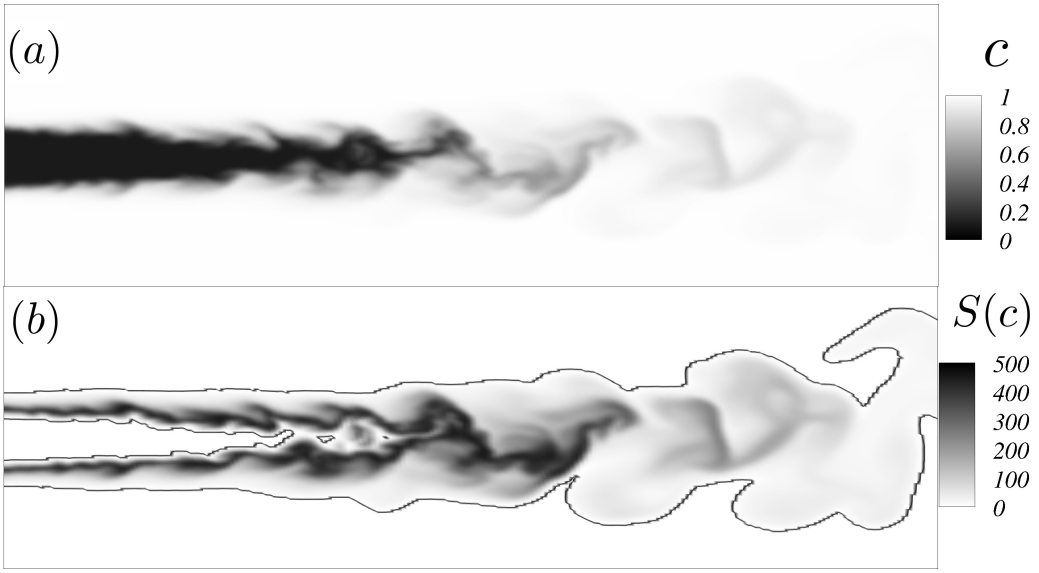

Figure 8.8: Instantaneous fields of the chemical reaction progress variable c, and the chemical reaction rate $S(c)$ at $t^* = 22.5$.

Figure (8.9) shows an evolution of instantaneous field of the chemical reaction progress c. It is evidenced also the evolution, in time of the isovalues of the $Q = 1.0E6$ property (JEONG; HUSSAIN, 1995), colored by values of chemical reaction rate. Although the simulation of the F3 flame is in its initial stage, coherent structures like the Kelvin-Helmholtz type structures can be very well identified. As can be noted in the figure at the top of the left-hand-side, that corresponds to the initial condition, a region composed by fresh gases, corresponding to the diameter of the jet nozzle is surrounded of burnt gases. As time evolves, such "tube" of fresh gases is burnt until it gives rise to the characteristic configuration of a bunsen flame.

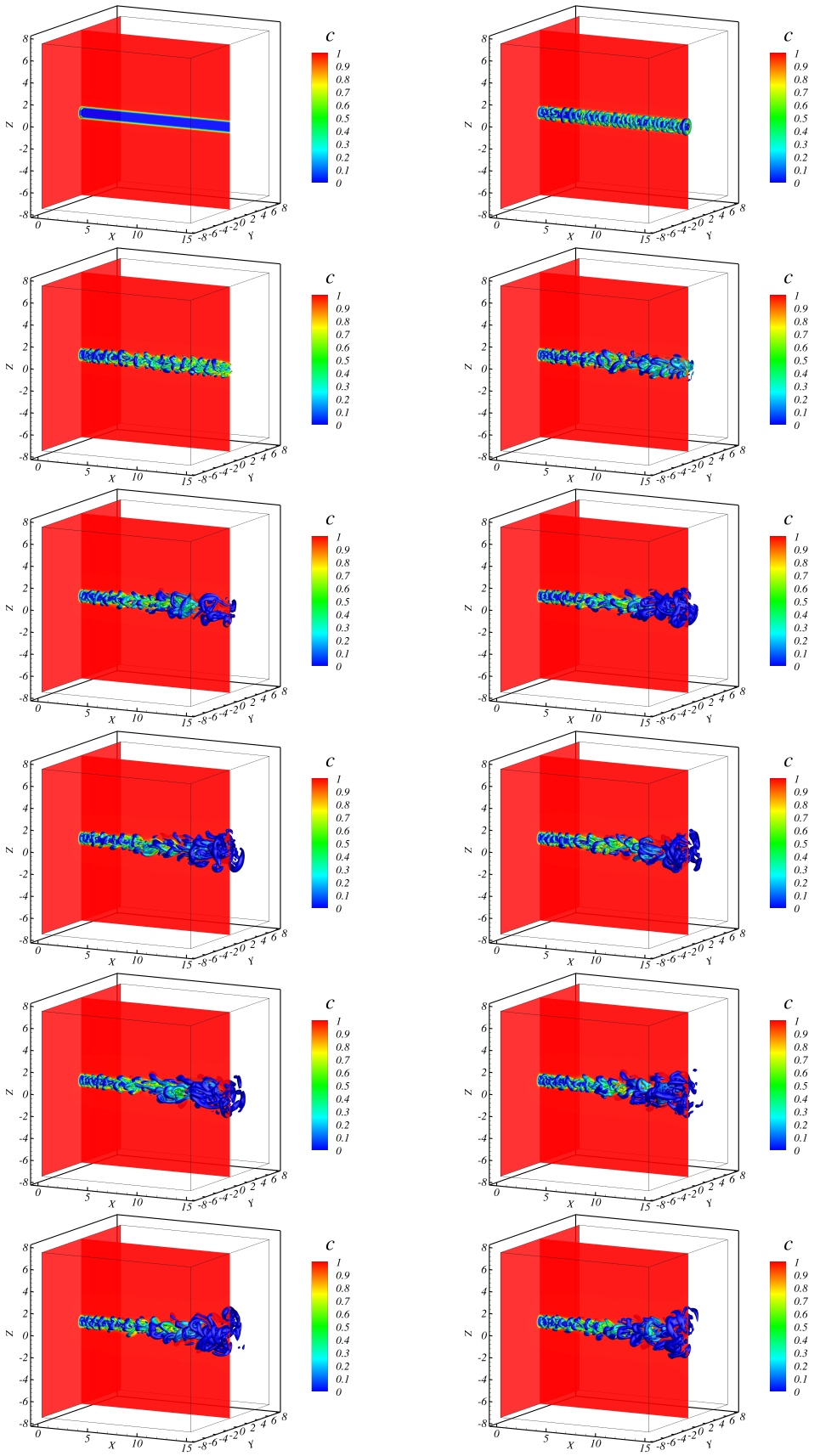

Figure 8.9: Instantaneous chemical reaction progress variable fields for $t^* = 0$ until $t^* = 22.5$. The non-dimensional time interval between figures is $t^* = 2.5$.

These preliminary results confirm the numerical capabilities of the computational model developed during the course of the present thesis work.

Further developments of the physical models are now required to address the specific issues associated with the simulation of this particular test case. This includes the consideration of a more representative chemistry model to include chain-branching reactions. Another important issue is related to the representation of a supplementary tracer (passive scalar), see Mura, Galzin and Borghi (2003) and Herrmann (2006), in order to represent the effects of dilution by surrounding air.

Such issues lie outside the scope of the present thesis work, which has been mainly devoted to the development of viable numerical tools. They offer further perspectives for our future developments though.

CHAPTER IX

CONCLUDING REMARKS AND FUTURE WORK

In this work, it was intended to develop a new numerical code able to perform Large Eddy Simulations of turbulent premixed reactive flows. It was presented a review of the literature on numerical methods suitable for simulating low-Mach Number variable density flows, turbulence modeling of free shear flows and turbulent combustion. Such a review was of paramount importance to choose the methods that would be implemented computationally. Once chosen such methods, the mathematical modeling necessary to simulate the flows of interest, including the simplifying assumptions, filtering of the transport equations for turbulence modeling, the mathematical background of the method of the transported PDF and the coupling between the Eulerian and Lagrangian approaches were presented in details. Concerning the numerical modeling retained in the present work, the fully implicit discretization and the variable time-step temporal integration of the finite volume approach retained was presented. A variable coefficient Poisson solver is used to simulate the corresponding low Mach number flow and a physically consistent constraint is used to ensure that the velocity field is solved correctly. The numerical approach retained to obtain the solution of the system of stochastic differential equations (SDE) is explained and its consistence with the Eulerian approach checked; excellent results are obtained for both constant density and variable density flows.

Since the problems we intend to simulate require a very detailed analysis of the flows,

the resort to refined three-dimensional grids is unavoidable, therefore the code developed is capable of massively parallel computing. Although the efficiency of the parallelization and the speed-up factor analysis was made in only one set of machines (a SGI Altix cluster in the MFLab[1]), such tests have shown that the parallelization of the Eulerian-Lagrangian approach implemented is very promising.

A very important aspect of the development of such a code is that it was extensively verified. The Method of Manufactured Solutions was used to demonstrate that the code developed presents acceptable error convergence rates for LES, i.e, at least two. The numerical code was verified in different situations: in the limit of a zero Mach number flow, and a second set of tests aiming at mimicking the propagation of an analytical corrugated flame front that separates heavy from light gases.

Another remarkable contribution of the present work devoted to the LES of reactive flows is the analysis of influence of the specification of the realistic turbulent inflow boundary conditions. Three different methods of prescribing turbulent inflow data: superimposing white noise over an average profile of velocity, the method proposed by Klein, Sadiki and Janicka (2003), based on digital filtering of a random signal, and the *Random Flow Generator - RFG*, proposed in Smirnov, Shi and Celik (2001), which is based on a Fourier analysis. The three different methods of prescribing turbulent inflow data were fully assessed and their effects were analyzed for a spatially developing mixing layer. First, in an analysis of the inert flow, it was found that the specification of a correct velocity fluctuation is of fundamental importance to predict the average profiles of velocity and even more important to correctly predict the RMS of the velocity. The effects of the turbulent inflow data generator is also evidenced for reactive flows. Basically, it is observed that a more physically consistent boundary condition at the inlet may lead to a shorter and thicker flame brush.

It is worth recalling that although the methods of Klein, Sadiki and Janicka (2003) and Smirnov, Shi and Celik (2001) provide more accurate results than when white noise is

[1]more precisely a SGI/Altix XE1300 Linux cluster consisting of 30 Intel Xeon processors (26 processors E5650 2.67GHz and 4 E5520 2.27GHz),connected via an Infiniband IB QDR / 10GigE interconnect

retained, there are two crucial differences between the methods of Klein, Sadiki and Janicka (2003) and Smirnov, Shi and Celik (2001). The first does not present temporal correlations whatsoever. Only spatial correlations are guaranteed. Moreover, the method of Klein, Sadiki and Janicka (2003), does not generate a divergence-free velocity field at the inlet. It is suggested to use the method of Smirnov, Shi and Celik (2001) in further works.

In the last Chapter, devoted to the simulation of reactive and non-reactive turbulent round reactive jets, it was demonstrated that, first for an inert case, the use of the dynamic Smagorinsky model presented superior results if compared to classical Smagorinsky models. Indeed, the classical Smagorinsky model even presented stability issues in the simulations of the inert jet, for this reason only the dynamic model was retained in the simulations of the reactive turbulent jet. To the date that the present thesis is being finalized, only qualitative, but encouraging, results of the stoichiometric premixed bunsen flame are presented.

As proposals for future work, different directions can be adopted, for instance, concerning the overall low-Mach number solver, the order of the discretization of the spatial and temporal derivative may be increased to yield a convergence rate of at least four or even Fourier spectral methods (MOREIRA, 2011). Moreover, different approaches for the discretization of the advective part of the transport equations may be implemented. It would improve the robustness of the computational code when dealing with flows featuring higher density and velocity ratios.
The resort to multigrid methods in the solutions of the linear system solvers may certainly improve the robustness and efficiency of the low-Mach number flow solver. An important improvement that could be mentioned is the implementation of a dynamic load balancing in the parallelization of the code. It would be important in cases where there are regions with finer meshes or great amount of notional particles.

Another direction that deserves more attention than currently afforded concerns the prescription of realistic boundary conditions at the inlet of the computational domain, especially for LES and DNS. It is suggested the implementation and assessment of new model

like the Synthetic Eddy Method presented by Jarrin et al. (2009). Moreover, the effects of prescribing such realistic turbulent boundary conditions still remain very poorly explored.

It is strongly suggested that in further works the resort to a more complex - and physically realizable - chemical kinetics approach is adopted. It would allow the use of the computational code developed to give better results for realistic problems, including the possibility of its use in the simulation of partially premixed combustion. In the same line it seems of paramount importance to verify the necessity of implementation of more realistic micro-mixing models. As aforementioned the IEM model, although suitable for certain applications like flames with low Damköhler number and in the distributed wrinkled flames regime, it does not contain information of the scalar gradients. To study and implement different micro-mixing models, able to describe thickened flame as well as flamelet regimes, would allow to perform more precise and elaborate analysis of turbulent premixed reactive flows.

Finally, considering the simulation of turbulent reactive flows over complex or deformable geometries, it is suggested the use of the Immersed Boundary Methodology. Through the Immersed Boundary methodology, the solid-fluid interface forces are evaluated by enforcing momentum to the fluid particles over the interface fluid-solid. Such a methodology is particularly suitable for problems involving fluid-structure interactions, once the difficulty of re-meshing the computational grid is circumvented by the use of two independent domains. The governing equations of fluid flow are solved in an Eulerian domain (fixed, cartesian for instance), while the immersed geometry (or geometries) is (are) represented by a set of Lagrangian points.

Such a methodology has been studied in the past decade in the MFLab, and has proven to be very promising. The coupling of the LES/PDF solver with such a methodology would allow the study of more practical configurations, like different types of burners or combustion chambers.

REFERENCES

AMSDEN, A. Kiva-ii: A computer program for chemically reactive flows with sprays. *Journal of Fusion Energy*, v. 12, n. 4, p. 405–405, 1989.

ANAND, M.; POPE, S. Calculations of premixed turbulent flames by pdf methods. *Combustion and Flame*, v. 67, n. 2, p. 127 – 142, 1987.

ANDERSON, J. D. *Computational Fluids Dynamics: the basics with applications.* [S.l.]: Mac Graw-Hill, 1995.

ANDRADE, F. O. D.; SILVA, L. F. Figueira da; MURA, A. large eddy simulation of turbulent premixed combustion at moderate damkohler numbers stabilized in a high speed flow. *Combustion Science and Technology*, v. 183, 2011.

ANDRADE, F. Oliveira de. *Contribuição à Simulação das Grandes Escalas de uma Chama Turbulenta Pré-Misturada Estabilizada em um Escoamento a Alta Velocidade.* Thesis (Doctorate), Pontifícia Universidade Católica do Rio de Janeiro, Departamento de Engenharia Mecânica, 2009.

ASCHER, U. M.; RUUTH, S. J.; WETTON, B. T. R. Implicit-Explicit Methods for Time-Dependent Partial Differential Equations. *Society for Industrial and Applied Mathematics*, v. 32, n. 3, p. 797–823, 1995.

BELL, J. Amr for low mach number reacting flow. *Adaptive Mesh RefinementTheory and Applications*, Springer, v. 41, p. 203–221, 2005.

BELL, J. AMR for low Mach number reacting flow. *Adaptive Mesh Refinement-Theory and Applications*, Springer, p. 203–221, 2005.

BIRCH, S. F.; LYUBIMOV, D.; SECUNDOV, A. N.; YAKUBOVSKY, K. Numerical modeling requirements for coaxial and chevron nozzle flows. *AIAA Paper*, v. 3287, n. May, 2003.

BLEVINS, J. R. A generic linked list implementation in fortran 95. *SIGPLAN Fortran Forum*, ACM, New York, NY, USA, v. 28, p. 2–7, December 2009.

BODONY, D. Analysis of sponge zones for computational fluid mechanics. *Journal of Computational Physics*, v. 212, n. 2, p. 681–702, mar. 2006.

BOERSMA, B. J.; BRETHOUWER, G.; NIEUWSTADT, F. T. M. A numerical investigation on the effect of the inflow conditions on the self-similar region of a round jet. *Physics of Fluids*, v. 10, n. 4, p. 899–909, 1998.

BOGEY, C.; BAILLY, C. A family of low dispersive and low dissipative explicit schemes for flow and noise computations. *Journal of Computational Physics*, v. 194, n. 1, p. 194 – 214, 2004.

BORGHI, R. On the structure and morphology of turbulent premixed flames. In: _____. *Recent Advances in Aerospace Sciences*. [S.l.]: Plenum, New York, 1985. p. 117–138.

BORGHI, R.; CHAMPION, M. *Modélisation et théorie des flammes*. Technip, 2000.

BRAY, K.; LIBBY, P. A.; MOSS, J. Unified modeling approach for premixed turbulent combustion–part i: General formulation. *Combustion and Flame*, v. 61, n. 1, p. 87 – 102, 1985.

BROWAND, F. K.; LATIGO, B. O. Growth of the two-dimensional mixing layer from a turbulent and nonturbulent boundary layer. *Physics of Fluids*, v. 22, n. 6, 1979.

BROWN, G. L.; ROSHKO, A. On density effects and large Structure in turbulent mixing layers. *Journal of Fluid Mechanics*, v. 64, part 4, p. 775–816, 1974.

BROWN, P. N.; BYRNE, G. D.; HINDMARSH, A. C. Vode: a variable-coefficient ode solver. *SIAM J. Sci. Stat. Comput.*, Society for Industrial and Applied Mathematics, Philadelphia, PA, USA, v. 10, p. 1038–1051, September 1989.

BRUCKER, K. a.; SARKAR, S. Evolution of an initially turbulent stratified shear layer. *Physics of Fluids*, v. 19, n. 10, p. 105105, 2007.

BYRNE, G. D.; DEAN, A. M. The numerical solution of some kinetics models with vode and chemkin ii. *Computers & Chemistry*, v. 17, n. 3, p. 297 – 302, 1993.

CAMPREGHER, R. *Modelagem matemática tridimensional para problemas de interação fluido-estrutura*. 179 f. Thesis (Doctorate) — Universidade Federal de Uberlândia, Uberlândia, 2005.

CENICEROS, H.; ROMA, A. A nonstiff, adaptive mesh refinement-based method for the Cahn-Hilliard equation. *Journal of Computational Physics*, v. 225, n. 2, p. 1849–1862, ago. 2007.

CHAKRABORTY, N.; SWAMINATHAN, N. Influence of the damköhler number on turbulence-scalar interaction in premixed flames. i. physical insight. AIP, v. 19, n. 4, p. 045103, 2007.

CHEN, Y.; PETERS, N.; SCHNEEMANN, G.; WRUCK, N.; RENZ, U.; MANSOUR, M. The detailed flame structure of highly stretched turbulent premixed methane-air flames. *Combustion and Flame*, v. 107, n. 3, p. 223–226, nov. 1996.

CHOI, Y. H.; MERKLE, C. L. The application of preconditioning in viscous flows. *Journal of Computational Physics*, v. 105, n. 2, p. 207–223, 1993.

CHORIN, A. J. Numerical solution of the navier-stokes equations. *Mathematics of Computation*, v. 22, p. 745–762, 1968.

CHORIN, A. J.; MARSDEN, J. E. *A Mathematical Introduction to Fluid Mechanics*. [S.l.]: Springer-Verlag, 1993. 169 p.

COLELLA, P.; PAO, K. A projection method for low speed flows. *Journal of Computational Physics*, v. 149, n. 2, p. 245–269, 1999.

COLUCCI, P. J.; JABERI, F. a.; GIVI, P.; POPE, S. B. Filtered density function for large eddy simulation of turbulent reacting flows. *Physics of Fluids*, v. 10, n. 2, p. 499, 1998.

COLUCCI, P. J.; JABERI, F. a.; GIVI, P.; POPE, S. B. Filtered density function for large eddy simulation of turbulent reacting flows. *Physics of Fluids*, v. 10, n. 2, p. 499, 1998.

COOK, A. W.; RILEY, J. J. Direct numerical simulation of a turbulent reactive plume on a parallel computer. *Fuel*, v. 283, n. 2, p. 263–283, 1996.

CORRSIN, S. Investigation of Flow in an axially symmetrical heated jet of air. *National Advisory Committe for Aeronautics*, 1943.

CORRSIN, S.; UBEROI, M. S. Further experiments on the flow and heat transfer in a heated turbulent air jet. *National Advisory Committe for Aeronautics*, Report 988, 1950.

CORRSIN, S.; UBEROI, M. S. Spectrums and diffusion in a round turbulent jet. *National Advisory Committe for Aeronautics*, 1950.

COURTOIS, R. *Simulation aux Grandes Échelles de L'ecoulement Dans une Chambre de Combustion en Forme de Marche Descendante*. Thesis (Doctorate) — École Centrale de Paris, Paris, France, 2005.

CURL, R. L. Dispersed phase mixing: I. theory and effects in simple reactors. *AIChE Journal*, v. 9, n. 2, p. 175–181, 1963.

DA-SILVA, C. F. N. B. *The role of coherent structures in the control and interscale interactions of round, plane and coaxial jets*. Thesis (Doctorate) — Institute National Polytechnique de Grenoble, Grenoble, 2001.

DARMOFAL, D. L.; SCHMID, P. J. The importance of eigenvectors for local preconditioners of the euler equations. *Journal of Computational Physics*, v. 127, p. 346–362, 1996.

DOMINGO, P.; BRAY, K. N. C. Laminar flamelet expressions for pressure fluctuation terms in second moment models of premixed turbulent combustion. *Combustion and Flame*, v. 121, n. 4, p. 555 – 574, 2000.

DOPAZO, C.; O'BRIEN, E. E. An approach to the autoignition of a turbulent mixture. *Acta Astronautica*, v. 1, n. 9-10, p. 1239–1266, 1974.

DOURADO, W. M. C.; BRUEL, P.; AZEVEDO, J. a. L. F. A time-accurate pseudo-compressibility approach based on an unstructured hybrid finite volume technique applied to unsteady turbulent premixed flame propagation. *International Journal for Numerical Methods in Fluids*, John Wiley & Sons, Ltd., v. 44, n. 10, p. 1063–1091, 2004.

FERZIGER, J.; PERIC, M. *Computational Methods for Fluid Dynamics*. [S.l.]: Springer, 1996.

FOX, R. O. *Computational Models for Turbulent Reacting Flows*. [S.l.]: Cambridge University Press, 2003.

GARDINER, C. *Stochastic Methods: A Handbook for the Natural and Social Sciences*. [S.l.]: Springer, 2009. 447 p.

GERMANO, M.; PIOMELLI, U.; MOIN, P.; CABOT, W. H. A dynamic subgrid-scale eddy viscosity model. *Physics of Fluids A: Fluid Dynamics*, v. 3, n. 7, p. 1760, 1991.

GROPP, W.; THAKUR, R.; LUSK, E. *Using MPI-2: Advanced Features of the Message Passing Interface*. 2nd. ed. Cambridge, MA, USA: MIT Press, 1999.

HAM, F. An efficient scheme for large eddy simulation of low-Ma combustion in complex configurations. *Annual Research Briefs (Center for Turbulence Research, Stanford University)*, p. 41, 2007.

HARLOW, F. H.; WELCH, J. E. Numerical calculation of time-dependent viscous incompressible flow of fluid with free surface. *Physics of Fluids*, v. 8, n. 12, p. 2182–2189, 1965.

HAWKES, E. R.; CANT, R. S. Implications of a flame surface density approach to large eddy simulation of premixed turbulent combustion. *Combustion and Flame*, v. 126, n. 3, p. 1617 – 1629, 2001.

HAWORTH, D. Progress in probability density function methods for turbulent reacting flows. *Progress in Energy and Combustion Science*, Elsevier Ltd, v. 36, n. 2, p. 168–259, abr. 2010.

HAWORTH, D. Progress in probability density function methods for turbulent reacting flows. *Progress in Energy and Combustion Science*, Elsevier Ltd, v. 36, n. 2, p. 168–259, abr. 2010.

HERON, N.; LEMAIRE, S.; DASSAULT, M.; CANDEL, S.; BAILLY, C. Coaxial-jet-noise predictions from statistical and stochastic source models. *AIAA Paper*, v. 2205, n. May, 2001.

HERRMANN, M. Numerical simulation of turbulent Bunsen flames with a level set flamelet model. *Combustion and Flame*, v. 145, n. 1-2, p. 357–375, abr. 2006.

HIGHAM, D. J. An Algorithmic Introduction to Numerical Simulation of Stochastic Differential Equations. *Society for Industrial and Applied Mathematics*, v. 43, n. 3, p. 525–546, 2001.

HUSSEIN, H. J.; CAPPS, S. P.; GEORGE, W. K. Velocity measurements in a high-Reynolds-number, momentum-conserving, axisymmetric, turbulent jet. *Journal of Fluid Mechanics*, v. 258, p. 31–75, 1994.

JAMESON, A.; SCHMIDT, W.; TURKEL, E. Numerical solution of the euler equations by finite volume methods using runge kutta time stepping schemes. *AIAA, Fluid and Plasma Dynamics Conference, 14th, Palo Alto, CA, June 23-25, 1981. 15 p.*, 1981.

JANICKA, J.; KOLBE, W.; KOLLMANN, W. Closure of the transport equation for the probability density funcfion of turbulent scalar fields. *Journal of Non-Equilibrium Thermodynamics*, p. 47–66, 1979.

JARRIN, N.; PROSSER, R.; URIBE, J.-C.; BENHAMADOUCHE, S.; LAURENCE, D. Reconstruction of turbulent fluctuations for hybrid RANS/LES simulations using a Synthetic-Eddy Method. *International Journal of Heat and Fluid Flow*, Elsevier Inc., v. 30, n. 3, p. 435–442, jun. 2009.

JEONG, J.; HUSSAIN, F. On the identification of a vortex. *Journal of Fluid Mechanics*, Cambridge Univ Press, v. 285, n. -1, p. 69–94, 1995.

KARKI, K.; PATANKAR, S. V. Pressure based calculation procedure for viscous fows at all speeds in arbitrary configurations. *AIAA Journal*, v. 27, n. 9, p. 1167–1178, 1989.

KLEIN, M. Investigation of the influence of the Reynolds number on a plane jet using direct numerical simulation. *International Journal of Heat and Fluid Flow*, v. 24, n. 6, p. 785–794, dez. 2003.

KLEIN, M.; SADIKI, A.; JANICKA, J. A digital filter based generation of inflow data for spatially developing direct numerical or large eddy simulations. *Journal of Compututational Physics*, Academic Press Professional, Inc., San Diego, CA, USA, v. 186, p. 652–665, April 2003.

KLOEDEN, P. E.; PLATEN, E. *Numerical Solution of Stochastic Differential Equations (Stochastic Modelling and Applied Probability)*. Springer, 2000.

KNIO, O. M.; NAJM, H. N.; WYCKOFF, P. S. A semi-implicit numerical scheme for reacting flow: Ii. stiff, operator-split formulation. *Journal of Computational Physics*, v. 154, n. 2, p. 428–467, 1999.

KNUDSEN, E.; PITSCH, H. A dynamic model for the turbulent burning velocity for large eddy simulation of premixed combustion. *Combustion and Flame*, v. 154, n. 4, p. 740–760, set. 2008.

KRAICHNAN, R. H. Diffusion by a random velocity field. *Physics of Fluids*, v. 13, n. 1, p. 22–31, 1970.

LANDIS, F.; SHAPIRO, A. H. The turbulent mixing of co-axial gas jets. Heat Transfer and Fluid Mechanics Institute, Standford University Press, California, 1951.

LE, H.; MOIN, P.; KIM, J. Direct numerical simulation of turbulent flow over a backward-facing step. *Journal of Fluid Mechanics*, Cambridge Univ Press, v. 330, p. 349–374, 1997.

LEE, S.; LELE, S. K.; MOIN, P. Simulation of spatially evolving turbulence and the applicability of taylor's hypothesis in compressible flow. *Physics Of Fluids A Fluid Dynamics*, v. 4, n. May 1991, p. 1521–1530, 1992.

LESIEUR, M.; MÉTAIS, O. New Trends in Large-Eddy Simulations of Turbulence. *Annual Review of Fluid Mechanics*, v. 28, n. 1, p. 45–82, jan. 1996.

LESIEUR, M.; MÉTAIS, O.; COMTE, P. *Large-Eddy Simulations of Turbulence*. New York: Cambridge University Press, 2005. 219 p.

LESSANI, B.; PAPALEXANDRIS, M. Time-accurate calculation of variable density flows with strong temperature gradients and combustion. *Journal of Computational Physics*, v. 212, n. 1, p. 218–246, 2006.

LESSANI, B.; PAPALEXANDRIS, M. Time-accurate calculation of variable density flows with strong temperature gradients and combustion. *Journal of Computational Physics*, v. 212, n. 1, p. 218–246, fev. 2006.

LI, N.; BALARAS, E.; PIOMELLI, U. Inflow conditions for large-eddy simulations of mixing layers. *Physics of Fluids*, AIP, v. 12, n. 4, p. 935–938, 2000.

LIBBY, P. A.; BRAY, K. N. C. Countergradient diffusion in premixed turbulent flames. *AIAA Journal*, v. 19, p. 205–213, 1981.

LIBBY, P. A. W.; WILLIAMS, F. A. *Fundamental Aspects and a Review. in Turbulent Reacting Flows London*. [S.l.]: Academic Press, 1994. 1-61 p.

LILLY, D. A proposed modification of the Germano subgrid-scale closure method. *Physics of Fluids A: Fluid Dynamics*, v. 4, p. 633, 1992.

LIMA-E-SILVA, A.; SILVEIRA-NETO, A.; DAMASCENO, J. Numerical simulation of two dimensional flows over a circular cylinder using the immersed boundary method. *Journal of Computational Physics*, v. 189, p. 351–370, 2003.

LUND, T. Generation of Turbulent Inflow Data for Spatially-Developing Boundary Layer Simulations. *Journal of Computational Physics*, v. 140, n. 2, p. 233–258, mar. 1998.

MAGRE, P.; MOREAU, P.; COLLIN, G.; BORGHI, R.; PéALAT, M. Further studies by cars of premixed turbulent combustion in a high velocity flow. *Combustion and Flame*, v. 71, n. 2, p. 147 – 168, 1988.

MALLARD, E.; CHATELIER, H. L. Sur la vitesse de propagation de l'inflamation dans les mélanges explosifs. *Ann. Mines, Paris series*, v. 8, p. 274, 1883.

MARIANO, F. P. *Solução Numérica das Equações de Navier-Stokes Usando Uma Hibridação das Metodologias Fronteira Imersa e Pseudo-Espectral de Fourier*. 151 p. Thesis (Doctor of Philosophy) — Universidade Federal de Uberlândia, 2011.

MENEVEAU, C.; LUND, T. S.; CABOT, W. H. A Lagrangian dynamic subgrid-scale model of turbulence. *Journal of Fluid Mechanics*, v. 319, n. -1, p. 353, abr. 2006.

MERCI, B.; MASTORAKOS, E.; MURA, A. Modeling of turbulent combustion. In: _____. *Handbook of Combustion*. Wiley-VCH Verlag GmbH & Co. KGaA, 2010.

MEYER, D.; JENNY, P. Micromixing models for turbulent flows. *Journal of Computational Physics*, Elsevier Inc., v. 228, n. 4, p. 1275–1293, mar. 2009.

MöBUS, H. Comparison of Eulerian and Lagrangian Monte Carlo PDF methods for turbulent diffusion flames. *Combustion and Flame*, v. 124, n. 3, p. 519–534, fev. 2001.

MOIN, P. A dynamic global-coefficient subgrid-scale model for compressible turbulence in complex geometries. *Physics of Fluids*, 2008.

MOIN, P.; SQUIRES, K.; CABOT, W.; LEE, S. A dynamic subgrid?scale model for compressible turbulence and scalar transport. AIP, v. 3, n. 11, p. 2746–2757, 1991.

MOREAU, P.; BOUTIER, A. Laser velocimeter measurements in a turbulent flame. *Symposium (International) on Combustion*, v. 16, n. 1, p. 1747 – 1756, 1977.

MOREIRA, L. d. Q. *Modelagem Matematica de Jatos em Jatos em Desenvolvimento Espacial Usando a Metodologia Pseudo Espectral de Fourier*. 177 p. Thesis (Doctor of Philosophy) — Univerrsidade Federal de Uberlândia, 2011.

MURA, A. *Contribuition à la Modélisation de la Combustion Turbulente Inhomogène dans les Moteurs IDE à Charge Stratifiée*. 212 p. Thesis (Doctor of Philosophy) — Université d'Aix-Marseille II, Ecole Supérieur de Mécanique de Marseille, 2002.

MURA, A.; BORGHI, R. Towards an extended scalar dissipation equation for turbulent premixed combustion. *Combustion and Flame*, v. 133, n. 1-2, p. 193–196, abr. 2003.

MURA, A.; CHAMPION, M. Relevance of the bray number in the small-scale modeling of turbulent premixed flames. *Combustion and Flame*, v. 156, n. 3, p. 729 – 733, 2009.

MURA, A.; GALZIN, F.; BORGHI, R. A unified pdf-flamelet model for turbulent premixed combustion. *Combustion Science and Technology*, v. 175, n. 9, p. 1573–1609, set. 2003.

MURA, a.; ROBIN, V.; CHAMPION, M. Modeling of scalar dissipation in partially premixed turbulent flames. *Combustion and Flame*, v. 149, n. 1-2, p. 217–224, abr. 2007.

NAJM, P. S. W. H. N.; NAJIM, H.; WYCKOFF, P. A semi-implicit numerical scheme for reacting flow. i. stiff chemistry. *Journal of Computational Physics*, v. 143, n. 2, p. 381–402, 1998.

NICOUD, F. Conservative High-Order Finite-Difference Schemes for Low-Mach Number Flows. *Journal of Computational Physics*, v. 158, n. 1, p. 71–97, fev. 2000.

ORBEGOSO, E.; SILVA, L. F. Figueira da. Study of stochastic mixing models for combustion in turbulent flows. *Proceedings of the Combustion Institute*, v. 32, n. 1, p. 1595–1603, 2009.

ORBEGOSO, E. M. M. *Estudo de Modelos de Mistura Estocasticos para a Combustao em Escoamentos Turbulentos*. Pontifícia Universidade Católicado Rio de Janeiro, Departamento de Engenharia Mecânica: [s.n.], 2007.

ORLANSKI, I. A simple boundary condition for unbounded hyperbolic flows. *Journal of Computational Physics*, v. 21, n. 3, p. 251 – 269, 1976.

PAPAGEORGAKIS, G. C.; ASSANIS, D. N. Rng-based $k - \varepsilon$ models for incompressible turbulent flows. *Numerical Heat Transfer Part B Fundamentals*, Taylor & Francis, v. 35, n. 1, p. 1–22, 1999.

PATANKAR, S. V. *Numerical Heat Transfer and Fluid Flow*. [S.l.]: Hemisphere Publishing Corporation, 1980. 197 p.

PETERS, N. Four lectures on turbulent combustion. *ERCOFTAC Summer School, Aachen, Germany*, 1997.

PETERS, N. The turbulent burning velocity for large-scale and small-scale turbulence. *Journal of Fluid Mechanics*, v. 384, p. 107–132, 1999.

PIERCE, C. D. *Progress-Variable Approach For Large-Eddy Simulation of Turbulent Combustion*. 106 p. Thesis (Doctor of Philosophy) — Stanford University, 2001.

PITSCH, H. Large-Eddy Simulation of Turbulent Combustion. *Annual Review of Fluid Mechanics*, v. 38, n. 1, p. 453–482, jan. 2006.

PITSCH, H.; LAGENESTE, L. Duchamp de. Large-eddy simulation of premixed turbulent combustion using a level-set approach. *Proceedings of the Combustion Institute*, v. 29, n. 2, p. 2001–2008, 2002.

POINSOT, T.; VEYNANTE, D. *Theoretical and Numerical Combustion, Second Edition*. [S.l.]: R.T. Edwards, Inc., 2005.

POINSOT, T. J.; LELE, S. K. Boundary conditions for direct simulations of compressible viscous flows. *Journal of Computational Physics*, v. 101, n. 1, p. 104 – 129, 1992.

POPE, S. *Turbulent Flows*. New York: Cambridge University Press, 2000.

POPE, S. B. Pdf methods for turbulent reactive flows. *Progress in Energy and Combustion Science*, Elsevier, v. 11, n. 2, p. 119–192, 1985.

POPE, S. B. *Turbulent Flows*. [S.l.]: Cambridge University Press, 2000. 771 p.

POPE, S. B. Ten questions concerning the large-eddy simulation of turbulent flows. *New Journal of Physics*, v. 6, p. 35–35, mar. 2004.

PRASAD, R. O. S.; GORE, J. P. An evaluation of flame surface density models for turbulent premixed jet flames. *Combustion and Flame*, v. 116, n. 1-2, p. 1 – 14, 1999.

PRESS, W. H.; TEUKOLSKY, S. A.; VETTERLING, W. T.; FLANNERY, B. P. *Numerical Recipes in FORTRAN (2nd ed.): The Art of Scientific Computing*. New York, NY, USA: Cambridge University Press, 1992.

RAMAN, V. Hybrid finite-volume/transported PDF simulations of a partially premixed methane-air flame. *Combustion and Flame*, v. 136, n. 3, p. 327–350, fev. 2004.

RAMSHAW, J. D.; O'ROURKE, P. J.; STEIN, L. R. Pressure gradient scaling method for fluid flow with nearly uniform pressure. *Journal of Computational Physics*, v. 58, p. 361–376, 1985.

RAUWOENS, P.; VIERENDEELS, J.; MERCI, B. A solution for the odd-even decoupling problem in pressure-correction algorithms for variable density flows. *Journal of Computational Physics*, v. 227, n. 1, p. 79–99, 2007.

RAYLEIGH, L. On the stability, or instability, or certain fluid motions. *Proc London Math Soc*, Oxford University Press, v. 1, n. 1, p. 361–371, 1880.

REYNOLDS, O. An experimental investigation of the circumstances which determine whether the motion of water shall be direct or sinuous, and of the law of resistance in parallel channels. *Philosophical Transactions of the Royal Society of London*, JSTOR, v. 174, n. 1883, p. 935–982, 1883.

RHIE, C. M.; CHOW, W. L. Numerical study of the turbulent flow past an airfoil with trailing edge separation. *AIAA Journal*, American Institute of Aeronautics and Astronautics, v. 21, n. 11, p. 1525–1532, 1983.

RIDER, W. J.; KOTHE, D. B.; PUCKETT, E. G.; ALEINOV, I. D. Accurate and robust methods for variable density incompressible flows with discontinuities. *Barriers and Challenges in Computational Fluid Dynamics*, p. 213–230, 1998.

ROACHE, P. J. Numerical study of the turbulent flow past an airfoil with trailing edge separation. *AIAA Journal*, American Institute of Aeronautics and Astronautics, v. 36, n. 05, p. 696–702, 1998.

ROACHE, P. J. *Verification and Validation in Computational Science and Engineering*. [S.l.]: Hermosa Publishers, 1998.

ROBIN, V.; CHAMPION, M.; MURA, A. A Second-Order Model for Turbulent Reactive Flows with Variable Equivalence Ratio. *Combustion Science and Technology*, v. 180, n. 10, p. 1709–1734, out. 2008.

ROBIN, V.; MURA, a.; CHAMPION, M.; DEGARDIN, O.; RENOU, B.; BOUKHALFA, M. Experimental and numerical analysis of stratified turbulent V-shaped flames. *Combustion and Flame*, v. 153, p. 288–315, dez. 2007.

ROGALLO, R. S. Numerical experiments in homogeneous turbulence. *Nasa Technical Memorandum*, v. 81, n. 81835, 1981.

ROLLER, S.; MUNZ, C. A low Mach number scheme based on multi-scale asymptotics. *Computing and Visualization in Science*, Springer, v. 3, n. 1, p. 85–91, 2000.

SABEL'NIKOV, V.; GOROKHOVSKI, M.; N, B. The extended iem mixing model in the framework of the composition pdf approach: Applications to diesel spray combustion. *Combustion Theory and Modelling*, Taylor & Francis, v. 10, n. 1, p. 155–169, 2006.

SALARI, K.; KNUPP, P. M. Code verification by the method of manufactured solutions. *Sandia Report*, 2000.

SCHLICHTING, H. *Boundary-Layer Theory*. 7. ed. London - UK: McGraw-Hill Classical Textbook Reissue, 1951.

SCHNEIDER, G. E.; ZEDAN, M. A modified strongly implicit procedure for the numerical solution of field problems. *Numerical Heat Transfer*, v. 4, p. 1–19, mar. 1981.

SCHUMANN, U. Large-eddy simulation of turbulent diffusion with chemical reactions in the convective boundary layer. *Atmospheric Environment (1967)*, v. 23, n. 8, p. 1713 – 1727, 1989.

SCOTTI, A.; MENEVEAU, C.; LILLY, D. K. Generalized Smagorinsky model for anisotropic grids. *Physics of Fluids A: Fluid Dynamics*, v. 5, n. 9, p. 2306, 1993.

SELLE, L.; LARTIGUE, G.; POINSOT, T.; KOCH, R.; SCHILDMACHER, K. U.; KREBS, W.; PRADE, B.; KAUFMANN, P.; VEYNANTE, D. Compressible large eddy simulation

of turbulent combustion in complex geometry on unstructured meshes. *Combustion and Flame*, v. 137, n. 4, p. 489 – 505, 2004.

SHEN, W. Z.; MICHELSEN, J. a.; SORENSEN, J. N. Improved Rhie Chow Interpolation for Unsteady Flow Computations. *AIAA Journal*, v. 39, n. 12, p. 2406–2409, dez. 2001.

SHUNN, L.; KNUPP, P. Verification of low-mach number combustion codes using the method of manufactured solutions. *CSRI SUMMER PROCEEDINGS 2007*, p. 126–136, 2007.

SILVA, C. B. D.; MéTAIS, O. Vortex control of bifurcating jets: A numerical study. *Physics of Fluids*, v. 14, n. 11, p. 3798–3819, 2002.

SILVA, C. B. D.; PEREIRA, J. C. F. The effect of subgrid-scale models on the vortices computed from large-eddy simulations. *Physics of Fluids*, v. 16, n. 12, p. 4506, 2004.

SILVA, L. F. Figueira da; AZEVEDO, J. L.; KORZENOWSKI, H. Unstructured adaptive grid flow simulations of inert and reactive gas mixtures. *Journal of Computational Physics*, v. 160, n. 2, p. 522–540, 2000.

SILVEIRA-NETO, A. Turbulência nos fluidos aplicada. *Apostila da Disciplina Mecânica dos Fluidos do Programa de Pós-Graduação da Universidade Federal de Uberlândia*, v. 1, 2002.

SILVEIRA-NETO, A.; GRAND, D.; MÉTAIS, O.; GONZE, M.; LESIEUR, M. A numerical investigation of the coherent vortices in turbulence behind a backward-facing step. *Journal of Fluid Mechanics*, v. 256, p. 1–25, 1993.

SMAGORINSKY, J. General circulation experiments with the primitive equations. *Monthly Weather Review*, American Meteorological Society, v. 91, n. 3, p. 99–164, 1963.

SMIRNOV, A. Random flow generation procedure technical manual. p. 1–13, 2004.

SMIRNOV, A.; SHI, S.; CELIK, I. Random flow generation technique for large eddy simulations and particle-dynamics modeling. *Journal of Fluids Engineering*, v. 123, p. 359–371, 2001.

SOTERIOU, M.; GHONIEM, A. Effects of the free-stream density ratio on free and forced spatially developing shear layers. *Physics of Fluids*, v. 7, n. 8, p. 2036, 1995.

SPALDING, D. B. Mixing and chemical reaction in steady confined turbulent flames. *Thirteenth Symposium International on Combustion*, The Combustion Institute, Pittsburgh, v. 13, p. 649–657, 1971.

STANLEY, S. A.; SARKAR, S. Influence of Nozzle Conditions and Discrete Forcing on the Developing Region of Turbulent Planar Jets. *AIAA Journal*, Lawrence Berkeley National Lab., CA (US), v. 38, n. LBNL-43150, p. 1–40, 1999.

STEINBERG, S.; ROACHE, P. J. Symbolic manipulation and computational fluid dynamics. *Journal of Computational Physics*, v. 57, n. 2, p. 251–284, 1985.

STROZZI, C.; SOTTON, J.; MURA, A.; BELLENOUE, M. Experimental and numerical study of the influence of temperature heterogeneities on self-ignition process of methane-air mixtures in a rapid compression machine. *Combustion Science and Technology*, v. 180, n. 10-11, p. 1829–1857, 2008.

TABOR, G.; BABA-AHMADI, M. Inlet conditions for large eddy simulation: A review. *Computers & Fluids*, v. 39, n. 4, p. 553–567, 2010.

TODDE, V.; SPAZZINI, P. G.; SANDBERG, M. Experimental analysis of low-Reynolds number free jets Evolution along the jet centerline and Reynolds number effects. *Experiments in Fluids*, v. 3, n. 47, p. 279–294, 2009.

TURKEL, E. Review of preconditioning methods for fluid dynamics. *Applied Numerical Mathematics*, v. 12, n. 1-3, p. 257–284, 1992.

TURKEL, E.; RADESPIEL, R.; KROLL, N. Assessment of preconditioning methods for multidimensional aerodynamics. *Computers & Fluids*, v. 26, n. 6, p. 613 – 634, 1997.

TURNS, S. R. *An introduction to combustion: Concepts and applications*. 2. ed. [S.l.]: McGraw-Hill, 2000.

UZUN, A. *3-D large eddy simulation for jet aeroacoustics*. 2003 p. Thesis (Doctor of Philosophy) — Purdue University, 2003.

VEDOVOTO, J. M.; NETO, A. da S.; MURA, A.; SILVA, L. F. F. da. Application of the method of manufactured solutions to the verification of a pressure-based finite-volume numerical scheme. *Computers & Fluids*, v. 51, n. 1, p. 85 – 99, 2011.

VERSTEEG, H. K.; MALALASEKERA, W. *An Introduction to Computional Fluid Dynamics: The Finite Volume Method*. [S.l.]: Pearson Education, 2007.

VEYNANTE, D.; TROUVé, A.; BRAY, K. N. C.; MANTEL, T. Gradient and counter-gradient scalar transport in turbulent premixed flames. *Journal of Fluid Mechanics*, v. 332, p. 263–293, 1997.

VILLAR, M. *Análise numérica detalhada de escoamentos multifásicos bidimensionais*. Thesis (Doctorate) — Universidade Federal de Uberlândia, Uberlândia, 2007.

VILLERMAUX, J.; DEVILLON, J. C. Representation de la coalescence et de la redispersion des domaines de segregation dans un fluide par un modele d'interaction phenomenologique. *Second International Symposium on Chemical Reaction Engineering*, p. 1–13, 1972.

VINCOVIK, I. *Dispersion et Mélange Turbulents de Particules Solides et de Gouttelettes par Une Simutation des Grandes Échelles et Une Modélisation Stochastique Lagrangienne*. 225 f. Thesis (Doctorate) — L'Ecole Central de Lyon, Lyon, 2005.

VORST, H. A. van der. Iterative solution methods for certain sparse linear systems with a non-symmetric matrix arising from pde-problems. *Journal of Computational Physics*, v. 44, n. 1, p. 1 – 19, 1981.

WANG, D. *Variable step size implicit explicit linear multistep methods for time dependent variables*. Thesis (Doctorate) — Simon Fraser University, 2005.

WANG, Y.; TROUVé, A. Artificial acoustic stiffness reduction in fully compressible, direct numerical simulation of combustion. *Combustion Theory and Modelling*, v. 8, n. 3, p. 633–660, set. 2004.

WESTBROOK, C. K.; MIZOBUCHI, Y.; POINSOT, T. J.; SMITH, P. J.; WARNATZ, J. Computational combustion. *Proceedings of the Combustion Institute*, v. 30, n. 1, p. 125 – 157, 2005.

WILLIAMS, F. A. *Combustion Theory*. [S.l.]: The Benjamin/Cummings Publishing Company, Inc., 2nd ed., 1985.

XU, G.; ANTONIA, R. A. Effect of different initial conditions on a turbulent round free jet. *Experiments in Fluids*, v. 33, p. 677–683, 2002.

YILMAZ, S. *RANS/PDF and LES/FDF for prediction of turbulent premixed flames*. Thesis (Doctorate), University of Pittsburg, 2008.

YILMAZ, S.; NIK, M.; SHEIKHI, M.; STRAKEY, P.; GIVI, P. An irregularly portioned lagrangian monte carlo method for turbulent flow simulation. *Journal of Scientific Computing*, Springer Netherlands, v. 47, p. 109–125, 2011. 10.1007/s10915-010-9424-8.

YOSHIZAWA, A.; FUJIWARA, H.; ABE, H.; MATSUO, Y. Mechanisms of countergradient diffusion in turbulent combustion. *Physics of Fluids*, v. 21, n. 1, p. 015107, 2009.

ZHANG, Y. Z.; HAWORTH, D. C. A general mass consistency algorithm for hybrid particle/finite-volume pdf methods. *Journal of Computational Physics*, v. 194, n. 1, p. 156 – 193, 2004.